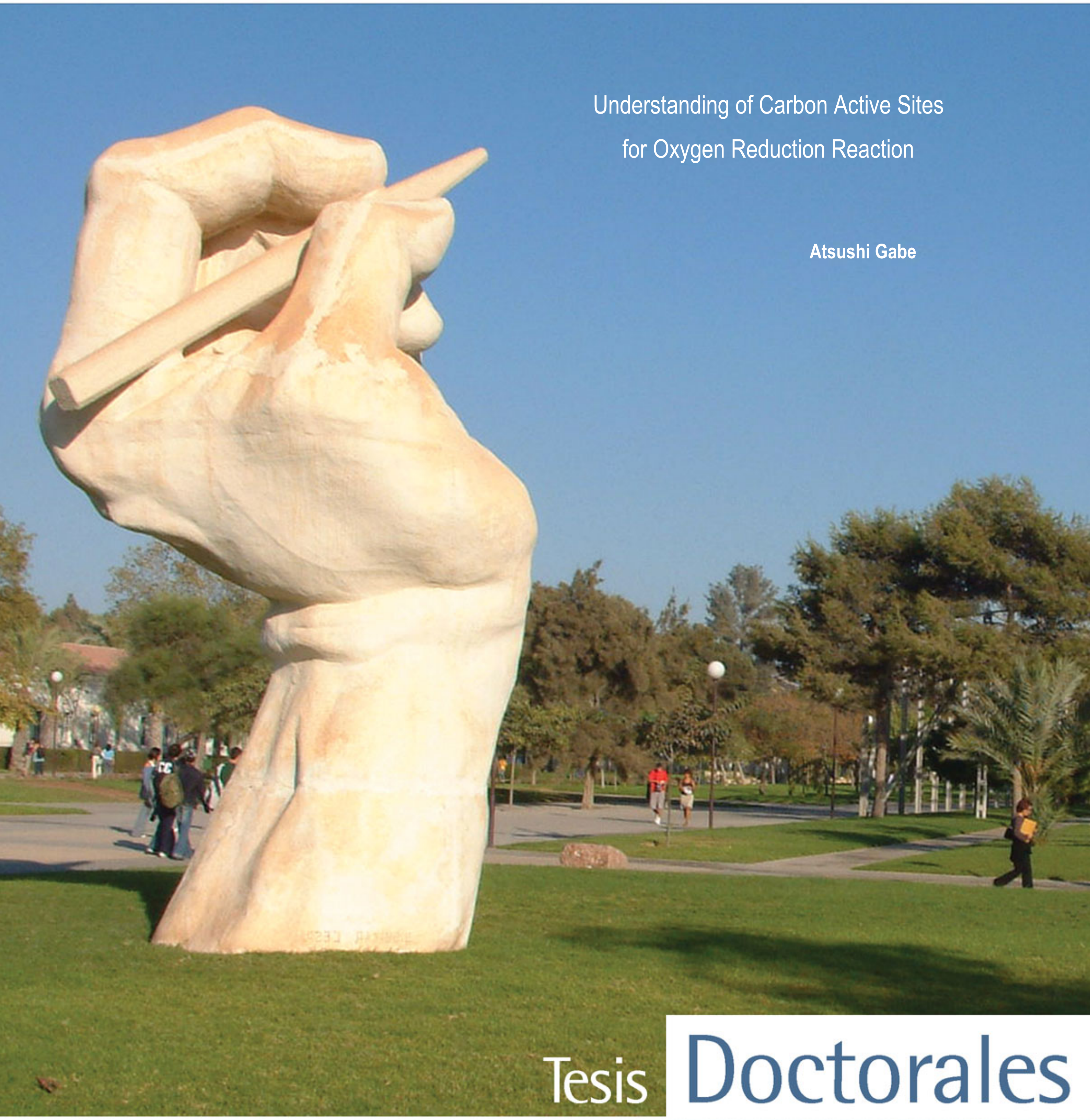

Understanding of Carbon Active Sites for Oxygen Reduction Reaction

Atsushi Gabe

Universitat d'Alacant
Universidad de Alicante

Grupo de Materiales Carbonosos y Medio Ambiente
Instituto Universitario de Materiales

Understanding of Carbon Active Sites for Oxygen Reduction Reaction

Atsushi Gabe

Tesis presentada para aspirar al grado de
DOCTOR POR LA UNIVERSIDAD DE ALICANTE

Doctorado en Ciencia de Materiales

Dirigida por:

Diego Cazorla Amorós	**Emilia Morallón Nuñez**
Catedrático de Química Inorgánica	*Catedrática de Química Física*

Alicante, Septiembre de 2018

Acknowledgements

Firstly, I would like to thank all people who have supported me during the PhD Thesis. Especially, I sincerely appreciate Prof. Diego Cazorla Amorós and Prof. Emilia Morallón Nuñez for the opportunity to be here and supervising me for the PhD Thesis. Their guidance helped me all of the time. Por las horas de discusión y todas las oportunidades que me han brindado para completar esta Tesis.

I would like to thank Heiwa Nakajima Foundation and MINECO (CTQ2015-66080-R) for the financial support.

Quiero agradecer también a todos las personas que integran el grupo de MCMA y GEPE de la Universidad de Alicante, por sus discusiones y buenos momentos pasados juntos, cafés, comidas etc.

最後に、スペインでの研究生活を常に支えて下さり、色々な面で私を理解し応援してくれた日本の家族に深く感謝致します。また、アリカンテでの生活を明るく楽しく、時には励まし続けてくれた香織、絵真、ブッチに心より感謝します。本当にありがとうございました。

Index

Objectives and structure of the PhD Thesis

1, Objectives of the PhD Thesis

The main objective of this PhD thesis is to deepen in the understanding of the performance of electrocatalysts for oxygen reduction reaction based on carbon materials. In order to get knowledge about the nature of active sites of these catalysts for oxygen reduction reaction, the three projects described below were conducted during the thesis period, which constitute the specific objectives of the work done.

1, "Understanding of Oxygen Reduction Reaction by examining carbon-oxygen gasification reaction and carbon active sites on metal and heteroatoms free carbon materials of different porosities and structure"

2, "Modeling of Oxygen reduction reaction in porous carbon materials in alkaline medium. Effect of microporosity"

3, "Key factors improving oxygen reduction reaction activity in cobalt nanoparticles modified carbon nanotubes"

2, Structure of the PhD Thesis

The PhD Thesis has been performed in two groups Materiales Carbonosos y Medio Ambiente (MCMA) and Grupo de Electrocatálisis y Electroquímica de Polímeros (GEPE), both belonging to the Materials Institute at the Universidad de Alicante.

This PhD Thesis is divided into 6 chapters which are briefly described below.

Chapter 1, General introduction

This general introduction is divided into four sections. Firstly, general information regarding structure of carbon materials is explained. Secondly, detailed information for the carbon materials used in this PhD Thesis is presented, followed by the description of surface chemistry and porous texture of carbon materials. Finally, their applications especially in energy generation in fuel cells are explained.

Part of this chapter has been published in the following book chapter, Atsushi Gabe, María José Mostazo-López, David Salinas-Torres, Emilia Morallón and Diego Cazorla-Amorós. Synthesis of conducting polymer/carbon material composites and their application in electrical energy storage. Hybrid Polymer Composite Materials, 173-209, chapter 8, 2017.

Chapter 2, Experimental section

Reagents and materials used for synthesis of the samples and experiments performed are described. Afterwards, different experimental techniques used for physicochemical and electrochemical characterization, employed during the PhD Thesis are presented. More details for experimental conditions will be described in each chapter.

Chapter 3, Understanding of oxygen Reduction Reaction by examining carbon-oxygen gasification reaction and carbon active sites on metal and heteroatoms free carbon materials of different porosities and structure.

Considering the nature of the carbon-oxygen interaction in active sites during the gasification reaction, it could be inferred that the sites for this reaction are the same as those participating in the ORR. In this chapter, metal and heteroatoms free ORR carbon catalysts including different structures and porosities were selected. The selected samples were extensively characterized regarding structural and electrochemical properties. Finally, the relationship between ORR activities and carbon-oxygen gasification properties (ASA and reactivity) were quantitatively examined.

Chapter 4, Modeling of oxygen reduction reaction in porous carbon materials in alkaline medium. Effect of microporosity.

The role of microporosity in the performance of carbon materials as ORR catalysts in alkaline medium was investigated. A highly microporous KOH-activated carbon and a microporous char have been prepared and their ORR performance were compared to that of two commercial carbon blacks with low and high surface areas. We demonstrated that the ORR is described by a two-wave process, where oxygen is reduced to hydrogen peroxide in a first step, while hydrogen peroxide is subsequently reduced to water.

In accordance to these findings, a model that takes into account both charge transfer reactions and the mass transfer rate of O_2 and H_2O_2 has been proposed. Finally, the validity of the proposed model for fitting the experimental electrochemical response during ORR of the porous carbon materials of different porosities was analyzed.

Chapter 5, Key factors improving oxygen reduction reaction activity in cobalt nanoparticles modified carbon nanotubes.

ORR catalysts doped with non-noble metal and heteroatom were prepared. In this chapter, as a candidate of non-noble metal Co was selected. In addition, nitrogen was doped on the catalysts. CNTs were employed as a supporting materials. Several conditions were investigated to elucidate the relationships between properties of CoOx, such as amount of CoOx, NPs sizes, chemical composition and oxidation states of Co, and ORR activities. A simple synthesis procedure of CoOx NPs supported on CNTs that achieved high ORR catalytic activity with only 1 wt.% of Co NP, is presented and insights into the factors governing the high catalytic activity are discussed. Finally, stability of the Co-containing catalyst was measured to confirm that they are interesting as catalysts for alkaline fuel cells.

These results were published in;
Atsushi Gabe, Jaime García-Aguilar, Ángel Berenguer-Murcia, Emilia Morallón, Diego Cazorla-Amorós. Key factors improving oxygen reduction reaction activity in cobalt nanoparticles modified carbon nanotubes. Applied Catalysis B: Environmental 217 (2017) 303–312

Chapter 6, General conclusions

This chapter contains the main conclusions of the PhD Thesis.

Chapter 7, Resumen y *conclusiones generales*

Este capitulo contiene un resumen del trabajo de Tesis que incluye una introducción general un resumen de las resultados de la discusiones organizado que acuerdo con los capitulo presentados tambien se incluyen las conclusions generals.

Chapter 1.

General introduction

Carbon materials have received much attention because of their variety of attractive structures, properties and applications. This general introduction is divided into four sections. Firstly, general information regarding structure of carbon materials are explained. Afterwards, detailed information for the carbon materials used in this PhD Thesis followed by surface chemistry and porous texture of carbon materials are described. Finally, their applications especially in the energy generation in fuel cells are explained.

1-1, Structure of carbon materials

All elements are unique, but carbon is especially exceptional [1]. Carbon is found in very different forms with varying micro-textures [2]. Carbons of widely differing properties can be prepared by starting with different precursors (in form of solids, liquids and gases) and treating these materials in various ways [3]. The diverse structures, morphologies and properties of carbon materials make them attractive materials that can be used in a large range of applications in engineering and science [2,3]

Since the 1960s various novel carbon materials have been developed. Carbon fibers derived from polyacrylonitrile (PAN), pyrolytic carbons produced by chemical vapor deposition of hydrocarbons and glass-like carbons derived from non-graphitizable precursors were invented. These had very different structures and textures from the conventional carbon materials (exemplified by graphite, carbon blacks and activated carbons) [4]. Furthermore, the discoveries of fullerenes in 1985 and of carbon nanotubes in 1991 opened a completely different perspective from that of carbon materials based on flat graphite-like hexagonal layers. At the same time, fullerenes and carbon nanotubes have given scientists who have worked on carbon materials related with graphite, a chance to revisit the hybrid orbitals ($sp + 2p$, $sp^2 + p$ and sp^3) for constructing C–C bonds [5].

Considering the huge synthetic and structural possibilities of carbon materials, they could be classified into classic and new carbon forms and the classic materials include graphite, activated carbon and carbon blacks; new carbon forms contain carbon materials developed since 1960 such as carbon fibers, glassy carbons, diamond-like carbons, and recent low-dimensional carbons, e.g., fullerenes, carbon nanotubes, and graphene [6]. Carbon materials produced when either their size or their structure were controlled at the nanometer scale are also defined as nanocarbons [5].

In summary, carbon is a fascinating element that can adopt different hybridizations: sp, sp^2 and sp^3 (Figure 1). The most often explored systems today remain sp^2 hybridized forms of carbon (Figure 1). New challenges for exploration of sp and sp^3 at the nanoscale level are now required [7]. Research on carbon-based materials is a very dynamic and growing area of study with nearly unlimited possibilities [6].

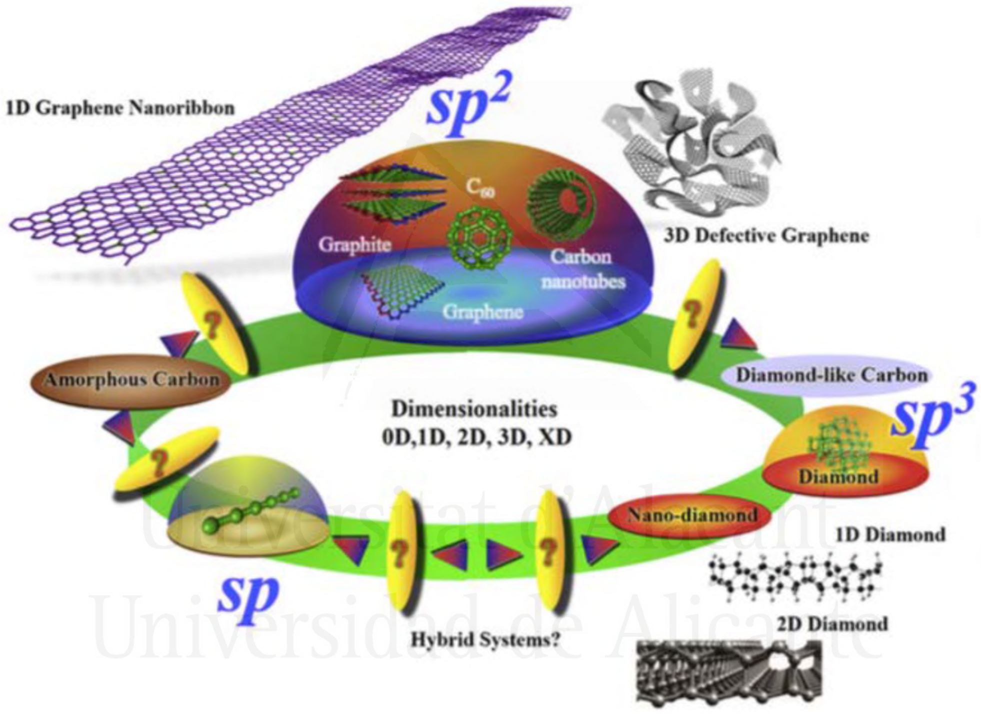

Figure 1. Diversity of carbon materials based on their hybridization. It is noteworthy that sp^2 hybridized carbon is currently the most explored subject while sp and sp^3 hybrids await exciting discoveries in the coming years [7].

Information of graphite, carbon blacks, activated carbons and carbon nanotubes, which were mainly used as the samples in this PhD Thesis, is presented in the sections from 1-1-1 to 1-1-4.

1-1-1, Graphite

Graphite is remarkable for the large variety of materials that can be produced from its basic form such as extremely strong fibers, easily sheared lubricants, gas-tight barriers, and gas adsorbents [1]. High-purity graphite is well known to have high electrical conductivity while its natural scarcity and high price will hinder the mass production [8]. As hybrid of graphite and clay (such as SiO_2, Al_2O_3), pencil rods are low-cost, meanwhile retaining relatively high conductivity, which have been applied as negative electrode in lithium–ion batteries [9], Li-air battery and zinc oxide ultraviolet sensor [8].

All these diverse materials have one characteristic in common: they are all built upon the trigonal sp^2 bonding of carbon atoms [1]. Graphite is a well-established allotrope of carbon and composed of series of stacked parallel layer planes as shown in Figure 2 with the trigonal sp^2 bonding. Within each layer plane, the carbon atom is bonded to three others through 3 σ bonds forming a series of continuous hexagons, leaving one electron to participate in delocalized π bonding. The bond is covalent and has a short length (0.141 nm) and high strength (524 kJ/mole) [1,10].

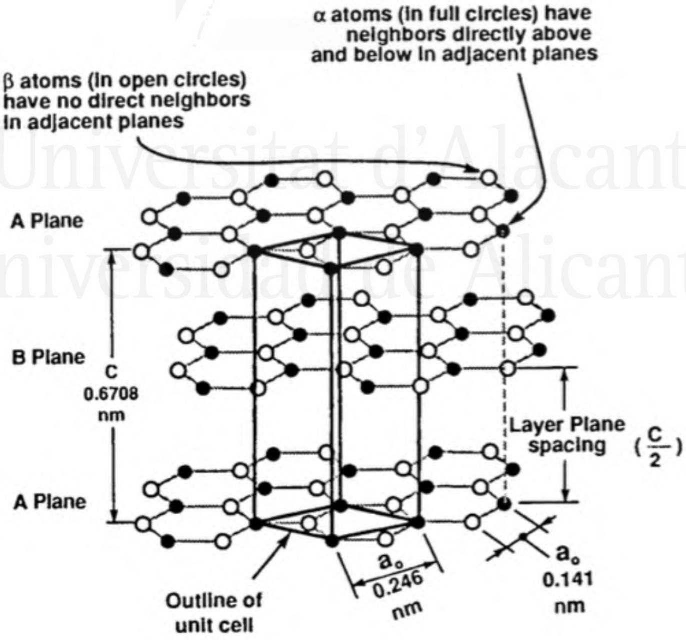

Figure 2. Crystal structure of graphite showing ABAB stacking sequence and unit cell. [1].

1-1-2, Activated carbon

Activated carbons (ACs) are porous materials with high surface areas and tunable surface chemistry that enable their use in a wide range of applications, such as wastewater treatment, gas separation and purification, catalysis and, more recently, energy storage [11–16]**.** ACs are usually synthesized with a relatively small amount of chemically bonded heteroatoms (mainly oxygen and hydrogen). In addition, activated carbons may contain up to 15% of mineral matter (the nature and amount is a function of the precursor), which is usually given as ash content [11]. It is now generally accepted that the average structure (Figure 3(a)) consists of aromatic sheets and strips, often bent and resembling a mixture of wood shavings and crumpled paper, with variable gaps of molecular dimensions between them, these being the micropores [17]. Moreover, ACs have graphite-like units, and they obviously deviate from the pure microcrystalline graphite in terms of orientation and curvature. The dimension of these units varies but in general there are about three or four graphite layers with interlayer spacings of about 0.344 - 0.365 nm. The microcrystalline length is of the order of 10 nm. In terms of orientation, these microcrystalline units are arranged in a random fashion with strong cross-linking between them (Figure 3(b)). This cross-linking region is disordered and is composed of a lattice of carbon hexagons (Figure 3(b)) [18].

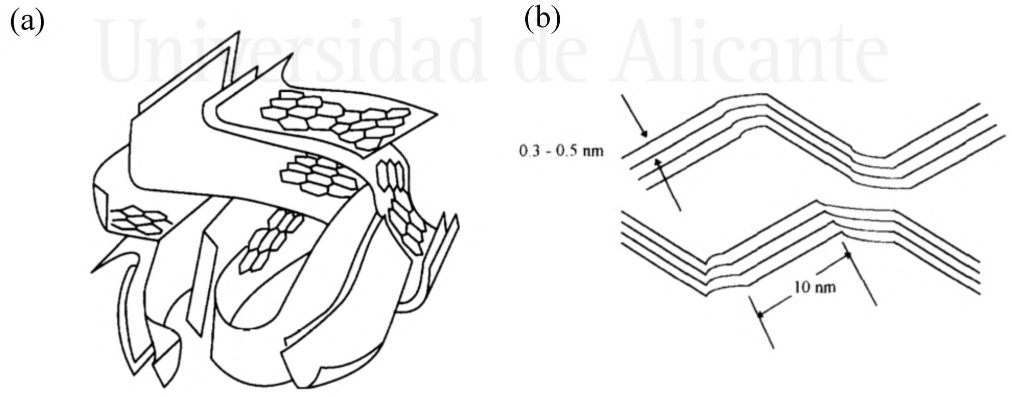

Figure 3. (a) Schematic representation of the structure of ACs [17], (b) Microcrystalline orientation of ACs [18].

1-1-3, Carbon Blacks

Nowadays, among all kinds of carbon supports, carbon blacks are the most commonly used due to their wide mesopores distribution and their graphite characteristics. There are many types of carbon blacks, such as acetylene black, Ketjen Black, Black Pearl, or Vulcan XC-72 [19]. Vulcan XC-72 is the most frequently used in the preparation of commercial electrocatalysts because of its good compromise between electrical conductivity and high surface area [19]. Indeed, platinum supported on Vulcan XC72 is still the most widely used electrocatalyst in low temperature polymer electrolyte fuel cells for both the anode and the cathode reaction [20]. The crystalline graphitic portion of carbon black has sp^2 hybridization [2]. Figure 4 shows a sketch of a carbon black primary particle, aggregates and agglomerates [21]. The carbon black has a quasi-graphitic structure. A few layers form crystallites, which combine to form “spherical” primary particles, the diameter of which are in the order of 50 nm [22]. The primary particles continue to grow into aggregates and form agglomerates (~250 nm diameter) [23], with the exception of some special carbon blacks [22]. An aggregate represents the carbon black unit. By Van der Waals interactions or by external mechanical energy, the aggregates are more or less agglomerated and the resistance to this agglomeration process is dependent on the charge carrier concentration [22].

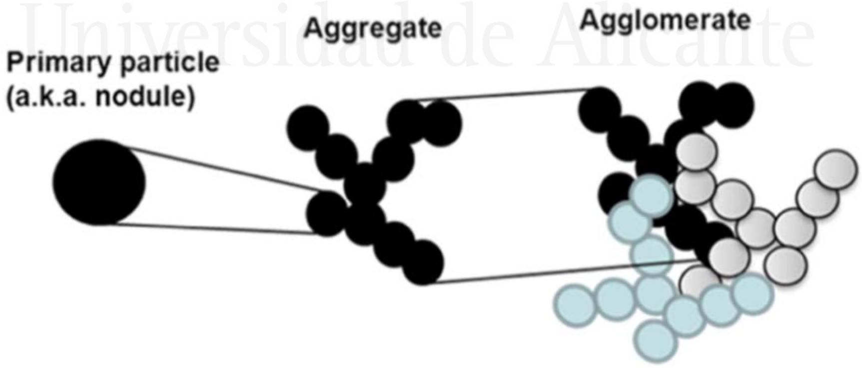

Figure 4. Sketch of a carbon black primary particle, aggregates and agglomerates [21].

1-1-4, Carbon nanotube

Carbon nanotubes (CNTs) caused tremendous interest when Sumio Iijima published his paper in Nature in 1991 [24]. From the discovery of CNTs and after the reports about the experimental conditions for the synthesis of large quantities of CNTs, an intensive investigation in this field has been done [25].

CNTs are attracting a lot of attention due to their high stability, mechanical properties, high degree of order, high thermal (>3000 W m^{-1} K^{-1}) and electrical (≈10^3 S cm^{-1}) conductivities and high surface area (80 - 900 m^2 g^{-1}) [26,27] and thus CNTs based samples show the possibility of many applications in different fields [28–31].

In general, carbon nanotubes can be categorized into several forms such as single-walled carbon nanotubes (SWCNTs), multi-walled carbon nanotubes (MWCNTs) and bamboo-structured carbon nanotubes [28] while SWCNTs and MWCNTs are principle forms of CNTs. Figure 5 shows the model of SWCNTs and MWCNTs.

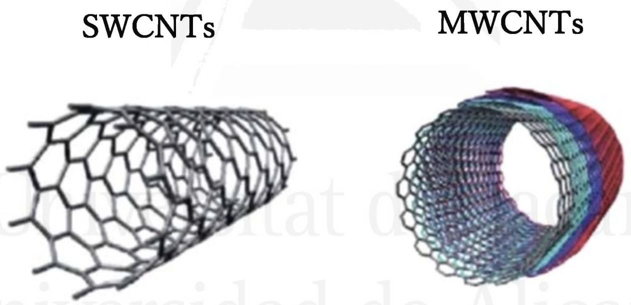

Figure 5. Model for SWCNTs and MWCNTs [29].

As shown in Figure 5, structurally, SWCNTs consist of a single tube of "rolled up" graphite sheet whereas MWCNTs consist of several concentric tubes of graphite fitted one inside the other. The diameter of a CNTs can range from just a few nanometers in the case of SWCNTs to tens of nanometers for MWCNTs [10,32]. The graphene sheet of SWCNTs can be formed into a tube in different ways and depending on the chiral angle θ (or "rolling direction"), "armchair", "zigzag" or "chiral" tubes can be differentiated. This rolling direction determines the electrical nature (conductor or semiconductor) and the mechanical properties of the material [25]. MWCNTs can be produced as "hollow-tube" form where the axis of the graphite planes is parallel to the axis of the nanotube, "herringbone" form where the graphite planes are formed at an angle to the axis of the tube or finally in a "bamboo-like" form which is similar to the herringbone form except that the nanotubes are periodically closed along the length of the tube into compartments rather like bamboo or a "stack of paper cups fitted one inside the other", Figure 6 [10,33,34].

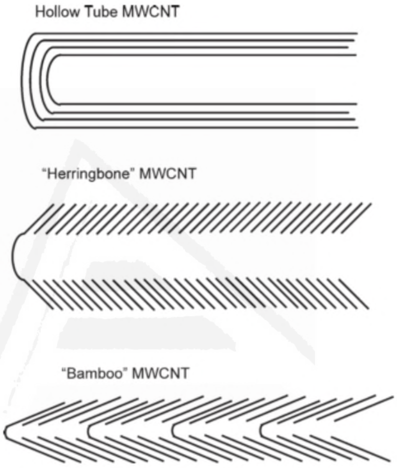

Figure 6. A schematic cross-section through a "hollow-tube", "herringbone" and "bamboo" MWCNT showing the orientation of the graphene sheets within the tube [10].

1-2, Surface chemistry of Carbon Materials

Surface chemistry has a significant influence on the physicochemical properties of the carbons materials. Therefore, their performance in applications such as the dispersions in liquids, the dispersion of metallic compounds and the adsorption of vapors on carbons can be very different [35–38].

Thanks to valuable published results and the development and spreading of new analytical tools, it is possible to find nowadays a whole body of technical literature that deals with the measurement and characterization of surface functional groups structure [38,39].

Indeed, there are two functionalization methods, covalent and non-covalent functionalization for modification of surface chemistry of the carbon materials [38].

1-2-1, Non-covalent bonding

While the basal plane is far to be inactive, the high π electron density of the basal plane increases the dispersive adsorption potential of graphene [40], allowing noncovalent functionalization and providing for some basicity to the carbon surface[41]. In addition, the noncovalent functionalization by π-interactions (as in the case of carbon nanotubes) is an attractive synthetic method, because it offers the possibility of attaching functional groups to graphene without disturbing the electronic network [42]. In this case, polymers, surfactants, enzymes, proteins, and amino-containing molecules, among others, have been extensively used for application as electrochemical sensors and biosensors [31,43,44]

1-2-2, Covalent bonding

In order to tailor the properties of the carbon material by the addition of certain heteroatoms or molecules, covalent functionalization has been strongly developed. The incorporation of heteroatoms like oxygen, nitrogen, sulfur, phosphorus and boron is not difficult compared to grafting of other organic molecules in which the yield of the process is generally low and is mainly applicable to carbon nanostructures like CNTs, carbon nanofibers, and graphene [38]. Substitutional doping of heteroatoms to various carbon materials, including graphene, graphite, porous carbons, carbon nanotubes and nanofibers, and fullerenes, has attracted attention as one of possible techniques for modifying the electronic and chemical properties of carbon [45]. For instance, the presence of heteroatoms (N, P, S, or B) in the carbon network has an impact on the electro-donor/acceptor properties or wettability, which directly influences the final material performance [46,47]

Basal and edge carbon atoms are considered as two different sites distinguished in their interactions with other molecules and in their susceptibility to undergo chemical reactions. The reactivity of the carbon surface is also linked to its disordered fraction, which contains a large number of imperfections and defects (e.g., structural carbon vacancies, nonaromatic rings). These imperfections and defects along the edges of graphene layers are the most active sites, owing to the high density of unpaired electrons [48–50]. Therefore, on the edges of graphene layers, heteroatoms such as oxygen, hydrogen, nitrogen, and sulfur can be chemisorbed, leading to stable surface compounds [51].

1-2-3, Oxygen functional groups

Many properties of carbon materials, in particular their wetting and adsorption behavior, are decisively influenced by chemisorbed oxygen [52]. In addition, electrochemical performance (e.g specific capacitance by means of pseudocapacitive processes) of carbon materials can be significantly improved through the introduction of oxygen on carbons [36,53–55]. Oxygen-containing groups are the most common functionalities present on the carbon surface [51] and can be bound in the form of various functional groups which are similar to those known from organic chemistry [52].

Wet oxidation [56,57] and dry oxidation [58–60] methods are traditional routes to introduce surface oxygen complexes, while there are numerous methods for the determination of various types of oxygen surface functionalities on carbon materials such as acidimetric titration techniques, infrared spectroscopy, X-ray photoelectron spectroscopy (XPS), temperature-programmed desorption (TPD), electrokinetic measurements, and cyclic voltammetry [52,55,57,60–63].

Traditionally, surface oxygen groups are considered as acidic and basic nature [52,64]. The most habitual surface oxygen groups on graphene layer are illustrated in Figure 7. The surface oxygen complexes would decompose upon heating and release CO and/or CO_2 at different temperatures. General trends are that a CO_2 peak results from carboxylic acids at low temperatures, or lactones at high temperatures; carboxylic anhydrides simultaneously generate a peak for CO and a peak for CO_2; phenols and carbonyls generate a CO peak [62,63,65].

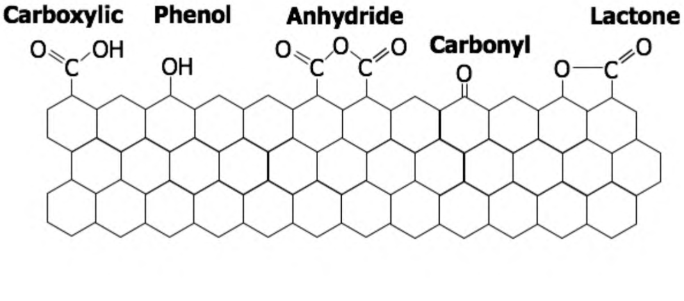

Figure 7. Structures of surface oxygen functional groups present at edge carbon.

1-2-4, Nitrogen functional groups

In contrast to oxygen functionalities, nitrogen-containing functionalities are not formed spontaneously on carbon surfaces by contact with air. Usually, the nitrogen content in carbonaceous materials is very small unless it is a constituent of the carbon precursor, for example, carbazole, nitrogen-enriched polymers, acridine, or melamine. Treatment with nitrogen-containing reagents (e.g., ammonia, urea, melamine, HCN) is another way of introducing nitrogen to the carbon matrix [51]. Presence of nitrogen has been shown to be the key parameter for the performance of carbon materials as adsorbents, catalyst supports, and for catalytic activity such as removal of NOx and SOx and acetaldehyde adsorption [16,66,67]

Furthermore, some studies have shown that the modification of the carbon materials with nitrogen species causes the improvement in the electrochemical charge storage with changing electronic structure [68–70]. This change in the electrochemical performance can be related with the improvement in the wettability, surface polarity, electrical conductivity, electron transfer rate, stability, decrease of electron spin resonance, contribution of space-charge-layer capacitance or pseudocapacitance [69,71].

Many efforts have been focused on understanding the effect of the incorporation of N-functional groups into the carbon network on the electrochemical properties of the resulting materials. For this purpose, it is necessary to know which kind of species can be formed under certain synthesis conditions. At this point, the monitoring of the evolution of the nitrogen species with the temperature is a powerful tool to produce particular nitrogen groups and allows clarifying the real effect on the material [46,71].

Mainly, three types of N atoms doped in graphene layer are identified; pyridinic, pyrrolic and graphitic as shown schematically in Figure 8 [45,67]. Kuroki and coworkers observed with a solid-state NMR study that amine groups of the benzenoid unit lead to pyrrole and N-quaternary (graphitic) groups, whereas mostly pyridine species were obtained from quinoid at 600 °C. When temperature is increased up to 800 °C, the amount of five-membered rings containing nitrogen atom diminishes, while the amount of six-membered rings increases [72]. It is noteworthy to mention that the surface chemistry of final carbon material can be tailored by controlling the temperature conditions [46,73].

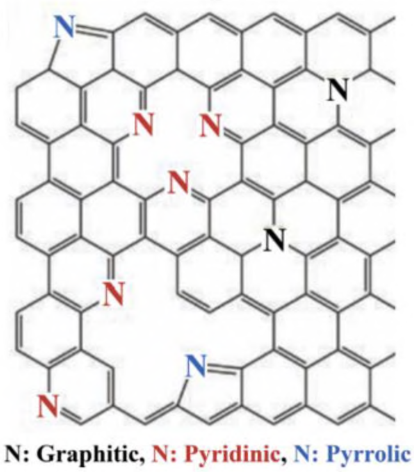

Figure 8. Various configurations of N atoms doped in graphene layer [45].

1-2-5, P, B and S doping

Other heteroatoms such as phosphorus, boron and sulfur also can be doped on carbon materials [74–78]. Oxidation resistance is a crucial feature in the development of durable C/C composites for engineering applications [74]. Doping of boron and phosphorus show an important oxidation inhibition effect and have been studied for a long time [74,79,80]. Sulfur doping on carbon materials can be profited in heterogeneous catalysis, adsorbents of specific contaminants from liquid phase or toxic gases and energy conversion/storage [81]. While effect of phosphorus, boron and sulfur on the capacitance enhancement has not been clearly demonstrated [46], recent studies have proven that metal free carbon materials doped with heteroatom (e.g. B, P or S) have shown striking electrocatalytic performance for oxygen reduction reaction and become an important category of potential candidates for replacing Pt-based catalysts [82].

1-3, Porous texture of Carbon Materials

Porous carbon materials or ACs are characterized by their highly developed internal surface area and porosity. Especially the development of micro- and mesopores is of great importance in a wide variety of industrial applications because it allows the carbons to adsorb large amounts and various types of chemicals from gases or liquids, such as VOC (Volatile Organic Compounds), inorganics and heavy metal pollutants [11,83–87] Furthermore, since ACs are highly porous and they have large internal surface areas per unit weight [17], ACs are the most widely used as electrodes for electrochemical double layer capacitors (EDLCs) [69,88,89].

Physical (CO_2, steam or a combination of both) and chemical (phosphoric acid, zinc chloride, KOH and NaOH) activation processes are well-known studied strategies to produce highly porous carbons from carbonaceous precursors [12,90–92]. The activation process leads to the development of a porous carbon network in the bulk of the carbon particles; micropores (< 2 nm), mesopores (between 2 and 50 nm) and macropores (larger than 50 nm size) are randomly created as illustrated in Figure 9 [88].

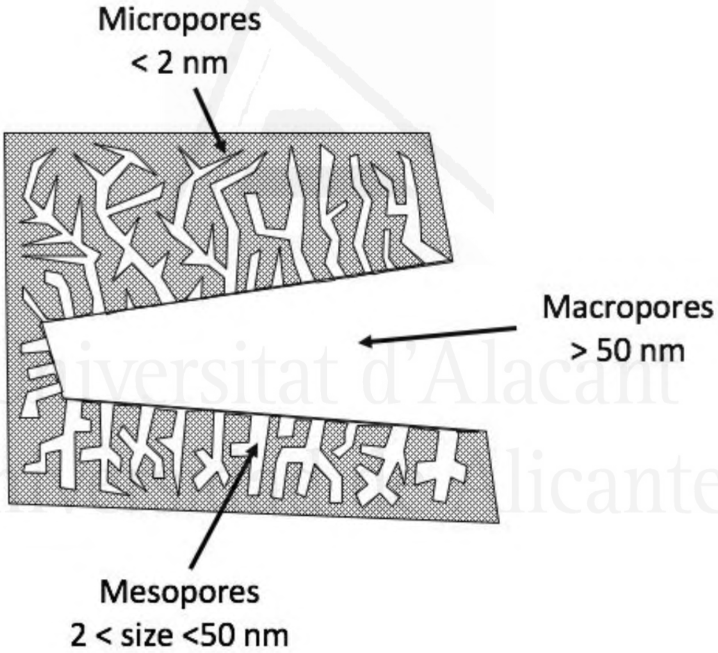

Figure 9. Schematic diagram of the pore size network of an activated carbon grain.

Most commercial ACs have a specific surface area of the order of 800 - 1500 $m^2 g^{-1}$. The maximum of the distribution curve of their volume versus their radii is mostly in the microporous range of 0.4 - 2.0 nm, indicating that ACs are microporous materials. On the other hand, the mesopore volumes usually lie between the limits 0.1 - 0.5 $cm^3 g^{-1}$ and mesopore surface are in the range of 20-100 $m^2 g^{-1}$ [93].

Template carbonization method is another preparation method of porous carbons [94,95].

While highly activated carbons produced by KOH chemical activation contain a very high BET surface area of around 3000 m^2 g^{-1} (almost the upper limit for conventional activated carbons), zeolite-templated carbon (ZTC) has a further higher BET surface area close to 4000 m^2 g^{-1}. Another remarkable feature of ZTC is its very large micropore volume (1.69 cm^3 g^{-1}) without mesopores [94]. In the case of a conventional activation method, not only micropores but also mesopores are inevitably formed whereas in the case of ZTC, 95% of its total pore volume is microporosity [94]. Having very high surface area without the presence of mesopores, this material is important especially for energy-storage applications such as hydrogen storage and electric double-layer capacitors [95,96], because mesopores usually lower the density of the porous materials, resulting in a lower energy density per unit volume [97].

One hand, mesopores of porous carbon materials have a very important role in adsorption, and especially in applications, such as catalytic supports, battery electrodes, capacitor electrodes, gas storage and bio-medical engineering applications [93,98,99]. For such applications, the carbon materials should possess not only high surface area, but also high ratio of mesopores or macropores to micropores, because many macromolecules and ions larger than the pore diameter of micropores are not able to enter the micropores [93]. Pore size distributions (PSD) is also important factor to foresee the application of porous carbon materials. For instance, the PSD is related to mobility of ions within the porosity leading to the formation of the electrical double layer (ion-sieving effect) [96,100].

1-4, Application of Carbon Materials

Carbon materials form the basis of numerous applications in a wide variety of research and engineering areas. This causes publications on carbon-based materials to appear traditionally in various journals from both scientific and engineering domains [6]. In this section, along with the general carbon material applications, detailed information regarding the carbon gasification and fuel cell applications, which are especially related to this PhD Thesis, are described.

Applications regarding environmental protection (adsorbents, CO_2 capture), energy storage and generation (hydrogen storage, methane storage, solar cells, solar evaporation, electrochemical capacitors, batteries and fuel cells), semiconductors, transparent conducting materials, structural materials, composite reinforcements, biomaterials, chemical sensors, biosensors, catalysis, and photocatalysis, summarize most of the fields in which the presence of carbon materials play an essential role [6,101–103].

During the past half century, renewable and green energy technologies (supercapacitors, batteries and fuel cells) have been developed with the use of carbon nanomaterials including fullerene, carbon nanotube (CNT), graphene, and porous carbon due to their remarkable mechanical, electrical, catalytic, optical, and thermal properties [69]. Carbon materials continue to play a critical role in the energy field [69], and yet there is plenty of room in the development of energy storage and conversion systems trying to get high energy and high power devices [6].

Energy-storage and conversion devices can be classified, in a very general way, according to their energy density (energy stored per volume unit or weight unit) and according to their power (speed of access to the energy stored) [100]. Figure 10 shows Ragone plots for different types of energy-storage and conversion devices. As revealed in Figure 10, batteries and low temperature fuel cells are typical low power devices, whereas conventional capacitors may have a specific power of $>10^6$ Watts per kg at very low specific energy [104]. Supercapacitors fill the gap between batteries and conventional capacitors in terms of both specific energy and power [105]. The mechanisms of operation are different in these devices. In the batteries, the essential process is Faradaic, i.e. electron transfer takes place across the interface electrolyte / electrode. In double layer supercapacitors, the charge storage process is non-Faradaic, i.e. ideally no electron transfer takes place across the electrolyte/electrode interface [13,100,104].

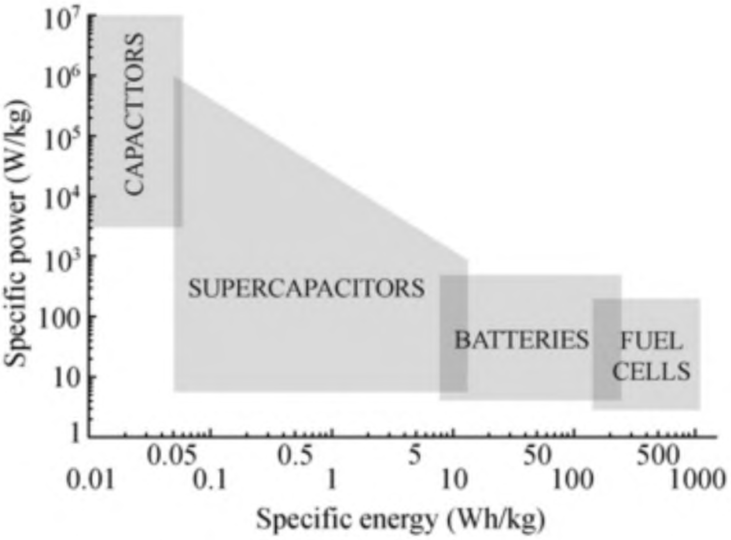

Figure 10. Ragone plots for different types of energy-storage and conversion devices

[104].

Apart from energy storage materials, the successful conversion of chemical energy into electrical energy in primitive fuel cells (FCs) was first demonstrated over 160 years ago. However, in spite of the attractive system efficiencies and environmental benefits associated with FCs technology, it has proved difficult to develop the early scientific experiments into commercially viable industrial products. These problems have often been associated with the lack of appropriate materials or manufacturing routes that would enable the cost of electricity per kWh to compete with the existing technology [106]. Along with developing new carbon-based catalysts supports, the synthesis of new non-precious metal containing catalysts is a critical objective for FCs applications [6].

1-4-1, FCs application

FCs is an electrochemical device which transforms directly the heat of combustion of a fuel (hydrogen, natural gas, methanol, ethanol, hydrocarbons, etc.) into electricity. The fuel is oxidized electrochemically at the anode, producing only water and/or carbon dioxide, whereas the oxidant (oxygen from the air) is reduced at the cathode [22]. Unlike batteries, FCs do not need recharging as long as fuel and oxidant are continuously supplied [107]. The electrochemical process of FCs does not follow the Carnot's theorem. Therefore, theoretical efficiency of FCs is much greater (by a factor of about 2) than that of a thermal combustion engine [22]. Because of the advantages of FCs such as high efficiencies, no environmental pollution and unlimited sources of reactant, there is now great interest in developing different kinds of FCs with several applications depending on their nominal power [22,107].

Previously, emphasis had been placed on the development of large FCs in the 200-300 kW range for these applications. Several demonstration projects of 1 MW and larger FCs have been undertaken, usually composed of units of 250 kW output. Smaller fuel cells in the range of 50-75 kW are now under intense development for use in automobile and bus propulsion, where their low emission characteristic finds favor [108]. Indeed, FCs technology undoubtedly has entered into our life with the first introduction of Toyota Mirai Fuel Cell Vehicle (FCV) by Toyota Motor Co. in December of 2014 [109].

FCs are classified according to the nature of the electrolyte and the working temperature, in high-, medium-, and low (ambient) temperature [110]. Two types of FCs are classified as "low or medium temperature FCs" because their operating temperature does not exceed

120 ˚C: proton-exchange membrane FCs (PEMFC), alkaline FCs (AFC), and solid alkaline FCs (SAFC). The three other types of FCs (phosphoric acid fuel cells (PAFC), molten carbonate FCs (MCFC), and solid oxide FCs (SOFC)) are classified as "high temperature" as they operate from 200 ˚C to 1000 ˚C [111]. The different types of FCs classified according to the electrolyte, operating temperature are represented in Figure 11.

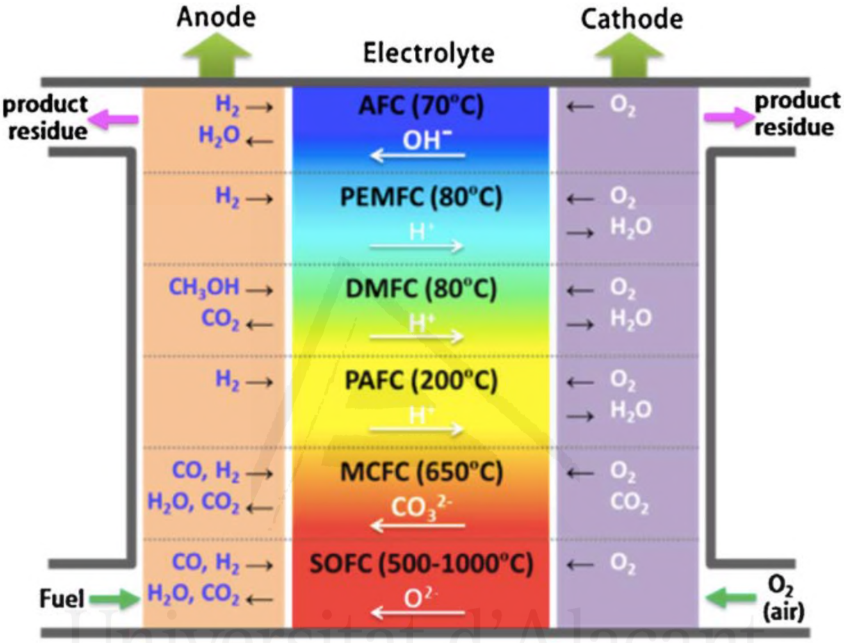

Figure 11. Fuel-cell types, chemical reactions and processes that occur in various systems [112].

The fuel oxidation reaction on the anode involves the liberation of electrons (e.g., $O^{2-} + H_2 = H_2O + 2e^-$ or $H_2 = 2H^+ + 2e^-$). These electrons travel through the external circuit producing electrical energy by means of the external load, and arrive at the cathode to participate in the reduction reaction (e.g., $\frac{1}{2} O_2 + 2e^- = O^{2-}$ or $\frac{1}{2} O_2 + 2H^+ + 2e^- = H_2O$). The reaction products such as H_2O are formed on the anode for SOFCs, MCFCs and AFCs, and on the cathode for PAFCs and PEMFCs [112].

For instance, AFCs use an aqueous solution of potassium hydroxide as the electrolyte, with typical concentrations of about 30%. The overall chemical reactions are given by [113].

Anode reaction	$2H_2 + 4OH^- \rightarrow 4H_2O + 4e^-$
Cathode reaction	$O_2 + 2H_2O + 4e^- \rightarrow 4OH^-$
Overall cell reaction	$2H_2 + O_2 \rightarrow 2H_2O$ + electric energy + heat

Hydrogen as a fuel is electrochemically oxidized while oxygen is electrochemically reduced at the cathode of FCs, respectively.

In terms of catalyst composition, Pt has been used for decades as a typical catalyst for fuel cell applications, since Pt is highly promising as a catalyst for both hydrogen oxidation reaction (HOR) and oxygen reduction reaction (ORR) [114]. The reaction rate of HOR on Pt is extremely fast so that the Pt loading at the anode can be reduced to less than 0.05 mg cm^{-2}. On the other hand, at the cathode, the sluggish reaction kinetics of ORR even on the best Pt-based catalyst requires much higher Pt loading (~0.4 mg cm^{-2}) to achieve a desirable fuel cell performance [107].

High loading of precious metal-containing catalysts (e.g., Pt) unfavorably increases the cost of these electrochemical energy conversion devices. For example, according to a United States Department of Energy's (DOE) study in 2007, 56% of the cost in a FCs stack comes from the platinum-based catalyst layers based on a projected cost for large scale fuel cell production [115].

Furthermore, poor durability/stability and slow electron-transfer kinetics of Pt-based catalysts still has to be improved [82]. The performance degradation of Pt-based catalysts under FCs conditions is mainly caused by Pt dissolution and subsequent agglomeration. Pt-based catalysts susceptibility to CO and methanol poisoning caused by fuel cross-over through the membrane is another disadvantage [28].

In summary, the increasing cost and reduced electrochemical stability of platinum and other precious metals currently employed as electrocatalyst for the ORR constitute one of the main problems to be solved for full development of FCs. Therefore, alternative catalysts which are free of them are urgent.

1-4-2, Development of ORR electrocatalysts

In order to tackle the above issues, numerous studies have been dedicated to screening more efficient ORR electrocatalytic materials that do not contain platinum (Pt-free) or contain only tiny amounts of this noble metal (low-Pt). Significant progress in rational designing and synthesizing excellent Pt-based or Pt-free catalysts has been achieved due to the development of material science and nanotechnology in the past few decades [115]. These materials include Pt alloys, core–shell structures, transition metal oxides and chalcogenides, and carbon based non-noble metal composite catalysts [107,116]. Various Pt-based alloy catalysts, such as Pt-M (where M is Co, Ni, Fe, V, Mn, and Cr), alloys have been studied as promising catalysts with decreased Pt loadings and enhanced electrocatalytic activities [117]. The idea of core–shell structure is to improve the utilization of Pt atoms by depositing a thin Pt-based shell around a less expensive core, such as Pd-, Ru-, and Re-based nanoparticles [107]. High ORR activities were reported with transition-metal centers embedded in a chalcogenide matrix [118].

1-4-3, Carbon based non-noble metal composite catalysts

Considerable efforts have been aimed at developing non-precious metal oxide (CoO, Co_3O_4, $MnCo_2O_4$ and MnO_2) and metal-nitrogen complex (Fe-Nx, Co-Nx and FeCo-Nx) doped carbons as potential substitutes for platinum and its alloys in electrocatalytic ORR [75,77,119–124]. New classes of carbon-based nanomaterials such as, graphene and CNTs have relatively high electrical conductivity, large surface area, high mechanical strength, and structural flexibility, making them useful substrates for producing hybrid and composite materials for various applications [125]. In particular, due to their desirable electrical and mechanical properties, together with excellent stability, graphene and CNTs could be used to derive advanced electrocatalysts [126–128].

Catalytically active metal species exhibit unique properties depending on their size, morphology, and structure. In particular, the size of the metal nanoparticles (NPs), directly affects the catalytic activity [129–131]. Although size-dependent catalytic activity of NPs were extensively reported and understood in heterogeneous catalysis, the particle-size effect on the ORR is rarely studied [132]. On one hand, it has been proposed that "M–Nx" could be a possible ORR active site in some catalyst systems [133]. Moreover, influence of several factors such as metal loading and oxidation state were investigated to further improve the catalytic performance and elucidate the ORR active site for the non-precious metal based catalysts [134–136].

1-4-4, Heteroatoms doped carbon catalysts

More innovative alternative is the development of metal-free catalysts based on carbon materials doped with different heteroatoms [137]. Heteroatom-doped metal-free carbon or graphene based materials are likely candidates which contain substantial amount of effective ORR active sites [138]. Recently, phosphorus and nitrogen co-doped carbons were reported to improve ORR activities and heteroatom co-doping remains the most robust approach to tuning the catalytic activities of metal-free materials [138]. In fact, the effect of nitrogen doping on carbons toward ORR activity is of great interest and it has been analyzed in a tremendous number of studies [139–141]. In spite of extensive investigations, the exact catalytic mechanism of nitrogen-doped graphene is still under debate [142]. Currently, the debate focuses on whether the active sites are created by pyridinic N (N bonded to two carbon atoms) or graphitic N (N bonded to three carbon atoms, also called substituted N or quaternary N) [143].

1-4-5, Metal and heteroatoms free carbon catalysts

Intrinsic structural defects (pentagonal, zig-zag edge, etc.) in dopant-free nanocarbons have also been claimed to possess considerable ORR activity, and are even better than some heteroatom-doped nano-carbons [144–148]. Edge-rich and dopant-free carbon nanotubes, graphene and graphite revealed enhanced ORR activity [149–151]. Great advances have been achieved at the level of both material engineering and fundamental understanding for dopant-free nanocarbons based ORR. For instance, density functional theory calculations indicate that pentagon and zigzag edge defects are responsible for the high ORR activity as supported by results of the annealing contrast experiments. The mutually corroborated experimental and theoretical results demonstrate the significant contribution of the intrinsic carbon defects to ORR activity, which is a crucial step for clarifying the origin for ORR catalytic activity and for understanding the controversial viewpoints of ORR [152]. Molecular dynamics simulations suggested that topological defects in the form of pentagon–heptagon defect pairs and curvature at nanotube tips can improve the activation behavior of ORR [153].

1-4-6, Mechanism for ORR in Carbon Materials

An atomic-level understanding of the ORR mechanism is still in its early stages because of the high complexity of ORR kinetics [115]. The fundamental understanding of the ORR has been largely based on the surface science approach to electrocatalysis. The surface science approach relies on pure metal single crystals and well-characterized bulk alloys which are used as model systems for commercial electrocatalysts. The most popular model system has been the Pt (111) surface [154]. However, an overview of the literature on the ORR on carbon surfaces reveals that there is no consensus on the mechanism or even the identity of adsorbed intermediates. Most researchers conclude that the adsorption of O_2 or superoxide is involved [155],[156], but changes in surface conditions and pretreatment cause wide variations in electrode behavior. Consequently, there is substantial disagreement among ORR mechanism proposed in the literature [157]. Meanwhile, extensive investigations regarding carbon-oxygen gasification were carried out from which interesting information about the active sites and the reaction mechanism were reached. Considering the nature of the carbon-oxygen interaction in active sites during the gasification reaction, it could be inferred that the sites for this reaction are the same as those participating in the ORR [158].

Carbon gasification, a group of reactions which encompasses the combustion of carbonaceous materials, was probably the first chemical process consciously employed in the service of man [159]. Control of the carbon gasification reactions is also of prime importance in manufacturing carbonaceous adsorbents like activated carbon of high adsorption characteristics [160]. Furthermore, the carbon gasification is an important topic nowadays in view of the energy market, bioenergy trends and the bio-refinery concept, which is expanding due to recent political and economic developments [161]. The main carbon gasification systems are briefly listed in Table 1: gases used (reactants and products), thermodynamics, catalysts and temperature changes observed in catalyst particles [161].

Table 1. Main carbon gasification systems [161].

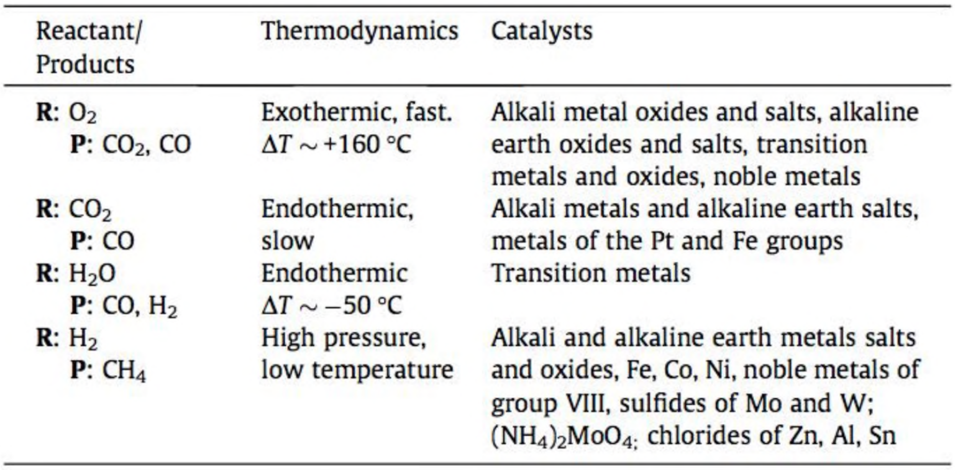

Reactant/ Products	Thermodynamics	Catalysts
R: O_2 **P**: CO_2, CO	Exothermic, fast. $\Delta T \sim +160$ °C	Alkali metal oxides and salts, alkaline earth oxides and salts, transition metals and oxides, noble metals
R: CO_2 **P**: CO	Endothermic, slow	Alkali metals and alkaline earth salts, metals of the Pt and Fe groups
R: H_2O **P**: CO, H_2	Endothermic $\Delta T \sim -50$ °C	Transition metals
R: H_2 **P**: CH_4	High pressure, low temperature	Alkali and alkaline earth metals salts and oxides, Fe, Co, Ni, noble metals of group VIII, sulfides of Mo and W; $(NH_4)_2MoO_4$; chlorides of Zn, Al, Sn

A fundamental understanding of the kinetics of coal gasification requires the knowledge of the role of carbon active sites, inherently present catalysts and diffusivity of the reactant and product gases within the pores of the devolatilized char [162]. Laine et al [48] emphasized that a fundamental rate constant for the carbon-oxygen reaction cannot be obtained on the basis of the total surface area (TSA) of the reacting carbon. Oxygen chemisorption was employed to measure the fraction of the total surface area of carbons which participates in the gasification by O_2. Finally, Laine et al. gave meaning to the term Active surface area (ASA) which was used to calculate meaningful rate constants for the carbon-oxygen reaction [48].

In addition, due to interest in coal-conversion processes for producing liquid and gaseous fuels [163], numerous reactivity studies in oxygen, carbon-dioxide and steam have been conducted on coal, chars, and cokes and the measurements have been used as an indication of the oxidation behavior of carbonaceous solids [159,163–166].

The soundness of the concept of ASA was demonstrated by the interpretation of the experimental results of Walker et al. The ASA values correlate much better with the measured reactivity, a finding which has been confirmed by other research teams in many cases [160,167]. Two general mechanisms first proposed for catalytic carbon gasification were based on electron-transfer and oxygen transfer [161]. Overall, oxygen-transfer reactions of carbon materials are at the heart of fuel combustion and gasification processes. While much progress has been made in achieving their fundamental understanding, the key details of metal/carbon interactions are not fully understood yet, especially regarding mechanism of the electrochemical ORR [168].

Clear evidences about the involved active sites and the reaction mechanism were collected for carbon-oxygen gasification, Radovic et al have questioned if the sites which are related to carbon gasification and ORR are different or not. And hence, it was concluded that this line of reasoning had not been explored before and, arguably, this has been the main obstacle in understanding the ORR mechanism and in suitably tailoring carbon surfaces [158].

1-4-7, Effect of porosity towards ORR and H_2O_2 *reduction*

Appleby and Marie reported that ORR activity increased linearly with BET surface area for carbon blacks, whereas no clear trend was found in the case of ACs. They argued that either the electrolyte, dissolved oxygen or the solvated HO_2^- anion, cannot reach the micropores on ACs and hence catalytic activity of AC_S are lower than expected considering their BET surface area [169].

Recently, it was proposed that surface features with oxygen groups being populated enough on the surface in large pores are able to promote the transport of electrolyte with dissolved oxygen to small pores and from there its release from water to hydrophobic pores of high adsorption energy. It is proposed that there, owing to strong physical adsorption forces and charge transfer from a carbon surface to adsorbed oxygen, the O−O bond weakens and dissociation of oxygen takes place. This is accompanied by an electron transfer to oxygen from the electrode and the protonation process. The size of pores and their volume and chemistry are crucial factors for the ORR process on these catalysts [170].

Meanwhile, it is known that H_2O_2 electrochemical reduction on carbon materials proceeds during the ORR experiments. The HO_2^- produced by 2 electron pathways of O_2, when trapped in a porous carbon layer, has a possibility to be chemically disproportionated ($2HO_2^- \rightarrow O_2 + 2OH^-$) [171]. Regarding the H_2O_2 reduction, Arman et al. investigated ORR experiment by increasing the mass of the catalysts (apparent % H_2O_2 decreases with increasing catalyst loading i.e., electrode thickness) and concluded that for thick electrodes, H_2O_2 produced inside the electrode must, prior to its release in the bulk electrolyte and subsequent detection by the Pt outer ring, diffuse throughout the electrode. Along this diffusion path, some H_2O_2 molecules produced in the bulk of the electrode may further react on catalytic sites, either electrochemically to produce only water ($H_2O_2 + 2H^+ + 2e^- \rightarrow 2H_2O$) or chemically to produce water and oxygen ($2H_2O_2 \rightarrow 2H_2O + O_2$, with no exchange of electrons with the disk). Only the H_2O_2 molecules produced close to the electrolyte bulk would have the possibility to leave the electrode before further reacting with the catalyst surface [172,173]. These results suggest that further reduction of H_2O_2 is related to a trapping effect which might rely on porous texture of carbon catalyst. However, Jing Liu reported that both the catalytic and trapped effects from carbon in alkaline solutions are rarely referred to [171]. On the other hand, Ishii et al. examined the reduction of H_2O_2 on the prepared carbon catalysts (nanoshell carbon co-doped with boron and nitrogen) to understand a further aspect of the catalysts surface chemistry. It was indicated that the introduced boron and nitrogen atoms enhance the H_2O_2 reduction activity [76]. These results imply that the presence of catalytic species has made challenging for any clear assessment of porosity influence toward ORR and

H_2O_2 reduction reaction.

In summary, the effect of porosity on the kinetics and mechanism of oxygen reduction as well as hydrogen peroxide reduction by carbon materials is often ignored, and, when considered, the presence of any catalytic species has made the mechanisms complicated. Thus, only a few works can be found where a systematic approach for assessing the role of microporosity of bare carbon materials in ORR is reported.

1-5, References

[1] H.O. Pierson, Handbook of Carbon, Graphite, Diamond and Fullerenes, Handb. Carbon, Graph. Diam. Fullerenes. (1993) 25–69. doi:http://dx.doi.org/10.1016/B978-0-8155-1339-1.50008-6.

[2] P. Trogadas, T.F. Fuller, P. Strasser, Carbon as catalyst and support for electrochemical energy conversion, Carbon. 75 (2014) 5–42. doi:10.1016/j.carbon.2014.04.005.

[3] J. P.L. WALKER, Carbon-an old but new material, (1972) 369–382.

[4] M. Inagaki, L.R. Radovic, Nanocarbons, Carbon. 40 (2002) 2279–2281. doi:Pii S0008-6223(02)00204-X.

[5] M. Inagaki, K. Kaneko, T. Nishizawa, Nanocarbons - Recent research in Japan, Carbon. 42 (2004) 1401–1417. doi:10.1016/j.carbon.2004.02.032.

[6] D. Cazorla-Amorós, Grand Challenges in Carbon-Based Materials Research, Front. Mater. 1 (2014) 1–3. doi:10.3389/fmats.2014.00006.

[7] A. Bianco, Y. Chen, Y. Chen, D. Ghoshal, R.H. Hurt, Y.A. Kim, N. Koratkar, V. Meunier, M. Terrones, A carbon science perspective in 2018: Current achievements and future challenges, Carbon. 132 (2018) 785–801. doi:10.1016/j.carbon.2018.02.058.

[8] B. Yao, L. Yuan, X. Xiao, J. Zhang, Y. Qi, Paper-based solid-state supercapacitors with pencil-drawing graphite / polyaniline networks hybrid electrodes, Nano Energy. 2 (2013) 1071–1078. doi:10.1016/j.nanoen.2013.09.002.

[9] D. Guerard, A. Herold, Intercalation of lithium into graphite and other carbons, Carbon. 13 (1975) 337–345. doi:https://doi.org/10.1016/0008-6223(75)90040-8.

[10] C.E. Banks, T.J. Davies, G.G. Wildgoose, R.G. Compton, Electrocatalysis at graphite and carbon nanotube modified electrodes: edge-plane sites and tube ends

are the reactive sites, Chem. Commun. (2005) 829. doi:10.1039/b413177k.

[11] R. Chand Bansal, M. Goyal, Activated Carbon Adsorption, CRC Press, 2005. doi:10.1201/9781420028812.

[12] F. Quesada-Plata, R. Ruiz-Rosas, E. Morallón, D. Cazorla-Amorós, Activated Carbons Prepared through H3PO4-Assisted Hydrothermal Carbonisation from Biomass Wastes: Porous Texture and Electrochemical Performance, Chempluschem. 81 (2016) 1349–1359. doi:10.1002/cplu.201600412.

[13] E. Frackowiak, F. Béguin, Carbon materials for the electrochemical storage of energy in capacitors, Carbon. 39 (2001) 937–950. doi:10.1016/S0008-6223(00)00183-4.

[14] M.J. Mostazo-López, R. Ruiz-Rosas, E. Morallón, D. Cazorla-Amorós, Generation of nitrogen functionalities on activated carbons by amidation reactions and Hofmann rearrangement: Chemical and electrochemical characterization, Carbon. 91 (2015) 252–265. doi:10.1016/j.carbon.2015.04.089.

[15] S. Leyva-García, D. Lozano-Castelló, E. Morallón, T. Vogl, C. Schütter, S. Passerini, A. Balducci, D. Cazorla-Amorós, Electrochemical performance of a superporous activated carbon in ionic liquid-based electrolytes, J. Power Sources. 336 (2016) 419–426. doi:10.1016/j.jpowsour.2016.11.010.

[16] Y. El-Sayed, T.J. Bandosz, Acetaldehyde adsorption on nitrogen-containing activated carbons, Langmuir. 18 (2002) 3213–3218. doi:10.1021/la0116948.

[17] F. Rodríguez-Reinoso, The role of carbon materials in heterogeneous catalysis, Carbon. 36 (1998) 159–175. doi:10.1016/S0008-6223(97)00173-5.

[18] D.D. Do, A model for surface diffusion of ethane and propane in activated carbon, Chem. Eng. Sci. 51 (1996) 4145–4158. doi:10.1016/0009-2509(96)00251-5.

[19] M. Lazaro, L. Calvillo, V. Celorrio, J.. Pardo, S. Perathoner, R. Moliner, Study and application of Vulcan XC-72 in low temperature fuel cells B LACK V ULCAN XC-72R IN P OLYMERIC, Carbon Black Prod. Prop. Uses. (2011) 1–28.

[20] U.A. Paulus, T.J. Schmidt, H.A. Gasteiger, R.J. Behm, Oxygen reduction on a high-surface area Pt/Vulcan carbon catalyst: A thin-film rotating ring-disk electrode study, J. Electroanal. Chem. 495 (2001) 134–145. doi:10.1016/S0022-0728(00)00407-1.

[21] X. Qi, B. Blizanac, A. Dupasquier, M. Oljaca, J. Li, M. Winter, Understanding the influence of conductive carbon additives surface area on the rate performance of

LiFePO4cathodes for lithium ion batteries, Carbon. 64 (2013) 334–340. doi:10.1016/j.carbon.2013.07.083.

[22] C. Lamy, Fuel Cell Systems : Which Technological Breakthrough for Industrial Development ?, in: E.F. François Béguin (Ed.), Carbons Electrochem. Energy Storage Convers. Syst., CRC Press, 2010: pp. 377–410.

[23] A.L. Dicks, The role of carbon in fuel cells, J. Power Sources. 156 (2006) 128–141. doi:10.1016/j.jpowsour.2006.02.054.

[24] S. Iijima, Helical microtubules of graphitic carbon, Nature. 354 (1991) 56. http://dx.doi.org/10.1038/354056a0.

[25] M. et al M. Jordá-Beneyto, Hydrogen storage in carbon materials, PhD Thesis. Universidad de Alicante, 2008.

[26] F. Li, Y. Wang, D. Wang, F. Wei, Characterization of single-wall carbon nanotubes by N_2 adsorption, Carbon. 42 (2004) 2375–2383. doi:10.1016/j.carbon.2004.02.025.

[27] P. Delhaes, M. Couzi, M. Trinquecoste, J. Dentzer, H. Hamidou, C. Vix-Guterl, A comparison between Raman spectroscopy and surface characterizations of multiwall carbon nanotubes, Carbon. 44 (2006) 3005–3013. doi:10.1016/j.carbon.2006.05.021.

[28] N. Daems, X. Sheng, I.F.J. Vankelecom, P.P. Pescarmona, Metal-free doped carbon materials as electrocatalysts for the oxygen reduction reaction, J. Mater. Chem. A. 2 (2014) 4085–4110. doi:10.1039/C3TA14043A.

[29] H. Hanaei, M.K. Assadi, R. Saidur, Highly efficient anti reflective and self-cleaning coatings that incorporate carbon nanotubes (CNTs) into solar cells : A review, Renew. Sustain. Energy Rev. 59 (2016) 620–635. doi:10.1016/j.rser.2016.01.017.

[30] K. Lota, V. Khomenko, E. Frackowiak, Capacitance properties of poly(3,4-ethylenedioxythiophene)/carbon nanotubes composites, J. Phys. Chem. Solids. 65 (2004) 295–301. doi:10.1016/j.jpcs.2003.10.051.

[31] M.M. Barsan, M.E. Ghica, C.M.A. Brett, Electrochemical sensors and biosensors based on redox polymer/carbon nanotube modified electrodes: A review, Anal. Chim. Acta. 881 (2015) 1–23. doi:10.1016/j.aca.2015.02.059.

[32] X. Pan, X. Bao, The effects of confinement inside carbon nanotubes on catalysis, Acc. Chem. Res. 44 (2011) 553–562. doi:10.1021/ar100160t.

[33] G. Zhong, H. Wang, H. Yu, F. Peng, The effect of edge carbon of carbon nanotubes on the electrocatalytic performance of oxygen reduction reaction, Electrochem. Commun. 40 (2014) 5–8. doi:10.1016/j.elecom.2013.12.017.

[34] K. Matsubara, K. Waki, Oxygen reduction characteristics of bamboo-shaped, multi-walled carbon nanotubes without nitrogen in acid media, Electrochim. Acta. 55 (2010) 9166–9173. doi:10.1016/j.electacta.2010.08.040.

[35] V. V. Strelko, N.T. Kartel, I.N. Dukhno, V.S. Kuts, R.B. Clarkson, B.M. Odintsov, Mechanism of reductive oxygen adsorption on active carbons with various surface chemistry, Surf. Sci. 548 (2004) 281–290. doi:10.1016/j.susc.2003.11.012.

[36] M. Seredych, D. Hulicova-Jurcakova, G.Q. Lu, T.J. Bandosz, Surface functional groups of carbons and the effects of their chemical character, density and accessibility to ions on electrochemical performance, Carbon. 46 (2008) 1475–1488. doi:10.1016/j.carbon.2008.06.027.

[37] J. Lahaye, P. Ehrburger, Surface chemistry of carbon: an atomistic approach, Pure Appl. Chem. 61 (1989) 1853–1858. doi:10.1351/pac198961111853.

[38] C. González-Gaitán, Electrochemical Methods to Functionalize Carbon Materials, PhD Thesis. Universidad de Alicante, 2016.

[39] A. Dandekar, Characterization of Activated Carbon , Graphitized Carbon Fibers and Synthetic, 36 (1998) 1821–1831.

[40] L.R. Radovic, I.F. Silva, J.I. Ume, J.A. Menéndez, C.A. Leon Y Leon, A.W. Scaroni, An experimental and theoretical study of the adsorption of aromatics possessing electron-withdrawing and electron-donating functional groups by chemically modified activated carbons, Carbon. 35 (1997) 1339–1348. doi:10.1016/S0008-6223(97)00072-9.

[41] C.A. Leon y Leon, J.M. Solar, V. Calemma, L.R. Radovic, Evidence for the protonation of basal plane sites on carbon, Carbon. 30 (1992) 797–811. doi:https://doi.org/10.1016/0008-6223(92)90164-R.

[42] V. Georgakilas, M. Otyepka, A.B. Bourlinos, V. Chandra, N. Kim, K.C. Kemp, P. Hobza, R. Zboril, K.S. Kim, Functionalization of graphene: Covalent and non-covalent approaches, derivatives and applications, Chem. Rev. 112 (2012) 6156–6214. doi:10.1021/cr3000412.

[43] M. Ates, A review study of (bio)sensor systems based on conducting polymers, Mater. Sci. Eng. C. 33 (2013) 1853–1859. doi:10.1016/j.msec.2013.01.035.

[44] C. González-Gaitán, R. Ruiz-Rosas, E. Morallón, D. Cazorla-Amorós, Effects of the surface chemistry and structure of carbon nanotubes on the coating of glucose oxidase and electrochemical biosensors performance, RSC Adv. 7 (2017) 26867–26878. doi:10.1039/C7RA02380D.

[45] M. Inagaki, M. Toyoda, Y. Soneda, T. Morishita, Nitrogen-doped carbon materials, Carbon.132 (2018) 104–140. doi:10.1016/j.carbon.2018.02.024.

[46] A. Gabe, M.J. Mostazo-López, D. Salinas-Torres, E. Morallón, D. Cazorla-Amorós, Synthesis of conducting polymer/carbon material composites and their application in electrical energy storage, 2017. doi:10.1016/B978-0-08-100789-1.00013-7.

[47] J.P. Paraknowitsch, A. Thomas, Doping carbons beyond nitrogen: An overview of advanced heteroatom doped carbons with boron, sulphur and phosphorus for energy applications, Energy Environ. Sci. 6 (2013) 2839–2855. doi:10.1039/c3ee41444b.

[48] N.R. Laine, F.J. Vastola, P.L. Walker, The importance of active surface area in the carbon-oxygen reaction, J. Phys. Chem. 67 (1963) 2030–2034. doi:10.1021/j100804a016.

[49] T. Ishii, S. Kashihara, Y. Hoshikawa, J.I. Ozaki, N. Kannari, K. Takai, T. Enoki, T. Kyotani, A quantitative analysis of carbon edge sites and an estimation of graphene sheet size in high-temperature treated, non-porous carbons, Carbon. 80 (2014) 135–145. doi:10.1016/j.carbon.2014.08.048.

[50] L.R. Radovic, Active Sites in Graphene and the Mechanism of CO_2 Formation in Carbon Oxidation, JACS. 131(2009) 17166–17175.

[51] T.J. Bandosz, Surface Chemistry of Carbon Materials, in: Carbon Mater. Catal., 2009: pp. 45–92. doi:10.1002/9780470403709.ch2.

[52] H.P. Boehm, Surface oxides on carbon and their analysis: A critical assessment, Carbon. 40 (2002) 145–149. doi:10.1016/S0008-6223(01)00165-8.

[53] E. Raymundo-Piñero, F. Leroux, F. Béguin, A high-performance carbon for supercapacitors obtained by carbonization of a seaweed biopolymer, Adv. Mater. 18 (2006) 1877–1882. doi:10.1002/adma.200501905.

[54] M.J. Bleda-Martínez, J.A. Maciá-Agulló, D. Lozano-Castelló, E. Morallón, D. Cazorla-Amorós, A. Linares-Solano, Role of surface chemistry on electric double layer capacitance of carbon materials, Carbon. 43 (2005) 2677–2684.

doi:10.1016/j.carbon.2005.05.027.

[55] M.J. Bleda-Martínez, D. Lozano-Castelló, E. Morallón, D. Cazorla-Amorós, A. Linares-Solano, Chemical and electrochemical characterization of porous carbon materials, Carbon. 44 (2006) 2642–2651. doi:10.1016/j.carbon.2006.04.017.

[56] C. Moreno-Castilla, M. V. López-Ramón, F. Carrasco-Marín, Changes in surface chemistry of activated carbons by wet oxidation, Carbon. 38 (2001) 1995–2001.

[57] G.S. Szymański, Z. Karpiński, S. Biniak, A. Świątkowski, The effect of the gradual thermal decomposition of surface oxygen species on the chemical and catalytic properties of oxidized activated carbon, Carbon. 40 (2002) 2627–2639. doi:10.1016/S0008-6223(02)00188-4.

[58] R. Phillips, F.J. Vastola, P.L. Walker, The thermal decomposition of surface oxides formed on Graphon, Carbon. 8 (1970) 197–203. doi:10.1016/0008-6223(70)90114-4.

[59] R.C. Bansal, F.J. Vastola, P.L. Walker, Studies on ultra-clean carbon surfaces-IV. Decomposition of carbon-oxygen surface complexes, Carbon. 8 (1970) 443–448. doi:10.1016/0008-6223(70)90004-7.

[60] Y. Otake, R.G. Jenkins, Characterization of oxygen-containing surface complexes created on a microporous carbon by air and nitric acid treatment, Carbon. 31 (1993) 109–121. doi:10.1016/0008-6223(93)90163-5.

[61] J.L. Figueiredo, M.F.R. Pereira, M.M.A. Freitas, J.J.M. Órfão, Modification of the surface chemistry of activated carbons, Carbon. 37 (1999) 1379–1389. doi:10.1016/S0008-6223(98)00333-9.

[62] S. Haydar, C. Moreno-Castilla, M.A. Ferro-García, F. Carrasco-Marín, J. Rivera-Utrilla, A. Perrard, J.P. Joly, Regularities in the temperature-programmed desorption spectra of CO_2 and CO from activated carbons, Carbon. 38 (2000) 1297–1308. doi:10.1016/S0008-6223(99)00256-0.

[63] J.H. Zhou, Z.J. Sui, J. Zhu, P. Li, D. Chen, Y.C. Dai, W.K. Yuan, Characterization of surface oxygen complexes on carbon nanofibers by TPD, XPS and FT-IR, Carbon. 45 (2007) 785–796. doi:10.1016/j.carbon.2006.11.019.

[64] M.A. Montes-Morán, D. Suárez, J.A. Menéndez, E. Fuente, On the nature of basic sites on carbon surfaces: An overview, Carbon. 42 (2004) 1219–1224. doi:10.1016/j.carbon.2004.01.023.

[65] M.C. Román-Martínez, D. Cazorla-Amorós, A. Linares-Solano, C.S.-M. de Lecea,

TPD and TPR characterization of carbonaceous supports and Pt/C catalysts, Carbon. 31 (1993) 895–902. doi:10.1016/0008-6223(93)90190-L.

[66] I. Mochida, Y. Korai, M. Shirahama, S. Kawano, T. Hada, Y. Seo, M. Yoshikawa, A. Yasutake, Removal of SOx and NOx over activated carbon fibers, Carbon. 38 (2000) 227–239. doi:10.1016/S0008-6223(99)00179-7.

[67] E. Raymundo-Piñero, D. Cazorla-Amorós, A. Linares-Solano, The role of different nitrogen functional groups on the removal of SO_2 from flue gases by N-doped activated carbon powders and fibres, Carbon. 41 (2003) 1925–1932. doi:10.1016/S0008-6223(03)00180-5.

[68] L. Lai, L. Wang, H. Yang, N.G. Sahoo, Q.X. Tam, J. Liu, C.K. Poh, S.H. Lim, Z. Shen, J. Lin, Tuning graphene surface chemistry to prepare graphene/polypyrrole supercapacitors with improved performance, Nano Energy. 1 (2012) 723–731. doi:10.1016/j.nanoen.2012.05.012.

[69] Z. Yang, J. Ren, Z. Zhang, X. Chen, G. Guan, L. Qiu, Y. Zhang, H. Peng, Recent Advancement of Nanostructured Carbon for Energy Applications, Chem. Rev. 115 (2015) 5159–5223. doi:10.1021/cr5006217.

[70] F. Banhart, J. Kotakoski, A. V. Krasheninnikov, Structural Defects in Graphene RID A-3473-2009, ACS Nano. 5 (2011) 26–41. doi:10.1021/nn102598m.

[71] D. Salinas-Torres, S. Shiraishi, E. Morallón, D. Cazorla-Amorós, Improvement of carbon materials performance by nitrogen functional groups in electrochemical capacitors in organic electrolyte at severe conditions, Carbon. 82 (2015) 205–213. doi:10.1016/j.carbon.2014.10.064.

[72] S. Kuroki, Y. Hosaka, C. Yamauchi, A solid-state NMR study of the carbonization of polyaniline, Carbon. 55 (2013) 160–167. doi:10.1016/j.carbon.2012.12.022.

[73] P.H. Matter, L. Zhang, U.S. Ozkan, The role of nanostructure in nitrogen-containing carbon catalysts for the oxygen reduction reaction, J. Catal. 239 (2006) 83–96. doi:10.1016/j.jcat.2006.01.022.

[74] J.M. Rosas, R. Ruiz-Rosas, J. Rodríguez-Mirasol, T. Cordero, Kinetic study of the oxidation resistance of phosphorus-containing activated carbons, Carbon. 50 (2012) 1523–1537. doi:10.1016/j.carbon.2011.11.030.

[75] S. CHAO, W. GUO, Using 2-Mercaptobenzothiazole as a Nitrogen and Sulfur Precursor to Synthesize Highly Active Co-N-S/C Electrocatalysts for Oxygen Reduction, Anal. Sci. 29 (2013) 619–623. doi:10.2116/analsci.29.619.

[76] T. Ishii, T. Maie, N. Kimura, Y. Kobori, Y. Imashiro, J.-I. Ozaki, Enhanced catalytic activity of nanoshell carbon co-doped with boron and nitrogen in the oxygen reduction reaction, Int. J. Hydrogen Energy. 42 (2017) 5–12. doi:10.1016/j.ijhydene.2017.05.003.

[77] B. You, P. Yin, J. Zhang, D. He, G. Chen, F. Kang, H. Wang, Z. Deng, Y. Li, Hydrogel-derived non-precious electrocatalysts for efficient oxygen reduction., Sci. Rep. 5 (2015) 11739. doi:10.1038/srep11739.

[78] S.A. Wohlgemuth, R.J. White, M.G. Willinger, M.M. Titirici, M. Antonietti, A one-pot hydrothermal synthesis of sulfur and nitrogen doped carbon aerogels with enhanced electrocatalytic activity in the oxygen reduction reaction, Green Chem. 14 (2012) 1515–1523. doi:10.1039/c2gc35309a.

[79] D.W. Mckee, C.L. Spiro, E.J. Lamby, the Inhibition of Graphite Oxidation By Phosphorus Additives, Carbon. 22 (1984) 285–290.

[80] D.W. McKee, C.L. Spiro, E.J. Lamby, The effects of boron additives on the oxidation behavior of carbons, Carbon. 22 (1984) 507–511. doi:https://doi.org/10.1016/0008-6223(84)90083-6.

[81] W. Kiciński, M. Szala, M. Bystrzejewski, Sulfur-doped porous carbons: Synthesis and applications, Carbon. 68 (2014) 1–32. doi:10.1016/j.carbon.2013.11.004.

[82] Z. Yang, H. Nie, X. Chen, X. Chen, S. Huang, Recent progress in doped carbon nanomaterials as effective cathode catalysts for fuel cell oxygen reduction reaction, J. Power Sources. 236 (2013) 238–249. doi:10.1016/j.jpowsour.2013.02.057.

[83] T. Kyotani, Control of pore structure in carbon, Carbon. 38 (2000) 269–286. doi:10.1016/S0008-6223(99)00142-6.

[84] F.I. Khan, A. Kr. Ghoshal, Removal of Volatile Organic Compounds from polluted air, J. Loss Prev. Process Ind. 13 (2000) 527–545. doi:https://doi.org/10.1016/S0950-4230(00)00007-3.

[85] J. Pattanayak, K. Mondal, S. Mathew, S.B. Lalvani, A Parametric Evaluation of the Removal of As (V) and As (III) by Carbon-Based Adsorbents A parametric evaluation of the removal of As (V) and As (III) by carbon-based adsorbents, 38 (2016) 589–596. doi:10.1016/S0008-6223(99)00144-X.

[86] L. Monser, Modified activated carbon for the removal of copper, zinc, chromium and cyanide from wastewater, 26 (2002) 137–146.

[87] R. Gong, T.C. Keener, A Qualitative Analysis of the Effects of Water Vapor on

Multi-Component Vapor-Phase Carbon Adsorption, Air Waste. 43 (1993) 864–872. doi:10.1080/1073161X.1993.10467169.

[88] P. Simon, A. Burke, Nanostructured carbons: Double-layer capacitance and more, Electrochemical Society Interface. 17 (2008) 38–43. doi:10.1016/j.carbon.2005.06.046.

[89] G. Yu, X. Xie, L. Pan, Z. Bao, Y. Cui, Hybrid nanostructured materials for high-performance electrochemical capacitors, Nano Energy. 2 (2013) 213–234. doi:10.1016/j.nanoen.2012.10.006.

[90] M.A. Lillo-Ródenas, D. Cazorla-Amorós, A. Linares-Solano, Understanding chemical reactions between carbons and NaOH and KOH: An insight into the chemical activation mechanism, Carbon. 41 (2003) 267–275. doi:10.1016/S0008-6223(02)00279-8.

[91] D. Lozano-Castelló, M.A. Lillo-Ródenas, D. Cazorla-Amorós, A. Linares-Solano, Preparation of activated carbons from Spanish anthracite: I. Activation by KOH, Carbon. 39 (2001) 741–749. doi:10.1016/S0008-6223(00)00185-8.

[92] M.A. Lillo-Ródenas, D. Lozano-Castelló, D. Cazorla-Amorós, A. Linares-Solano, Preparation of activated carbons from Spanish anthracite - II. Activation by NaOH, Carbon. 39 (2001) 751–759. doi:10.1016/S0008-6223(00)00186-X.

[93] Z. Hu, M.P. Srinivasan, Y. Ni, Novel activation process for preparing highly microporous and mesoporous activated carbons, Carbon. 39 (2001) 877–886. doi:10.1016/S0008-6223(00)00198-6.

[94] H. Nishihara, T. Kyotani, Zeolite-Templated Carbon - Its Unique Characteristics and Applications, Novel Carbon Adsorbents, Elsevier Ltd, (2012) 295-322. doi:10.1016/B978-0-08-097744-7.00010-7.

[95] H. Itoi, H. Nishihara, T. Ishii, K. Nueangnoraj, R. Berenguer-Betrián, T. Kyotani, Large pseudocapacitance in quinone-functionalized zeolite-templated carbon, Bull. Chem. Soc. Jpn. 87 (2014) 250–257. doi:10.1246/bcsj.20130292.

[96] M.J. Mostazo-López, R. Ruiz-Rosas, A. Castro-Muñiz, H. Nishihara, T. Kyotani, E. Morallón, D. Cazorla-Amorós, Ultraporous nitrogen-doped zeolite-templated carbon for high power density aqueous-based supercapacitors, Carbon. 129 (2018) 510–519. doi:10.1016/j.carbon.2017.12.050.

[97] H. Nishihara, T. Simura, T. Kyotani, Enhanced hydrogen spillover to fullerene at ambient temperature, Chem. Commun. 54 (2018) 3327–3330.

doi:10.1039/C8CC00265G.

[98] J. Lee, S. Yoon, T. Hyeon, M. Oh, K. Bum, Synthesis of a new mesoporous carbon and its application to electrochemical double-layer capacitors, Chem. Commun. (1999) 2177–2178.

[99] H. Chang, S.H. Joo, C. Pak, Synthesis and characterization of mesoporous carbon for fuel cell applications, J. Mater. Chem. 17 (2007) 3078–3088. doi:10.1039/b700389g.

[100] D. Lozano-Castelló, D. Cazorla-Amorós, A. Linares-Solano, S. Shiraishi, H. Kurihara, A. Oya, Influence of pore structure and surface chemistry on electric double layer capacitance in non-aqueous electrolyte, Carbon. 41 (2003) 1765–1775. doi:10.1016/S0008-6223(03)00141-6.

[101] Z. Li, Z. Liu, H. Sun, C. Gao, Superstructured Assembly of Nanocarbons: Fullerenes, Nanotubes, and Graphene, Chem. Rev. 115 (2015) 7046–7117. doi:10.1021/acs.chemrev.5b00102.

[102] H. Nishihara, T. Kyotani, Zeolite-templated carbons - Three-dimensional microporous graphene frameworks, Chem. Commun. 54 (2018) 5648–5673. doi:10.1039/C8CC01932K.

[103] D.S. Su, S. Perathoner, G. Centi, Nanocarbons for the development of advanced catalysts, Chem. Rev. 113 (2013) 5782–5816. doi:10.1021/cr300367d.

[104] C. Peng, S. Zhang, D. Jewell, G.Z. Chen, Carbon nanotube and conducting polymer composites for supercapacitors, Prog. Nat. Sci. 18 (2008) 777–788. doi:10.1016/j.pnsc.2008.03.002.

[105] G.A. Snook, P. Kao, A.S. Best, Conducting-polymer-based supercapacitor devices and electrodes, J. Power Sources. 196 (2011) 1–12. doi:10.1016/j.jpowsour.2010.06.084.

[106] B.C.H. Steele, A. Heinzel, Materials for fuel-cell technologies, Nature. 414 (2001) 345–352. doi:10.1038/35104620.

[107] M. Shao, Q. Chang, J.-P. Dodelet, R. Chenitz, Recent Advances in Electrocatalysts for Oxygen Reduction Reaction, Chem. Rev. 116 (2016) 3594–3657. doi:10.1021/acs.chemrev.5b00462.

[108] M. Winter, R.J. Brodd, What Are Batteries, Fuel Cells, and Supercapacitors?, Chem. Rev. 104 (2004) 4245–4270. doi:10.1021/cr020730k.

[109] A. Serov, I. V. Zenyuk, C.G. Arges, M. Chatenet, Hot topics in alkaline exchange

membrane fuel cells, J. Power Sources. 375 (2018) 149–157. doi:10.1016/j.jpowsour.2017.09.068.

[110] K. V. Kordesch, G.R. Simader, Environmental Impact of Fuel Cell Technology, Chem. Rev. 95 (1995) 191–207. doi:10.1021/cr00033a007.

[111] G. Couture, A. Alaaeddine, F. Boschet, B. Ameduri, Polymeric materials as anion-exchange membranes for alkaline fuel cells, Prog. Polym. Sci. 36 (2011) 1521–1557. doi:10.1016/j.progpolymsci.2011.04.004.

[112] Y. Yang, C. Han, B. Jiang, J. Iocozzia, C. He, D. Shi, T. Jiang, Z. Lin, Graphene-based materials with tailored nanostructures for energy conversion and storage, Mater. Sci. Eng. R. 102 (2016) 1–72. doi:10.1016/j.mser.2015.12.003.

[113] G.F. McLean, T. Niet, S. Prince-Richard, N. Djilali, An assessment of alkaline fuel cell technology, Int. J. Hydrogen Energy. 27 (2002) 507–526. doi:10.1016/S0360-3199(01)00181-1.

[114] N. Jung, D.Y. Chung, J. Ryu, S.J. Yoo, Y.E. Sung, Pt-based nanoarchitecture and catalyst design for fuel cell applications, Nano Today. 9 (2014) 433–456. doi:10.1016/j.nantod.2014.06.006.

[115] Y. Nie, L. Li, Z. Wei, Recent advancements in Pt and Pt-free catalysts for oxygen reduction reaction, Chem. Soc. Rev. 44 (2015) 2168–2201. doi:10.1039/C4CS00484A.

[116] F. Jaouen, E. Proietti, M. Lefèvre, R. Chenitz, J.-P. Dodelet, G. Wu, H.T. Chung, C.M. Johnston, P. Zelenay, Recent advances in non-precious metal catalysis for oxygen-reduction reaction in polymer electrolyte fuel cells, Energy Environ. Sci. 4 (2010) 114–130. doi:10.1039/C0EE00011F.

[117] H. Yang, W. Vogel, C. Lamy, Structure and Electrocatalytic Activity of Carbon-Supported Pt - Ni Alloy Nanoparticles Toward the Oxygen Reduction Reaction, J. Phys. Chem. B. 108 (2004) 11024–11034. doi:10.1021/jp049034+.

[118] N. Alonso-Vante, Platinum and non-platinum nanomaterials for the molecular oxygen reduction reaction, ChemPhysChem. 11 (2010) 2732–2744. doi:10.1002/cphc.200900817.

[119] C.H. Choi, M.W. Chung, H.C. Kwon, J.H. Chung, S.I. Woo, Nitrogen-doped graphene/carbon nanotube self-assembly for efficient oxygen reduction reaction in acid media, Appl. Catal. B Environ. 144 (2014) 760–766. doi:10.1016/j.apcatb.2013.08.021.

[120] Y. Liang, Y. Li, H. Wang, J. Zhou, J. Wang, T. Regier, H. Dai, Co3O4 nanocrystals on graphene as a synergistic catalyst for oxygen reduction reaction, Nat. Mater. 10 (2011) 780–786. doi:10.1038/nmat3087.

[121] C. González-Gaitán, R. Ruiz-Rosas, E. Morallón, D. Cazorla-Amorós, Relevance of the Interaction between the M-Phthalocyanines and Carbon Nanotubes in the Electroactivity toward ORR, Langmuir. 33 (2017) 11945–11955. doi:10.1021/acs.langmuir.7b02579.

[122] G. Wu, K.L. More, C.M. Johnston, P. Zelenay, High-Performance Electrocatalysts for Oxygen Reduction Derived from Polyaniline, Iron, and Cobalt, Science (443-447). 332 (2011) 443–447. doi:10.1126/science.1200832.

[123] J. Ahmed, Y. Yuan, L. Zhou, S. Kim, Carbon supported cobalt oxide nanoparticles-iron phthalocyanine as alternative cathode catalyst for oxygen reduction in microbial fuel cells, J. Power Sources. 208 (2012) 170–175. doi:10.1016/j.jpowsour.2012.02.005.

[124] L. Osmieri, A.H.A. Monteverde Videla, M. Armandi, S. Specchia, Influence of different transition metals on the properties of Me–N–C (Me = Fe, Co, Cu, Zn) catalysts synthesized using SBA-15 as tubular nano-silica reactor for oxygen reduction reaction, Int. J. Hydrogen Energy. 41 (2016) 22570–22588. doi:10.1016/j.ijhydene.2016.05.223.

[125] Y. Liang, H. Wang, P. Diao, W. Chang, G. Hong, Y. Li, M. Gong, L. Xie, J. Zhou, J. Wang, T.Z. Regier, F. Wei, H. Dai, Oxygen reduction electrocatalyst based on strongly coupled cobalt oxide nanocrystals and carbon nanotubes, J. Am. Chem. Soc. 134 (2012) 15849–15857. doi:10.1021/ja305623m.

[126] S. Zhao, B. Rasimick, W. Mustain, H. Xu, Highly durable and active Co3O4 nanocrystals supported on carbon nanotubes as bifunctional electrocatalysts in alkaline media, Appl. Catal. B Environ. 203 (2017) 138–145. doi:10.1016/j.apcatb.2016.09.048.

[127] Y. Liang, Y. Li, H. Wang, J. Zhou, J. Wang, T. Regier, H. Dai, Co3O4 nanocrystals on graphene as a synergistic catalyst for oxygen reduction reaction, Nat. Mater. 10 (2011) 780–786. doi:10.1038/nmat3087.

[128] M. Wang, Y. Hou, R.C.T. Slade, J. Wang, D. Shi, D. Wexler, H. Liu, J. Chen, Core-Shell Co/CoO Integrated on 3D Nitrogen Doped Reduced Graphene Oxide Aerogel as an Enhanced Electrocatalyst for the Oxygen Reduction Reaction, Front.

Chem. 4 (2016) 1–10. doi:10.3389/fchem.2016.00036.

[129] K. Nakatsuka, T. Yoshii, Y. Kuwahara, K. Mori, H. Yamashita, Controlled synthesis of carbon-supported Co catalysts from single-sites to nanoparticles: characterization of the structural transformation and investigation of their oxidation catalysis, Phys. Chem. Chem. Phys. 19 (2017) 4967–4974. doi:10.1039/C6CP06388H.

[130] J. García-Aguilar, M. Navlani-García, Á. Berenguer-Murcia, K. Mori, Y. Kuwahara, H. Yamashita, D. Cazorla-Amorós, Evolution of the PVP-Pd surface interaction in nanoparticles through the case study of formic acid decomposition, Langmuir. 32 (2016) 12110–12118. doi:10.1021/acs.langmuir.6b03149.

[131] Y. Yang, K. Chiang, N. Burke, Porous carbon-supported catalysts for energy and environmental applications : A short review, Catal. Today. 178 (2011) 197–205. doi:10.1016/j.cattod.2011.08.028.

[132] J. Liu, L. Jiang, B. Zhang, J. Jin, D.S. Su, S. Wang, G. Sun, Controllable synthesis of cobalt monoxide nanoparticles and the size-dependent activity for oxygen reduction reaction, ACS Catal. 4 (2014) 2998–3001. doi:10.1021/cs500741s.

[133] C.W.B. Bezerra, L. Zhang, K. Lee, H. Liu, A.L.B. Marques, E.P. Marques, H. Wang, J. Zhang, A review of Fe-N/C and Co-N/C catalysts for the oxygen reduction reaction, Electrochim. Acta. 53 (2008) 4937–4951. doi:10.1016/j.electacta.2008.02.012.

[134] Z. Luo, B. Zhao, Y. Liu, H. Zhang, Z. Tang, J. Li, J. Yang, Influence of annealing temperature on oxygen reduction activity of sputtered Co catalysts on vertically-aligned carbon nanotubes, Electrochim. Acta. 161 (2015) 72–79. doi:10.1016/j.electacta.2015.01.225.

[135] Q. He, Q. Li, S. Khene, X. Ren, F.E. López-Suárez, D. Lozano-Castelló, A. Bueno-López, G. Wu, High-loading cobalt oxide coupled with nitrogen-doped graphene for oxygen reduction in anion-exchange-membrane alkaline fuel cells, J. Phys. Chem. C. 117 (2013) 8697–8707. doi:10.1021/jp401814f.

[136] Y. Huang, M. Zhang, P. Liu, L. Wang, F. Cheng, Improved performance of cobalt-based spinel by the simple solvothermal method as electrocatalyst for oxygen reduction reaction in alkaline solution, Ionics. 22 (2016) 1425–1432. doi:10.1007/s11581-016-1667-4.

[137] J. Quílez-Bermejo, C. González-Gaitán, E. Morallón, D. Cazorla-Amorós, Effect

of carbonization conditions of polyaniline on its catalytic activity towards ORR. Some insights about the nature of the active sites, Carbon. 119 (2017) 62–71. doi:10.1016/j.carbon.2017.04.015.

[138] G.-L. Chai, K. Qiu, M. Qiao, M.-M. Titirici, C. Shang, Z. Guo, Active sites engineering leads to exceptional ORR and OER bifunctionality in P,N Co-doped graphene frameworks, Energy Environ. Sci. 10 (2017) 1186–1195. doi:10.1039/C6EE03446B.

[139] K. Gong, F. Du, Z. Xia, M. Durstock, L. Dai, Nitrogen-doped carbon nanotube arrays with high electrocatalytic activity for oxygen reduction, Science (760-764). 323 (2009) 760–764. doi:10.1126/science.1168049.

[140] G. Chai, Z. Hou, T. Ikeda, K. Terakura, Active Sites and Mechanisms for Oxygen Reduction Reaction on Nitrogen - Doped Carbon Alloy Catalysts: Stone−Wales Defect and Curvature Effect, J. Am. Chem. Soc. (2014) 13629–13640. doi:10.1021/ja502646c.

[141] P. Chen, T. Xiao, Y. Qian, S. Li, S. Yu, A Nitrogen-Doped Graphene / Carbon Nanotube Nanocomposite with Synergistically Enhanced Electrochemical Activity, Adv. Mater. 25 (2013) 3192–3196. doi:10.1002/adma.201300515.

[142] T. Xing, Y. Zheng, L.H. Li, B.C.C. Cowie, D. Gunzelmann, S.Z. Qiao, S. Huang, Y. Chen, Observation of active sites for oxygen reduction reaction on nitrogen-doped multilayer graphene, ACS Nano. 8 (2014) 6856–6862. doi:10.1021/nn501506p.

[143] D. Guo, R. Shibuya, C. Akiba, S. Saji, T. Kondo, J. Nakamura, Active sites of nitrogen-doped carbon materials for oxygen reduction reaction clarified using model catalysts, Science (361-365). 351 (2016) 361–365. doi:10.1126/science.aad0832.

[144] C. Tang, Q. Zhang, Nanocarbon for Oxygen Reduction Electrocatalysis: Dopants, Edges, and Defects, Adv. Mater. 29 (2017). doi:10.1002/adma.201604103.

[145] C. Tang, H.-F. Wang, X. Chen, B.-Q. Li, T.-Z. Hou, B. Zhang, Q. Zhang, M.-M. Titirici, F. Wei, Topological Defects in Metal-Free Nanocarbon for Oxygen Electrocatalysis, Adv. Mater. 28 (2016) 6845–6851. doi:10.1002/adma.201601406.

[146] K. Waki, R.A. Wong, H.S. Oktaviano, T. Fujio, T. Nagai, K. Kimoto, K. Yamada, Non-nitrogen doped and non-metal oxygen reduction electrocatalysts based on carbon nanotubes: mechanism and origin of ORR activity, Energy Environ. Sci. 7

(2014) 1950–1958. doi:10.1039/c3ee43743d.

[147] X. Yan, Y. Jia, T. Odedairo, X. Zhao, Z. Jin, Z. Zhu, X. Yao, Activated carbon becomes active for oxygen reduction and hydrogen evolution reactions, Chem. Commun. 52 (2016) 8156–8159. doi:10.1039/C6CC03687B.

[148] M. Liu, J. Li, Heating treated carbon nanotubes as highly active electrocatalysts for oxygen reduction reaction, Electrochim. Acta. 154 (2015) 177–183. doi:10.1016/j.electacta.2014.12.039.

[149] L. Tao, Q. Wang, S. Dou, Z. Ma, J. Huo, S. Wang, L. Dai, Edge-rich and dopant-free graphene as a highly efficient metal-free electrocatalyst for the oxygen reduction reaction, Chem. Commun. 52 (2016) 2764–2767. doi:10.1039/c5cc09173j.

[150] A. Shen, Y. Zou, Q. Wang, R.A.W. Dryfe, X. Huang, S. Dou, L. Dai, S. Wang, Oxygen reduction reaction in a droplet on graphite: Direct evidence that the edge is more active than the basal plane, Angew. Chemie - Int. Ed. 53 (2014) 10804–10808. doi:10.1002/anie.201406695.

[151] M. Gara, R.G. Compton, Activity of carbon electrodes towards oxygen reduction in acid: A comparative study, New J. Chem. 35 (2011) 2647. doi:10.1039/c1nj20612e.

[152] Y. Jiang, L. Yang, T. Sun, J. Zhao, Z. Lyu, O. Zhuo, X. Wang, Q. Wu, J. Ma, Z. Hu, Significant Contribution of Intrinsic Carbon Defects to Oxygen Reduction Activity, ACS Catal. 5 (2015) 6707–6712. doi:10.1021/acscatal.5b01835.

[153] P.J. Britto, K.S. V. Santhanam, A. Rubio, J.A. Alonso, P.M. Ajayan, Improved Charge Transfer at Carbon Nanotube Electrodes, Adv. Mater. 11 (1999) 154–157. doi:10.1002/(SICI)1521-4095(199902)11:2<154::AID-ADMA154>3.0.CO;2-B.

[154] H.A. Hansen, V. Viswanathan, J.K. NØrskov, Unifying kinetic and thermodynamic analysis of 2 e- and 4 e - reduction of oxygen on metal surfaces, J. Phys. Chem. C. 118 (2014) 6706–6718. doi:10.1021/jp4100608.

[155] B. Šljukić, C.E. Banks, R.G. Compton, An overview of the electrochemical reduction of oxygen at carbon-based modified electrodes, J. Iran. Chem. Soc. 2 (2005) 1–25. doi:10.1007/BF03245775.

[156] D.T. Sawyer, E.T. Seo, One-Electron Mechanism for the Electrochemical Reduction of Molecular Oxygen, Inorg. Chem. 16 (1977) 499–501. doi:10.1021/ic50168a059.

[157] H.-H. Yang, R.L. McCreery, Elucidation of the Mechanism of Dioxygen Reduction on Metal-Free Carbon Electrodes, J. Electrochem. Soc. 147 (2000) 3420–3428. doi:10.1149/1.1393915.

[158] L.R. Radovic, Surface Chemical and Electrochemical Properties of Carbons, in: F. Beguin, E. Frackowiak (Eds.), Carbons Electrochem. Energy Storage Convers. Syst., Taylor & Francis (CRC Press), Boca Raton, FL, 2010: pp. 163–219.

[159] J. P.L. Walker, M. Shelef, R.A. Anderson, Catalysis of carbon gasification, Chem. Phys. Carbon Vol 4. 4 (1968) 287–383. doi:10.1063/1.2914601.

[160] P. Ehrburger, E. Dallies-Labourdette, J. Lahaye, Fundamental issues in control of carbon gasification reactivity, Prot. Carbon against Oxid. Role Act. Sites. 192 (2013) 1689–1699. doi:10.1017/CBO9781107415324.004.

[161] L.S. Lobo, S.A.C. Carabineiro, Kinetics and mechanism of catalytic carbon gasification, Fuel. 183 (2016) 457–469. doi:10.1016/j.fuel.2016.06.115.

[162] L.R. Radović, P.L. Walker, R.G. Jenkins, Importance of carbon active sites in the gasification of coal chars, Fuel. 62 (1983) 849–856. doi:10.1016/0016-2361(83)90041-8.

[163] A. Linares-Solano, O.P. Mahajan, P.L. Walker, Reactivity of heat-treated coals in steam, Fuel. 58 (1979) 327–332. doi:10.1016/0016-2361(79)90148-0.

[164] R.G. Jenkins, S.P. Nandi, P.L. Walker, Reactivity of heat-treated at 500 ° C coals in air, Fuel. 52 (1973) 288–293.

[165] E. Hippo, P.L. Walker, Reactivity of heat-treated coals in carbon dioxide at 900 °C, Fuel. 54 (1975) 245–248. doi:10.1016/0016-2361(75)90037-X.

[166] D. Cazorla-Amorós, A. Linares-Solano, C.S.-M. de Lecea, T. Kyotani, H. Yamashita, A. Tomita, Carbon gasification catalyzed by calcium: A high vacuum temperature programmed desorption study, Carbon. 30 (1992) 995–1000. doi:https://doi.org/10.1016/0008-6223(92)90127-I.

[167] K.H. Van Heek, Progress of Coal Science in the 20 th Century, 48 (2003) 144–146.

[168] F. Vallejos-Burgos, S. Utsumi, Y. Hattori, X. García, A.L. Gordon, H. Kanoh, K. Kaneko, L.R. Radovic, Pyrolyzed phthalocyanines as surrogate carbon catalysts: Initial insights into oxygen-transfer mechanisms, Fuel. 99 (2012) 106–117. doi:10.1016/j.fuel.2012.03.055.

[169] A.J. Appleby, J. Marie, Kinetics of oxygen reduction on carbon materials in alkaline solution, Electrochim. Acta. 24 (1979) 195–202. doi:10.1016/0013-

4686(79)80024-9.

[170] M. Seredych, A. Szczurek, V. Fierro, A. Celzard, T.J. Bandosz, Electrochemical Reduction of Oxygen on Hydrophobic Ultramicroporous PolyHIPE Carbon, ACS Catal. 6 (2016) 5618–5628. doi:10.1021/acscatal.6b01497.

[171] J. Liu, L. Jiang, Q. Tang, B. Zhang, D.S. Su, S. Wang, G. Sun, Coupling effect between cobalt oxides and carbon for oxygen reduction reaction, ChemSusChem. 5 (2012) 2315–2318. doi:10.1002/cssc.201200563.

[172] A. Bonakdarpour, M. Lefevre, R. Yang, F. Jaouen, T. Dahn, J.-P. Dodelet, J.R. Dahn, Impact of Loading in RRDE Experiments on Fe–N–C Catalysts: Two- or Four-Electron Oxygen Reduction?, Electrochem. Solid-State Lett. 11 (2008) B105. doi:10.1149/1.2904768.

[173] A. Bonakdarpour, T.R. Dahn, R.T. Atanasoski, M.K. Debe, J.R. Dahn, H_2O_2 Release during Oxygen Reduction Reaction on Pt Nanoparticles, Electrochem. Solid-State Lett. 11 (2008) B208. doi:10.1149/1.2978090.

Chapter 2.

Experimental section

2-1, Introduction

In this chapter, firstly, reagents and materials used for synthesis of the samples and experiments are described. Secondly, different experimental techniques used for physicochemical and electrochemical characterization, employed during the PhD Thesis are presented. More details for experimental conditions will be described in each chapter.

2-2, Reagents and materials

2-2-1 Reagents and gases

Several commercial reactants were purchased for synthesis of electrocatalysts. Cobalt(II) nitrate hexahydrate ($Co(NO_3)_2 \cdot 6H_2O$), polyvinylpyrrolidone (PVP 40T), sodium borohydride ($NaBH_4$) and ammonia solution (NH_4OH, 25 wt.%) from Sigma-Aldrich were used. Ethanol (C_2H_5OH, 96%), potassium hydroxide (KOH, 85.9%), hydrogen peroxide (H_2O_2, 30%), perchloric acid ($HClO_4$, 60%), hydrochloric acid (HCl, 60%) and nitric acid (HNO_3, 65%) from VWE Chemicals were used. Methanol (CH_3OH, 99.9%) and iso-propanol (C_3H_7OH, 99.9%) purchased from PANREAC Applichem were used. Nafion® (5% weight Nafion® perfluorinated resin solution) from Sigma-Aldrich was used as received. All the solutions used in electrochemical experiments were prepared with ultrapure water (18 Mohms cm, Millipore ® *Milli-Q® water).* For purification process of the samples, distilled water was used. N_2 (99.999%), O_2 (99.995%), H_2 (99.999%), He (99.999%) and synthetic dry air (20 vol.% of O_2 in N_2 base) from Air Liquide were used.

2-2-2 Carbon materials

Experiments in this thesis were performed with carbon based materials containing different structures and porosities. As new-carbon forms [1], carbon nanotubes (CNTs) and carbon nanofiber (CNF) were used. Multi-walled CNTs (MWCNTs) and Single-walled CNTs (SWCNTs) purchased from Cheap Tubes Inc were used. Herring-bone CNTs was purchased from TOKYO CHEMICAL INDUSTRY. CNTs with different purity, length and diameters were also selected from the same industry. More detailed information regarding the CNTs will be explained in each chapter. CNF was synthesized by our lab. As classic carbon forms [1], graphite, activated carbons, carbon blacks and microporous char were used. Graphite (KS4) from TIMCAL Ltd., commercial XC-72F Vulcan carbon black (XC72) from Cabot Corporation, CD-6008 carbon black (CB) from

COLUMBIAN CHEMICALS and highly microporous activated carbon (YPF) supplied from KURARAY were selected. A microporous char (AC) derived by carbonization of phenolformaldehyde polymer resin was used. Moreover, a highly microporous activated carbon (KUA) prepared by chemical activation of Spanish anthracite with KOH was used. The detailed material synthesis method for AC and KUA can be found elsewhere [2,3].

2-3, Characterization techniques

Physicochemical characterization

2-3-1 Thermogravimetric analysis (TGA)

TGA is a technique in which the mass of a substance is monitored as a function of temperature or time as the sample specimen is subjected to a controlled temperature program in a controlled atmosphere [4]. All TGA were conducted by thermogravimetric equipment (TA Instruments, SDT Q600 Simultaneous). Non-isothermal TGA was carried out to analyze residual concentration of ash in the studied samples. In addition, as carbon-oxygen gasification properties, active surface area (ASA) and reactivity of the carbon materials were measured by isothermal TGA under synthetic dry air (20 vol.% of O_2 in N_2). The heat treatment process for the prepared electrocatalysts were also performed by TA system under N_2 atmosphere.

2-3-2, Temperature programmed desorption (TPD)

TPD measurements have become a standard and useful technique for the analysis of the state of adsorbed surface species and been extensively used for characterizing the surface functionalities of carbon materials [5–8]. Decomposition of acidic groups as carboxylic, anhydrides, and lactones proceeds with CO_2 evolution at temperatures between 200°C and 700°C, while neutral and basic groups as phenols, esters, carbonyls, and quinones decompose as CO at

temperatures from 500°C to more than 1000°C [9,10]. TPD experiments in this PhD Thesis were performed in a thermogravimetric system (TA Instruments, SDT Q600 Simultaneous) coupled to a mass spectrometer (Thermostar, Balzers, BSC 200). The heating program of conventional TPD is illustrated in Figure 1. Firstly, about 5 mg of the samples were heat treated up to 120 ℃ at heating rate of 20 ℃ min^{-1} followed by keeping this temperature for 2 h under a Helium flow rate of 100 mL min^{-1} as a sample drying process. After that, the samples were heat treated up to 920 ℃ at heating rate of 20 ℃ min^{-1}. During this heating up to 920 ℃, the different types and amount of gases decomposed from the samples were monitored (TPD experiment). Amounts of CO and CO_2 desorbed from the samples during the TPD experiments have been quantified by calibration of 28 and 44 mz^{-1} using calcium oxalate ($CaC_2O_4{\bullet}H_2O$) as calibration compound. The well-defined decomposition process of $CaC_2O_4{\bullet}H_2O$ are shown below with the overall reaction. Step 1 involves loss of crystallization water to form anhydrous calcium oxalate. Calcium oxalate then thermally decomposes to calcium carbonate in step 2 with the loss of carbon monoxide. The final step involves thermal decomposition of calcium carbonate to calcium oxide with the loss of carbon dioxide [11].

Overall Reaction: $CaC_2O_4{\bullet}H_2O \rightarrow CaO + H_2O + CO + CO_2$

Step 1) $CaC_2O_4{\bullet}H_2O \rightarrow CaC_2O_4 + H_2O$

Step 2) $CaC_2O_4 \rightarrow CaCO_3 + CO$

Step 3) $CaCO_3 \rightarrow CaO + CO_2$

For several samples, TPD experiments were done after the heat treatment process at 920 ℃ for 0.5 h (HT-TPD).

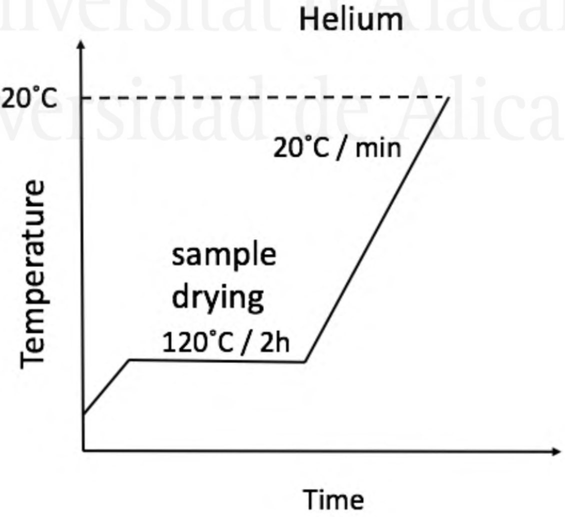

Figure 1. The heating program for the conventional TPD runs up to 920 ℃ in He.

2-3-3, Transmission electron microscopy (TEM)

TEM is a powerful and unique technique for structure characterization. TEM is a technique whereby a beam of electrons is transmitted through an ultrathin section, interacting with the samples as it passes [12]. The most important application of TEM is the atomic-resolution real-space imaging of nanoparticles [13]. The greatest advantages that TEM offers are the high magnification ranging from 50 to 10^6 and its ability to provide both image and diffraction information from a single sample [14]. All of the TEM images in this PhD Thesis were taken with a JEOL JEM-2010 microscope. A modern TEM is composed of an illumination system, a specimen stage, an objective lens system, the magnification system, the data recording system(s), and the chemical analysis system [13]. The electron gun which is the heart of the illumination system uses LaB_6 thermionic emission source and the operated voltage is 200 kV for this microscopy. The samples were suspended in ethanol to obtain a homogeneous dispersion before drop-casting them on a copper grid and then placed in the measurement chamber. The size of metal nanoparticles and structure of the catalysts and carbon materials were investigated by TEM.

2-3-4, Inductively coupled plasma optical emission spectroscopy (ICP-OES)

The ICP-OES is a powerful technique for the quantification of a variety of a large number of elements which are present at very low concentrations in an acid aqueous solution [4]. With this technique, liquid samples are injected into a radiofrequency-induced argon plasma using one of a variety of nebulizers or sample introduction techniques. The sample mist reaching the plasma is quickly dried, vaporized, and energized through collisional excitation at high temperature. The atomic emission emanating from the plasma is viewed in either a radial or axial configuration, collected with a len or mirror, and imaged onto the entrance slit of a wavelength selection device, monochromator or polychromator to monitor emission from different elements [15,16]. The wavelength allows to identify the specific element and the intensity of the emitted radiation allows the quantification of the element using a calibration pattern for the specific element. The amount of introduced Co into the carbon supports was examined by ICP-OES. The ICP-OES results were obtained using a PerkinElmer Optima 4300 system. The samples were dissolved in 2 ml of concentrated aqua regia (HNO_3 and HCl in a molar ratio of 1:3) and filtered. The solutions were adjusted to a final Co concentration between 0 and 20 ppm for its determination in the linear signal range.

2-3-5, X-ray photoelectron spectroscopy (XPS)

XPS is a versatile surface analysis technique that can be used for compositional and chemical states analysis. Since X-rays are used for the incident beam in XPS, the XPS technique causes very little charging of samples and thus it is useful for both electrically conductive and non-conductive materials [17,18]. Currently, the chemical state identification with XPS has become routine for most elements in the periodic table [19]. Photo-electrons produced in XPS cannot pass through more than perhaps 1 to 5 nm of a solid. Thus, XPS mainly gives information about the surface composition [4]. The elemental composition, chemical state and electronic state of the material are measured by irradiating a material with a beam of X-rays under high vacuum conditions ($<10^{-7}$ Pa). Finally, the spectra are obtained with the kinetic energy and number of electrons that escape from the top of the materials by photoelectric effect. The surface composition of our prepared catalysts were investigated by using XPS in a K-Alpha Thermo-Scientific spectrometer, equipped with an Al anode. Elemental analysis of the surfaces was calculated from the areas under the main peak of each atom. Deconvolution of the XPS were done by least squares fitting using Gaussian-Lorentzian curves, and as the background determination, a Shirley line was used.

2-3-6, X-ray diffraction (XRD)

XRD is a very important and useful characterization tool that has long been used to address all issues related to the crystal structure of solids, including lattice constants and geometry, identification of unknown materials, orientation of single crystals, preferred orientation of polycrystals, defects, stresses, etc [14]. It can also be used to measure various structural properties of these crystalline phases such as strain, grain size, phase composition, and defect structure [20]. In XRD, a collimated beam of X-rays, with a wavelength typically ranging from 0.7 to 2 Å, is incident on a specimen and is diffracted by the crystalline phases in the specimen according to Bragg's law [14]. X-ray diffraction (XRD) measurements in this PhD Thesis were performed using CuKα radiation (λ = 1.5406 Å) in the 2θ region between 5° and 70°. The X-ray generator was set to 45 kV at 40 mA on a Bruker D8 Advance diffractometer. The dimensions of carbon crystallites, Lc and La were obtained by applying Scherrer's formula to the (002) and (110) diffractions, respectively [21–23].

2-3-7, Gas adsorption isotherms

Gas adsorption measurements are widely used for determining the surface area and pore size distribution of a variety of different solid materials, such as industrial adsorbents, catalysts, pigments, ceramics and building materials. The measurement of adsorption at the gas/solid interface also forms an essential part of many fundamental and applied investigations of the nature and behavior of solid surfaces [24].

The porosity of the carbon materials used in this thesis were analyzed by CO_2 and N_2 adsorption isotherms at 0 ℃ and -196 ℃, respectively, using an Autosorb-6B apparatus (Quantachrome). For characterization of the porosity, the samples were outgassed at 200 ℃ for at least 8 hours.

Principles of the Brunauer-Emmett-Teller (BET) method

The BET method continues to be the most widely used procedure for evaluating the surface area of porous and finely-divided materials [24,25]. The BET model is based on the kinetic model of adsorption proposed by Langmuir and was extended to describe the multilayer adsorption by the introduction of some assumptions [26,27]. Two stages are involved in the application of the BET method. First, it is necessary to transform a physisorption isotherm into the 'BET plot'. From the 'BET plot', value of the BET monolayer capacity (n_m) can be derived. In the second stage, the BET-area is calculated from n_m by adopting an appropriate value of the molecular cross-sectional area, A_m [25].

The BET adsorption isotherm is denoted as follows,

$$\frac{\frac{P}{P_0}}{n(1-\frac{P}{P_0})} = \frac{1}{n_m C} + \frac{C-1}{n_m C} \cdot \frac{P}{P_0} \qquad (1)$$

where n is the specific amount adsorbed at the relative pressure P/P_0 and n_m is the specific monolayer capacity, and C is a constant related exponentially with the heat of adsorption of the first layer [24]. Finally, Equation (1) gives a linear relation between P/(n

(P_0 − P)) and P/ P_0, with the slope equal to (C−1)/(n_mC) and with 1/(n_mC) as the interception with the Y-axis. From this, the values of both n_m and C are obtained [27]. Then, the surface area of the adsorbent (S) expressed in m^2/g, is

$$S_{BET} = n_m \cdot A_m \cdot N_A \cdot 10^{-18} \qquad (2)$$

where N_A is the Avogadro constant. The monolayer capacity (n_m) and the cross-sectional area of the adsorbed molecule (A_m) are expressed in mol g^{-1} and nm^2 [27]. BET surface areas (S_{BET}) for the samples have been determined in the 0.02-0.20 range of relative pressures.

Assessment of microporosity

Micropore volume

One of the widely used method for evaluation of the micropore volume (MPV) is based on Dubinin's pore-volume-filling theory. In accordance with the Dubinin–Radushkevich (DR) equation, a plot of log W versus $\log^2$ (P_0/P) is linear provided the micropore size has a uniform Gaussian distribution and its extrapolation to the ordinate will give the micropore capacity, where W is volume filling [25]. Then, the well-known DR equation is obtained in equation (3) [28,29]:

$$logW = logW_0 - Dlog^2 \cdot (\frac{P_0}{P}) \quad (3)$$

where D = 2.303(RT/Eo β): Eo is characteristic energy and β is called affinity coefficient. Wo is total MPV. From its intercept, Wo can be obtained. The total MPV for our samples were determined applying the DR theory for P/P_0 from 0.01 to 0.05.

The narrow micropore volume

The narrow micropore volume (i.e., pore sizes below 0.7nm) has been calculated from the CO_2 adsorption isotherm at 0 °C. The narrow micropore volume also has been assessed by applying DR theory for P/P_0 from 0.003 to 0.22 [30].

Mesopore volume

Mesopore volume has been assessed by the difference of amount adsorbed at relative pressure between 0.20 and 0.95, assuming that the pores are filled with N_2 as liquid [31]. Total pore volume of the samples were calculated from the adsorption amount at $P/P_0 = 0.95$ [32].

Pore size distribution (PSD)

Pore size distribution (PSD) governs to a great extent the adsorption properties and its applications, such as development of supercapacitors [33,34], hydrogen storage at room temperature [35] and oxygen reduction process [36]. The PSD has been obtained from the N_2 adsorption isotherms (range of relative pressures from $5 \bullet 10^{-4}$ to 0.98) considering the 2D-NLDFT Heterogeneous surface model [37] and by applying the Solution of Adsorption Integral Equation Using Splines (SAIEUS, available online at http://www.nldft.com/) Software.

Electrochemical characterization

Electrochemical techniques are very powerful to follow reactions involving electron transfer and they relate the flow of electrons to chemical changes [38].

2-3-8, Cyclic Voltammetry (CV)

CV is a powerful electrochemical technique commonly employed to investigate the processes occurring in the interphase electrode/electrolyte which can be associated to the reduction or the oxidation of electroactive species [38]. In addition, the electrochemical capacitance and charge storage properties of carbon materials have been extensively studied by CV [39,40]. CV is also invaluable to study electron transfer-initiated chemical reactions, such as heterogeneous rate constant, electroactive surface area and amount of electroactive sites [41,42].

A schematic representation of an electrochemical cell is presented in Figure 2. This setup is typical for common electrochemical experiments, including CV and the three electrodes represent a working electrode (WE), counter electrode (CE), and reference electrode (RE), respectively. While the current flows between the WE and CE, the RE is used to accurately measure the applied potential relative to a stable reference reaction (reference electrode). The WE carries out the electrochemical event of interest. A potentiostat is used to control the applied potential of the WE as a function of the RE potential. It is used as a reference point against which the potential of other electrodes can be measured in an electrochemical cell. When a potential is applied to the WE such that reduction (or oxidation) of the sample occurs, current begins to flow between WE and CE. The purpose of the CE is to complete the electrical circuit [38,43].

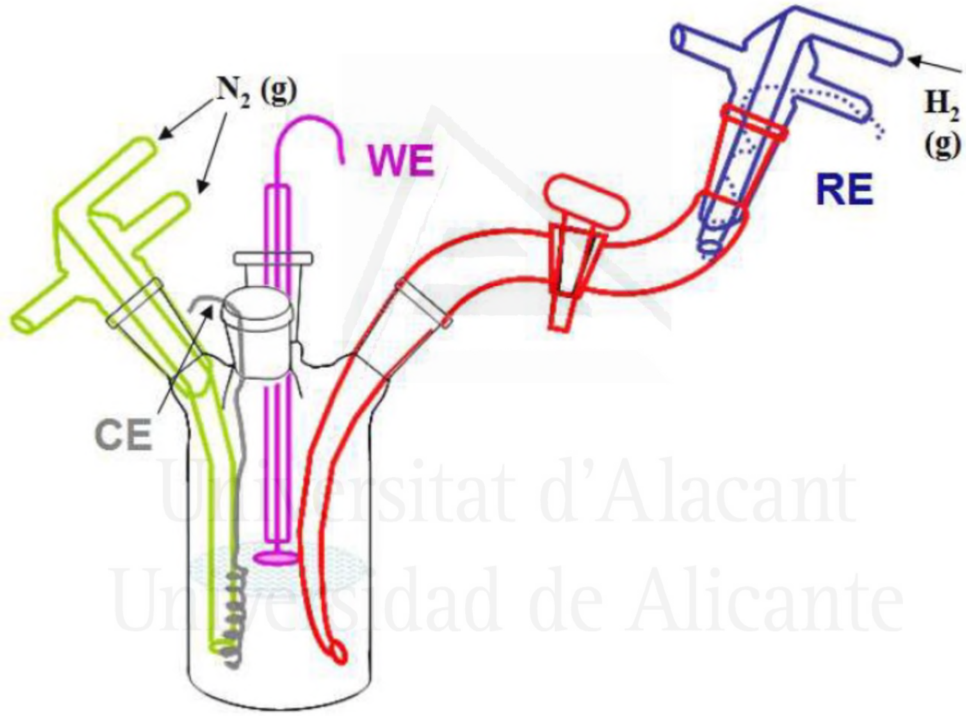

Figure 2. A schematic representation of an electrochemical cell.

In this PhD Thesis, typically, CV were carried out in a three-electrode cell using 0.1M KOH or 0.1M $HClO_4$ electrolyte, a Pt wire or graphite bar as CE and Reversible Hydrogen Electrode (RHE) introduced in the same working electrolyte or Ag/AgCl/Cl^- (3M) as RE and glassy carbon (typically 3 mm diameter) was used as a WE. The CVs were performed between 0 V and 1 V (vs. RHE) in a N_2 or O_2-saturated electrolyte at 5 mVs^{-1}. By performing CV in N_2 atmosphere at scan rate of 50, 10 and 5 mV s^{-1}, gravimetric capacitance of prepared electrodes has been also determined from the integration of the CVs [44].

2-3-9, Rotating disk electrode

Rotating disk electrode (RDE) is one of the few convective electrode systems and well characterized hydrodynamic electrode [45]. By rotating the electrode, the spinning disk is able to drag the fluid at its surface and, due to its centrifugal force, flings the solution outward from the center to a radial direction occur as presented in Figure 3 [43]. This technique has been used for the study of oxygen reduction reaction. Because of the symmetry of the system, it is convenient to write the hydrodynamic equations in terms of cylindrical coordinates of the RDE. A vector representation of the flow velocities is also presented in Figure 3. Once the velocity profile has been determined, the convective-diffusion equation can be solved.

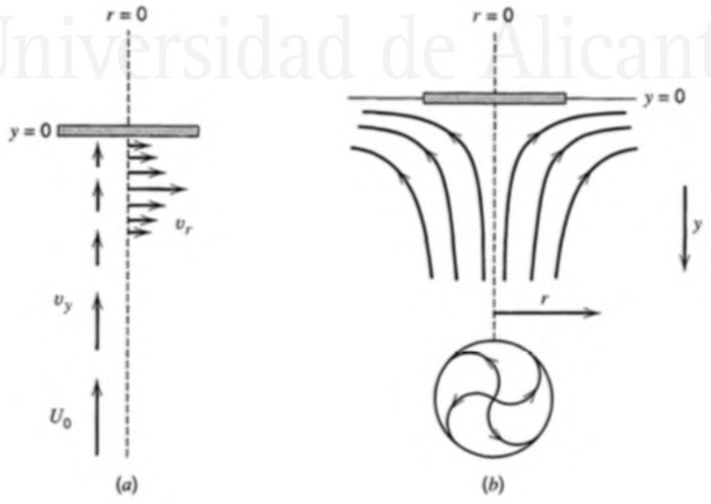

Figure 3. (a) Vector representation of fluid velocities near a rotating disk, (b) Schematic resultant streamlines (or flows) [43].

In mass-transfer-limited condition at the RDE and considering the electrode process reaction indicated below [45],

$$A + ne^- \rightarrow B$$

Levich equation can be obtained as equation (4) and the diffusion-limiting current during RDE experiments (j_{O2}^{L}, mA cm^{-2}) has been defined [43]:

$$j_{O2}^{L} = n \cdot F \cdot 0.62 \cdot D_{O_2}^{2/3} \cdot \upsilon^{-1/6} \cdot \omega^{1/2} \cdot C_{O_2}^{B} = n \cdot F \cdot k_L^f \cdot C_{O_2}^{B} \quad (4)$$

In Eqn. 4, n is the number of electrons transferred in the electrochemical reaction, F stands for the Faraday constant (96,485 C mol^{-1}), D_{O2} is the diffusion coefficient of oxygen ($1.8 \cdot 10^{-5}$ cm^2 s^{-1}), υ is the kinematic viscosity of the solution (0.01 cm^2 s^{-1}) and ω is the rotation rate (rad s^{-1}). $C_{O2}{}^{B}$ is oxygen concentration in the bulk of the solution ($1.2 \cdot 10^{-6}$ mol cm^{-3}). Advantages of RDE include that the rate of mass transport of reactants to a RDE surface is controlled precisely by fixing the rotational velocity (ω) of the electrode. The current quickly achieves steady-state values for a given applied electrode potentials for moderate-to-high rates of rotational rate [46].

Moreover, for non-limiting-current conditions, kinetically-limited current densities (j_k) can be shown in equation (5) which is constant at certain potential [47–49]:

$$j_K = n \cdot F \cdot k \cdot C_{O_2}^{B} \quad (5)$$

where k stands for rate constant for O_2 reduction.

For reactions which are controlled by both diffusion and reaction kinetics at RDE, the total current density, j, of the reacting electroactive species is related to the speed of rotation of the electrode (ω), commonly known as the Koutecky-Levich equation [45],

$$\frac{1}{j} = \frac{1}{j_K} + \frac{1}{j_{O2}^{L}} \quad (6)$$

Where j is the measured current density, j_K and j_{O2}^{L} are the kinetic and diffusion-limiting current densities, respectively. The resultant n value from the slope of K-L plot drawn at different potentials can be obtained, which will be explained in this section later.

2-3-10, Rotating Ring Disk Electrode (RRDE)

The thin-film RDE technique can also be applied to rotating ring-disk electrodes (RRDE) which allows detailed study of the oxygen reduction reaction (ORR). Scheme of the RRDE system is illustrated in Figure 4. In this case, the H_2O_2 formed in the disk electrode during the ORR (i.e. the so-called two-electron pathway) diffuse to the ring electrode, in which it can be oxidized. By fixing the potential of the ring electrode during cathodic or anodic sweeps of the disk electrode potential, free H_2O_2 generated at the disk and passing near the ring by convection, is oxidized and produces the current [50]. Overall, the oxidation current of H_2O_2 can be determined simultaneously to the overall ORR activity. In this PhD Thesis the different electrode materials used for the ORR are placed on the disk electrode (glassy carbon) and the ring electrode is Pt.

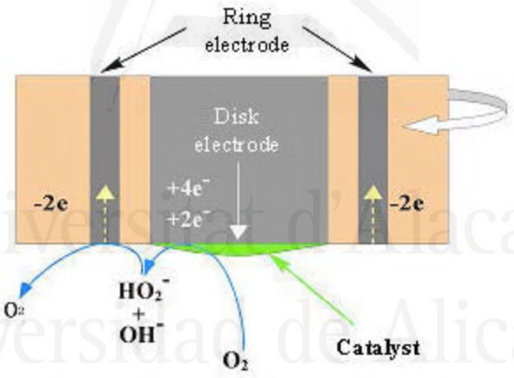

Figure 4. Scheme of the RRDE system.

2-3-11, ORR characterization

Electrochemical activity tests towards ORR were also carried out in a three-electrode cell using 0.1M KOH or 0.1M $HClO_4$ electrolyte, three electrode cell configuration is the same as for CV. A rotating ring-disk electrode (RRDE, Pine Research Instruments, USA) equipped with a glassy carbon (GC) disk (5.61 mm diameter) and an attached Pt ring was used as working electrode. The catalysts were dispersed in a solution of 80 vol.% of isopropanol, 20 vol.% of water and 0.02 vol.% of Nafion@ to prepare a final dispersion of 1 mg ml^{-1} of the material. Typically, 100 µl (mass of electrode is 400 $\mu g.cm^{-2}$) of the dispersion was pipetted on a GC electrode to obtain uniform catalysts layer for ORR study although the effect of the mass of electrode (80, 800 and 1600 µg.cm^{-2}) was also studied. The sample on the GC was dried by heating lamp for evaporation of the solvent. The Linear sweep voltammetry (LSV) was done in an O_2-saturated atmosphere for different rotation rates of 400, 625, 900, 1025, 1600 and 2025 rpm at 5 mV s^{-1}. The potential of the ring electrode was kept at 1.5 V (vs. RHE) and the ring current by H_2O_2 oxidation was also measured during the LSV measurement.

Electron transfer number (n) for ORR was determined by the following equation [47]:

$$n = \frac{4 \cdot I_D}{I_D + I_R/N} \quad (7)$$

where I_D is disk current, I_R is ring current, and N is the collection efficiency of the RRDE used in this PhD Thesis. The N was experimentally determined to be 0.37 which depends only on diameter of RRDE and is independent of ω, D_{O_2}, $C_{O_2}^{B}$, etc. For the calibration experiments of N, a solution containing 0.1 M NaOH with 10 mM $K_3Fe(CN)_6$ was used. At ring electrode, the oxidation of $[Fe(CN_6)]^{4-}$, which is produced at the disk electrode, to $[Fe(CN)_6]^{3-}$, proceeds under pure diffusion control, while oxygen evolution current at the Pt-ring are still negligible. The collection efficiency is then determined from the ring and disk currents [51].

Furthermore, the number of electrons has been determined from the slope of the Koutecky -Levich (K-L) plots at different potentials [52] using LSV recorded at several rotation rates (400, 625, 900, 1225 and 1600 rpm). The electron transfer number was deduced from the slope of the linear plot of J^{-1} (mA^{-1} cm^{2}) versus $\omega^{-1/2}$ (rad^{-1} s^{-1}). The slope of the straight line from a K-L plot referred to as "B factor". The theoretical "B factor" for a direct four-electron process can be described to 0.46 mA cm^{-2} s$^{1/2}$ [53]. Thus, n was calculated by dividing "B factor" by $0.62 \cdot F \cdot D_{O_2}^{2/3} \cdot \upsilon^{-1/6} \cdot C_{O_2}^{B}$.

2-3-12, H_2O_2 reduction experiment

Additional LSV experiments in N_2- and O_2-saturated 0.1 M KOH solution containing 3 mM H_2O_2 were performed using the RRDE with the same experimental conditions reported for the ORR experiments. By conducting the experiment N_2-saturated atmosphere, the current relating only H_2O_2 reduction for the prepared samples were determined.

2-4, References

[1] M. Inagaki, L.R. Radovic, Nanocarbons, Carbon. 40 (2002) 2279–2281. doi:Pii S0008-6223(02)00204-X.

[2] M.C. Román-Martínez, D. Cazorla-Amorós, A. Linares-Solano, C. Salinas-Martínez De Lecea, F. Atamny, Structural study of a phenolformaldehyde char, Carbon. 34 (1996) 719–727. doi:10.1016/0008-6223(95)00194-8.

[3] D. Lozano-Castelló, M.A. Lillo-Ródenas, D. Cazorla-Amorós, A. Linares-Solano, Preparation of activated carbons from Spanish anthracite: I. Activation by KOH, Carbon. 39 (2001) 741–749. doi:10.1016/S0008-6223(00)00185-8.

[4] D.A. Skoog, F.J. Holler, S.R. Crouch, Principles of Instrumental Analysis, 2007. doi:10.15713/ins.mmj.3.

[5] Y. Otake, R.G. Jenkins, Characterization of oxygen-containing surface complexes created on a microporous carbon by air and nitric acid treatment, Carbon. 31 (1993) 109–121. doi:10.1016/0008-6223(93)90163-5.

[6] J.L. Figueiredo, M.F.R. Pereira, M.M.A. Freitas, J.J.M. Órfão, Modification of the surface chemistry of activated carbons, Carbon. 37 (1999) 1379–1389. doi:10.1016/S0008-6223(98)00333-9.

[7] P.J. Hall, J.M. Calo, Secondary Interactions upon Thermal Desorption of Surface Oxides from Coal Chars, Energy and Fuels. 3 (1989) 370–376. doi:10.1021/ef00015a020.

[8] J.M. Calo, D. Cazorla-Amorós, A. Linares-Solano, M.C. Román-Martínez, C. Salinas-Martínez De Lecea, The effects of hydrogen on thermal desorption of oxygen surface complexes, Carbon. 35 (1997) 543–554. doi:10.1016/S0008-6223(96)00173-X.

[9] M.C. Román-Martínez, D. Cazorla-Amorós, A. Linares-Solano, C.S.-M. de Lecea, TPD and TPR characterization of carbonaceous supports and Pt/C catalysts, Carbon. 31 (1993) 895–902. doi:10.1016/0008-6223(93)90190-L.

[10] H.P. Boehm, Surface oxides on carbon and their analysis: A critical assessment, Carbon. 40 (2002) 145–149. doi:10.1016/S0008-6223(01)00165-8.

[11] K. Lawson-wood, I. Robertson, Study of the Decomposition of Calcium Oxalate Monohydrate using a Hyphenated Thermogravimetric Analyser - FT-IR System (TG-IR), (2016) 1–3. https://www.perkinelmer.com/lab-

solutions/resources/docs/APP_Decomposition_CalciumOxalate_Monohydrate(013078_01).pdf%0Ahttps://mondo.su.se/access/content/group/ee616fea-4bdd47d6-9eb9-1eb4cd1aa4ec/Labcompendium/APP_Decomposition_Calcium Oxalate Monohydr.

[12] David B. WilliamsC. Barry Carter, Transmission electron microscopy A Textbook for Materials Science, 2nd ed., Springer US, 1996. doi: 10.1007/978-0-387-76501-3

[13] Z.L. Wang, Transmission Electron Microscopy of Shape-Controlled Nanocrystals and Their Assemblies, J. Phys. Chem. B. 104 (2000) 1153–1175. doi:10.1021/jp993593c.

[14] M.L.T. Cossio, L.F. Giesen, G. Araya, M.L.S. Pérez-Cotapos, R.L. VERGARA, M. Manca, R.A. Tohme, S.D. Holmberg, T. Bressmann, D.R. Lirio, J.S. Román, R.G. Solís, S. Thakur, S.N. Rao, E.L. Modelado, A.D.E. La, C. Durante, U.N.A. Tradición, M. En, E.L. Espejo, D.E.L.A.S. Fuentes, U.A. De Yucatán, C.M. Lenin, L.F. Cian, M.J. Douglas, L. Plata, F. Héritier, Nanostructures and Nanomaterials, Synthesis, Properties & Applications, 2nd ed., Imperial College Press, 2004. doi:10.1007/s13398-014-0173-7.2.

[15] X. Hou, B.T. Jones, Inductively Coupled Plasma-Optical Emission Spectroscopy, Encycl. Anal. Chem. Instrum. Appl. (2000) 9468–9485.

[16] J.W. Olesik, Elemental analysis Using An Evaluation and Assessment of remaining problems, Analytical Chemistry, 63 (1991) 12-21.

[17] C.R. BRUNDLE, Xps, Encycl. Mater. Charact. (1992) 282–299. doi:10.1016/B978-0-08-052360-6.50028-X.

[18] T. Yamashita, P. Hayes, Analysis of XPS spectra of Fe2+ and Fe3+ ions in oxide materials, Appl. Surf. Sci. 254 (2008) 2441–2449. doi:10.1016/j.apsusc.2007.09.063.

[19] M.C. Biesinger, B.P. Payne, A.P. Grosvenor, L.W.M. Lau, A.R. Gerson, R.S.C. Smart, Resolving surface chemical states in XPS analysis of first row transition metals, oxides and hydroxides: Cr, Mn, Fe, Co and Ni, Appl. Surf. Sci. 257 (2011) 2717–2730. doi:10.1016/j.apsusc.2010.10.051.

[20] R. Sharma, D.P. Bisen, U. Shukla, B.G. Sharma, X-ray diffraction: a powerful method of characterizing nanomaterials, Recent Res. Sci. Technol. 4 (2012) 77–79. http://recent-science.com/.

[21] C. Vix-Guterl, M. Couzi, J. Dentzer, M. Trinquecoste, P. Delhaes, Surface Characterizations of Carbon Multiwall Nanotubes: Comparison between Surface Active Sites and Raman Spectroscopy, J. Phys. Chem. B. 108 (2004) 19361–19367. doi:10.1021/jp047237s.

[22] J.I. Ozaki, K. Nozawa, K. Yamada, Y. Uchiyama, Y. Yoshimoto, A. Furuichi, T. Yokoyama, A. Oya, L.J. Brown, J.D. Cashion, Structures, physicochemical properties and oxygen reduction activities of carbons derived from ferrocene-poly(furfuryl alcohol) mixtures, J. Appl. Electrochem. 36 (2006) 239–247. doi:10.1007/s10800-005-9054-2.

[23] B.C. Moore, J.A. Macia, Influence of carbon fibres crystallinities on their chemical activation by KOH and NaOH, Microporous and Mesoporous Materials, 101 (2007) 397–405. doi:10.1016/j.micromeso.2006.12.002.

[24] K.S.W. Sing, D.H. Everett, R.A.W. Haul, L. Moscou, R.A. Pierotti, J. Rouquérol, T. Siemieniewska, Reporting physisorption data for gas / solid systems with Special Reference to the Determination of Surface Area and Porosity, Pure & Appl. Chem., 57 (1985) 603–619.

[25] M. Thommes, K. Kaneko, A. V. Neimark, J.P. Olivier, F. Rodriguez-Reinoso, J. Rouquerol, K.S.W. Sing, Physisorption of gases, with special reference to the evaluation of surface area and pore size distribution (IUPAC Technical Report), Pure Appl. Chem. 87 (2015) 1051–1069. doi:10.1515/pac-2014-1117.

[26] S. Brunauer, P.H. Emmett, E. Teller, Adsorption of Gases in Multimolecular Layers, J. Am. Chem. Soc. 60 (1938) 309–319. doi:citeulike-article-id:4074706.

[27] D. Lozano-Castelló, F. Suarez-garcia, D. Cazorla-Amorós, Angel linares Solano, Porous Texture of Carbons, Carbons for Electrochemical Energy Storage and Conversion Systems, (2010) 115-162. doi:1420053078.

[28] M.M. Dubinin, H.F.stoeckli, Homogeneous and heterogeneous micropore structures in carbonaceous adsorbents, Journal of Colloid and Interface Science, 75, (1980) 34–42.

[29] M.M. Dubinin, Generalization of the theory of volume filling of micropores to nonhomogeneous microporous structures, Carbon. 23 (1985) 373–380. doi:https://doi.org/10.1016/0008-6223(85)90029-6.

[30] D. Cazorla-Amorós, J. Alcañiz-Monge, M.A. de la Casa-Lillo, A. Linares-Solano, CO_2 As an Adsorptive To Characterize Carbon Molecular Sieves and Activated

Carbons, Langmuir. 14 (1998) 4589–4596. doi:10.1021/la980198p.

[31] D. Salinas-Torres, R. Ruiz-Rosas, M.J. Valero-Romero, J. Rodríguez-Mirasol, T. Cordero, E. Morallón, D. Cazorla-Amorós, Asymmetric capacitors using lignin-based hierarchical porous carbons, J. Power Sources. 326 (2016) 641–651. doi:10.1016/j.jpowsour.2016.03.096.

[32] H. Nishihara, T. Simura, T. Kyotani, Enhanced hydrogen spillover to fullerene at ambient temperature, Chem. Commun. 54 (2018) 3327–3330. doi:10.1039/C8CC00265G.

[33] P. Simon, A. Burke, Nanostructured carbons: Double-layer capacitance and more, Electrochem. Soc. Interface. 17 (2008) 38–43. doi:10.1016/j.carbon.2005.06.046.

[34] M.J. Bleda-Martínez, D. Lozano-Castelló, D. Cazorla-Amorós, E. Morallón, Kinetics of double-layer formation: Influence of porous structure and pore size distribution, Energy and Fuels. 24 (2010) 3378–3384. doi:10.1021/ef901521g.

[35] M. Jordá-Beneyto, F. Suárez-García, D. Lozano-Castelló, D. Cazorla-Amorós, A. Linares-Solano, Hydrogen storage on chemically activated carbons and carbon nanomaterials at high pressures, Carbon. 45 (2007) 293–303. doi:10.1016/j.carbon.2006.09.022.

[36] M. Seredych, A. Szczurek, V. Fierro, A. Celzard, T.J. Bandosz, Electrochemical Reduction of Oxygen on Hydrophobic Ultramicroporous PolyHIPE Carbon, ACS Catal. 6 (2016) 5618–5628. doi:10.1021/acscatal.6b01497.

[37] J. Jagiello, J.P. Olivier, 2D-NLDFT adsorption models for carbon slit-shaped pores with surface energetical heterogeneity and geometrical corrugation, Carbon. 55 (2013) 70–80.

[38] N. Elgrishi, K.J. Rountree, B.D. McCarthy, E.S. Rountree, T.T. Eisenhart, J.L. Dempsey, A Practical Beginner's Guide to Cyclic Voltammetry, J. Chem. Educ. 95 (2018) 197–206. doi:10.1021/acs.jchemed.7b00361.

[39] E. Frackowiak, F. Béguin, Carbon materials for the electrochemical storage of energy in capacitors, Carbon. 39 (2001) 937–950. doi:10.1016/S0008-6223(00)00183-4.

[40] C. Peng, S. Zhang, D. Jewell, G.Z. Chen, Carbon nanotube and conducting polymer composites for supercapacitors, Prog. Nat. Sci. 18 (2008) 777–788. doi:10.1016/j.pnsc.2008.03.002.

[41] R.S. Nicholson, Theory and Application of Cyclic Voltammetry for Measurement

of Electrode Reaction Kinetics, Anal. Chem. 37 (1965) 1351–1355. doi:10.1021/ac60230a016.

[42] D. Salinas-Torres, F. Huerta, F. Montilla, E. Morallón, Study on electroactive and electrocatalytic surfaces of single walled carbon nanotube-modified electrodes, Electrochim. Acta. 56 (2011) 2464–2470. doi:10.1016/j.electacta.2010.11.023.

[43] A.J. Bard, L.R. Faulkner, Electrochemical Methods: Fundamentals and Applications, 2a., Wiley, 2001.

[44] M.J. Mostazo-López, R. Ruiz-Rosas, E. Morallón, D. Cazorla-Amorós, Nitrogen doped superporous carbon prepared by a mild method. Enhancement of supercapacitor performance, Int. J. Hydrogen Energy. 41 (2016) 19691–19701. doi:10.1016/j.ijhydene.2016.03.091.

[45] J. Masa, C. Batchelor-McAuley, W. Schuhmann, R.G. Compton, Koutecky-Levich analysis applied to nanoparticle modified rotating disk electrodes: Electrocatalysis or misinterpretation, Nano Res. 7 (2014) 71–78. doi:10.1007/s12274-013-0372-0.

[46] S. Treimer, A. Tang, D.C. Johnson, A consideration of the application of Koutecký-Levich plots in the diagnoses of charge-transfer mechanisms at rotated disk electrodes, Electroanalysis. 14 (2002) 165–171. doi:10.1002/1521-4109(200202)14:3<165::AID-ELAN165>3.0.CO;2-6.

[47] R. Zhou, Y. Zheng, M. Jaroniec, S.-Z. Qiao, Determination of the Electron Transfer Number for the Oxygen Reduction Reaction: From Theory to Experiment, ACS Catal. 6 (2016) 4720–4728. doi:10.1021/acscatal.6b01581.

[48] Y. Liu, K. Li, B. Ge, L. Pu, Z. Liu, Influence of Micropore and Mesoporous in Activated Carbon Air-cathode Catalysts on Oxygen Reduction Reaction in Microbial Fuel Cells, Electrochim. Acta. 214 (2016) 110–118. doi:10.1016/j.electacta.2016.08.034.

[49] C. González-Gaitán, R. Ruiz-Rosas, E. Morallón, D. Cazorla-Amorós, Functionalization of carbon nanotubes using aminobenzene acids and electrochemical methods. Electroactivity for the oxygen reduction reaction, Int. J. Hydrogen Energy. 40 (2015) 11242–11253. doi:10.1016/j.ijhydene.2015.02.070.

[50] A. Bonakdarpour, M. Lefevre, R. Yang, F. Jaouen, T. Dahn, J.-P. Dodelet, J.R. Dahn, Impact of Loading in RRDE Experiments on Fe–N–C Catalysts: Two- or Four-Electron Oxygen Reduction?, Electrochem. Solid-State Lett. 11 (2008) B105. doi:10.1149/1.2904768.

[51] U.A. Paulus, T.J. Schmidt, H.A. Gasteiger, R.J. Behm, Oxygen reduction on a high-surface area Pt/Vulcan carbon catalyst: A thin-film rotating ring-disk electrode study, J. Electroanal. Chem. 495 (2001) 134–145. doi:10.1016/S0022-0728(00)00407-1.

[52] G. Zhang, W. Lu, F. Cao, Z. Xiao, X. Zheng, N-doped graphene coupled with Co nanoparticles as an efficient electrocatalyst for oxygen reduction in alkaline media, J. Power Sources. 302 (2016) 114–125. doi:10.1016/j.jpowsour.2015.10.055.

[53] P.W. Menezes, A. Indra, D. González-Flores, N.R. Sahraie, I. Zaharieva, M. Schwarze, P. Strasser, H. Dau, M. Driess, High-Performance Oxygen Redox Catalysis with Multifunctional Cobalt Oxide Nanochains: Morphology-Dependent Activity, ACS Catal. 5 (2015) 2017–2027. doi:10.1021/cs501724v.

Chapter 3.

Understanding of oxygen reduction reaction by examining carbon-oxygen gasification reaction and carbon active sites on metal and heteroatoms free carbon materials of different porosities and structure.

3-1, Introduction

Fuel cells (FCs) convert chemical energy of fuel and oxidant into electric energy. Unlike batteries, they do not need recharging as long as fuel and oxidant are continuously supplied [1]. At the cathode of a proton exchange membrane fuel cell, oxygen is reduced by reaction with protons and electrons to produce water ($1/2O_2 + 2H^+ + 2e^- \rightarrow H_2O$) [1]. The sluggish reaction kinetics of Oxygen Reduction Reaction (ORR) even on the best Pt-based catalyst requires high Pt loading (~0.4 mg cm^{-2}) to achieve a desirable fuel cell performance. Pt is a scarce and expensive metal and the Pt-based electrodes suffer from CO deactivation [2–5]. Hence, cathode development requires special attention to find the best catalyst and electrode structure to combine performance and stability [3]. Indeed, heteroatom (N, S, P, B and F)-doped carbon materials, transition metal oxides (e.g., CoO, Co_3O_4, Cu_2O, MnO_2) and metal nitrogen complexes (Co-Nx, Fe-Nx) on carbon nanomaterials can be promising candidates as non-precious metal catalysts for ORR in alkaline medium [6–8]. Because of its desirable electrical and mechanical properties as well as large accessible surface area, new nanostructured carbon materials such as graphene and carbon nanotubes (CNT) have widely contributed to deriving advanced electrocatalysts [9].

Nowadays, dopants, edges, and defects have been demonstrated to generate promising ORR activity to metal-free nanocarbon materials by modification of electron structure of the materials [10]. In the case of nitrogen doping, in general, it is concluded that carbon atoms near nitrogen are the active sites for ORR, although there are discrepancies about the structure of the most active sites [11–14]. Regarding edges effects toward ORR, studies using highly oriented pyrolytic graphite by Shen et al. revealed that the activity is much higher at the edge of graphite than at the basal plane [15]. Similarly, Qu concluded that the specific catalytic activity of activated carbon is determined by the percentage of the edge orientation on the surface [16]. Tang et al. explained using DFT calculations that all-carbon topological defects can deliver an excellent activity for both ORR and OER, while topological defects containing nitrogen doping are expected to produce a higher enhancement [17]. In addition, structure of a nitrogen doped Stone-Wales defect provides active sites and its ORR activity can be tuned by the curvature around the active sites [18]. Defective activated carbon derived via heat treatment of the N-doped activated carbons demonstrated comparable activity to commercial Pt/C catalysts [19]. Combination of the defects or edge carbons and the electron transfer resistance ultimately determines the

ORR performance of drilled CNTs [20]. In consequence, it was proposed that the origin of ORR activity is a result of carbon restructuring and the possible formation of topological defects during the removal of high temperature CO desorbing functional groups [21].

To sum up, a wide range of metal free carbon based catalysts have been explored for improving ORR activities in recent years. However, knowledge of the critical active sites and underlying mechanism still remains confusing and controversial [17].

Meanwhile, extensive investigation regarding carbon-oxygen gasification were carried out from which clear evidences about the involved active sites and the reaction mechanism were collected [22,23]. Oxygen-transfer reactions of carbon materials are at the heart of fuel combustion and gasification processes and much progress has been made in achieving their fundamental understanding [24]. As described by reaction (1), in carbon gasification or combustion the oxygen molecule reacts with the carbon reactive site (Cf_1) from the carbon structure to desorb as CO or CO_2.

$$O_2 + 2Cf_1 = 2C\text{–}O \qquad (1)$$

In ORR, it was stablished that the first step in the reduction of oxygen is the one-electron reduction to superoxide ion, as detailed in Reaction (2) [25]

$$O_2 + e^- + Cf_2 = C\text{–}O_2^* \qquad (2)$$

Subsequent to Reaction (2) the adsorbed superoxide anion radical picks up a proton from the electrolyte solution to form and desorb a hydroperoxide ion HO_2^-, thus regenerating the same carbon active site (Cf_2). Radovic has questioned if the sites which are related to carbon gasification (Cf_1) and ORR (Cf_2) are different or not. Answering this question could bring light to the understanding of the ORR mechanism and in suitably tailoring carbon surfaces [26]. In this sense, the concept of active surface area (ASA), which is derived from the studies of carbon gasification, was extremely useful to understand the reactivity of carbon materials [27]. Reactivity is another extensively used measurement for analyzing the oxidation behavior of carbonaceous solids [28]. The ASA has been recently applied not only to the carbon gasification reactions but also to electrochemical processes [29–32].

For instance, the value of irreversible capacity of lithium ion batteries or the electrochemical storage of hydrogen are directly related with the ASA [30,32].

In summary, several electrochemical properties have been correlated with ASA. However, the correlations of ORR on carbon materials and carbon-oxygen gasification properties have not been identified. The aim of this study is to elucidate the relationship between carbon-oxygen gasification properties and ORR activities. For this purpose, carbon materials including different structures and porosities, such as activated carbons, carbon blacks, carbon nanotubes, carbon nanofiber and graphite were selected. After identifying structural and electrochemical properties of these materials, some insights about the mechanism for ORR in relation to carbon-oxygen gasification properties is proposed.

3-2, Experimental section

3-2-1, Material preparation

Commercial carbon materials and materials prepared in our laboratory were used in this study. Multi-wall Carbon Nanotubes (MW) and Single-Wall/Double-Wall Carbon Nanotubes (SW) were purchased from Cheap Tubes Inc. (Brattleboro, Vt, USA) with a 99 % of purity, outer diameter: 13-18 nm, length: 3–30 µm and with a 99 % of purity, outer diameter: 1-2 nm and length: 3–30 µm, respectively. Carbon nanotube herringbone (labeled as Herring along this work) from TOKYO CHEMICAL INDUSTRY with a 95 % of purity, outer diameter: 10-20 nm and length: 5–15 µm was also used. Graphite (KS4) from TIMCAL Ltd., commercial XC-72F Vulcan carbon black (XC72) from Cabot Corporation, CD-6008 carbon black (CB) from COLUMBIAN CHEMICALS and a highly microporous activated carbon (YPF) supplied from KURARAY were also used. A microporous char (AC) derived by carbonization of phenolformaldehyde polymer resin and carbon nanofiber (CNF) synthesized by our lab were also used.

It is known that presence of metallic impurities, such as those used as catalysts in the production of carbon nanotubes, do high catalytic activities with respect to oxygen reduction reaction [33] and carbon oxidation [34]. For this reason, the carbon materials used herein were demineralized by 5 M hydrochloric acid at 50 ˚C for overnight to remove the inorganic matter. In addition, SW treated with concentrated nitric acid at 70 ˚C for 12 h were also prepared [35]. This sample was labeled as SW_HNO_3. The resulting samples were filtered and washed several times by distilled water until the pH of the filtrate was the same as that of the distilled water. Finally, the materials were dried at 120

°C, what was followed by physicochemical and electrochemical characterizations for analyzing the purity of the samples.

3-2-2, Physicochemical characterization

Transmission electron microscopy (TEM) images of the materials were taken with a JEOL JEM-2010 microscope operated at 200 kV. The samples were suspended in ethanol to obtain a homogeneous dispersion before drop-casting them on a copper grid and then placed in the measurement chamber. Porous texture of all the samples were determined by physical adsorption (N_2 at -196 °C and CO_2 at 0 °C) using an automatic adsorption system (Autosorb-6, Quantrachrome) after samples out-gassing at 250 °C under vacuum for 4 h. The total micropore volume (pore size smaller than 2 nm) was calculated from the application of the Dubinin–Radushkevich theory to the N_2 adsorption at -196 °C. The narrow micropore volume (pore size smaller than around 0.7 nm) has been assessed from CO_2 adsorption at 0 °C using the DR equation [36,37]. The densities of the adsorbed phase used for the calculations were 0.808 and 1.023 g ml^{-1} for N_2 and CO_2, respectively. The specific surface area was calculated by the BET equation.

3-2-3, Carbon-oxygen gasification characterization

The severity of thermal treatment conditions such as residence time, temperature and heating-rate have a significant effect on the ASA as well as reactivity for carbon-oxygen reaction measurements [38]. Therefore, all of the carbon samples purified herein were treated by same thermal treatment conditions. The ASA gives a measurement of the number of reactive carbon atoms or active carbon sites corresponding mainly to edge planes and defects of a carbon sample [32]. The ASA for our samples was measured using an established method which is based on di-oxygen chemisorption [39]. Firstly, about 10 mg of purified samples were heat treated up to 920 °C at a heating rate of 20 °C min^{-1}, flow rate of 100 mL min^{-1} and kept at 920 °C for 0.5 h under N_2 to remove oxygen complexes on the carbon surface. Afterwards, temperature is lowered to 250 °C and kept for 1 h while keeping the inert atmosphere. Next, synthetic dry air (20 vol.% O_2 in N_2 base) is fed to the thermobalance for 7 h to perform the oxygen chemisorption step. The ASA was then determined from the weight uptake of the samples by the following equation assuming that each chemisorbed oxygen atom occupies an area of 0.083 nm^2 [39].

$$ASA = \frac{1}{w_0} \cdot \frac{A \times N \times (w_C - w_0)}{N_{O2}} \qquad (3)$$

where A is the area that one oxygen atom occupies per edge carbon atom, N is Avogadro constant, w_0 is the starting weight of carbon in the chemisorption step, w_c is the weight of carbon after oxygen chemisorption and N_{O2} is oxygen molecular weight.

Reactivities for carbon-oxygen gasification were determined by isothermal TGA analysis under synthetic dry air. About 10 mg of the purified samples were heated in a N_2 stream up to 920 °C at a rate of 20 °C min^{-1} and kept for 0.5 h. Next, temperature is lowered to the selected reaction temperature (typically from 500 °C to 670 °C) and kept for 1 h. Finally, synthetic dry air is fed, and the resulting weight changes were recorded continuously as a function of time. The reactivity was given by the following equation

$$R_T = -\frac{1}{w_0} \cdot \frac{dw}{dt} \qquad (4)$$

Where R_T is the initial reactivity at a temperature T (gg^{-1}h^{-1}), w_0 is the initial mass of the sample (g), on an ash free basis, and $\frac{dw}{dt}$ is the initial rectilinear weight loss rate (gh^{-1}) [34]. A TA thermobalance (SDT 600) with a sensitivity of 1 µg has been used for these measurements.

3-2-4, Surface chemistry

Temperature-Programmed Desorption (TPD) measurements are extensively used for characterizing the surface functionalities of carbon materials [40,41]. Oxygen complexes decomposed as CO_2 and CO can be followed by TPD techniques [40]. TPD experiments were performed in a thermogravimetric system (TA Instruments, SDT Q600 Simultaneous) coupled to a mass spectrometer (Thermostar, Balzers, BSC 200). The samples were heat treated up to 920 °C at rate of 20 °C min^{-1} followed by keeping this temperature for 0.5 h under a Helium flow rate of 100 mL/min to clean the carbon surfaces. During this heating up to 920 °C, types and amount of gases decomposed from the samples were monitored (TPD experiment). TPD experiments were also done for the samples after the heat treatment process (HT-TPD). Amounts of CO and CO_2 desorbed from the samples during the experiments were quantified by calibration of 28 and 44 m z^{-1} signals using calcium oxalate.

Furthermore, the surface composition of the catalysts was investigated by X-ray photoelectron spectroscopy (XPS) in a K-Alpha of Thermo-Scientific spectrometer, equipped with an Al anode.

3-2-5, Electrochemical characterization

Electrochemical activity tests towards ORR were carried out at 25 °C in a three-electrode cell with 0.1 M KOH electrolyte using a Autolab PGSTAT302 (Metrohm, Netherlands) potentiostat, a graphite bar as counter electrode and Reversible Hydrogen Electrode (RHE) electrode introduced in the working solution as reference electrode. A rotating ring-disk electrode (RRDE, Pine Research Instruments, USA) equipped with a glassy carbon (GC) disk (5.61 mm diameter) and an attached Pt ring was used as working electrode. Since this study aims to get information about carbon active sites and to compare with ASA and carbon-oxygen reactivity data, all the samples used in this evaluation were also heat treated at 920 °C for 0.5 h under N_2 to remove the surface oxygen complexes as it was done for ASA and reactivity measurements. After this thermal treatment the samples were immediately characterized for ORR to minimize the influence of contact with the atmosphere. The samples were dispersed in a solution of 20 vol.% of isopropanol, 80 vol.% of water and 0.02 vol.% of Nafion@ to prepare a final dispersion of 1mg/ml of the carbon material. Typically, 100 µl (mass of electrode is 400 µg cm^{-2}) of the dispersion was pipetted on the GC disk electrode to obtain uniform catalysts layer for ORR study. The sample on the GC was dried by heating lamp for evaporation of the solvent. Cyclic Voltammetry (CV) and linear sweep voltammetry (LSV) were carried out from 1 to 0 V (vs. RHE). The CV was performed in both N_2 and O_2 saturated atmosphere at 5 and 50 mV s^{-1}. The LSV was done in an O_2-saturated atmosphere for different rotation rates of 400, 625, 900, 1025, 1600 and 2025 rpm at 5 mV s^{-1}. LSVs of ORR were corrected for the capacitive current contribution, which was obtained from CV under N_2 at 5 mV/s. The potential of the Pt ring electrode was kept at 1.5 V (vs. RHE) and its current was also measured during the LSV measurement. The electron transfer number (n) of ORR on the catalysts modified electrode was determined by the following equation.

$$n = \frac{4 \times Id}{Id + Ir/N} \qquad (5)$$

where *Id* is disk current, *Ir* is ring current, and N is the collection efficiency of the ring which was experimentally determined to be 0.37.

3-3, Results and discussion

3-3-1, TEM images

TEM observations were carried out to get information about the carbon structure on a microscopic scale. The TEM images for KS4, XC72, CB, CNF, MW, Herring, SW, YPF and SW_HNO_3 are displayed in Figure 1. Highly developed and stacked structures of 002 lattice fringes, which are typical of graphitic materials, are observed for KS4, Figure 1a. For carbon black samples, namely XC72 and CB, nanosized spherical amorphous particles of different sizes are observed in TEM images, Figure 1b, c, being smaller for CB. This feature delivers more voids spaces (which could determine the porous texture of carbon blacks) between the nanosized particles on CB sample. Hence, larger BET surface area of CB than XC72 is measured as explained later in Table 2. CNF presented typical fibril structure (highlighted by white arrow) and irregular features, Figure 1d. TEM image of AC illustrates the amorphous carbon structure which was previously studied[42], Figure 1e. Finally, for carbon nanotubes samples, different structures are observed. First, TEM of multiwalled carbon nanotubes (MW) shows that the graphite planes of the MW walls are parallel to the axis of the nanotube, Figure 1f. Second, herringbone nanotubes (Herring) shows its characteristic nanostructure where the graphite plates forming the walls are most of them stacked forming an angle close to 45° with the axis of the tube Figure 1g. Contrarily, single walled carbon nanotubes (SW) presented bundles of very thin carbon nanotubes, Figure 1h. The diameter of nanotubes follows the order of Herring > MW > SW, in close agreement with their specific surface area values (Table 2). TEM images indicate that samples selected in this study have very different structure. The ordered, spherical particle and tube type structures of carbon materials are observed for KS4, XC72, MW, Herring and SW. In contrast, AC, CB, YPF and CNF displayed highly disordered carbon structure. TEM image for SW_HNO_3 illustrating amorphous and disordered structure of SW are presented in Figure 1. A bundle of SW_HNO_3 formed by several nanotubes are also observed in Figure 1.

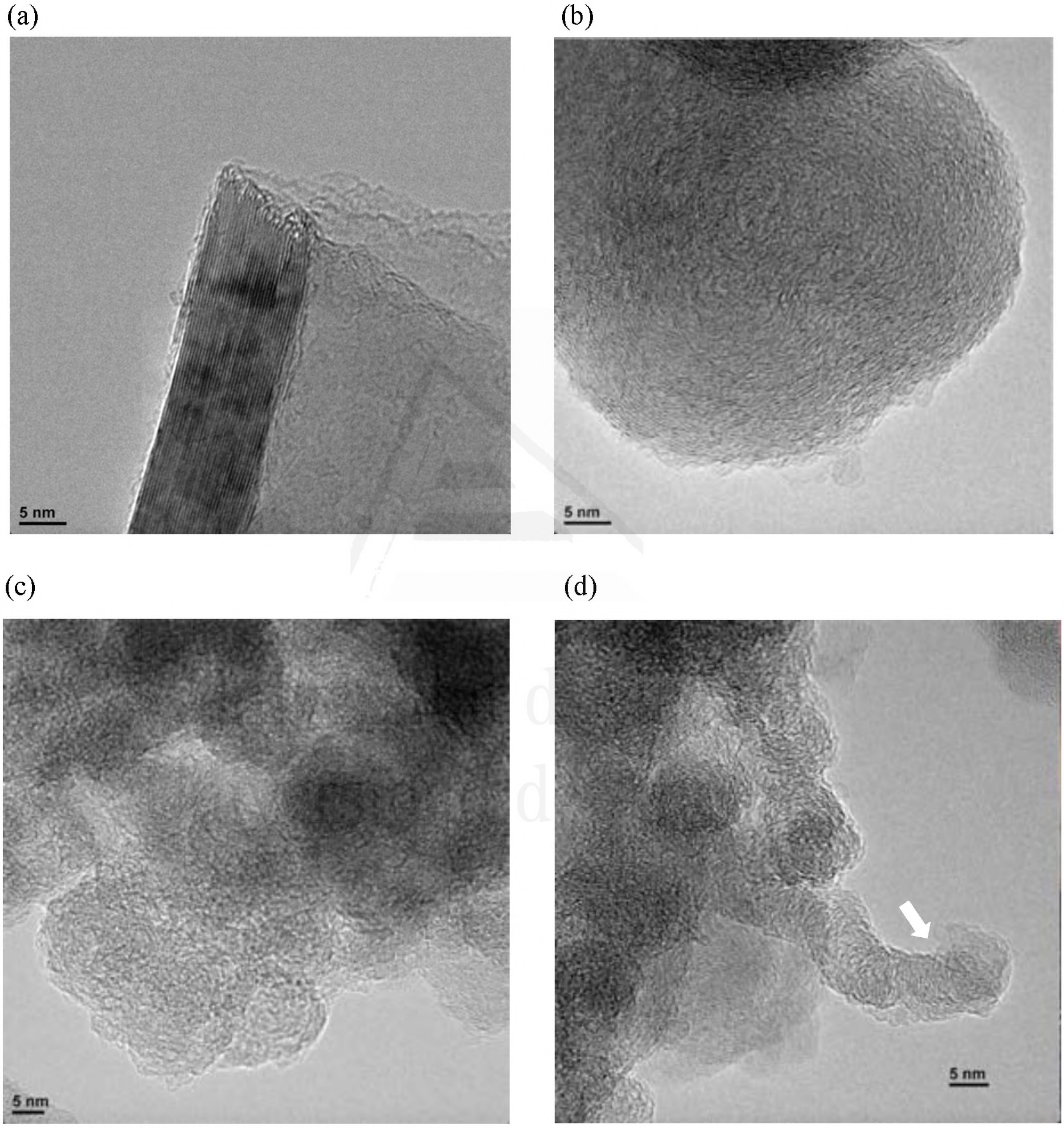
(a)
5 nm
(b)
5 nm
(c)
5 nm
(d)
5 nm

(e)

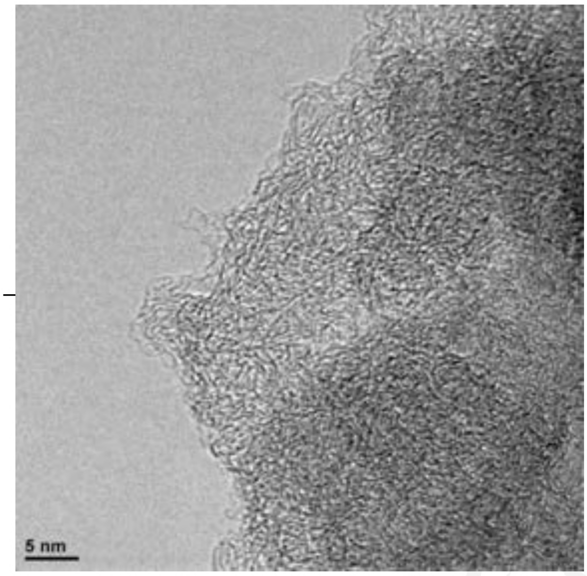

(f)

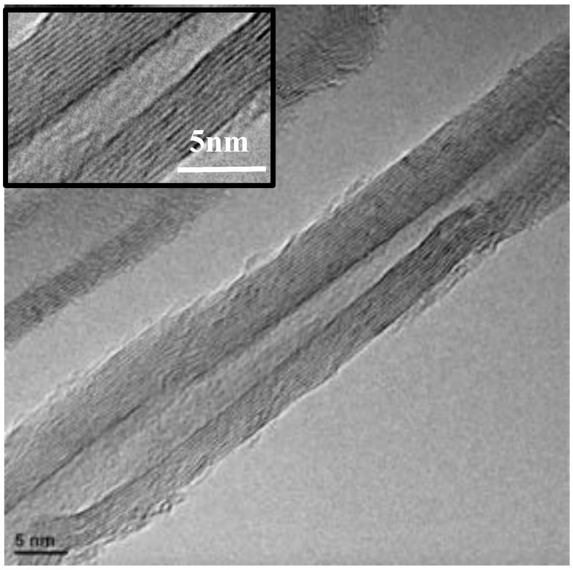

(g)

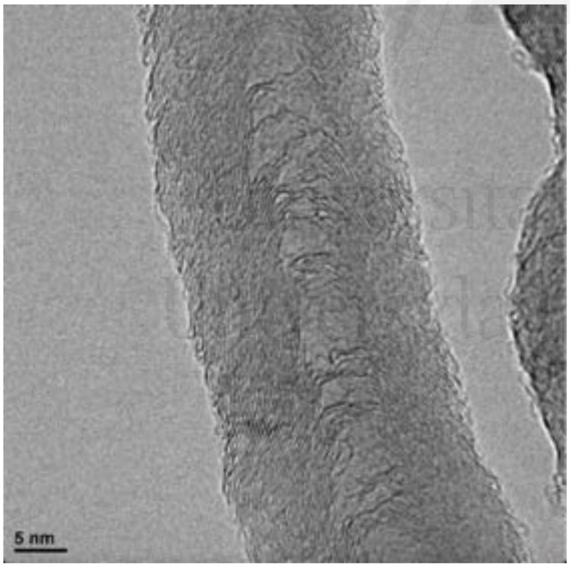

(h)

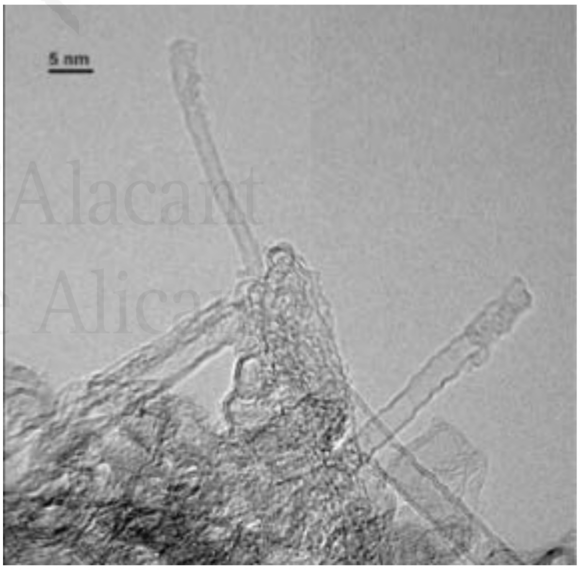

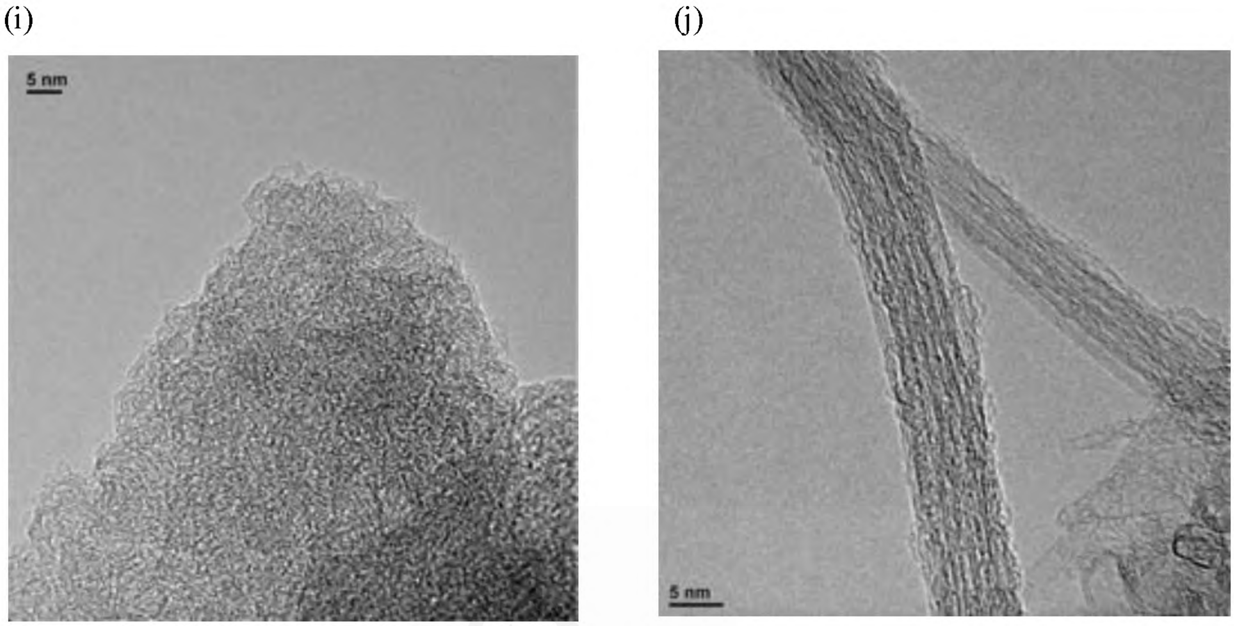

Figure 1. TEM images of (a) KS4, (b) XC72, (c) CB, (d) CNF, (e) AC, (f) MW, (g) Herring, (h) SW (i) YPF and (j) SW_HNO_3. The arrow indicates the location of fibril structure. All samples were heat treated at 920 °C for 0.5 h under N_2 before the analysis.

3-3-2, Thermogravimetric analysis

The inorganic matter content of the samples prepared in this work were analyzed by TGA under synthetic air. Figure 2 shows the TG curves of non-CNTs (KS4, XC72, CB, CNF and AC) and CNTs based samples (MW, Herring, SW and SW_HNO$_3$). The TG weight loss indicated that the samples have a carbon content higher than 99.8% and 98.8% (SW) for non-CNTs and CNTs based samples, confirming that most of the metal content was removed by our purification procedures. The possible contribution of residual metal impurities toward ORR are explained in ORR measurements section.

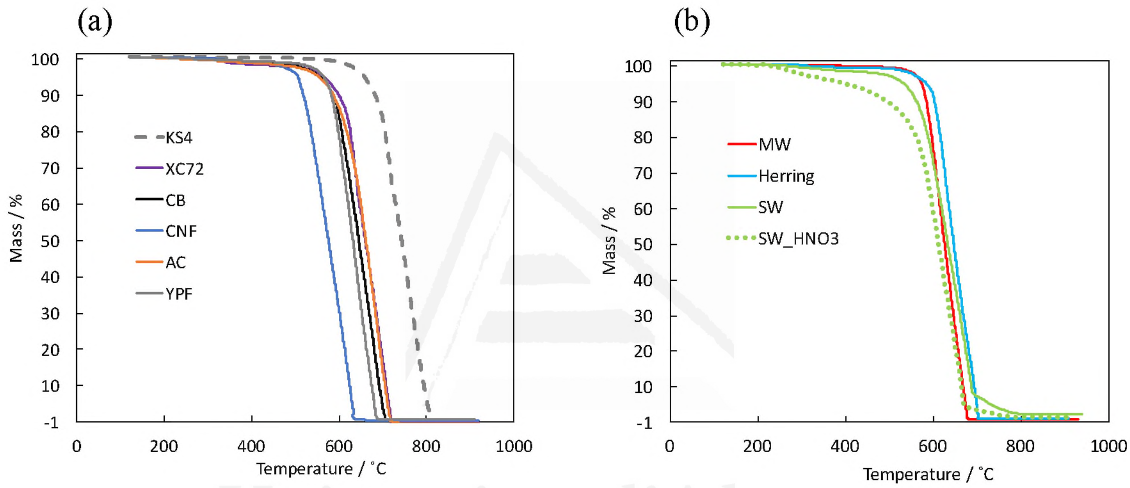

Figure 2. TG curves for (a) non-CNTs and (b) CNT-based samples.

3-3-3, Characterization of surface chemistry

Figure 3 and Figure 4 show the CO$_2$ and CO gas evolution profiles during TPD for all the carbon samples before and after heat-treatment at 920 ˚C for 0.5 h in He atmosphere, respectively. By comparing the TPD profiles between Figure 3 and Figure 4, removal of most of oxygen complexes on the carbon surface can be confirmed by the thermal treatment at 920 ˚C. Hence, the effect of oxygen functionalities on the carbon surface toward ORR activity should be negligible for our prepared carbon samples [43,44]. Nevertheless, the small peaks observed for samples Herring and CNF can be related to traces of metal still present in these samples.

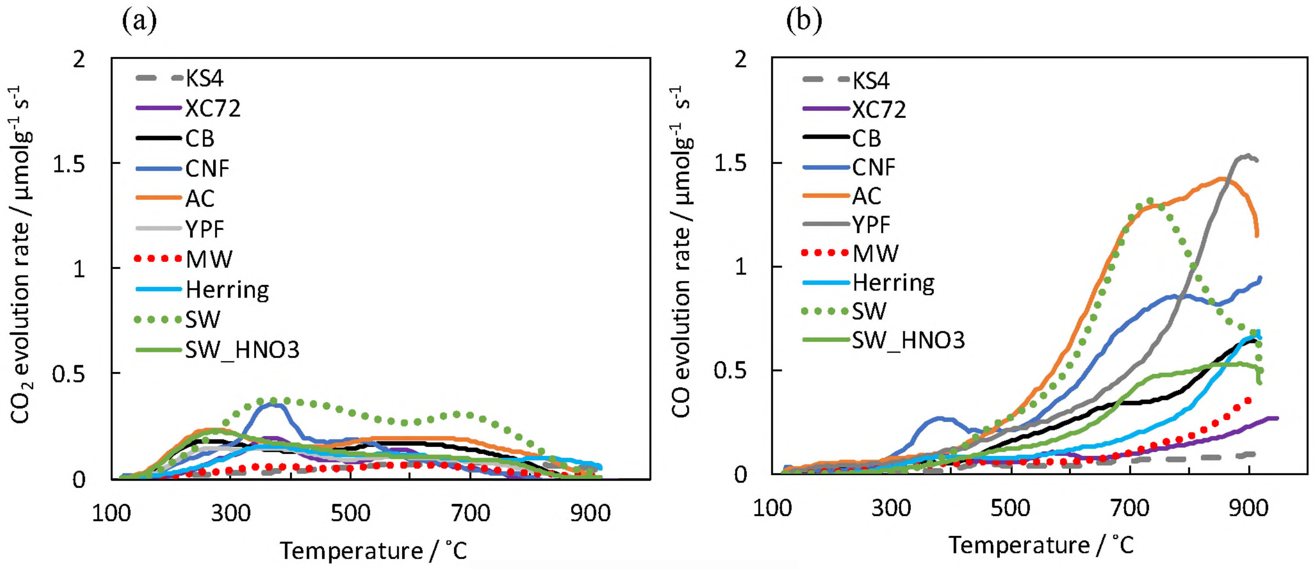

Figure 3. (a) CO_2 and (b) CO gas evolution profiles up to 920˚C at rate of 20˚C/min in He before heat treatment at 920˚C for 0.5h of the carbon samples.

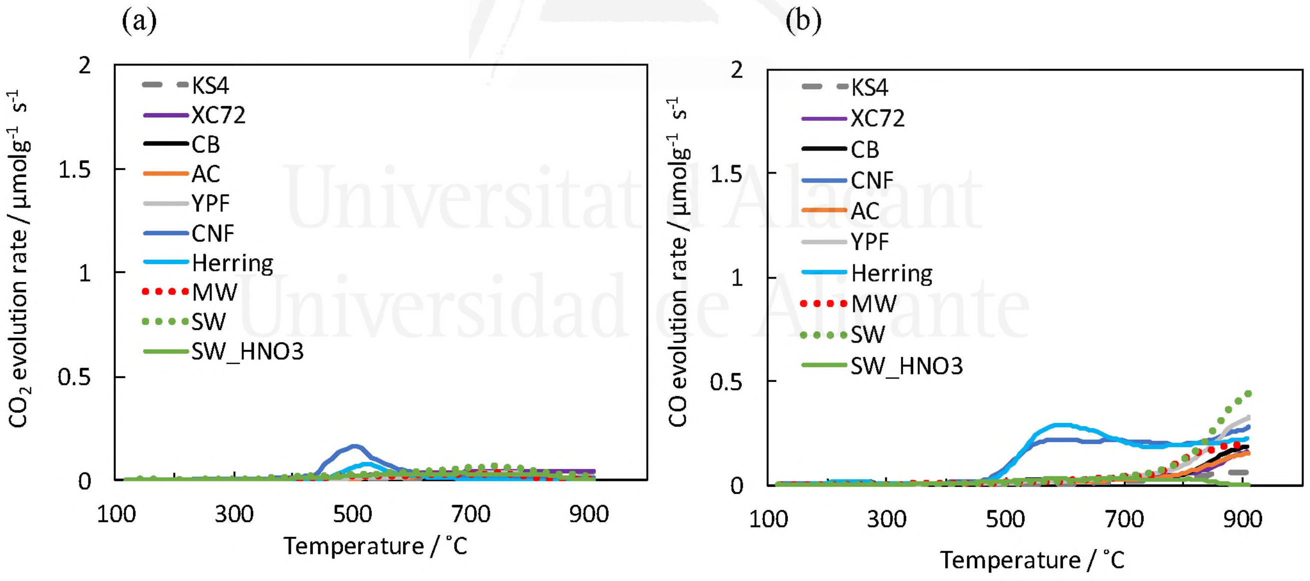

Figure 4. (a) CO_2 and (b) CO gas evolution profiles up to 920 ˚C at rate of 20 ˚C min^{-1} in He after heat treatment at 920 ˚C for 0.5 h of the carbon samples.

In addition, XPS spectra reveal the presence of C 1s and O 1s emissions only, Figure 5.

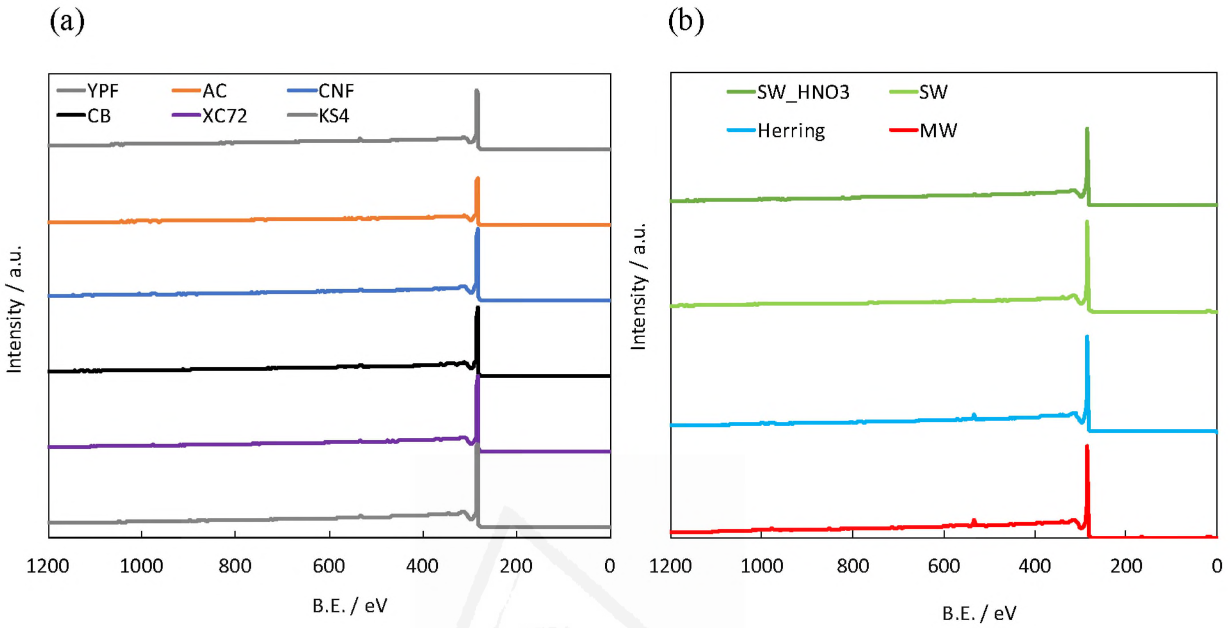

Figure 5. XPS survey scan for (a) non-CNTs and (b) CNT-based samples.

None of the high-resolution XPS spectra reveal the presence of other heteroatoms like nitrogen, phosphorus, halogens etc. (See the example of the N1s spectra in Figure 6).

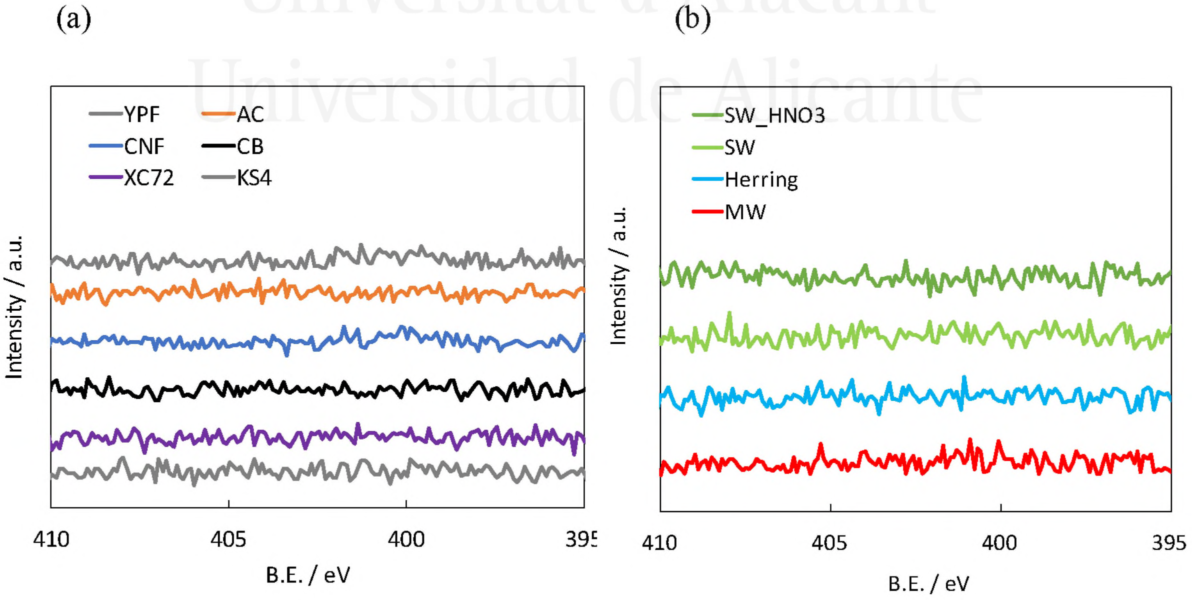

Figure 6. High resolution XPS spectra of nitrogen for (a) non-CNTs and (b) CNT-based samples.

The surface chemistry characterized by TPD and XPS for the samples is summarized in Table 1.

Table 1. Surface chemistry of the analyzed samples.

Sample*	Cxps / %at.	Oxps / %at.	CO^{TPD} / µmol g^{-1}	CO_2^{TPD} / µmol g^{-1}	O_{Total} / µmol g^{-1}
KS4	98.7	1.3	31	34	99
XC72	98.5	1.5	67	55	177
CB	97.7	2.2	75	31	137
CNF	98.0	1.9	276	69	414
AC	98.1	1.9	69	25	119
YPF	96.4	3.5	113	32	177
MW	98.8	0.9	96	33	162
Herring	96.8	2.8	285	28	341
SW	98.6	1.4	145	66	277
SW HNO_3	98.4	1.6	183	40	263

*All samples were heat treated at 920 °C for 0.5 h under inert atmosphere before the analysis.

3-3-4, Porous texture and carbon-oxygen gasification properties

N_2 adsorption isotherms at -196 °C and CO_2 adsorption isotherms at 0 °C have been determined in all the samples to characterize their porous textures. Table 2 compiles the BET surface area (S_{BET}), micropore volumes (V_{DR}^{N2}) and narrow micropore volume (V_{DR}^{CO2}) calculated from N_2 and CO_2 adsorption for each sample. It can be seen that the materials have different porous texture. Specific surface areas ranged from 36 $m^2\,g^{-1}$ (sample KS4) to more than 1700 $m^2\,g^{-1}$ (sample YPF). XC72, CNF and MW presented similar S_{BET} (196 ~ 287 $m^2\,g^{-1}$). CB, AC and SW showed intermediate S_{BET} values (580 ~ 600 $m^2\,g^{-1}$).

Table 2 also contains the values of ASA and reactivity for carbon-oxygen reaction measured under synthetic dry air at 250 °C and 550 °C, ASA and R_{550}. ASA is related to the structural ordering of the carbon materials [45]. Edge sites on carbon surface includes all types of defects that could be present in the carbon structures (stacking faults, single and multiple atom vacancies, dislocations) which constitute ASA [27,46]. Therefore, generally ordered structures include low amount of edge sites whereas undeveloped structures contain higher concentration of edge site which are responsible for dissociative oxygen chemisorption, and thus leading to high ASA. For our prepared samples, KS4, XC72, CB and CNTs based catalysts display relatively low ASA (<14 m^2 g^{-1}). On contrast, AC, CNF and YPF which showed disordered carbon structures as revealed in Figure 1, have higher ASA values (>20m^2 g^{-1}). Relationship between ASA_{250} and ASA_{300} for XC72, CB, YPF, CNF and AC is shown in Figure 7, which suggests that the experiment temperature is adequate.

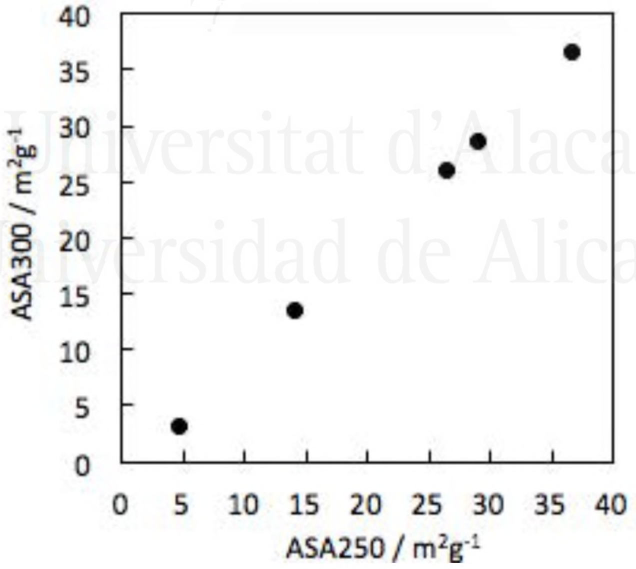

Figure 7. Relationship between ASA_{250} and ASA_{300} for XC72, CB, YPF, CNF and AC.

Moreover, Table 2 reveals that nitric acid oxidation of SW affects their porous texture as observed by the enhancement of S_{BET}, V_{DR}^{N2} and V_{DR}^{CO2}. Furthermore, SW_HNO$_3$ showed higher ASA and reactivity than SW which might be due to formation of structural defects during the wet oxidation of SW_HNO$_3$ [35,45]. Table 2 clearly depicts that S_{BET}, V_{DR}^{N2}, and V_{DR}^{CO2} are not the factors determining ASA and R_{550}.

Table 2. Porous texture, ASA and R_{550} of the selected samples.

Sample*	S_{BET} / $m^2 g^{-1}$	V_{DR}^{N2} / $cm^3 g^{-1}$	V_{DR}^{CO2} / $cm^3 g^{-1}$	ASA / $m^2 g^{-1}$	R_{550} / $gg^{-1}h^{-1}$
KS4	36	0.01	--	0.5	0.06
XC72	254	0.10	0.05	4.7	0.74
CB	583	0.26	0.17	14.0	1.14
CNF	287	0.11	0.07	28.9	1.99
AC	593	0.24	0.26	36.7	2.16
YPF	1757	1.24	0.48	26.4	2.20
MW	**196**	**0.07**	**0.02**	**2.8**	**2.00**
Herring	**123**	**0.05**	**0.03**	**2.2**	**0.47**
SW	**587**	**0.21**	**0.13**	**6.1**	**2.39**
SW HNO$_3$	**976**	**0.35**	**0.17**	**9.4**	**2.91**

*All samples were heat treated at 920°C for 0.5h under N_2 before the analyses.

Figure 8 illustrates the Arrhenius plots (rate vs. 1/T) [47] for the carbon gasification with oxygen obtained in this study. The activation energies in air for the samples were calculated from the slope in Figure 8 obtaining values between 60 kJ mol^{-1} and 249 kJ mol^{-1} , that are similar to those previously reported [22]. Thermogravimetric profiles of the samples at 480°C, 500°C, 530°C and 550°C under synthetic dry air are presented in Figures 9, 10, 11 and 12, respectively.

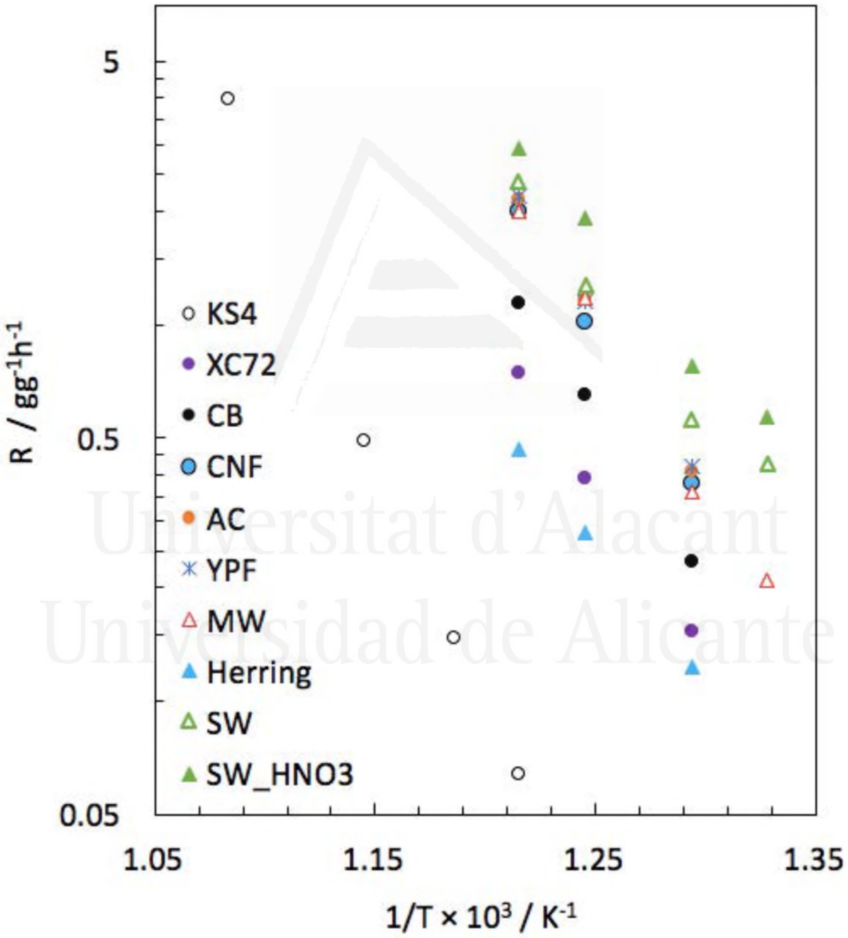

Figure 8. Arrhenius plots of reactivity for different structures of carbons.

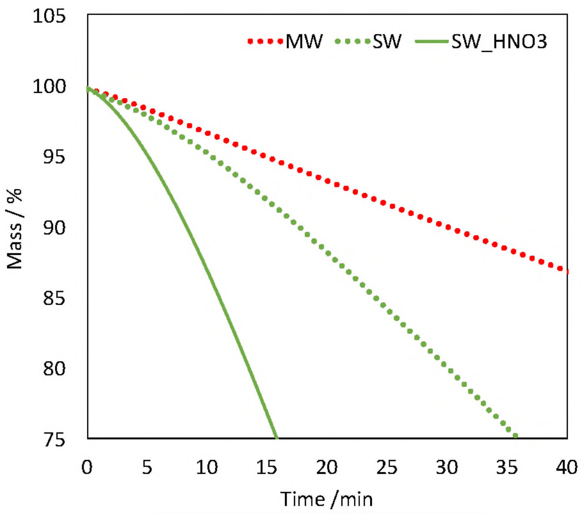

Figure 9. Thermogravimetric profiles of CNTs based samples at 480 ˚C under synthetic dry air.

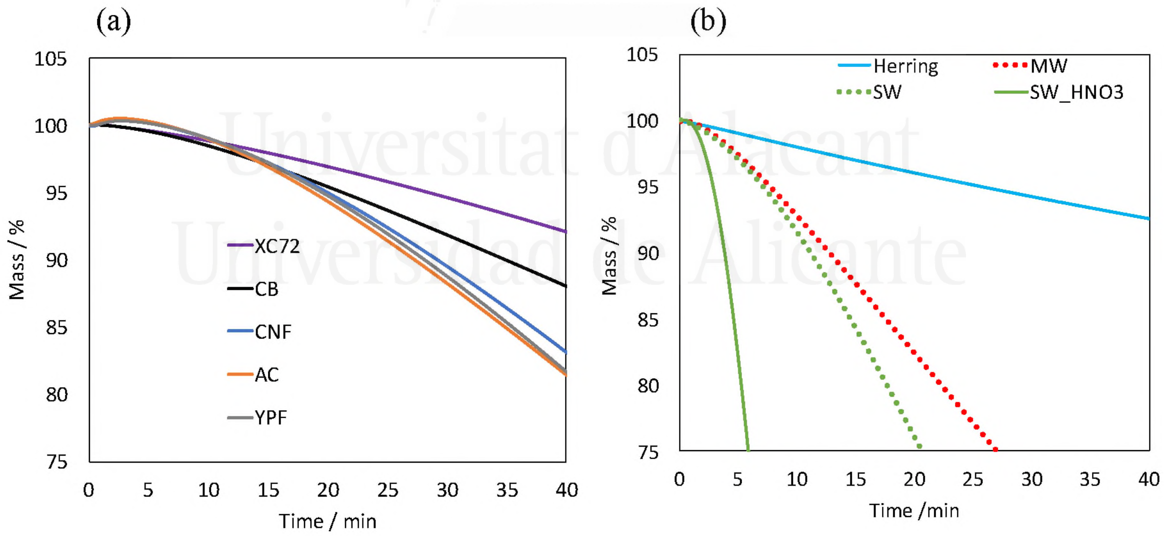

Figure 10. Thermogravimetric profiles of (a) non-CNTs and (b) CNTs based samples at 500 ˚C under synthetic dry air.

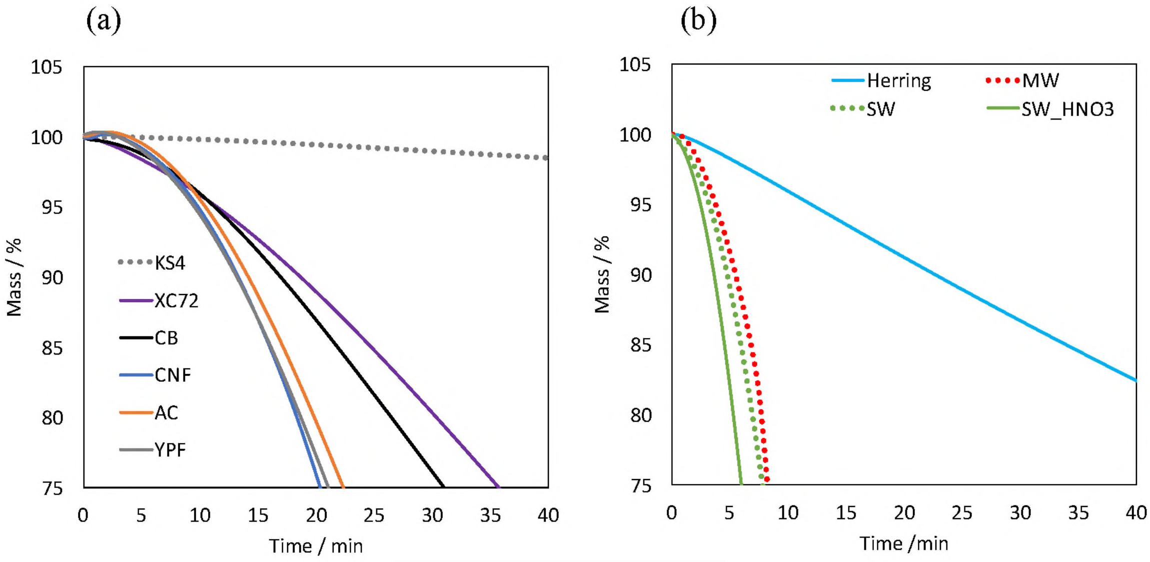

Figure 11. Thermogravimetric profiles of (a) non-CNTs and (b) CNTs based samples at 530 °C under synthetic dry air.

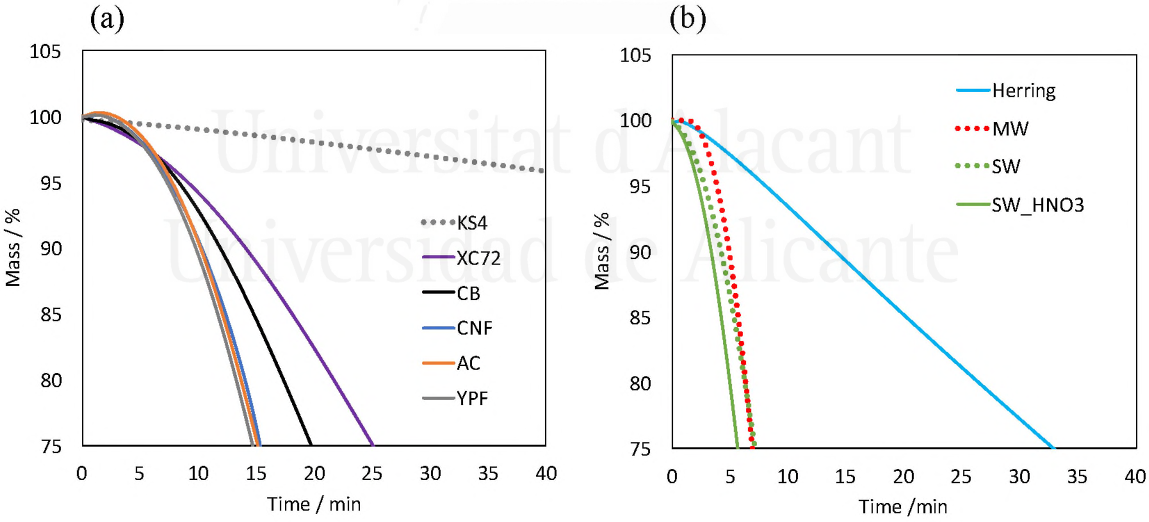

Figure 12. Thermogravimetric profiles of (a) non-CNTs and (b) CNTs based samples at 550 °C under synthetic dry air.

Literature provides evidences of ASA being a better descriptor of gasification reactivity than S_{BET}. According to Radovic et al., good correlations between ASA and reactivity toward air and steam could be established for the different chars and hydropyrolysis chars [23]. Additionally, Wang and McEnaney observed a positive correlation between ASA and reactivity for a series of demineralized coal chars, PVDC chars and electrode carbon gasified in CO_2 [23]. In accordance to these previous results, we have observed a good correlation between ASA and reactivity (R_{500}, R_{530} and R_{550}) for our demineralised carbons (Figure 13). Interestingly, the slope of the plot of reactivity versus ASA for CNTs based samples is higher than that for non-CNTs based samples, no matter the chosen temperature for R determination.

O_2 dissociation step on CNT is predicted to be more exothermic and spontaneous than on its graphene counterpart [48] suggesting that the higher reactivities of CNTs based samples could be due to their unique structure. Ebbesen et al. investigated the oxygen gasification of carbon nanotube-containing materials in air and reported that the strong local curvature and imperfect geometry and/or the presence of five-menbered carbon rings increase the reactivities of nanotubes [49]. Yao et al. concluded that oxidation of carbon nanotubes is influenced by curvature, pentagon and heptagon rings, and probably helicity. The helicity is an additional factor for nanotubes which implies the existence of relatively exposed steps with high chemical potential where oxidation may occur preferentially [50]. More specifically, the authors mentioned that a smaller tube diameter increases the curvature of the tube walls and the strain of the pentagons at the tip. Thus nanotubes with smaller diameter begin to oxidize first than those with higher diameter. From the thermodynamic analysis of O_2 adsorption on armchair and zigzag nanotubes, decreasing trend in the thermodynamic parameters with increasing CNT diameter were also obtained [48]. The high reactivities of SW and SW_HNO_3 samples could be then explained by their smaller diameters (1~2 nm). Morishita et al. studied the gasification behavior of MWCNTs [51,52]. The changes of appearance of a MWCNT in the initial stage of gasification were evaluated by a fixed point TEM observation. These TEM images indicated that the gasification occurred preferentially at the structural defects in the MWCNTs employed rather than at the strain points of the topological defects [51,52]. Since SW_HNO_3 contain more defects sites than SW, the reactivity of SW_HNO_3 is higher than that of SW.

In summary, CNTs based carbon samples show higher reactivities than non-CNTs based catalysts despite their lower ASA (< 9.4 m^2 g^{-1}). As aforementioned, ASA can be considered as a measure of the number of active sites for carbon gasification in a carbon sample. Then, it could be concluded that the intrinsic activity (i.e intrinsic kinetic constant) for carbon gasification of the active sites on CNTs is higher than those of non-CNTs samples.

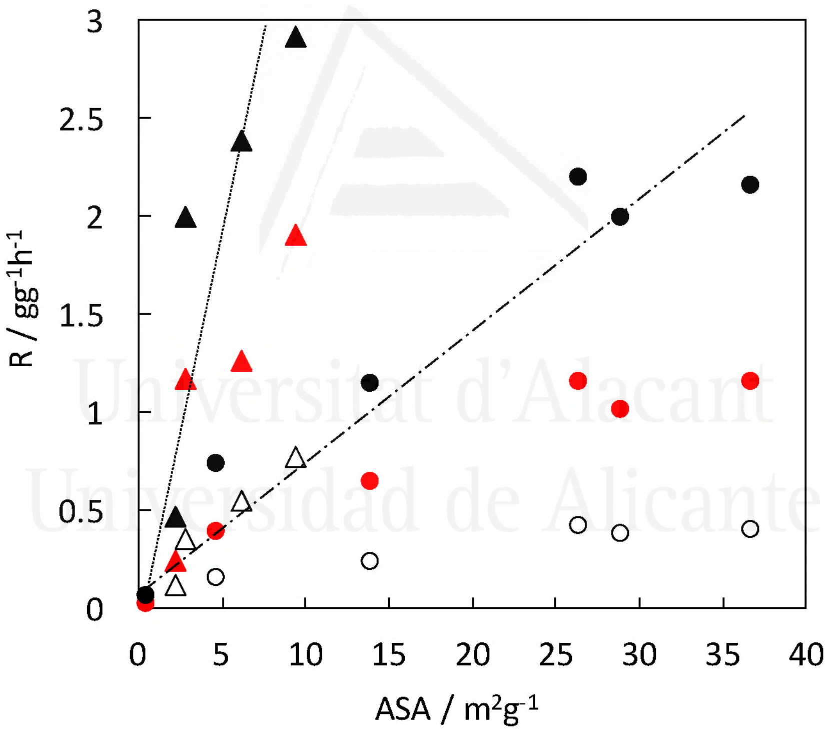

Figure 13. Relationship between ASA_{250} and R_{500} (white dot), R_{530} (red dot) and R_{550} (black dot) for prepared samples. Triangle dot: CNTs based samples (MW, Herring, SW and SW_HNO_3). Circle dot: non-CNTs based samples (KS4, XC72, CB, CNF, AC and YPF).

3-3-5, Electrochemical characterization

Figure 14 shows the voltammograms in N_2 saturated 0.1M KOH between 0 and 1 V at 50 mVs^{-1} of the samples that were previously heat-treated at 920°C under N_2. All the voltammograms have a quasi-rectangular shape which are typical of carbon materials where the capacitance is determined by electric double layer formation [53]. Gravimetric capacitance of the electrodes has been determined from the area inside the CVs (2, 14, 49, 33, 53 and 90 F g^{-1} for KS4, XC72, CB, CNF, AC and YPF, respectively, and 14, 8 46 and 60 F g^{-1} for MW, Herring, SW and SW_HNO_3, respectively) and the double layer capacitance of these materials is related to the S_{BET}, Table 2.

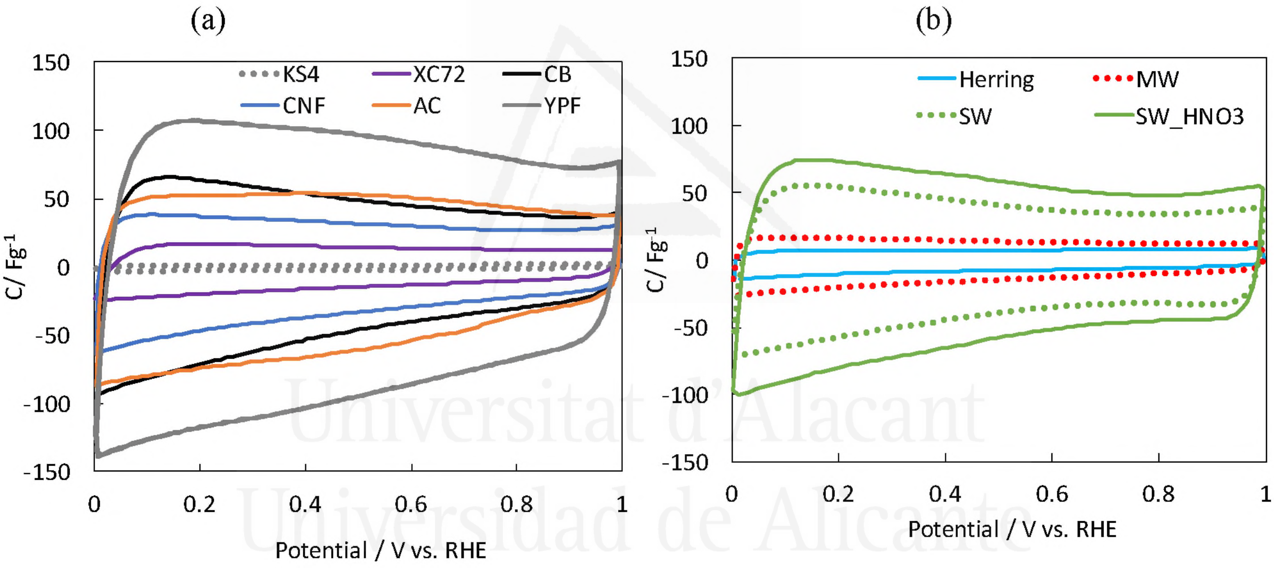

Figure 14. Steady state cyclic voltammograms for (a) KS4, XC72, CB, CNF, AC, YPF and (b) Herring, MW, SW, SW_HNO_3 in deoxygenated (solid line) 0.1 M KOH solution at 50 mV s^{-1} respectively. sample loading is 400 μg cm^{-2}.

3-3-6, Oxygen reduction reaction measurements

The ORR activity for all the samples has been determined by measuring LSVs experiments between 1 and 0 V at an electrode rotating rate of 1600 rpm in O_2-saturated 0.1M KOH. The shape of the recorded curves shows a two-wave electrocatalytic process, the first one starting at potentials around 0.80-0.95V, and the second one ca. 0.4V, Figure 15.

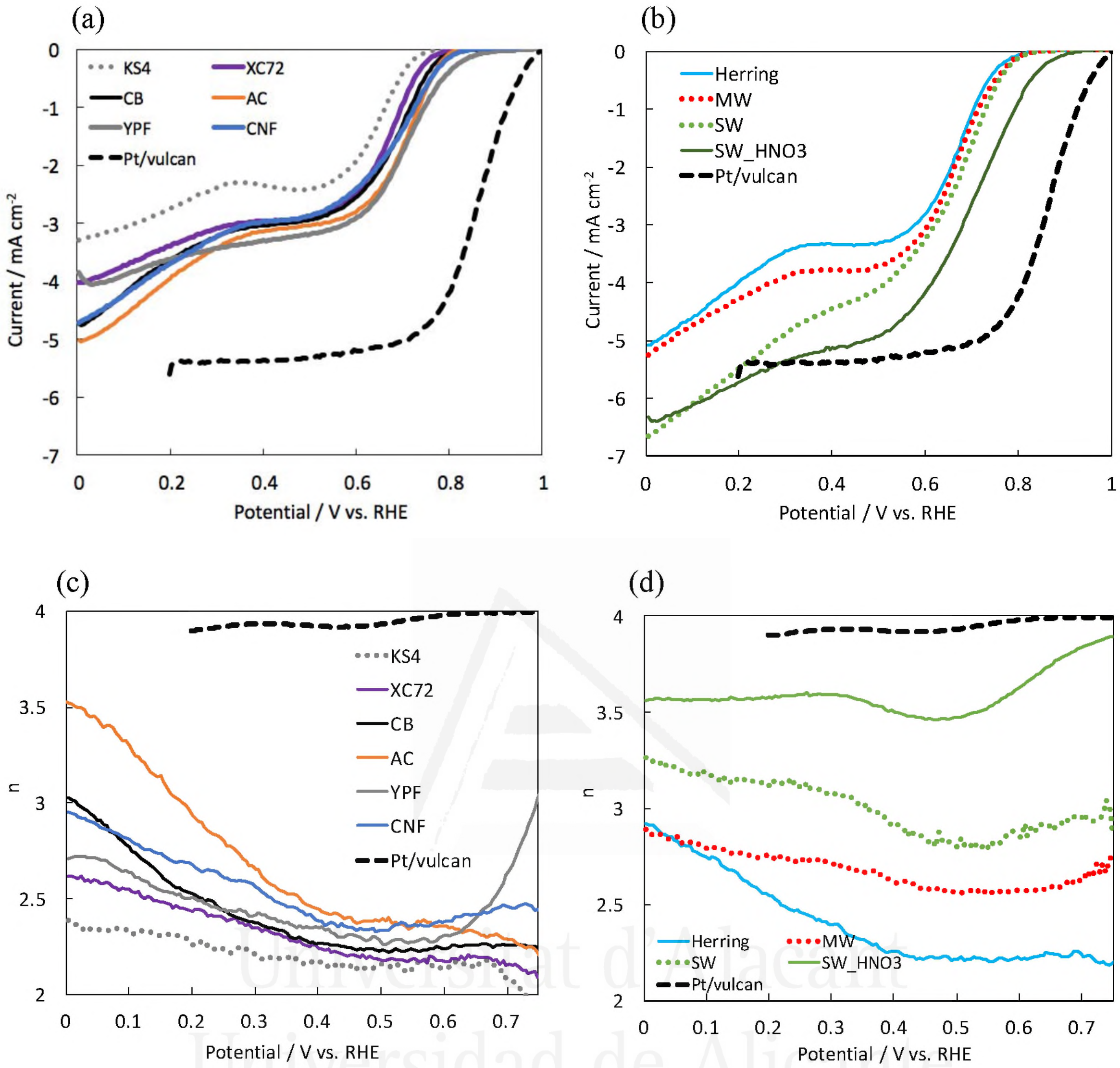

Figure 15. LSVs during ORR on the disk electrode for (a) KS4, XC72, CB, AC, YPF, CNF and (b) Herring, MW, SW, SW_HNO$_3$ and number of electrons (n) of the (c) KS4, Vulcan, CB, AC, YPF, CNF and (d) Herring, MW, SW, SW_HNO$_3$ in O_2 - saturated 0.1 M KOH solution at 1600 rpm with a sweep rate of 5 mV s^{-1} respectively. Sample loading is 400 µg cm^{-2}. All the catalysts were heat treated at 920 °C for 0.5 h under N_2 before this ORR activity measurement.

H_2O_2 electrochemical reduction experiments done in this PhD work (see Chapter 4) manifested that H_2O_2 produced from oxygen reduction reaction is subsequently reduced producing the second wave observed at around 0.4 V. In this sense, Figure 16 shows the LSV in kinetically controlled O_2 reduction reaction region and beginning of the diffusional control region (i.e., potential region between 0.4 and 1V). The ORR activity of a 20 wt.%Pt/Vulcan commercial catalyst and the limiting current for oxygen reduction through 2 and 4 e^- reaction pathways obtained from the Levich theory [54] (2.9 and 5.8 mA cm^{-2}) at 1600 rpm are also plotted. For the analyses of the number of electrons transferred, Figure 16 c and d, potentials between 0.4 at 0.75V were selected.

In order to compare ORR activity, current densities have been determined at 0.7 V for all samples within the kinetically controlled O_2 reaction region. The current density, number of electrons determined at 0.7 V and onset potential measured at -0.1 mA cm^{-2} on the LSV curves are summarized in Table 3.

Table 3. Current density at 0.7V, number of electrons and onset potential measured at -0.1 mA cm^{-2}

Sample*	Current / mA cm^{-2}	n	Onset potential / V vs RHE
KS4	0.38	2.1	0.74
XC72	0.89	2.2	0.77
CB	1.24	2.2	0.79
CNF	1.34	2.5	0.81
AC	1.62	2.3	0.80
YPF	1.72	2.6	0.85
MW	**1.16**	**2.6**	**0.80**
Herring	**1.00**	**2.3**	**0.78**
SW	**1.44**	**3.0**	**0.80**
SW HNO_3	**2.56**	**3.8**	**0.88**

*All samples were heat treated at 920°C for 0.5h under N_2 before the analyses.

SW_HNO_3 demonstrated the highest current density as well as *n* while KS4 showed the lowest values. In general, CNTs based samples exhibited higher ORR activities (current density and n) than those of non-CNTs based samples. It must be noted that if a very low amount of metal content in SW could be improving ORR activity, the activity of SW_HNO_3 should then be inferior to SW. However, the opposite is observed, which suggests that the residual metal impurities are not playing a relevant role toward ORR measurements herein reported. Moreover, the current density reached in diffusion control for CNTs based samples is higher than 2.9 mA cm^{-2} (i.e. ORR through 2e- mechanism) (Figure 16a). Since *n* does not reach 4 e-, Figure 16c, the current densities recorded for CNTs based samples could be the result of the combination of different active sites that catalyze ORR through 2e$^-$ and 4e$^-$ electron transfer pathways. This points out that active sites that are able to catalyze ORR to water through 4 e$^-$ reaction pathways are found in the surface of these samples and its concentration seems to be higher for sample SW-HNO$_3$.

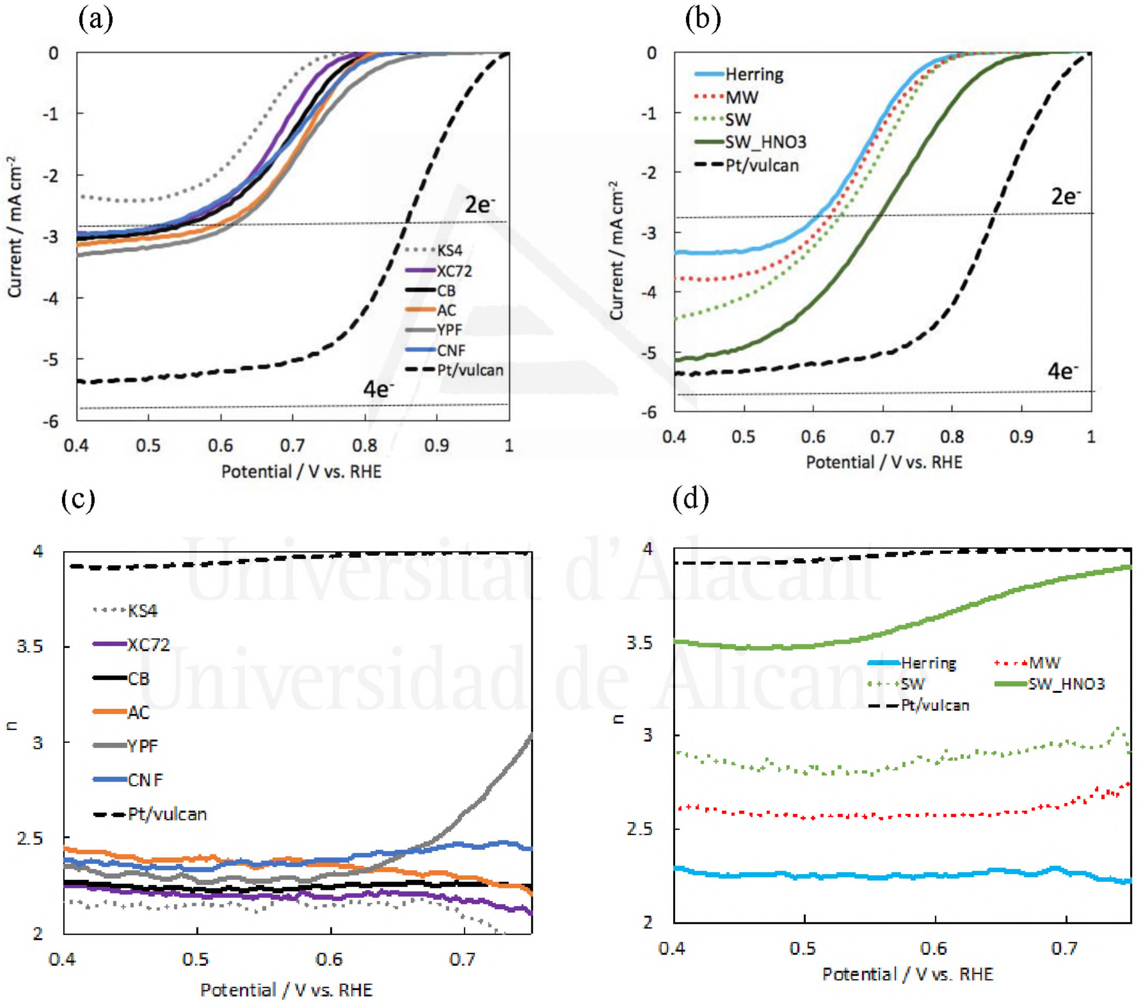

Figure 16. LSVs during ORR on the disk electrode for (b) KS4, Vulcan, CB, AC, YPF, CNF and (a) Herring, MW, SW, SW_HNO$_3$ and number of electrons (n) of the (d) KS4, XC72, CB, AC, YPF, CNF and (c) Herring, MW, SW, SW_HNO$_3$ in O$_2$ - saturated 0.1 M KOH solution at 1600 rpm with a sweep rate of 5 mV/s respectively. Sample loading is 400 µg cm^{-2}. All the samples were heat treated at 920 °C for 0.5 h under N$_2$ before this ORR activity measurement. The values of Pt/Vulcan are included as reference.

To deepen into the relationship between carbon-oxygen gasification properties and ORR activities, the current density and *n* measured at 0.7 V versus ASA250 and R_{550} are compared in Figure 17 and Figure 18, respectively.

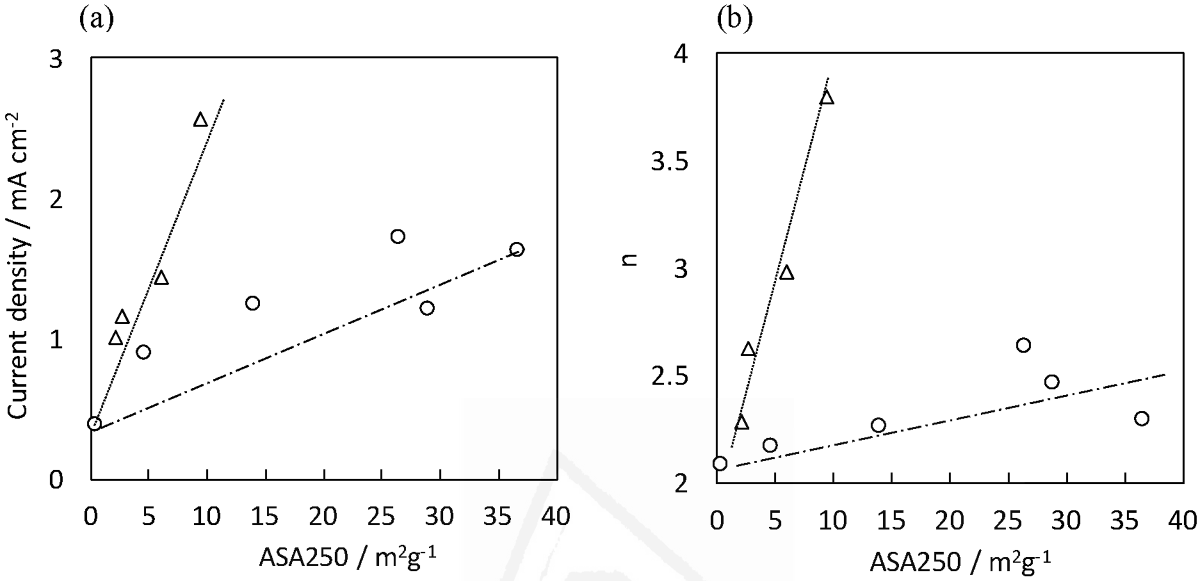

Figure 17. ASA dependence of (a) Current density and (b) n measured 0.7V in O_2 – saturated 0.1M KOH solution at 1600rpm. △: CNTs based samples (MW, SW, SW_HNO_3 and Herring). ○: rest of samples (KS4, XC72, CB, CNF, AC and YPF). Sample loading is 400 µg cm^{-2}.

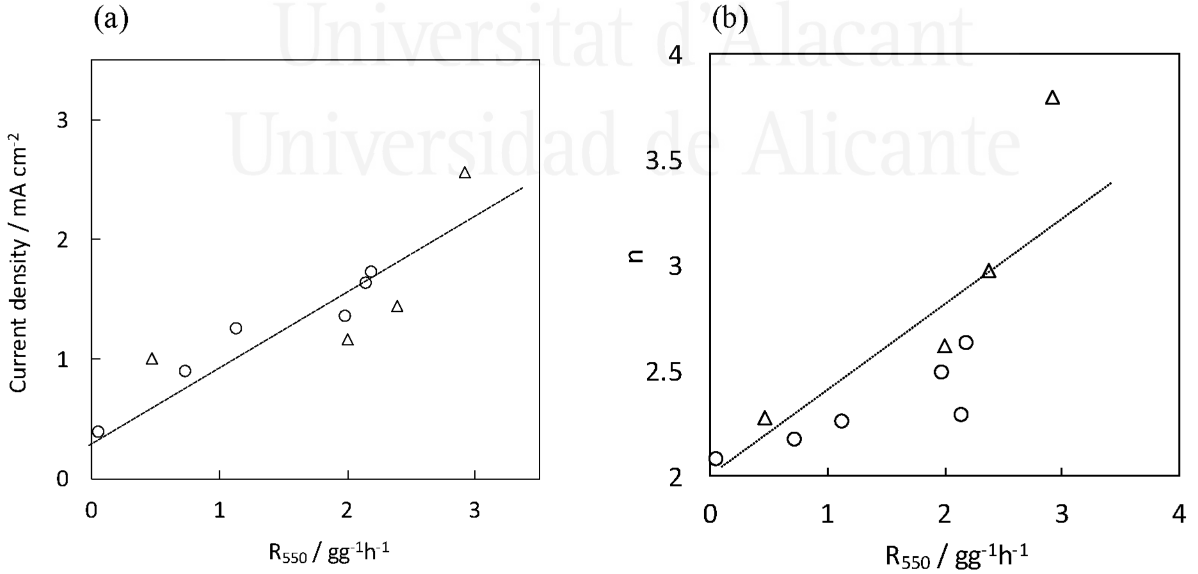

Figure 18. R_{550} dependence of (a) current density and (b) n measured at 0.7V in O_2 – saturated 0.1M KOH solution at 1600rpm. △: CNTs based samples (MW, SW, SW_HNO_3 and Herring). ○: the other samples (KS4, XC72, CB, CNF, AC and YPF). Sample loading is 400 µg cm^{-2}.

In general, the ORR current density and *n* rise with increasing ASA, Figure 17, indicating that the carbon edge sites measured are the active sites with higher activity for ORR. It is known that the electrode kinetics on the basal plane is slower than on edge planes sites (around 7 orders of magnitude slower) [55]. Besides, there are several reports which illustrated edge carbon atoms are able to improve ORR activity. Ball-milled graphite and CNTs with more exposed edges showed significantly improved ORR activity [13]. Gara et al. prepared basal and edge plane pyrolytic graphite and demonstrated that the current voltage for ORR on the latter one was superior due to a large number of edge sites containing higher activity toward ORR [55]. Interestingly, as previously observed for the reactivity experiments in Figure 13, the slope relating ORR current density and ASA is higher for CNTs based samples than that for non-CNTs based samples, Figure 17.

However, both the current density for ORR and *n* are well described for both set of samples by the carbon gasification reactivity, Figure 18. This proportional relationship between reactivity and the ORR current density and *n* is manifesting for the first time that carbon gasification reactivity and oxygen reduction reaction share active sites and at least some of the starting steps in the reaction mechanism, no matter the porosity and structure of the involved carbon materials

TEM observations in Figure 1 showed that the carbon samples possess different structures, while TPD and XPS analysis indicate that all of the samples contain very low amount of surface oxygen complexes and the absence of heteroatoms in their compositions, Table 1. Since dopants effects for the ORR activities can be discarded, the structural differences could be the factor determining the activities observed. Indeed, the role of structural effects on ORR activities in CNTs have been discussed. Zhang et al reported that the curvature plays important role in adsorption and reduction of oxygen for CNTs [56]. The limiting potential for ORR can be maximized by tuning the curvature around the active sites of CNTs [57]. Bamboo-shaped MWCNTs demonstrated superior ORR characteristics to hollow-shaped MWCNTs due to the disordered surface with pentagonal defects, rounded compartments, and edge plane sites [58]. CNTs walls can modify electronic interaction and diffusion behavior of reactants for further catalytic activities [59]. In this work, the highest ORR activity and gasification reactivity values have been achieved for highly defective SW (i.e., SW-HNO_3), confirming that the combination of large number of edge sites, a high curvature, helicity and diameter of the tube, and a high electrical conductivity are the most desirable features for the development of the most active carbon materials for ORR.

3-4, Conclusions

The relationship between ORR activities and carbon-oxygen gasification parameters (ASA and reactivity) were quantitatively identified for materials with different structures. In general, the ORR activities of carbon materials increase with increasing the ASA. However, for a similar ASA value, CNTs based samples showed higher ORR activities and carbon gasification reactivities than non-CNTs based samples. These results suggest that the active sites on CNTs have higher activity toward ORR and carbon gasification. By checking the absence of impurities and the presence of a low amount of surface oxygen groups by TPD and XPS analyses, it was clarified that not only active edge sites measured by ASA but also the structure of carbon materials are the critical factors determining ORR activity and the possibility of enabling a 4e$^-$ reaction pathway. The unique features of CNTs structure (curvature, helicity, bond strains, presence of Stone-Wales defects) can be responsible of such increase in ORR activity. In addition, ORR activities and carbon gasification reactivity were linearly correlated which suggests that both reactions share the same active sites as well as some steps of the reaction mechanism. It has been found that CNTs containing the highest amount of ASA and a low number of graphene layers (as in the case of SW) could be promising materials for designing effective ORR catalysts, what could be potential alternatives for the development practical cathodic materials in FCs.

3-5, References

[1] M. Shao, Q. Chang, J.-P. Dodelet, R. Chenitz, Recent Advances in Electrocatalysts for Oxygen Reduction Reaction, Chem. Rev. 116 (2016) 3594–3657. doi:10.1021/acs.chemrev.5b00462.

[2] K. Kakaei, Electrochemical characteristics and performance of platinum nanoparticles supported by Vulcan/polyaniline for oxygen reduction in PEMFC, Fuel Cells. 12 (2012) 939–945. doi:10.1002/fuce.201200053.

[3] M. Winter, R.J. Brodd, What Are Batteries, Fuel Cells, and Supercapacitors?, Chem. Rev. 104 (2004) 4245–4270. doi:10.1021/cr020730k.

[4] N. Daems, X. Sheng, I.F.J. Vankelecom, P.P. Pescarmona, Metal-free doped carbon

materials as electrocatalysts for the oxygen reduction reaction, J. Mater. Chem. A. 2 (2014) 4085–4110. doi:10.1039/C3TA14043A.

[5] I. Katsounaros, S. Cherevko, A.R. Zeradjanin, K.J.J. Mayrhofer, Oxygen electrochemistry as a cornerstone for sustainable energy conversion, Angew. Chemie - Int. Ed. 53 (2014) 102–121. doi:10.1002/anie.201306588.

[6] P. Trogadas, T.F. Fuller, P. Strasser, Carbon as catalyst and support for electrochemical energy conversion, Carbon. 75 (2014) 5–42. doi:10.1016/j.carbon.2014.04.005.

[7] A. Gabe, J. García-Aguilar, Á. Berenguer-Murcia, E. Morallón, D. Cazorla-Amorós, Key factors improving oxygen reduction reaction activity in cobalt nanoparticles modified carbon nanotubes, Appl. Catal. B Environ. 217 (2017) 303–312. doi:10.1016/j.apcatb.2017.05.096.

[8] C. González-Gaitán, R. Ruiz-Rosas, E. Morallón, D. Cazorla-Amorós, Relevance of the Interaction between the M-Phthalocyanines and Carbon Nanotubes in the Electroactivity toward ORR, Langmuir. 33 (2017) 11945–11955. doi:10.1021/acs.langmuir.7b02579.

[9] C.H. Choi, M.W. Chung, H.C. Kwon, J.H. Chung, S.I. Woo, Nitrogen-doped graphene/carbon nanotube self-assembly for efficient oxygen reduction reaction in acid media, Appl. Catal. B Environ. 144 (2014) 760–766. doi:10.1016/j.apcatb.2013.08.021.

[10] C. Tang, Q. Zhang, Nanocarbon for Oxygen Reduction Electrocatalysis: Dopants, Edges, and Defects, Adv. Mater. 29 (2017). doi:10.1002/adma.201604103.

[11] T. Xing, Y. Zheng, L.H. Li, B.C.C. Cowie, D. Gunzelmann, S.Z. Qiao, S. Huang, Y. Chen, Observation of active sites for oxygen reduction reaction on nitrogen-doped multilayer graphene, ACS Nano. 8 (2014) 6856–6862. doi:10.1021/nn501506p.

[12] D. Guo, R. Shibuya, C. Akiba, S. Saji, T. Kondo, J. Nakamura, Active sites of nitrogen-doped carbon materials for oxygen reduction reaction clarified using model catalysts, Science (361-365). 351 (2016) 361–365. doi:10.1126/science.aad0832.

[13] J. Quílez-Bermejo, C. González-Gaitán, E. Morallón, D. Cazorla-Amorós, Effect of carbonization conditions of polyaniline on its catalytic activity towards ORR. Some insights about the nature of the active sites, Carbon. 119 (2017) 62–71.

doi:10.1016/j.carbon.2017.04.015.

[14] J. Quílez-Bermejo, E. Morallón, D. Cazorla-Amorós, Oxygen-reduction catalysis of N-doped carbons prepared via heat treatment of polyaniline at over 1100 °C, Chem. Commun. 54 (2018) 4441–4444. doi:10.1039/C8CC02105H.

[15] A. Shen, Y. Zou, Q. Wang, R.A.W. Dryfe, X. Huang, S. Dou, L. Dai, S. Wang, Oxygen reduction reaction in a droplet on graphite: Direct evidence that the edge is more active than the basal plane, Angew. Chemie - Int. Ed. 53 (2014) 10804–10808. doi:10.1002/anie.201406695.

[16] D. Qu, Investigation of oxygen reduction on activated carbon electrodes in alkaline solution, Carbon. 45 (2007) 1296–1301. doi:10.1016/j.carbon.2007.01.013.

[17] C. Tang, H.-F. Wang, X. Chen, B.-Q. Li, T.-Z. Hou, B. Zhang, Q. Zhang, M.-M. Titirici, F. Wei, Topological Defects in Metal-Free Nanocarbon for Oxygen Electrocatalysis, Adv. Mater. 28 (2016) 6845–6851. doi:10.1002/adma.201601406.

[18] G. Chai, Z. Hou, T. Ikeda, K. Terakura, Active Sites and Mechanisms for Oxygen Reduction Reaction on Nitrogen - Doped Carbon Alloy Catalysts: Stone–Wales Defect and Curvature Effect, J. Am. Chem. Soc. (2014) 13629–13640. doi:10.1021/ja502646c.

[19] X. Yan, Y. Jia, T. Odedairo, X. Zhao, Z. Jin, Z. Zhu, X. Yao, Activated carbon becomes active for oxygen reduction and hydrogen evolution reactions, Chem. Commun. 52 (2016) 8156–8159. doi:10.1039/C6CC03687B.

[20] F.P. Guoyu Zhong, Hongjuan Wang*, Hao Yu, Haihui Wang, School, Chemically drilling carbon nanotubes for electrocatalytic oxygen reduction reaction, Electrochim. Acta. 190 (2016) 49–56.

[21] K. Waki, R.A. Wong, H.S. Oktaviano, T. Fujio, T. Nagai, K. Kimoto, K. Yamada, Non-nitrogen doped and non-metal oxygen reduction electrocatalysts based on carbon nanotubes: mechanism and origin of ORR activity, Energy Environ. Sci. 7 (2014) 1950–1958. doi:10.1039/c3ee43743d.

[22] J. P.L. Walker, M. Sheref, R.A. Anderson, Catalysis of carbon gasification, Chem. Phys. Carbon Vol 4. 4 (1968) 287–383. doi:10.1063/1.2914601.

[23] K.H. van Heek, H.-J. Miihlen, Chemical Kinetics of Carbon and Char Gasification, Kluwer Academic Publishers, Dordrecht, The Netherlands, 1991. doi:10.1007/978-94-011-3310-4.

[24] F. Vallejos-Burgos, S. Utsumi, Y. Hattori, X. García, A.L. Gordon, H. Kanoh, K.

Kaneko, L.R. Radovic, Pyrolyzed phthalocyanines as surrogate carbon catalysts: Initial insights into oxygen-transfer mechanisms, Fuel. 99 (2012) 106–117. doi:10.1016/j.fuel.2012.03.055.

[25] D.T. Sawyer, E.T. Seo, One-Electron Mechanism for the Electrochemical Reduction of Molecular Oxygen, Inorg. Chem. 16 (1977) 499–501. doi:10.1021/ic50168a059.

[26] L.R. Radovic, Surface Chemical and Electrochemical Properties of Carbons, in : F. Beguin, E. Frackowiak (Eds.), Carbons Electrochem. Energy Storage Convers. Syst., Taylor & Francis (CRC Press), Boca Raton, FL, 2010: pp. 163–219.

[27] J. Lahaye, P. Ehrburger, Surface chemistry of carbon: an atomistic approach, Pure Appl. Chem. 61 (1989) 1853–1858. doi:10.1351/pac198961111853.

[28] E. Hippo, P.L. Walker, Reactivity of heat-treated coals in carbon dioxide at 900 °C, Fuel. 54 (1975) 245–248. doi:10.1016/0016-2361(75)90037-X.

[29] T. Ishii, S. Kashihara, Y. Hoshikawa, J.I. Ozaki, N. Kannari, K. Takai, T. Enoki, T. Kyotani, A quantitative analysis of carbon edge sites and an estimation of graphene sheet size in high-temperature treated, non-porous carbons, Carbon. 80 (2014) 135–145. doi:10.1016/j.carbon.2014.08.048.

[30] F. Béguin, F. Chevallier, C. Vix, S. Saadallah, J.N. Rouzaud, E. Frackowiak, A better understanding of the irreversible lithium insertion mechanisms in disordered carbons, J. Phys. Chem. Solids. 65 (2004) 211–217. doi:10.1016/j.jpcs.2003.10.050.

[31] F. Béguin, F. Chevallier, C. Vix-Guterl, S. Saadallah, V. Bertagna, J.N. Rouzaud, E. Frackowiak, Correlation of the irreversible lithium capacity with the active surface area of modified carbons, Carbon. 43 (2005) 2160–2167. doi:10.1016/j.carbon.2005.03.041.

[32] M.J. Bleda-Martínez, J.M. Pérez, A. Linares-Solano, E. Morallón, D. Cazorla-Amorós, Effect of surface chemistry on electrochemical storage of hydrogen in porous carbon materials, Carbon. 46 (2008) 1053–1059. doi:10.1016/j.carbon.2008.03.016.

[33] L. Wang, A. Ambrosi, M. Pumera, “Metal-free” catalytic oxygen reduction reaction on heteroatom-doped graphene is caused by trace metal impurities, Angew. Chemie - Int. Ed. 52 (2013) 13818–13821. doi:10.1002/anie.201309171.

[34] R.G. Jenkins, S.P. Nandi, P.L. Walker, Reactivity of heat-treated at 500 ° C coals

in air, Fuel. 52 (1973) 288–293.

[35] C. Vix-Guterl, M. Couzi, J. Dentzer, M. Trinquecoste, P. Delhaes, Surface Characterizations of Carbon Multiwall Nanotubes: Comparison between Surface Active Sites and Raman Spectroscopy, J. Phys. Chem. B. 108 (2004) 19361–19367. doi:10.1021/jp047237s.

[36] D. Cazorla-Amorós, J. Alcañiz-Monge, M.A. de la Casa-Lillo, A. Linares-Solano, CO_2 As an Adsorptive To Characterize Carbon Molecular Sieves and Activated Carbons, Langmuir. 14 (1998) 4589–4596. doi:10.1021/la980198p.

[37] D. Lozano-Castelló, D. Cazorla-Amorós, A. Linares-Solano, Usefulness of CO_2 adsorption at 273 K for the characterization of porous carbons, Carbon. 42 (2004) 1233–1242. doi:10.1016/j.carbon.2004.01.037.

[38] L.R. Radović, P.L. Walker, R.G. Jenkins, Importance of carbon active sites in the gasification of coal chars, Fuel. 62 (1983) 849–856. doi:10.1016/0016-2361(83)90041-8.

[39] N.R. Laine, F.J. Vastola, P.L. Walker, The Importance of active surface area in the carbon-oxygen reaction J. Phys. Chem. 67 (1963) 2030–2034. doi:10.1021/j100804a016.

[40] Y. Otake, R.G. Jenkins, Characterization of oxygen-containing surface complexes created on a microporous carbon by air and nitric acid treatment, Carbon. 31 (1993) 109–121. doi:10.1016/0008-6223(93)90163-5.

[41] J.L. Figueiredo, M.F.R. Pereira, M.M.A. Freitas, J.J.M. Órfão, Modification of the surface chemistry of activated carbons, Carbon. 37 (1999) 1379–1389. doi:10.1016/S0008-6223(98)00333-9.

[42] M.C. Román-Martínez, D. Cazorla-Amorós, A. Linares-Solano, C. Salinas-Martínez De Lecea, F. Atamny, Structural study of a phenolformaldehyde char, Carbon. 34 (1996) 719–727. doi:10.1016/0008-6223(95)00194-8.

[43] R. Zhong, Y. Qin, D. Niu, J. Tian, X. Zhang, X.-G. Zhou, S.-G. Sun, W.-K. Yuan, Effect of carbon nanofiber surface functional groups on oxygen reduction in alkaline solution, J. Power Sources. 225 (2013) 192–199. doi:10.1016/j.jpowsour.2012.10.043.

[44] G. Panomsuwan, S. Chiba, Y. Kaneko, N. Saito, T. Ishizaki, In situ solution plasma synthesis of nitrogen-doped carbon nanoparticles as metal-free electrocatalysts for the oxygen reduction reaction, J. Mater. Chem. A. 2 (2014) 18677–18686.

doi:10.1039/c4ta03010a.

[45] P. Delhaes, M. Couzi, M. Trinquecoste, J. Dentzer, H. Hamidou, C. Vix-Guterl, A comparison between Raman spectroscopy and surface characterizations of multiwall carbon nanotubes, Carbon. 44 (2006) 3005–3013. doi:10.1016/j.carbon.2006.05.021.

[46] C. Vix-Guterl, J. Dentzer, P. Ehrburger, K. Méténier, S. Bonnamy, F. Béguin, Surface properties and microtexture of catalytic multi-walled carbon nanotubes, Carbon. 39 (2001) 318–320. doi:10.1016/S0008-6223(00)00247-5.

[47] D.W. Mckee, C.L. Spiro, K.E. J, P.G. Lamby, Catalytic Effects of Alkali Metal Salts in the Gasification of Coal Char, Symp. Coal Gasif. (1982) 74–86.

[48] A.B. Silva-Tapia, X. García-Carmona, L.R. Radovic, Similarities and differences in O_2 chemisorption on graphene nanoribbon vs. carbon nanotube, Carbon. 50 (2012) 1152–1162. doi:10.1016/j.carbon.2011.10.028.

[49] T.W. Ebbesen, P.M. Ajayan, H. Hiura, K. Tanigaki, Purification of nanotubes, Nature. 367 (1994) 519–519. doi:10.1038/367519a0.

[50] N. Yao, V. Lordi, S.X.C. Ma, E. Dujardin, A. Krishnan, M.M.J. Treacy, T.W. Ebbesen, Structure and oxidation patterns of carbon nanotubes, J. Mater. Res. 13 (1998) 2432–2437. doi:10.1557/JMR.1998.0338.

[51] K. Morishita, T. Takarada, Scanning electron microscope observation of the purification behaviour of carbon nanotubes, J. Mater. Sci. 34 (1999) 1169–1174. doi:10.1023/A:1004544503055.

[52] T. Shimada, H. Yanase, K. Morishita, J.I. Hayashi, T. Chiba, Points of onset of gasification in a multi-walled carbon nanotube having an imperfect structure, Carbon. 42 (2004) 1635–1639. doi:10.1016/j.carbon.2004.02.019.

[53] C. González-Gaitán, R. Ruiz-Rosas, E. Morallón, D. Cazorla-Amorós, Functionalization of carbon nanotubes using aminobenzene acids and electrochemical methods. Electroactivity for the oxygen reduction reaction, Int. J. Hydrogen Energy. 40 (2015) 11242–11253. doi:10.1016/j.ijhydene.2015.02.070.

[54] A.J. Bard, L.R. Faulkner, Electrochemical Methods: Fundamentals and Applications,2nd edition, JOHN WILEY & SONS, INC., 2001.

[55] M. Gara, R.G. Compton, Activity of carbon electrodes towards oxygen reduction in acid: A comparative study, New J. Chem. 35 (2011) 2647. doi:10.1039/c1nj20612e.

[56] P. Zhang, X. Hou, J. Mi, Y. He, L. Lin, Q. Jiang, M. Dong, From two-dimension to one-dimension: the curvature effect of silicon-doped graphene and carbon nanotubes for oxygen reduction reaction, Phys. Chem. Chem. Phys. 16 (2014) 17479–17486. doi:10.1039/C4CP02167C.

[57] G.-L. Chai, Z. Hou, D.-J. Shu, T. Ikeda, K. Terakura, Active Sites and Mechanisms for Oxygen Reduction Reaction on Nitrogen-Doped Carbon Alloy Catalysts: Stone–Wales Defect and Curvature Effect, J. Am. Chem. Soc. 136 (2014) 13629–13640. doi:10.1021/ja502646c.

[58] K. Matsubara, K. Waki, Oxygen reduction characteristics of bamboo-shaped, multi-walled carbon nanotubes without nitrogen in acid media, Electrochim. Acta. 55 (2010) 9166–9173. doi:10.1016/j.electacta.2010.08.040.

[59] X. Pan, X. Bao, The effects of confinement inside carbon nanotubes on catalysis, Acc. Chem. Res. 44 (2011) 553–562. doi:10.1021/ar100160t.

Chapter 4.

Modeling of oxygen reduction reaction in porous carbon materials in alkaline medium. Effect of microporosity.

4-1, Nomenclature

$C_{O_2}^{b}$: oxygen concentration in the bulk of the solution, mol cm^{-3}

C_i^{p}: concentration of *i* component within the pores of the electrode, mol cm^{-3}

D_{O_2}: diffusion coefficient of oxygen, $1.8 \cdot 10^{-5}$ cm^2 s^{-1} at 25 ºC

$j_{H_2O_2}$: modeled specific current for the electrochemical reduction of H_2O_2 to H_2O, mA cm^{-2}

j_{O_2}: modeled specific current for the electrochemical reduction of O_2 to H_2O_2, mA cm^{-2}

j_D^{ORR}: modeled specific current on the disk of the rotating ring-disk electrode, mA cm^{-2}

$J_{H_2O_2}^{D}$: Hydrogen peroxide diffusion rate, mol cm^{-2} s^{-1}

$J_{H_2O_2}^{K}$: intrinsic electrochemical reaction rate for H_2O_2 reduction, mol cm^{-2} s^{-1}

$J_{O_2}^{D}$: Oxygen diffusion rate, mol cm^{-2} s^{-1}

$J_{O_2}^{K}$: intrinsic electrochemical reaction rate for O_2 reduction, mol cm^{-2} s^{-1}

j_{O2}^{L}: Levich limiting current density, mA cm^{-2}

$k_{H_2O_2}^{f}$: effective mass transfer coefficient of H_2O_2 within the pores, cm s^{-1}

$k_{0,i}^{r}$: charge transfer rate constant of *i* component, cm s^{-1}

k_L^{f}: mass transfer coefficient of oxygen, 0.0125 cm s^{-1} at 1600 rpm

k_i^{r}: kinetic constant for the electrochemical reduction of *i* component, cm s^{-1}

α_i: electron transfer coefficient of i component

C_g: gravimetric capacitance, F g^{-1}

CO_2^{TPD}: CO_2-evolving surface oxygen groups from TPD, µmol g^{-1}

CO^{TPD}: CO-evolving surface oxygen groups from TPD, µmol g^{-1}

C^{XPS}: carbon atomic concentration by XPS, at.%

E: electrode potential vs the reversible hydrogen electrode, V

F: Faraday constant, 96485 C mol^{-1}

I_D: current measured at the disk of the rotating ring-disk electrode, mA

I_R: current measured at the ring of the rotating ring-disk electrode, mA

J: specific current measured on the disk of the rotating ring-disk electrode, mA cm^{-2}

La: crystallite thickness along the a-axis for a graphitic structure, nm

Lc: crystallite thickness along the c-axis for a graphitic structure, nm

n: number of transferred electrons

O^{TPD}: total evolved oxygen from TPD, µmol g^{-1}

O^{XPS}: oxygen atomic concentracion by XPS, at.%

R^{H2O2}: $k_{0,H_2O_2}^{r}/k_{H_2O_2}^{f}$ ratio

S_{BET}: apparent surface area from BET method, m^2 g^{-1}

V_{DR}^{CO2}: Dubinin-Raduskevich micropore volume from CO_2 adsorption isotherm, $cm^3\ g^{-1}$

V_{DR}^{N2}: Dubinin-Raduskevich micropore volume from N_2 adsorption isotherm, $cm^3\ g^{-1}$

Vmes: mesopore volume from N_2 adsorption isotherm, $cm^3\ g^{-1}$

υ: kinematic viscosity of 0.1M KOH electrolyte, 0.01 $cm^2\ s^{-1}$

ω: rotation rate, rad s^{-1}

η: electrode overpotential, V

ψ: ratio between effective surface area and geometric surface area of disk

4-2, Introduction

Due to their low cost, high stability, high electrical conductivity and tunable surface chemistry and porosity, carbon materials are attractive materials for their use in the formulation of catalysts for electrochemical energy conversion [1]. In the case of low temperature fuel cells, carbon materials are the main component of the electrodes, where they can be employed as a support for achieving well dispersed active phases, and, more recently, even as catalyst by themselves. Nowadays, carbon black currently constitutes the preferred support in commercial carbon catalyst layers [2,3].

Much attention is being paid to the development of novel catalysts for the oxygen reduction reaction (ORR) because it is a slow reaction that necessitates high Pt loadings. This reaction takes place at the cathode of all fuel cell systems and other energy storage devices such as metal-air batteries. The high cost, low chemical stability and performance of current platinum-based electrodes are one of the main obstacles for the commercial implementation of these systems, therefore explaining the growing interest in non-noble or metal-free ORR catalysts [4–7]. Even in the case of noble-metal based catalysts, the contribution of carbon support to ORR is far from being negligible, and can account for values as high as one third of the power delivered by a fuel cell [8], and can severely decline the stability of the cathode and the membrane when the 2-electron pathway towards hydrogen peroxide prevails [9]. This explains the huge interest in determining the parameters that drives the ORR activity of carbon materials. The ORR activity of undoped carbon materials is low. The highest activity is achieved at high pH values, although the reaction rate still is sluggish, and the reaction pathway delivers the formation of hydroperoxide ion through a 2-transferred electron process [10]. Nevertheless, the surface chemistry and the textural parameters of carbon materials can be modified for enhancing their electrocatalytic activity.

The effect of the surface chemistry on the ORR activity has been profusely studied in recent years. The functionalization of carbon materials for the production of metal free or carbon alloys catalysts is of great interest and constitutes the core of a large number of recent studies [5,11,12]. Nitrogen and oxygen functionalities in the vicinities of the carbon atom improve the ORR performance of N-doped carbon materials [13]. Moreover, it was reported that Co-containing catalysts with pyridinic N and quaternary N groups in the carbon framework seem to be one of the optimum combinations to create the most active sites for ORR [14]. Consequently, a great attention has been devoted to understand the effect of the surface chemistry on the catalysis of ORR by carbon materials and to reveal the actual nature of the active site [9,11,14–21]. However, the effect of porosity on the kinetics and mechanism of oxygen reduction by carbon materials is often ignored, and, when considered, the presence of catalytic species has made challenging any clear assessment [22–27]. Thus, only a few works can be found where a systematic approach for assessing the role of microporosity of bare carbon materials in ORR is reported. In this sense, Appleby and Marie reported ORR kinetic studies carried out on a large collection of carbon materials in alkaline solution [28], including several carbon blacks and activated carbons. They found that ORR activity increased linearly with BET surface area for carbon blacks, whereas no clear trend was found in the case of activated carbons. They argued that, even though the high surface area of ACs should provide a larger amount of active sites for ORR, those lying on micropores are unreachable either for the electrolyte (unwetted pores), for dissolved oxygen or for the solvated HO_2^- anion, explaining why their catalytic activity is actually lower than expected considering their BET surface areas. Recently, Liu et al. analyzed the influence of micro and mesoporosity on ORR cathode catalysts [29], and were able to conclude that activity is increased by the presence of microporosity and that mesoporosity was necessary to facilitate accessibility to active sites. On the other hand, Seredych et al. prepared ORR catalysts using a hydrophobic ultramicroporous carbon made from furfuryl alcohol and tannin [30]. The ORR experiments in rotating disk electrode revealed a clear inverse relationship between the micropore size and volume (especially those with sizes lower than 0.7 nm) and the catalytic activity at low potentials (i.e. the potentials required by these catalysts for achieving a 4 e- pathway). The authors proposed that a strong adsorption of oxygen takes place in hydrophobic ultramicropores, leading to weakening of O-O bonds and therefore promoting the dissociation of dioxygen. Again, the presence of a wider porosity of hydrophilic character is considered to be critical for achieving a good oxygen mass transfer rate to the ultramicropores. Finally, Qu reported the ORR catalytic activity of several activated carbons of different micropore sizes [31]. However, most of the work is devoted to find a relationship between the activated carbon structure and crystallinity rather than in the effect of microporosity, which is considered to be “not in use” in the gas diffusion layers of catalysts.

This work presents a study of the effect of porosity, and in particular microporosity, in carbon material electrodes in the ORR in alkaline conditions. For this purpose, several carbon materials with different textural properties but similar surface chemistry have been selected. This collection includes a highly microporous activated carbon, a char with a low microporosity development and two commercial carbon blacks of different surface area and pore size distributions. After determining the ORR activity of these materials, a kinetic model for the oxygen reduction reaction over porous carbon materials that takes into account the critical role of microporosity in the ORR mechanism is drawn. In accordance to this model, the current density of porous carbon materials in ORR is derived and its validity for describing the experimental results of the porous carbon samples is discussed.

4-3, Experimental section

4-3-1, Material synthesis

A highly microporous activated carbon (KUA) was prepared by chemical activation of Spanish anthracite with KOH. The impregnation ratio of KOH to carbon precursor has been set to 4:1. The activation has been carried out at 750 ºC (heating rate: 5 ºC /min, holding time: 2 hours) in a tubular furnace equipped with a quartz tube feed with 800 mL/min of nitrogen (99.999 %, Air Liquide). The pyrolyzed mixture was thoroughly stirred in 5 M HCl and distilled water until neutral pH in the eluate was achieved. The resulting activated carbon was recovered by filtration and dried at 120 ºC before being stored. More details about the preparation procedure can be found elsewhere [32]. Microporous char (AC) was prepared by carbonization of a phenolformaldehyde polymer resin in N_2, at 5 ºC /min to 1273 ºC with 1 h soaking time. Commercial Vulcan XC-72F carbon black (XC72) from Cabot corporation and CD-6008 carbon black (CB) supplied from COLUMBIAN CHEMICALS have been used as received.

4-3-2, Material characterization

The porosity of the porous carbons and the carbon black was analyzed by CO_2 and N_2 adsorption isotherms at 0 ºC and -196 ºC, respectively, using an Autosorb-6B apparatus (Quantachrome). Samples were outgassed at 200 ºC for at least 8 hours. BET surface areas (SBET) have been determined in the 0.02-0.20 range of relative pressures. The micropore volume has been assessed by applying Dubinin-Radushkevich theory (V_{DR}^{N2}) for P/P_0 from 0.005 to 0.05, whereas mesopore volume (V_{mes}) has been assessed by the difference of amount adsorbed at relative pressure between 0.20 and 0.98, assuming that the pores are filled with N_2 as liquid. The narrow micropore volume has been calculated from the CO_2 adsorption isotherm at 0 ºC (V_{DR}^{CO2}). Pore size distribution has been obtained from the N_2

adsorption isotherms (range of relative pressures from $5 \cdot 10^{-4}$ to 0.98) considering the 2D-NLDFT Heterogeneous surface model [33] and by applying the Solution of Adsorption Integral Equation Using Splines (SAIEUS, available online at http://www.nldft.com/) Software.

The structure of the samples was characterized by transmission electron microscopy (TEM) using a CM200 apparatus (Philips), working at a high voltage of 200 kV and X-ray Diffraction (XRD). XRD patterns of powder samples were acquired on a Philips X́Pert PROMPD diffractometer using CuKα radiation (λ = 1.5406 Å) in the 2θ region between 5° and 70°. The X-ray generator was set to 45 kV at 40 mA.

The surface chemistry has been assessed using X-Ray Photoelectron Spectroscopy (XPS) and Temperature Programmed Desorption (TPD) experiments. XPS analyses were carried out using a VG-Microtech Multilab 3000 spectrometer, equipped with an Al anode. Survey and high-resolution spectra (for the calculation of surface atomic concentration of the detected elements) of powdered samples were recorded with a constant pass energy value of 50 eV, using a 400 μm diameter analysis area. TPD experiments were performed by heating carbon samples (ca. 10 mg) from 120 ºC to 940 ºC using a heating rate of 20 ºC/min under a helium flow rate of 100 mL/min. These analyses were carried out in a thermogravimetric system (TA Instruments, SDT Q600 Simultaneous) coupled to a mass spectrometer (Thermostar, Balzers, BSC 200). Evolved amounts of CO and CO_2 during the TPD run were quantified by calibration of 28 and 44 m/z lines by following the thermal decomposition of a known amount of calcium oxalate in the aforementioned experimental setup.

4-3-3, ORR activity experiments

Electrochemical activity tests towards ORR were conducted at 25 ºC in a thermostated three-electrode cell filled with 0.1 M KOH solution using a Autolab 302N potentiostat (Metrohm), a platinum wire as the counter electrode and reversible hydrogen electrode (RHE) immersed in the same working solution (0.1 M KOH) and separated from the main compartment through a Luggin capillary as the reference electrode.

A rotating ring-disk electrode (RRDE, Pine Research Instruments) equipped with a glassy carbon disk (5.61 mm diameter) and a platinum ring was used as the working electrodes. The samples were dispersed in isopropanol-ethanol-water mixtures, drop-casted and dried over the glassy carbon disk. Nafion® (5% weight Nafion®

perfluorinated resin solution, Aldrich) was added to the mixture in order to deliver a 1:5 Nafion® to sample weight ratio. Active phase amounts of 100 μg were used for all these samples whereas additional experiments with 250 μg and 25 μg were performed for KUA. Cyclic voltammetry (CV) and linear sweep voltammetry (LSV) were performed between 0 V and 1 V (vs. RHE) in a O_2-saturated electrolyte under continuous O_2 bubbling at 5 mV s^{-1} at different rotation rates between 400 and 2025 rpm, while the potential of the ring was held constant at 1.5 V (vs. RHE). The contribution of the double layer capacitance during the LSV experiments has been discriminated by recording CV under inert N_2 atmosphere prior and after the LSV measurements.

The number of electrons transferred in the oxygen reduction reaction (n) has been followed during the LSV measurements from the oxidation of hydrogen peroxide over the platinum ring disk using the following equation:

$$n = \frac{4 \cdot I_D}{I_D + I_R/N} \qquad \textbf{(1)}$$

Where I_R and I_D stand for the currents measured at the ring and the disk, respectively, and N is the collection efficiency of the ring, which was experimentally determined to be 0.37. The number of electrons has also been determined from the slope of the Koutecky -Levich plots at different potentials [34] using LSV recorded at several rotation rates (400, 625, 900, 1225 and 1600 rpm).

The limiting current during RDE experiments (j_{O2}^{L}, mA cm^{-2}) has been defined in accordance to Levich model for RDE [34]:

$$j_{O2}^{L} = n \cdot F \cdot 0.62 \cdot D_{O_2}^{2/3} \cdot \upsilon^{-1/6} \cdot \omega^{1/2} \cdot C_{O_2}^{B} = n \cdot F \cdot k_{L}^{f} \cdot C_{O_2}^{B} \qquad \textbf{(2)}$$

In Eqn. 2, n is the number of electrons transferred in the reduction reaction, F stands for the Faraday constant (96485 C mol^{-1}), D_{O2} is the diffusion coefficient of oxygen ($1.8 \cdot 10^{-5}$ cm^2 s^{-1}), υ is the kinematic viscosity of the solution (0.01 cm^2 s^{-1}) and ω is the rotation rate (rad s^{-1}). The parameters $0.62 \cdot D_{O_2}^{2/3} \cdot \upsilon^{-1/6} \cdot \omega^{1/2}$ have been grouped in the so-called mass transfer coefficient of oxygen, k_{L}^{f}, having a value of 0.0125 cm s^{-1} for 1600 rpm. $C_{O_2}^{B}$ is oxygen concentration in the bulk of the solution ($1.2 \cdot 10^{-6}$ mol cm^{-3}). Finally, additional LSV experiments in N_2- and O_2-saturated 0.1 M KOH solution containing 3 mM H_2O_2 were performed using the RDE using the same experimental conditions reported for the ORR experiments.

4-4, Results and discussion

4-4-1, Characterization of porosity and structure

Figure 1A) compiles the N_2 adsorption-desorption isotherms at -196 ºC for all the carbon materials employed in this work. The collection of studied samples provides a set of different porosities, as can be visualized from the shape of the adsorption isotherms. Thus, KUA sample shows a type I isotherm according to IUPAC classification, which is characteristic of microporous solids [35], as well as the highest N_2 uptake. The rounded knee at low relative pressures (0-0.2) points out the presence of a wide micropore size distribution. AC shows a type I plus type IV isotherm shape, with a much lower N_2 uptake than KUA. The occurrence of a hysteresis loop on the desorption branch of the isotherm evidences the presence of mesopores. CB sample also exhibits a combination of type I and IV isotherms although with a large mesoporosity development in this sample. Finally, XC72 sample shows a type II isotherm, typical of non-porous solids where multilayer adsorption takes place in the external surface of the particles.

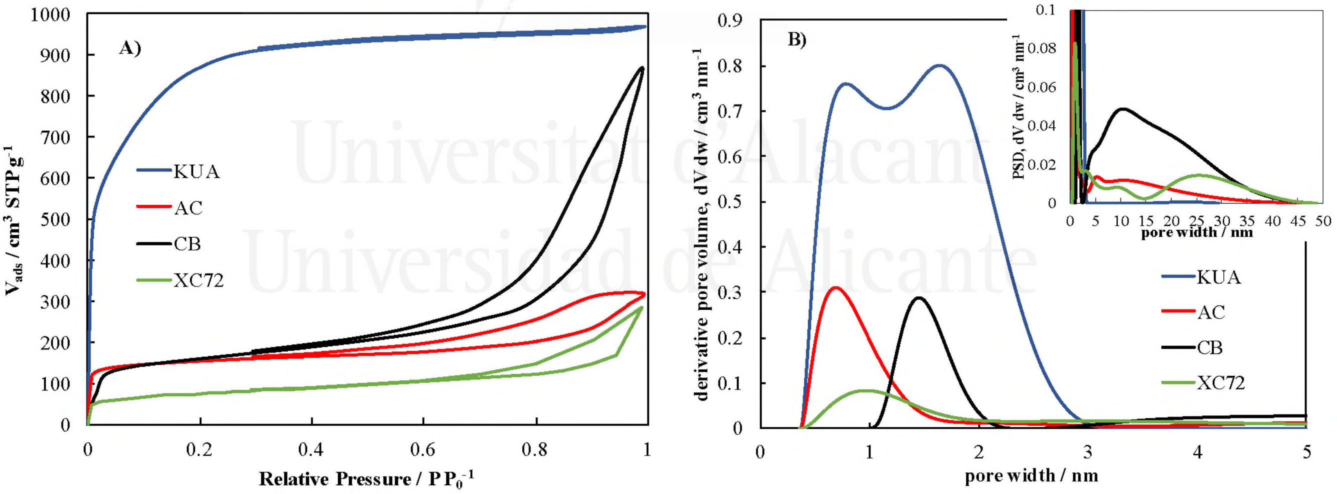

Figure 1. A) N_2 adsorption-desorption isotherms at -196 ºC and B) derived NL-DFT pore size distributions of KUA, AC, CB, and XC72.

Table 1 summarizes the porosity parameters of all the samples employed in this work. In the case of XC72 and CB, most of the surface area (S_{BET} in Table 1) comes from the external surface of the carbon black particles, since the contribution of microporosity is small when compared to the total pore volume of the sample (less than 25%). KUA has a well-developed microporosity (V_{DR}^{N2} in Table 1) and also presents a certain amount of mesopores (V_{meso} in Table 1) [32,36]. AC and CB share similar V_{DR}^{N2} and S_{BET} values, but the mesoporosity development is very different, with V_{meso} being 4 times larger in the carbon black sample.

Table 1. Textural and structural parameters of the analyzed samples.

Sample	**S_{BET}** **$m^2\ g^{-1}$**	**V_{DR}^{N2}** **$cm^3\ g^{-1}$**	**V_{DR}^{CO2}** **$cm^3\ g^{-1}$**	**V_{meso}** **$cm^3\ g^{-1}$**	**L_c** **nm**	**L_a** **nm**
KUA	3300	1.23	0.72	0.15	0.6	2.6
AC	590	0.24	0.26	0.22	0.9	3.6
CB	580	0.26	0.17	0.88	1.2	3.7
XC72	280	0.11	0.05	0.33	1.5	4.0

As for the pore volumes, AC contains both micropores and mesopores with a larger mesopore contribution than KUA (10% of total pore volume are mesopores for KUA, and 45% for AC). CB also combines micropores and wide mesopores, but with an even larger impact of mesoporosity (more than 60% of total porosity). Finally, XC72 did not present any relevant microporosity. It is important to note that the porosity of carbon black samples, namely CB and XC72, is mainly related with the particle size, with micro- and mesopores resulting from the void spaces between the nanosized particles (see ref. [37] for XC72 and TEM images for CB sample in Figure 2).

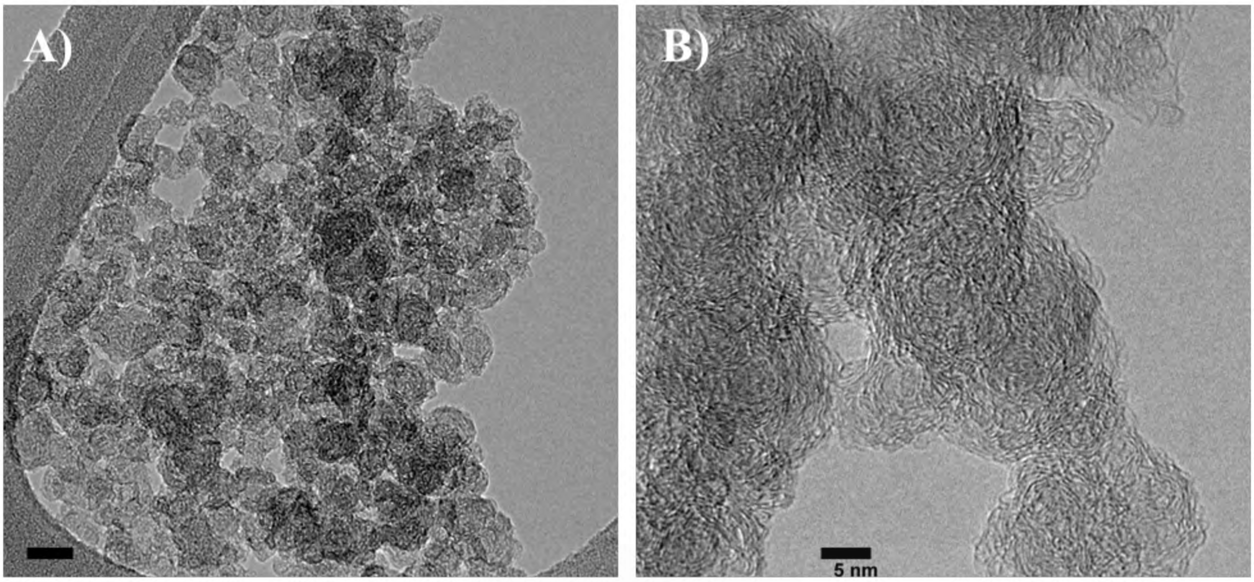

Figure 2. TEM images of CB. Scale bars: 20 nm (A) and 5 nm (B).

We have also evaluated narrow microporosity (pore sizes lower than about 0.7 nm) by using CO_2 adsorption at 0 ºC [38,39]. The similar micropore volume obtained by N_2 and CO_2 adsorption in AC revealed the presence of a narrow micropore size distribution with sizes around 0.7 nm in this sample, whereas CB and KUA have a larger contribution of wide micropores ($V_{DR}^{N2}>V_{DR}^{CO2}$).

The pore size distributions (PSD) for the materials have been calculated from the N_2 adsorption isotherms using NL-DFT method as proposed by Jagiello and Olivier [33] using SAIEUS© software and are shown in Figure 1B. These curves confirmed the wide micropore size distributions for KUA and the narrow micro PSD for the other materials. KUA has most of its porosity covering all the micropore range; however, its wide pore size distribution extends into the narrow mesoporosity region, what explains the origin of the V_{mes} value reported in Table 1. In the mesopore region, it is possible to see that AC and the carbon blacks show a broad pore size distribution, with mesopores of around 10 nm being the most frequent ones for AC and CB, and 25 nm for XC72 (see inset of Figure 1B).

XRD patterns of all samples have been recorded in order to provide information about their crystalline structure (Figure 3). In agreement with the presence of micropores, a large X-Ray scattering at low angles (below 10°) is clearly observed in porous carbon samples, being this feature maximized in the case of the highly porous KUA. The lattice parameters have been determined from the (002) and (100) peaks [40] of their respective XRD profiles and compiled in Table 1. It is possible to see that the carbon blacks have a larger structural ordering than the KOH-activated carbon, showing higher sizes of ordered domains in the parallel and perpendicular directions (L_a and L_c in Table 1), whereas AC has an intermediate ordering degree.

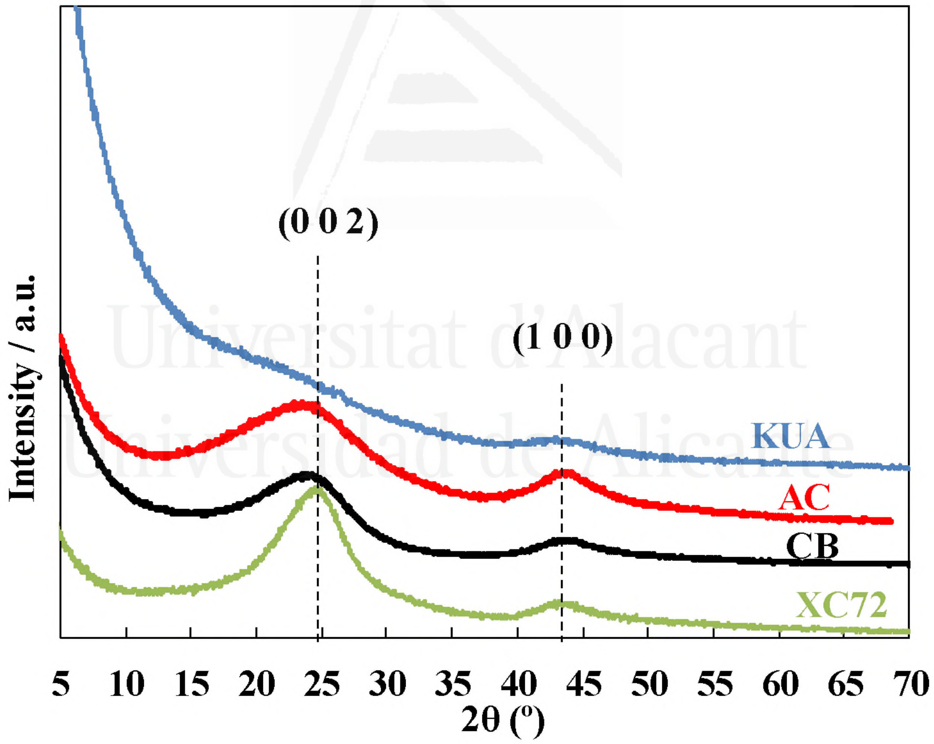

Figure 3. XRD patterns of all carbon samples.

4-4-2, Characterization of surface chemistry

The surface chemistry has been analyzed by XPS and TPD, Table 2. The microporous activated carbon has the highest oxygen content, while both carbon blacks show the lower amounts, as can be deduced from the XPS results (see Table 2). The absence of relevant amounts of other impurities such as sulfur, boron, iron or other heteroatoms was also confirmed. TPD experiments were performed in order to discriminate which kinds of functional oxygen groups can be found in the surface of these materials, Figure 4. Table 2 also summarizes the CO, CO_2 and the total amount of oxygen (O) calculated as CO +2(CO_2) evolved in these TPD. When the evolved amounts are normalized in terms of BET surface area, the amounts of evolved CO_2 are lower in KUA (0.10 μmol m^{-2} for KUA and ca. 0.5 μmol m^{-2} for the rest of samples), and those for CO are higher for AC (values of 0.54, 2.42, 1.00 and 1.05 μmol m^{-2} are found for KUA, AC, CB and XC72, respectively).

Table 2. Surface chemistry of the analyzed samples.

Sample	**C^{XPS} at.%**	**O^{XPS} at.%**	**CO^{TPD} μmol g^{-1}**	**CO_2^{TPD} μmol g^{-1}**	**O^{TPD} wt.%**
KUA	90.7	8.8	1780	330	3.9
AC	94.2	5.8	1430	340	3.5
CB	97.7	2.3	580	280	1.8
XC72	98.0	2.0	230	120	0.6

Surface oxygen groups can be classified during TPD runs attending to the evolution temperature and the nature of the evolved gas. Thus, CO_2 results from decomposition of carboxylic acids at low temperatures, or lactones at higher temperatures; carboxylic anhydrides yield both a CO and a CO_2 peak; finally, phenols, ethers, carbonyls/quinones and pyrones groups decompose as temperature increases in that order, and evolve as CO [41,42] . CO-TPD profiles in Figure 4 makes possible to endorse a large amount of phenols and carbonyls/quinones in KUA, while carbonyls/quinones are more frequent in AC. As for CO_2-evolving groups, their nature and number are fairly similar between KUA, AC and CB. The amounts of CO_2 evolving groups are clearly lower in XC72.

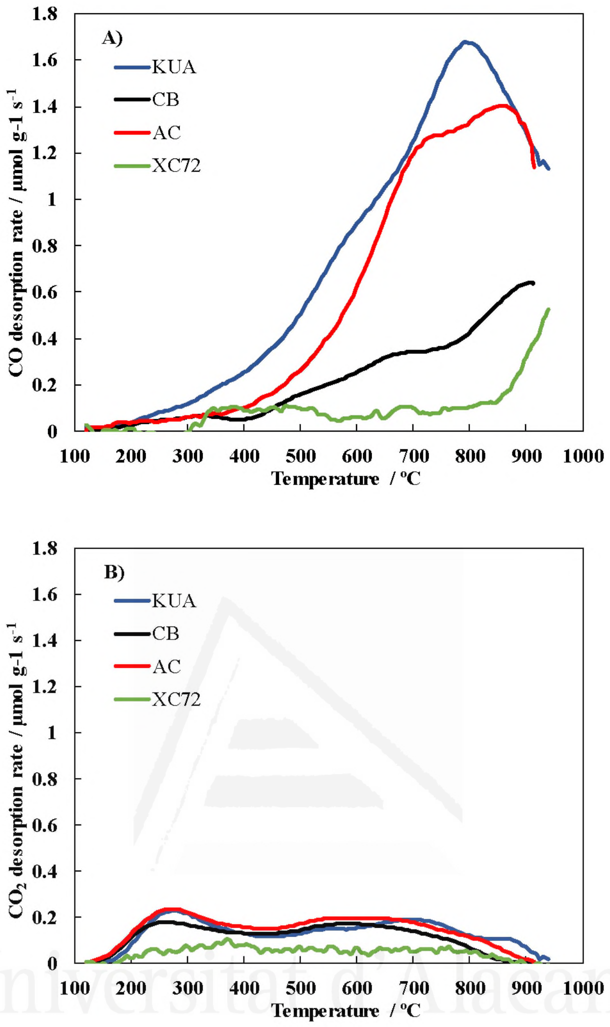

Figure 4. A) CO and B) CO_2 TPD profiles of KUA, AC, CB and XC72 samples.

4-4-3, Electrochemical characterization

The electrochemical behavior of all the samples has been analyzed by cyclic voltammetry in N_2 saturated 0.1M KOH (i.e. the electrolyte used in this work for the ORR measurements) between 0 and 1 V at 50 mV s^{-1}, Figure 5. As expected, all the electrodes have a voltammogram characteristic of capacitive materials. Gravimetric capacitance of these electrodes has been determined from the integration of the CVs, being 155, 80, 60 and 15 F g-1for KUA, AC, CB and XC72 at 50 mV s-1. In the case of KUA, the capacitance is strongly dependent on the scan rate. When capacitance of this electrode was determined at 10 mV s-1, a capacitance value of 195 F g-1 is achieved. Differently, capacitance of XC72, AC and CB remains mostly the same (Retention of capacitance from 10 to 50 mV s-1 of 90-93%). The more ordered carbon structure of the latter samples

(Table 1) and the lower content in microporosity may explain their higher retention of capacitance.

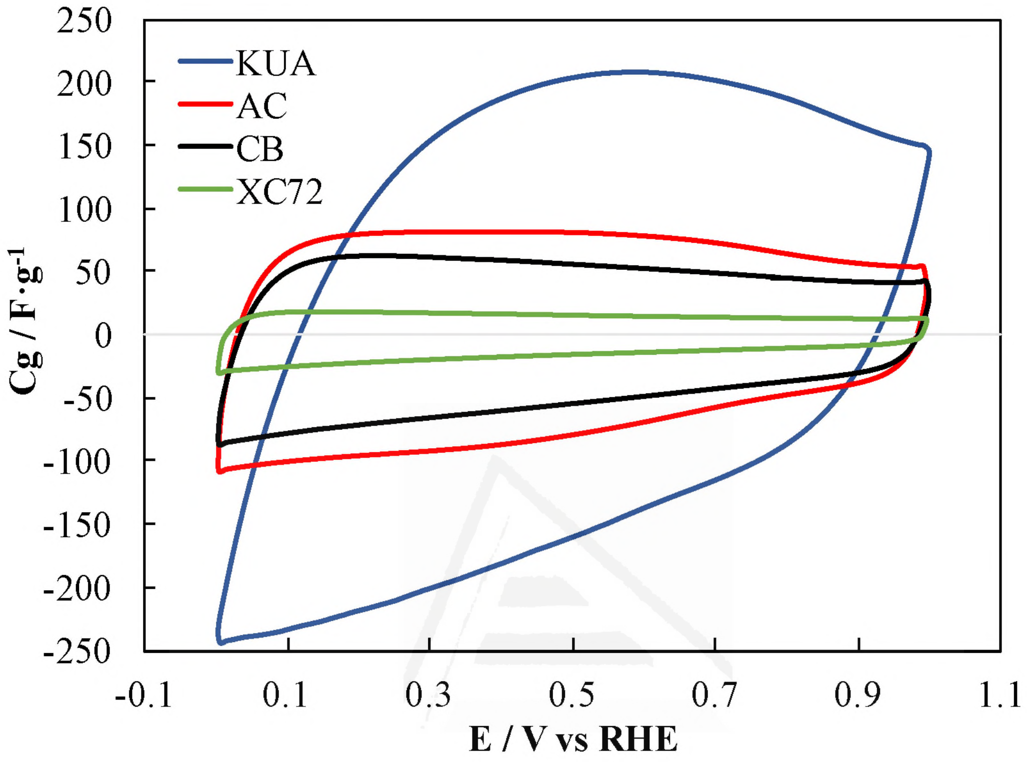

Figure 5. Steady state cyclic voltammograms in 0.1 M KOH. Scan rate: 50 mV s^{-1}. Electrode loading: 0.40 mg cm^{-2}.

Linear sweep voltammetry experiments were also recorded in O_2-saturated electrolyte at 10 mV s^{-1}, Figure 6. As potential was decreased from 1.0V to less positive values, all samples showed a reduction peak in presence of O_2 owing to the ORR, presenting a net reduction current when the CV is compared to that recorded in N_2-saturated electrolyte. Onset potentials (defined as the point where the slope of the CV cathodic scan in O_2-saturated electrolyte starts to deviate from that recorded in N_2-saturated electrolyte) were stablished to be 0.81 V for XC72 and AC, 0.84V for KUA and 0.83V for CB. Further set of experiments using a rotating ring disk electrode have been performed.

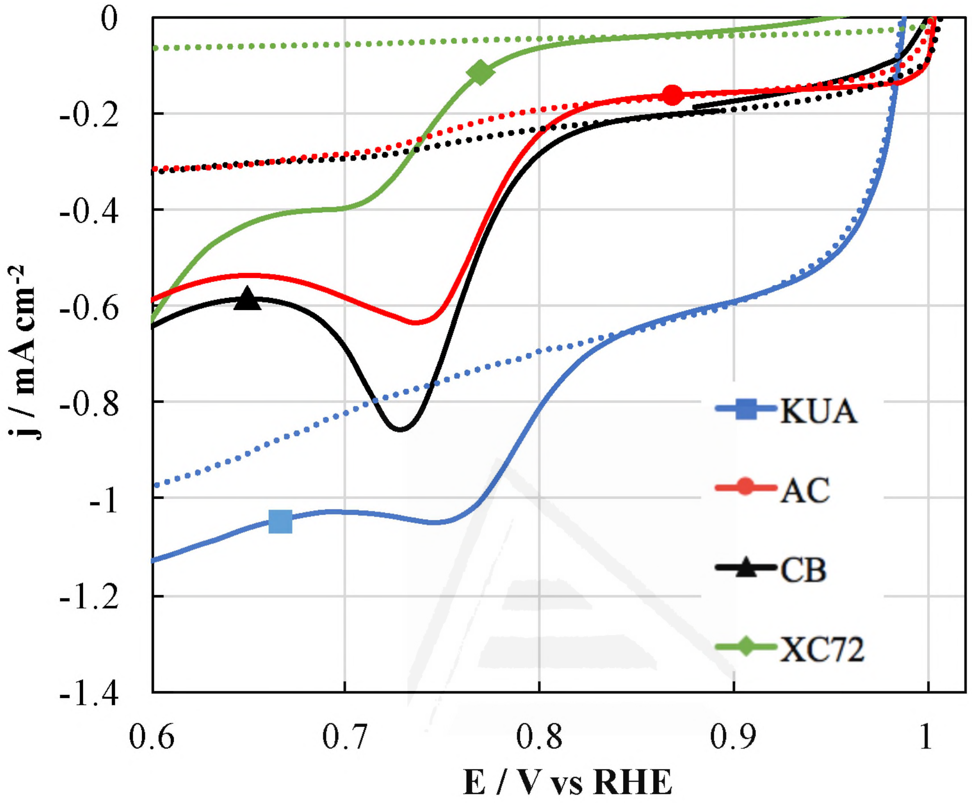

Figure 6. Linear Sweep Voltammetry profiles in N_2- (dashed lines) and O_2- (solid lines) saturated 0.1 M KOH solutions. KUA (blue), AC (red), CB (black) and XC72 (green). Scan rate: 10 mV s^{-1}. Electrode loading: 0.4 mg cm^{-2}.

4-4-4, ORR Rotating ring disk measurements

Figure 7 shows the LSV of all samples at rotation rate of 1600 rpm. The electrodes were stabilized by cycling for 10 minutes in O_2-saturated KOH at 10 mV s^{-1}. After that, the background current was recorded in N_2-saturated electrolyte. The LSV results herein reported were collected after these steps, with the ORR current being corrected by subtraction of the double layer current. The limiting currents for oxygen reduction through 2 and 4 e^- reaction pathways obtained from the Levich theory (2.9 and 5.8 mA cm^{-2} from eqn.2) at the selected experimental conditions are also plotted (dashed grey horizontal lines in Figure 7). The onset potential has been determined at j= -0.1 mA cm^{-2} on the LSV curves in Figure 7A. XC72 has the lowest ORR activity (onset potential of 0.76 V). AC and CB show similar onset potential, 0.80 and 0.79 V, respectively. Remarkably, the activated carbon has a higher onset potential being 0.85 V. Two-wave shape on their LSVs can be observed being less pronounced in the case of KUA and this behavior has been found for a large number of carbon materials. These voltammetric profiles are observed independently of the selected rotation rate, Figure 7, what demonstrates that this behavior is not related to external mass transfer issues. The same study has been performed using the bare surface of the glassy carbon disk, Figure 7E, F, showing that the activity of the disk surface is much lower than that for the tested samples, and it always shows a two-wave shape. Moreover, the diffusion controlled region on the glassy carbon surface starts at much less positive potentials (down to 0.3 V), confirming that LSV measurements are truly dictated by the deposited carbon materials.

The number of transferred electrons during ORR have been calculated from the ring to disk current ratio at 1600 rpm and from Koutecky-Levich (K-L) in eqn.1, Figure 8B. The ORR activity in these samples involve a 2-electron pathway. An increase on the polarization of the electrode shifts the oxygen reduction reaction to a more favorable pathway involving a higher number of electrons (2.4, 2.7, 2.6 and 3.0 electrons at 0.05 V for XC72, CB, AC and KUA samples according to RRDE experiments, and 2.5, 3.1, 2.8 and 3.4 electrons according to K-L theory). The increase in the number of transferred electrons at that potential region seems to be correlated with the presence of microporosity, Table 1, rather than with any other textural, structural or surface chemistry parameter. This would be in agreement with recent findings where ORR activity of milled N-doped carbon nanotubes has been reported to increase due to the formation of microporosity [22].

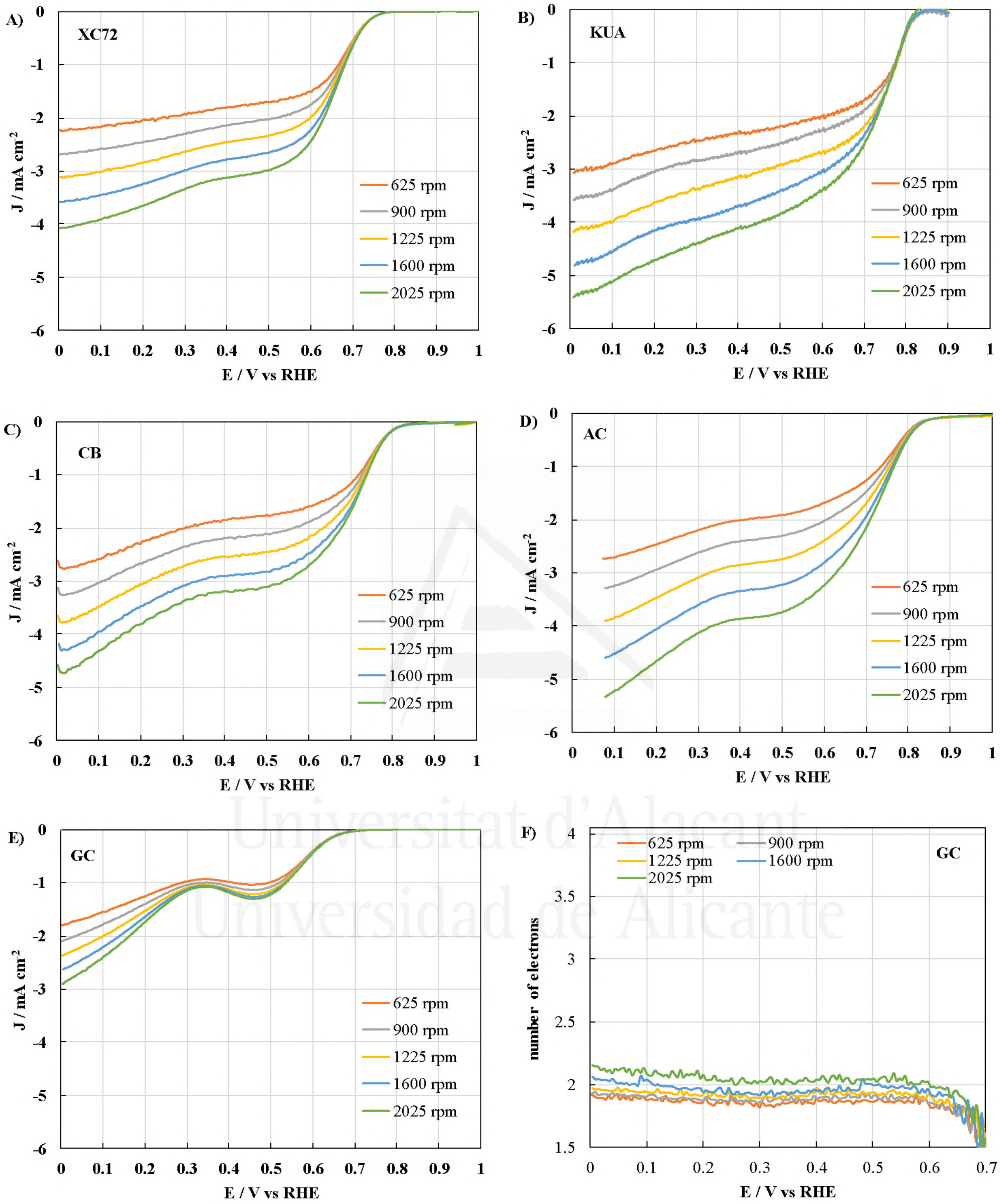

Figure 7. Oxygen reduction reaction study from the RRDE at different rotation rates in 0.1M KOH solution. A) XC72, B) KUA, C) CB, D) AC. Catalyst loading: 1.0 mg cm^{-2}. The same ORR study has been also conducted on the bare glassy carbon surface of the disk, including the RRDE determination of number of transferred electrons at different rotation rates (E,F).

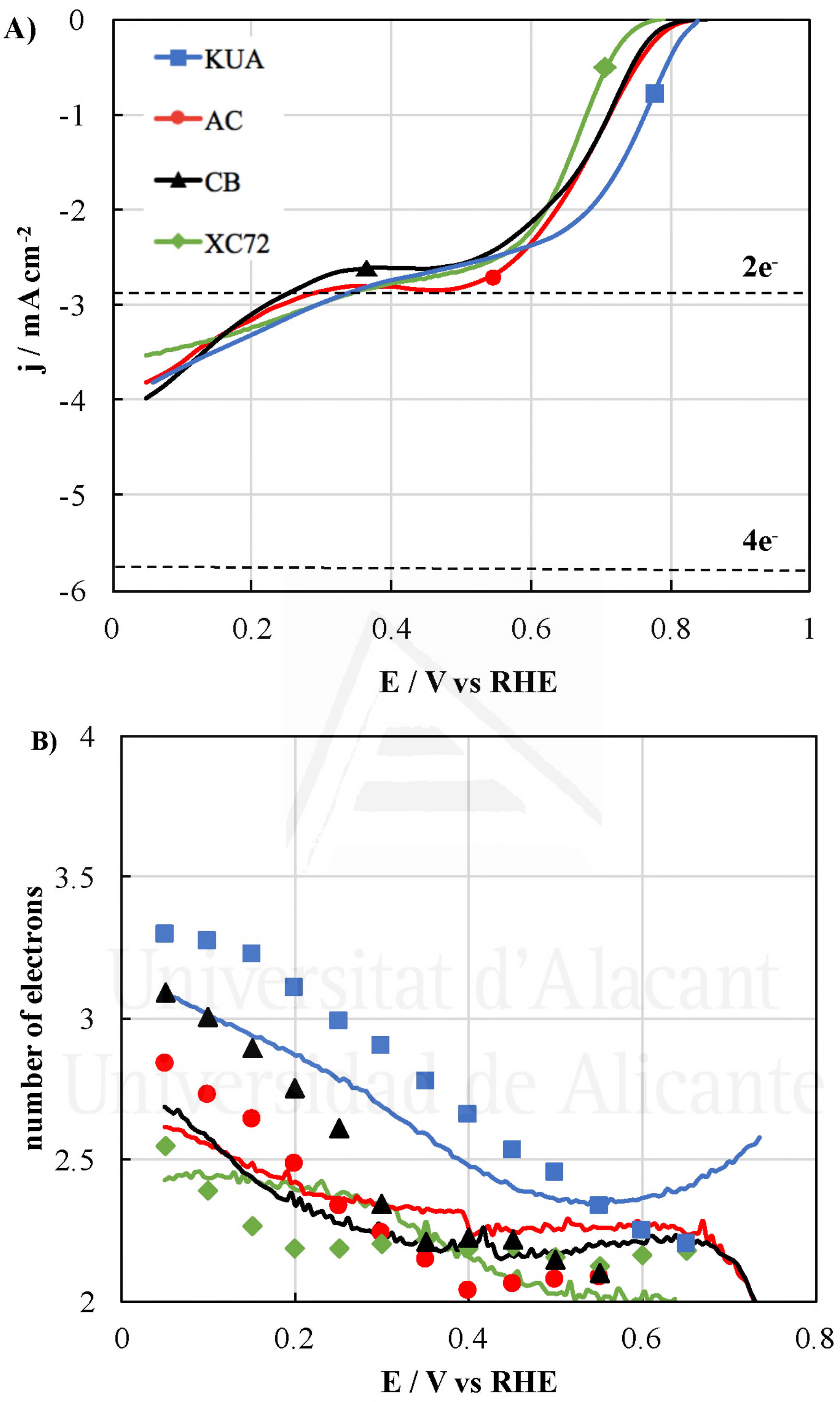

Figure 8. Oxygen reduction reaction study from the RRDE at 1600 rpm in 0.1M KOH solution. A) LSV in the disk electrode (scan rate: 5 mV/s, capacitive currents corrected). B) number of electrons measured from the ring vs disk currents (full lines) and from Koutecky-Levich theory (dots). KUA (blue), AC (red), CB (black) and XC72 (green). Catalyst loading: 0.4 mg cm^{-2}.

4-4-5, Mass loading effect in ORR

Measurements were conducted using two additional sample loadings (0.10 and 1.00 mg cm^{-2}) for KUA, Figure 9A, B. The LSV curves have been also expressed in gravimetric terms, Figure 9C, D. Both kinetic and diffusion rates are negatively impacted by a low surface loading, as manifested by the current decrease and the onset potential being shifted to less positive potentials at 0.10 mg cm^{-2}. In addition, the shape of the LSV profile becomes similar to that of bare glassy carbon surface at medium and low potentials (see dotted, blue line vs dotted, black line in Figure 9A). Decline on ORR activity derived from very low catalyst loading in RRDE experiments have been reported in the past, and they have been accounted to the catalyst particles being unable to fully cover the whole surface of the disk, rendering a lower effective surface of the electrode [43]. It has been also proposed that a high diffusion film resistance in the electrode could result from excessive thickness, reducing the current density [44]. The effect of the different loadings is easily observed when the LSV profiles are normalized in terms of weight. It can be seen that the normalized current in the vicinity of the onset potential goes through a maximum at medium surface loadings, Figure 9C, confirming that kinetic control is reached at that loading, while lower or higher loadings have a negative impact on the ORR activity due to the aforementioned reasons.

Differently, an improvement in the mass transfer rate on the diffusional controlled region (i.e. higher limiting current due to higher oxygen diffusion rate) is observed when raising the loading from 0.40 to 1.00 mg cm^{-2}, Figure 9A. The impact of the ratio between the effective surface area available for oxygen diffusion and reduction and the geometrical area of the disk (which is the used one in the Levich theory for determining oxygen diffusion rate on a rotating flat electrode surface) in the oxygen mass transfer rate on RDE measurements has been already exposed in the literature [34,45,46]. At 0.40 mg cm^{-2}, the disk surface is not fully covered by KUA particles. When KUA loading increases, so does the effective area of the electrode. Therefore, the higher current registered in the diffusional controlled region for 1.00 mg cm^{-2}, Figure 9A, is in agreement with recent findings regarding an enhanced ORR activity in RDE experiments of porous electrodes and nanoparticles-based catalysts due to a higher effective surface area [45,47,48]. As expected, the gravimetric current values in the diffusional controlled region decrease with the loading of the catalyst, Figure 9D. In this region, all oxygen molecules are electrochemically reduced once they reach the electrodic surface, and therefore the current is only determined by the oxygen diffusional flow towards the electrode and the number of transferred electrons during the reaction (i.e. limiting current is reached).

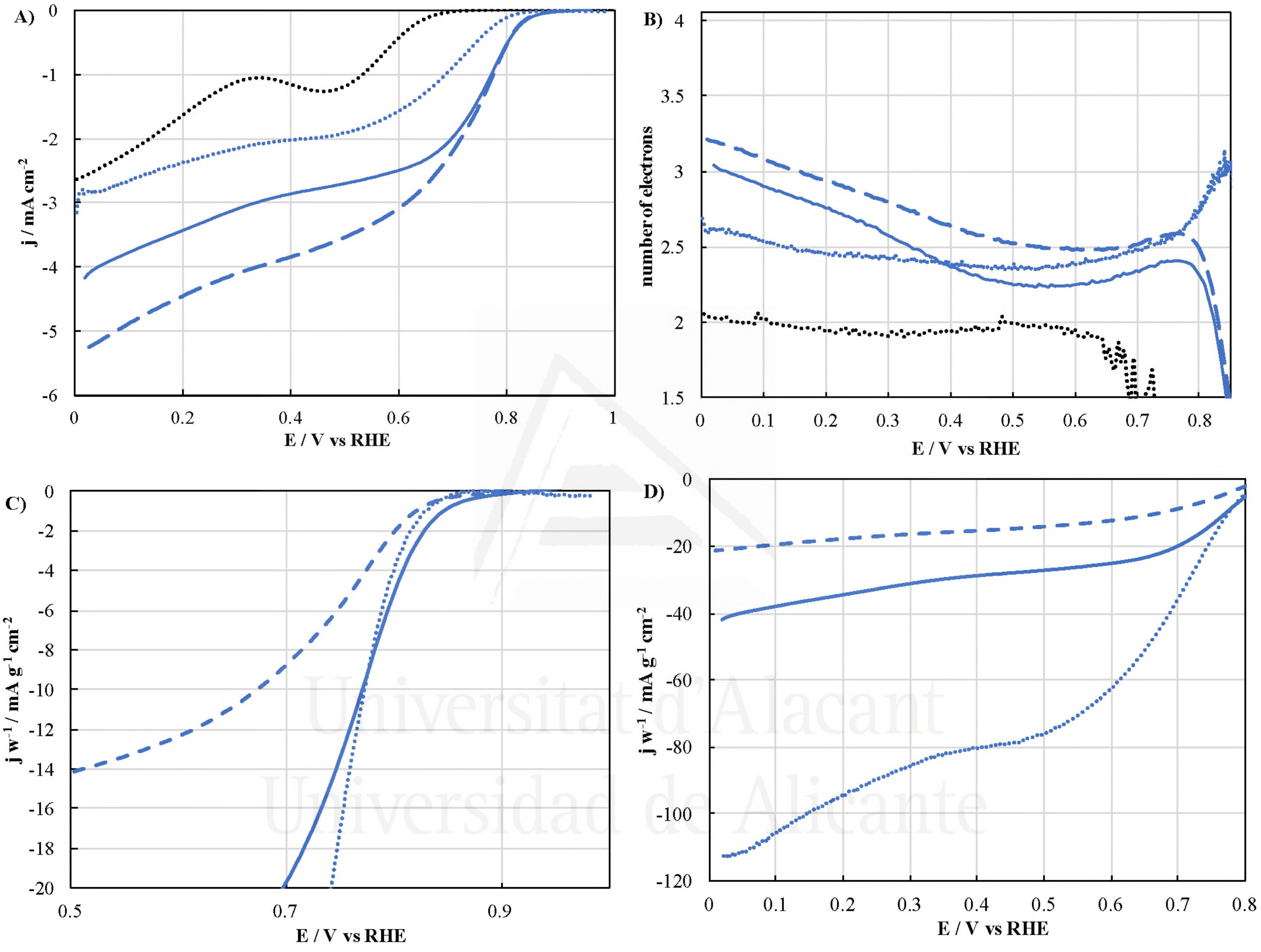

Figure 9. A) LSV ORR profiles in O_2-saturated 0.1M KOH and **B)** number of electrons transferred measured in a RRDE covered with KUA at surface loadings of 0.10 (dotted line), 0.40 (solid lines) and 1.00 (dashed lines) mg cm^{-2}. **C, D)** weight-normalized KUA LSV profiles. Rotation rate: 1600 rpm.

The number of electrons transferred is positively related to the surface loading, Figure 9B. We propose that *n* values between 2 and 4 e^- observed once the diffusion-controlled region is reached, are due to the occurrence of two electrochemical reduction reactions: i) the reduction of all the oxygen molecules arriving to the surface of the electrodes to hydrogen peroxide, involving two electrons, ii) the reduction of some of the hydrogen peroxide produced in reaction i) to hydroxide, what involves 2 additional electrons. The number of electrons is then determined by the ratios between the H_2O_2 diffusion and electrochemical reaction rates. When the electrochemical reaction rate for H_2O_2 reduction is much higher than the diffusion rate, the number of transferred electrons would be close to 4, whereas a high mobility of H_2O_2 would decrease the contact time with the active sites, and a relevant part of H_2O_2 could diffuse out the surface of the electrode, delivering a number of electrons for ORR close to 2. Then, the presence of micropores (which favour the adsorption of H_2O_2) may increase the residence time of H_2O_2, increasing the probability for further reduction reaction. As KUA loading increases, so does the amount of micropores and residence time of H_2O_2 and, consequently, the H_2O_2 reduction rate.

4-4-6, Electrochemical reduction of hydrogen peroxide in RRDE

In order to check the validity of this assumption, the electrochemical reduction of H_2O_2 has been analyzed in the RRDE under similar conditions to those employed in ORR measurements in Figure 8. The concentration of hydrogen peroxide has been set to 3 mM so that it would be in agreement with the concentration of H_2O_2 in the micropores produced by the 2-electron reduction reaction of O_2. Figure 10A compares the LSV curves for all the samples recorded in 3 mM H_2O_2 and N_2-saturated electrolyte. A net reduction current is observed as potential decreases, and the three porous samples delivered a much higher reduction current than XC72. In addition, the LSV for hydrogen peroxide reduction share the same potentials intervals as those observed in the transition between the 2 and the 4 electrons pathway detected in Figures 8 and 9. The onset potentials for the electrochemical reduction of H_2O_2 follow the order KUA >> CB ~ AC > XC72. This order is similar to that of V_{DR}^{N2}, Table 1. The shape of the LSV reveals that no limiting current is achieved in these experiments, probably due to the poor electron transfer rate of active sites located within micropores.

When the ORR activity is determined in the presence of H_2O_2, Figures 10B-D, the resulting LSV are in agreement with a linear addition of the profiles for ORR and hydrogen peroxide reduction reactions experiments. Therefore, no competition between H_2O_2 and O_2 for the active sites seems to take place.

The electrochemical reduction of H_2O_2 by porous carbon electrodes has been studied in the past. Most works relate this reduction with a longer contact time between the surface of the carbon electrodes and hydrogen peroxide [46,49,50].

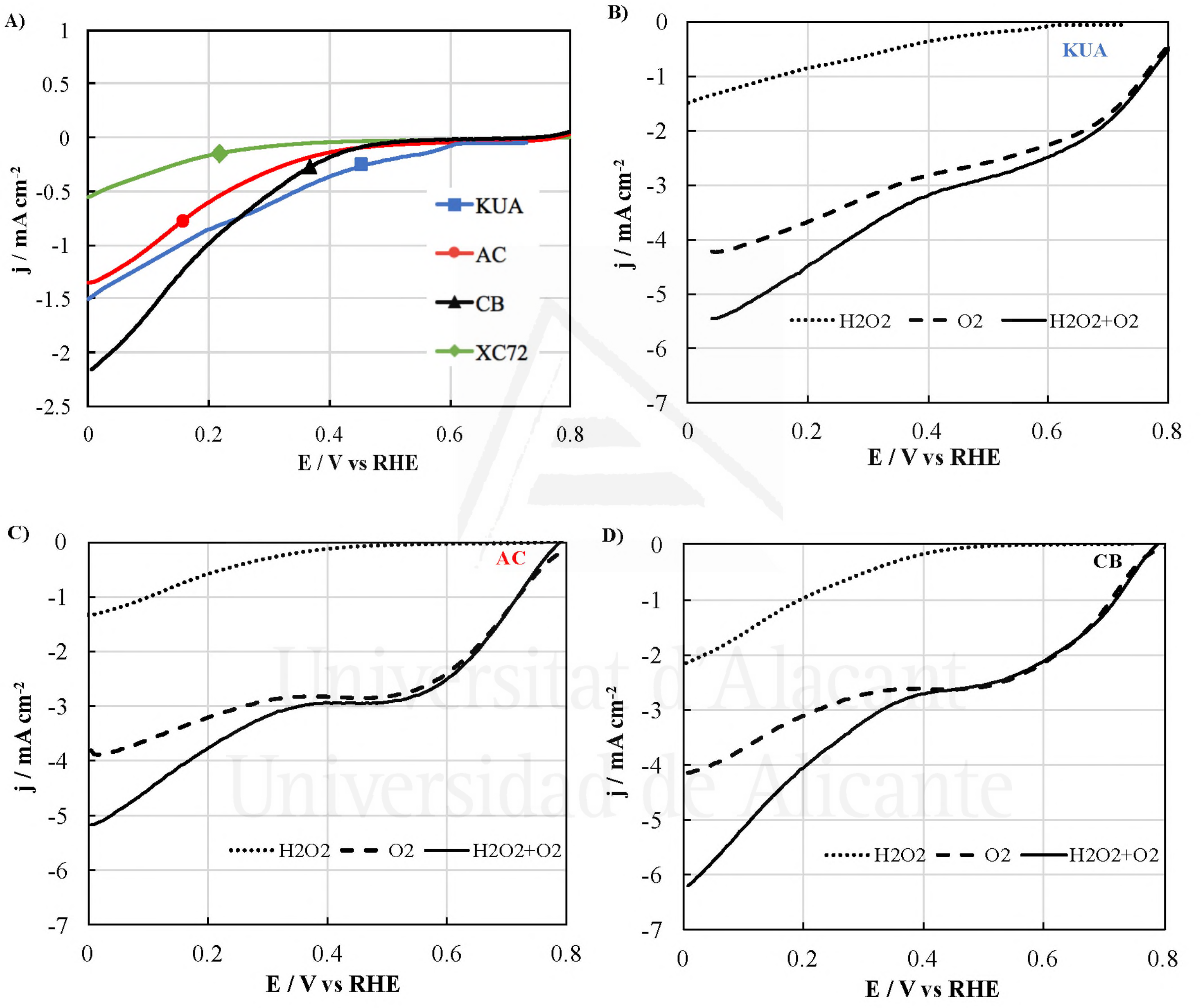

Figure 10. A) LSV profiles of hydrogen peroxide reduction ($[H_2O_2]$: 3 mM) obtained using RRDE at 1600 rpm in N_2-saturated 0.1M KOH. B) KUA, C) AC and D) CB LSV at 1600 rpm in 0.1 M KOH in H_2O_2 and N_2-saturated electrolyte (dotted lines), H_2O_2 and O_2-saturated electrolyte (solid lines), and O_2-saturated electrolyte (dashed lines).

4-4-7, Effect of rotation rate on ORR activity

Additional experiments have been conducted at different rotation rates in order to discard that H_2O_2 formed during ORR is electrochemically reduced at the external surface of the electrode due to an increased contact time (Figure 11**)**. This premise is derived from the work by Zhou et al., who have recently proposed that ORR of nitrogen-doped carbon materials cannot be properly analyzed using RRDE due to the dependence of hydrogen peroxide concentration at the surface of their catalysts [51]. We have observed that the selectivity towards hydrogen peroxide at less positive potentials (where hydrogen peroxide reduction takes place) is unrelated to the rotation rate or even slightly decreases with the rotation rate (which, in any case, is the opposite behavior to that proposed by Zhou et al.), Figure 11. Therefore, the internal diffusion rates of oxygen and hydrogen peroxide, which are independent of the rotation rate, are responsible for the conversion rate of hydrogen peroxide to hydroxide in microporous carbon electrodes.

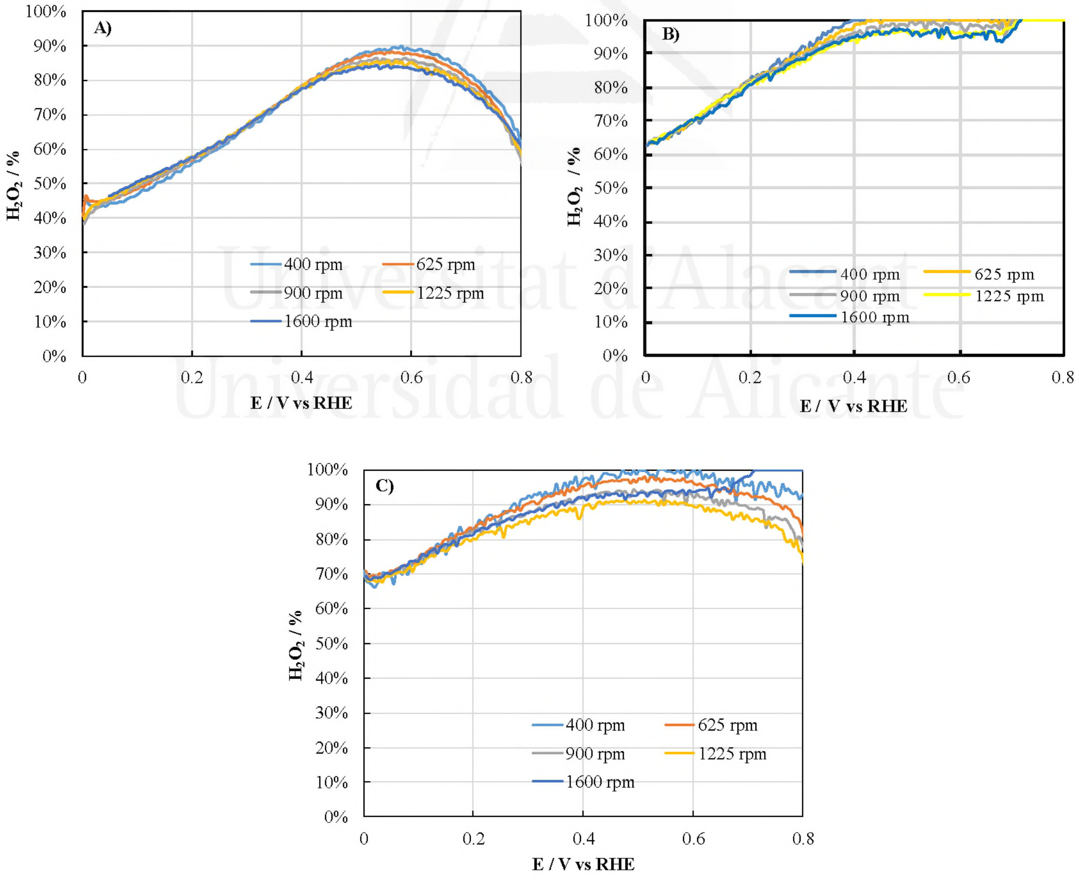

Figure 11. LSV profiles at different rotation rates in O_2-saturated 0.1 M KOH. A) KUA. B) CB. C) AC. Scan rate: 5 mV s^{-1}. Electrode loading: 0.40 mg cm^{-2}.

4-4-8, Effect of oxygen adsorption time

Seredych et al. recently proposed that the strong adsorption of oxygen in narrow micropores weakens the O-O bond, favoring the oxygen reduction to water via 4-electron pathway at less positive potentials [30]. These micropores are highly hydrophobic and it is claimed that they withdraw oxygen from the electrolyte that is later electrochemically reduced. Nevertheless, oxygen must diffuse through wider, wetted pores before reaching the narrower ones. The low mass transfer rate in wetted pores has been pointed out as the origin of the performance decay of microporous Me-N-C catalysts; as pores get flooded with water formed during ORR, oxygen change its diffusion mode from gaseous diffusion to liquid diffusion through the wetted pores, what results in a higher mass transfer resistance [12]. Therefore, a very low oxygen mass transfer rate is expectable. In this sense, we have checked if ORR activity is increased due to a higher local concentration of O_2 within the pores. For that purpose, Figure 12 compares the LSV ORR profile at 1600 rpm of KUA recorded right after a previous LSV experiment and after 12 hours of O_2 bubbling. If oxygen can be accumulated in narrow micropores, achieving a larger concentration than in the electrolyte, the additional adsorption time of 12 hours should render a higher reduction current. Contrarily, the LSV profiles for both experiments were observed to be fairly similar in the whole potential range, so either the oxygen concentration within narrow micropores is not playing a relevant effect, or all the active sites hosted in the micropores and that are active in ORR can be reached by oxygen in short times. Consequently, hydrogen peroxide reduction to water at micropores, rather than the direct oxygen reduction to water in narrow micropores, is considered to be the prevailing mechanism behind the improved ORR activity shown by porous carbon electrodes at less positive potentials.

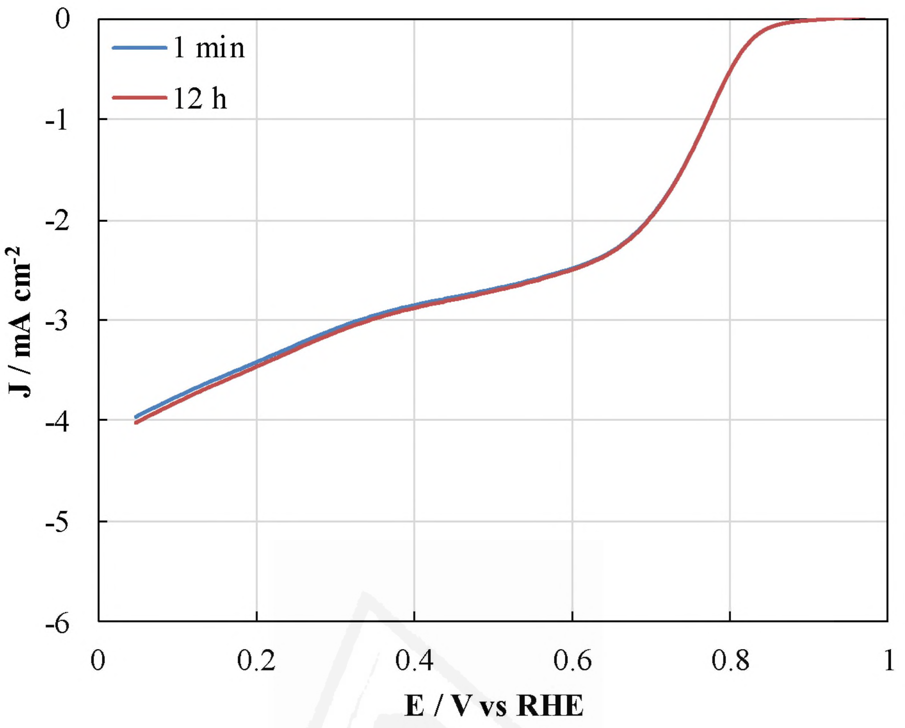

Figure 12. LSV profiles at 1600 rpm in O_2-saturated 0.1 M KOH. Scan rate: 5 mV s^{-1}. Electrode loading: 0.40 mg cm^{-2}.

4-4-9, Structural order and ORR activity

The higher ORR activity of microporous activated carbons has been studied in the past by Qu and it has been connected to their structural order parameters derived from XRD [31]. In the case of the porous carbon studied in this work, it is quite straightforward that the relationship between order-related parameters calculated from the XRD profiles, as those compiled in Table 1, and ORR activity is not found (i.e., see the well-defined and intense (002) peak of XC72 and the almost absent peak in KUA, Figure 3, whereas ORR activity is higher in KUA). Nonetheless, a higher concentration of edge sites is in general expectable in microporous activated carbons, so the identification of edge sites as an active site for ORR could be valid [2], and, in fact, it has been claimed elsewhere in the literature [9,21,49,52–54].

4-4-10, Modeling of ORR in porous carbon materials

Assuming that dioxygen reduction to hydroxide in undoped carbon materials occurs through consecutive two-electron reduction reactions, i) O_2 reduction to H_2O_2 and ii) H_2O_2 reduction to H_2O, and that the presence of micropores can have an influence in the residence time of the reactants and reaction products, we present a model to describe the ORR in porous carbons which is described as follows.

- The current registered at the disk during the RRDE measurements ($\boldsymbol{j_D^{ORR}}$, mA cm^{-2}) is produced by the electrochemical reduction of oxygen to hydrogen peroxide (2 e$^-$, $\boldsymbol{j_{O_2}}$) and the electrochemical reduction of hydrogen peroxide to hydroxide (2 e$^-$, $\boldsymbol{j_{H_2O_2}}$).

$$\boldsymbol{j_D^{ORR} = j_{O_2} + j_{H_2O_2}} \qquad \textbf{(3)}$$

- The effective number of electrons transferred (n) during ORR can be estimated from the ratio between the reduction currents of oxygen and hydrogen peroxide (i.e. when all the produced hydrogen peroxide is further reduced to hydroxide, the overall number of transferred electrons is 4):

$$\boldsymbol{n = 2 \cdot \left(1 + \frac{j_{H_2O_2}}{j_{O_2}}\right)} \qquad \textbf{(4)}$$

- The intrinsic electrochemical reaction rates for O_2 and H_2O_2 reduction (respectively denoted as $\boldsymbol{J_{O_2}^K}$ and $\boldsymbol{J_{H_2O_2}^K}$, mol cm^{-2} s^{-1}) are related to the disk current through the number of electrons transferred (2 e$^-$) and the Faraday constant, F (96485 C mol^{-1} e^{-1}):

$$\boldsymbol{j_D^{ORR} = j_{O_2} + j_{H_2O_2} = 2 \cdot F \cdot (J_{O_2}^K + J_{H_2O_2}^K)} \qquad \textbf{(5)}$$

- First order dependence with oxygen and hydrogen peroxide concentration in the porosity of the electrodes has been considered in the electrochemical reaction rate for these reactions, while the kinetic constant ($\boldsymbol{k_i^r}$) has been calculated following the Butler-Volmer model [35]:

$$\boldsymbol{J_i^K = k_i^r \cdot C_i^p = k_{0,i}^r \cdot exp(-\alpha_i \cdot f \cdot \eta) \cdot C_i^p} \qquad \textbf{(6)}$$

In this expression, $k_{0,i}^{r}$ is the charge transfer rate constant (cm·s^{-1}) for the reduction reaction of the *i* reagent (either O_2 or H_2O_2), α_i is the electron transfer coefficient, η is the overpotential applied to the electrode (V) and C_i^p stands for the concentration (mol·cm^{-3}) of the *i* reagent in the pores involved in the reduction reaction. Standard potentials of 1.17 V / vs NHE for ORR and 0.935 V / vs NHE for H_2O_2 reduction reaction at pH 13 have been considered for calculating the electrode overpotential. Furthermore, f stands for F/RT, where R is gas constant (8.314 J K^{-1} mol^{-1}) and T is the temperature of ORR experiment (25 ºC).

- Oxygen and hydrogen peroxide diffusion rate ($J_{O_2}^D$ and $J_{H_2O_2}^D$, respectively, mol cm^{-2} s^{-1}) from bulk solution to the porosity of the electrode has been considered for solving the mass balance and determining O_2 ($C_{O_2}^p$, mol cm^{-3}) and H_2O_2 ($C_{H_2O_2}^p$, mol cm^{-3}) concentration in the porosity of the electrodes. Diffusion molar fluxes have been defined using a linear driving force model:

$$\boldsymbol{J_{O_2}^D = \psi \cdot k_L^f \cdot \left(C_{O_2}^b - C_{O_2}^p\right)} \qquad \textbf{(7)}$$

$$\boldsymbol{J_{H_2O_2}^D = \psi \cdot k_{H_2O_2}^f \cdot \left(C_{H_2O_2}^p - C_{H_2O_2}^b\right)} \qquad \textbf{(8)}$$

In **Eqn. 8**, $k_{H_2O_2}^f$ is the effective mass transfer coefficient of H_2O_2 within the pores (cm s^{-1}). This equation can be understood as a film diffusion resistance, where $k_{H_2O_2}^f$ is taking the role of the ratio between the diffusion coefficient and the film thickness [35]. On the other hand, k_L^f is mass transfer coefficient of oxygen, having a value of 0.0125 cm s^{-1} for 1600 rpm, whereas ψ represents the ratio between the effective surface area and the geometrical surface area of the disk. Given the large volume of the cell, the low formation rate of hydrogen peroxide and the short analysis times, the bulk concentration of hydrogen peroxide, $C_{H_2O_2}^b$, can be considered negligible.

- The concentrations of the reagents are estimated from their mass balances assuming that quasi-equilibrium conditions are achieved:

$$J_{O_2}^{D} = J_{O_2}^{K} \therefore C_{O_2}^{P} = \frac{\psi \cdot k_L^f \cdot C_{O_2}^b}{\psi \cdot k_L^f + k_{O_2}^r} \qquad \textbf{(9)}$$

$$J_{O_2,p}^{K} = J_{H_2O_2}^{K} + J_{H_2O_2}^{D} \therefore C_{H_2O_2}^{p} = \frac{k_{O_2}^r \cdot C_{O_2}^p}{k_{H_2O_2}^r + \psi \cdot k_{H_2O_2}^f} \qquad \textbf{(10)}$$

- The model parameters are those defining the intrinsic reaction constants, i.e. k_{0,O_2}^r, $k_{0,H_2O_2}^r$, α_{O_2} and $\alpha_{H_2O_2}$, and those related with mass transfer rates, i.e. ψ and $k_{H_2O_2}^f$. However, a linear relationship was found between $\boldsymbol{k_{H_2O_2}^f}$ and $\boldsymbol{k_{0,H_2O_2}^r}$ what means that the same fitting can be reached by keeping constant the ratio between these parameters. The existence of this linear relationship is checked when **Eqn. 8** and **10** are combined. Therefore, the optimization parameters were cut down to five, being α_{O_2}, k_{0,O_2}^r, $k_{0,H_2O_2}^r / k_{H_2O_2}^f$, $\alpha_{H_2O_2}$ and ψ. These parameters are optimized in order to minimize the square difference between the experimentally measured current densities and those predicted by the model (**Eqn. 3**).

Figure 13 presents a graphical summary of the mathematical model herein proposed for estimating the ORR activity during RRDE experiments of porous carbon materials.

ORR Scheme

$$\begin{tikzcd}
C^b_{O_2} \arrow[r, leftrightarrow, "J^D_{O_2}"] & C^p_{O_2} \arrow[d, "J^K_{O_2}"] \\
C^b_{H_2O_2} \arrow[r, leftrightarrow, "J^D_{H_2O_2}"] & C^P_{H_2O_2} \arrow[d, "J^K_{H_2O_2}"] \\
 & C^p_{H_2O}
\end{tikzcd}$$

Reaction mechanism

$$O_2 + H_2O + 2e^- \xrightarrow{J^K_{O_2}} OH_2^- + OH^-$$

$$OH_2^- + H_2O + 2e^- \xrightarrow{J^K_{H_2O_2}} 3OH^-$$

Intrinsic electrochemical reaction and mass transfer rates

$$J^K_{O_2} = k^r_{0,O2} \cdot exp(-\alpha_{O2} \cdot f \cdot \eta_{O2}) \cdot C^p_{O_2}$$

$$J^K_{H_2O_2} = k^r_{0,H2O2} \cdot exp(-\alpha_{H2O2} \cdot f \cdot \eta_{H2O2}) \cdot C^P_{H_2O_2}$$

$$J^D_{O_2} = \psi \cdot k^f{}_L \cdot \left(C^b_{O_2} - C^p_{O_2}\right)$$

$$J^D_{H_2O_2} = \psi \cdot k^f_{H_2O_2} \cdot \left(C^p_{H_2O_2} - C^b_{H_2O_2}\right)$$

Mass balance

$$J^D_{O_2} = J^K_{O_2} \therefore C^p_{O_2} = \frac{\psi \cdot k^f_L \cdot C^b_{O_2}}{\psi \cdot k^f_L + k^r_{0,O2} \cdot exp(-\alpha_{O2} \cdot f \cdot \eta_{O2})}$$

$$J^K_{O_2} = J^D_{H_2O_2} + J^K_{H_2O_2} \therefore C^p_{H_2O_2} = \frac{k^r_{0,O2} \cdot exp(-\alpha_{O2} \cdot f \cdot \eta_{O2}) \cdot C^p_{O_2}}{\psi \cdot k^f_{H_2O_2} + k^r_{0,H2O2} \cdot exp(-\alpha_{H2O2} \cdot f \cdot \eta_{H2O2})}$$

Disk current and number of electrons for RDE ORR experiments

$$j^D_{ORR} = 2 \cdot \mathrm{F} \cdot (J^K_{O_2} + J^K_{H_2O_2})$$

$$n = 2 \cdot \left(1 + j_{H_2O_2}/j_{O_2}\right)$$

Figure 13. Scheme of the model proposed for the mathematical description of the ORR mechanism of porous carbon materials.

4-4-11, Application of the proposed model for predicting the ORR activity of porous carbon materials

The ORR model described in the previous section has been fitted to the LSV profiles at 1600 rpm of the porous carbon samples shown in Figure 8. Figure 14 compares the experimental data with the obtained theoretical curves, while Table 3 compiles the optimized model parameters obtained for each sample. After fitting the LSV curves, Figure 14 demonstrates that, in general, the model is able to reproduce the ORR activity of porous carbon materials in the RRDE system. The largest source of divergence is the number of electrons transferred at potentials higher than 0.5 V, where the negligible contribution of the H_2O_2 reduction reaction to the overall reduction current in the proposed model cannot explain a number of transferred electrons larger than 2. The presence of a very small fraction of active sites that are able to catalyze ORR to hydroxide through a 4-electron pathway in the surface of porous carbon materials could be responsible of such deviations.

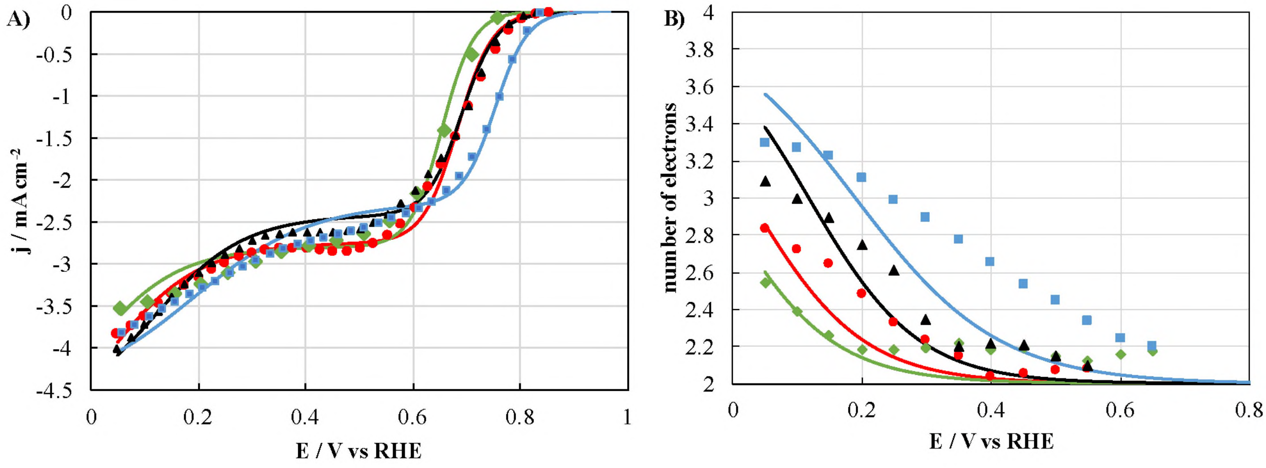

Figure 14. Experimental (dots) and modelled (lines) for A) LSV and B) number of transferred electrons profiles during ORR at 1600 rpm in 0.1 M KOH. KUA (blue), AC (red), CB (black) and XC72 (green). Scan rate: 5 mV s^{-1}.

Table 3. Optimized model parameters.

Parameter	**KUA**	**AC**	**CB**	**XC72**
ψ	0.78	0.95	0.83	0.97
α_{O_2}	0.85	0.79	0.80	0.87
k^r_{0,O_2} (cm s^{-1})	11.1·10^{-9}	3.8·10^{-9}	3.7·10^{-9}	0.3·10^{-9}
$\alpha_{H_2O_2}$	0.23	0.29	0.30	0.30
$k^r_{0,H_2O_2}/k^f_{H_2O_2}$	90.4·10^{-5}	2.7·10^{-5}	5.2·10^{-5}	1.3·10^{-5}

Tafel analyses have been performed for the LSV curves in the vicinity of the kinetically controlled region in order to calculate the kinetic parameters for the oxygen reduction reaction to hydrogen peroxide. These constants have been calculated from Eqn. 5 and 6 assuming that the oxygen concentration in the pores, C^p_{O2}, is the same than in the bulk of the solution, and it remains constant. The Tafel plots are shown in Figure 15A. α_{O2} is estimated from the slope of the linear region of the curves, being 0.82, 0.78, 0.86 and 0.89 for KUA, AC, CB and, XC72 respectively, while k^r_{0,O_2} values of 10·10^{-9}, 7.1·10^{-9}, 1.4·10^{-9} and 0.25·10^{-9} cm s^{-1} are determined from the Y-intercept for the same set of samples. The kinetic parameters obtained from Tafel analyses and the least square fitting of the proposed model are comparable, exception made of CB. $\boldsymbol{\alpha_{O2}}$ and the slope of the first-wave on LSV are positively related. The proposed model delivers a lower $\boldsymbol{\alpha_{O2}}$value for CB due to the decrease on the LSV slope ca. 0.6 V, Figure 14, a potential region that is outside the range of data covered by the Tafel analysis (0.7-0.8V). Tafel slope of KUA, AC, CB and, XC72 are similar values (around 45-50 mV decade^{-1}) reported in previous investigations for carbon material electrodes [28].

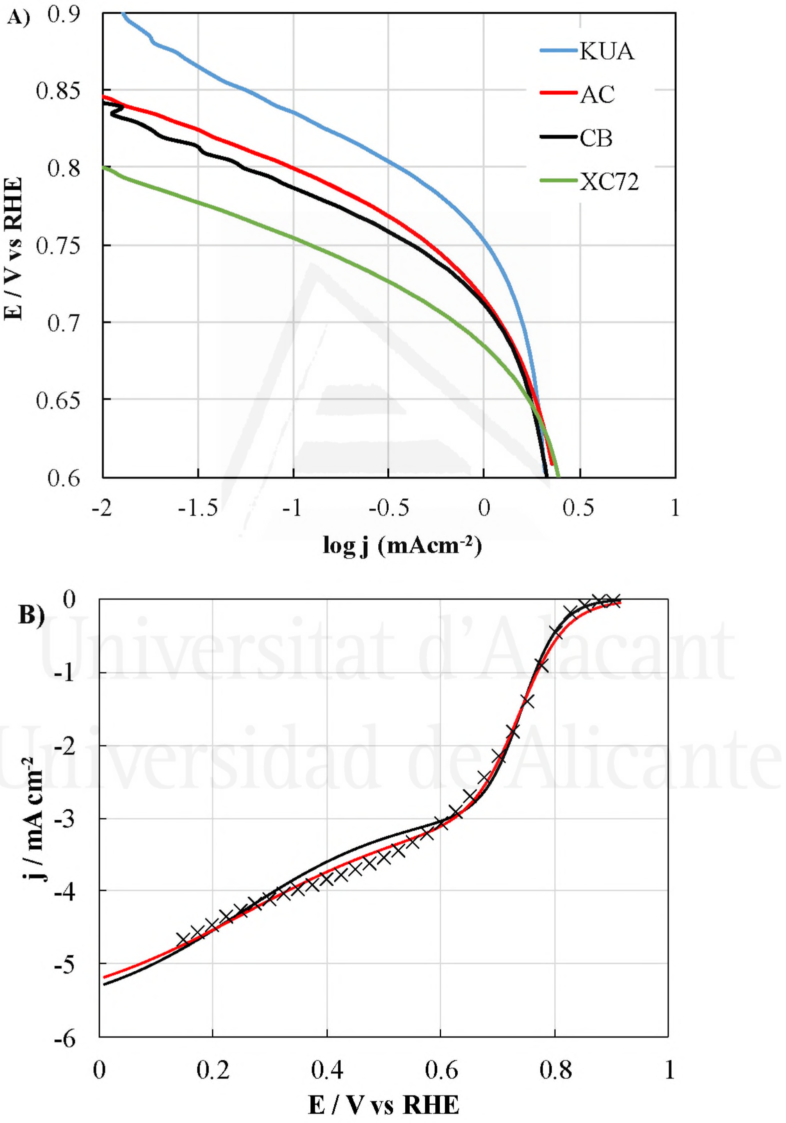

Figure 15. A) Log(j) vs E curves for the analyzed samples. **B)** LSV Experimental (dots) and modelled (lines) for KUA using a loading of 1.00 mg cm^{-2}. Black line has been modelled fixing the $\boldsymbol{\alpha_{O_2}}$ and $\boldsymbol{\alpha_{H_2O_2}}$values obtained for a KUA loading of 0.4 mg cm^{-2}, red line has been calculated by including these values as model parameters. Rotating rate: 1600 rpm. Scan rate: 5 mV s^{-1}.

The parameter ψ (which is proportional to the effective surface area) follows the order XC72 > AC > CB > KUA. No clear relationship can be made with textural parameters derived from the N_2 adsorption isotherms. This can be explained by the different sizes of the micro and mesoporosity of the samples, that are defined in the range of a few to several nanometers, and that of the diffusion layer, which is expected to show a thickness in the range of several micrometers. Therefore, on the scale of the diffusion layer, the electrode can be considered as flat [34]. Effective surface areas lower than 1 can reflect that the surface of the disk is not fully covered for some of the samples. A similar argument has been provided for RRDE involving electrocatalytic nanoparticles [45,48]. The effective surface area of the electrodes can be also affected by the amount of Nafion® in the thin film or the particle distribution on top of the surface of the disk [55]. Nevertheless, samples XC72, with the lowest micropore volume, and KUA, with the highest micropore volume, have the highest and the lowest ψ parameter, respectively. This is in agreement with the expected higher mass transfer limitations in highly microporous materials.

Interestingly, the charge transfer rate constants, k_{0,O_2}^{r}, seem to be linearly connected to the N_2 micropore volume of the samples (Figure 16A). A similar good agreement has been found between k_{0,O_2}^{r} and S_{BET}. However, the value of mesopore volume is unconnected to k_{0,O_2}^{r}. All these findings proof that the higher amount of ORR actives sites are present in micropores.

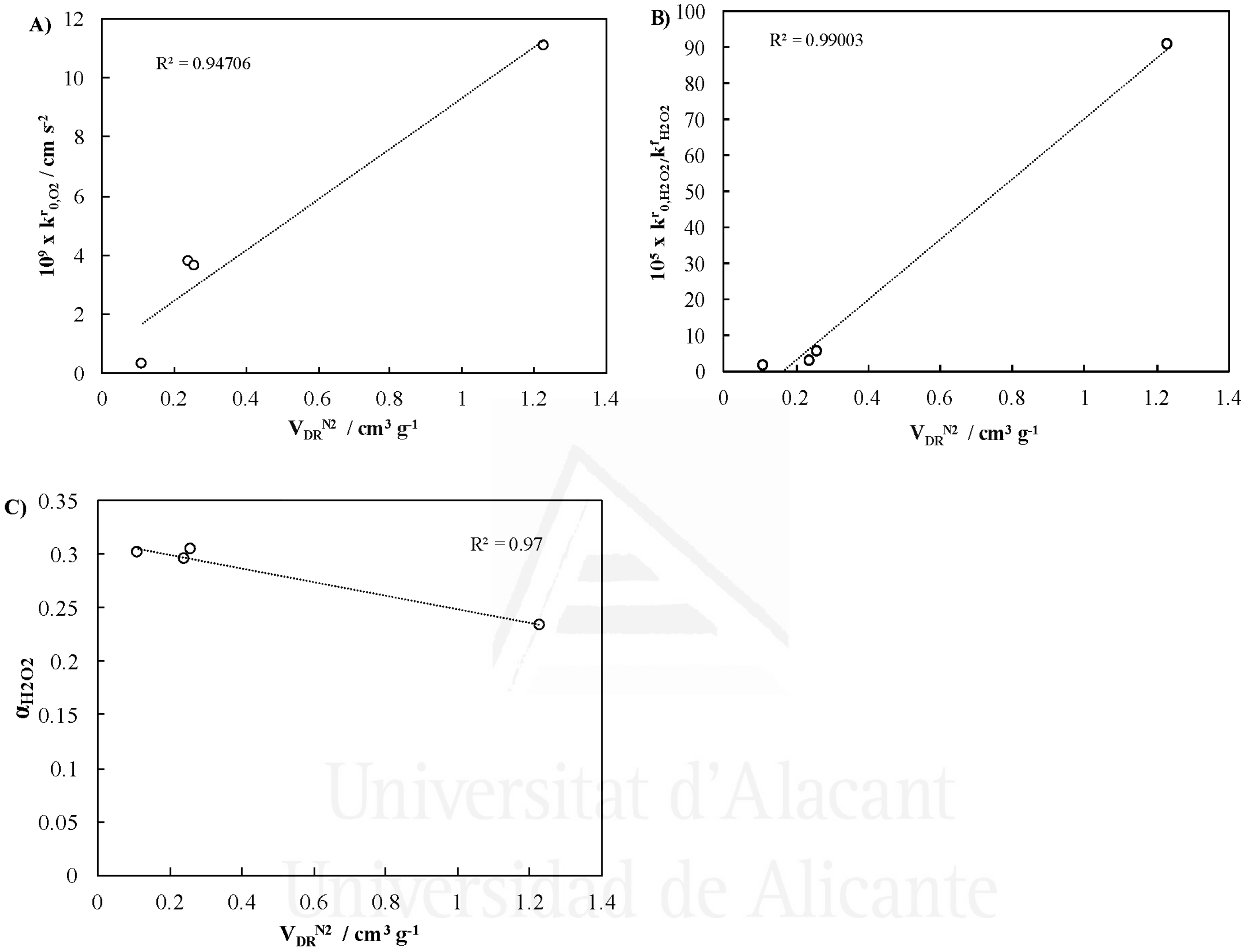

Figure 16. Relationships between V_{DR}^{N2} and different model parameters **A)** k^r_{0,O_2}. **B)** $k^r_{0,H_2O_2}/k^f_{H_2O_2}$ and **C)** $\alpha_{H_2O_2}$.

As for the kinetic parameters of H_2O_2 reduction reaction, it has not been possible to deliver a constant value of $\alpha_{H_2O_2}$for all the samples while keeping accurate description of the experimental curves. This is a consequence of the very different slopes of the second wave of the LSVs, as observed in Figure 14 and also in the H_2O_2 RRDE experiments compiled in Figure 10. The highest $\alpha_{H_2O_2}$ value has been recorded for CB, while KUA shows the lowest one. The electron transfer coefficient values are low compared to α_{O_2}. A similar value has been recently found for the electrocatalytic reduction of hydrogen peroxide on dispersed gold nanoparticles [56]. The low activity of undoped carbon materials towards H_2O_2 electrochemical reduction is known from a long time, and it is beneficial for the preparation of electrodes selective to the formation of hydrogen peroxide from ORR [50]. In the case of $\boldsymbol{k^r_{0,H_2O_2}/k^f_{H_2O_2}}$, although linear trends with mesopore volume or external to internal volumes ratios (V_{DR}^{N2}/V_{mes}) have been tried, the best correlation is found for V_{DR}^{N2}, Figure 16B. The low value of the electron transfer coefficient along with the positive relationship between $\boldsymbol{k^r_{0,H_2O_2}/k^f_{H_2O_2}}$ and micropore volume could be reflecting that the reaction is taking place within the microporosity, where additional charge transfer resistance could be found. In this sense, a clear negative trend is attained when $\alpha_{H_2O_2}$ is plotted vs V_{DR}^{N2}, Figure 16C.

Finally, the LSV curve of KUA using a loading of 1.00 mg cm^{-2} has also been fitted to the proposed model, Figure 15B. The charge transfer rates should include the weight of the catalysts loaded on the electrode. In consequence, the model was first applied fixing the $\boldsymbol{\alpha}$ values compiled in Table 3 for KUA, while the charge transfer rate constants and ψ were fitted, achieving values of $\boldsymbol{k^r_{0,O_2}}$=11.0·10^{-9} cm s^{-1} and $\boldsymbol{k^r_{0,H_2O_2}/k^f_{H_2O_2}}$=199·10^{-5} and $\boldsymbol{\psi}$ =0.99. Effective surface area is now close to one, what is explained by the surface of the disk of the electrode being fully covered by the carbon sample. As for the charge transfer rates, neither of them increased 2.5 times, as was expected. $\boldsymbol{k^r_{0,O_2}}$ is found to be independent of loading, while the hydrogen peroxide charge transfer to mass transfer ratio is increased ca. 110% when the electrode loading is doubled, indicating that more active sites for H_2O_2 reduction are available within the electrode film. When the electron transfer coefficients are also included in the fitting (red line in Figure 15B), the sum of the least square root differences is reduced (ie a more accurate description of the curve is obtained), and both coefficients are lowered, α_{O_2}=0.62, $\alpha_{H_2O_2}$= 0.15, what could be indicating that the electrode resistance is increased with the electrode loading, worsening the charge propagation. In view of the above findings, further experiments and more complex description of the electrode system is required for providing a more accurate description of the effect of the electrode loading.

Once the model has been verified, it can be also useful as a tool to analyze the effect of each parameter on the ORR activity of porous carbon materials. In this sense, all the model parameters that describes KUA activity have been varied one by one and the outcomes are plotted in Figure 17. In first place, the effect of the effective to geometrical surface area factor on the RDE has been studied. The value of this parameter is directly related to the plateau current achieved at the end of the first wave of the LSV process, Figure 17A. In a rough approximation, it is identified as the ratio between this current value and the theoretical Levich limiting current for a 2-electron process. This parameter has a negligible impact on the number of transferred electrons (i.e. n decreases from 2.94 to 2.85 when ψ is increased from 0.78 to 1.00 as consequence of the higher H_2O_2 diffusional flow rate, Eqn. 8, leaving the electrode).

Regarding the effect of the oxygen reduction reaction kinetic parameters, Figure 17B, it can be seen that electron transfer coefficient has a higher impact on the onset potential than the charge transfer rate constant. Thus, five-fold increase of the latter parameter produces a lower positive shifting of the onset potential than just a 20% increase of the former one. Similar decreases of both parameters deliver a more negative impact in the case of electron transfer coefficient (onset potential drops to 0.775 V). No effect in the number of transferred electrons is expected at this point, since this number is only ruled by the ratio of the intrinsic reduction rate to diffusion mass transfer rate of hydrogen peroxide.

In the case of the hydrogen peroxide reduction reaction, the specific current of the second wave, (Figure 17 C, E) or the number of electrons (Figure 17D, F) are greatly affected by both the electron transfer coefficient and the $\boldsymbol{k^{r}_{0,H_2O_2}/k^{f}_{H_2O_2}}$ ratio (referred as R^{H2O2}). An improvement in the charge transfer rate seems to be the most effective way to enhance the ORR activity of the porous carbon material at high and medium potentials (which is the most desirable feature from the applied point of view), Figure 17C, while the electron transfer coefficient reduces the transition region and allows reaching full 4-electron pathway at low potentials, Figure 17F.

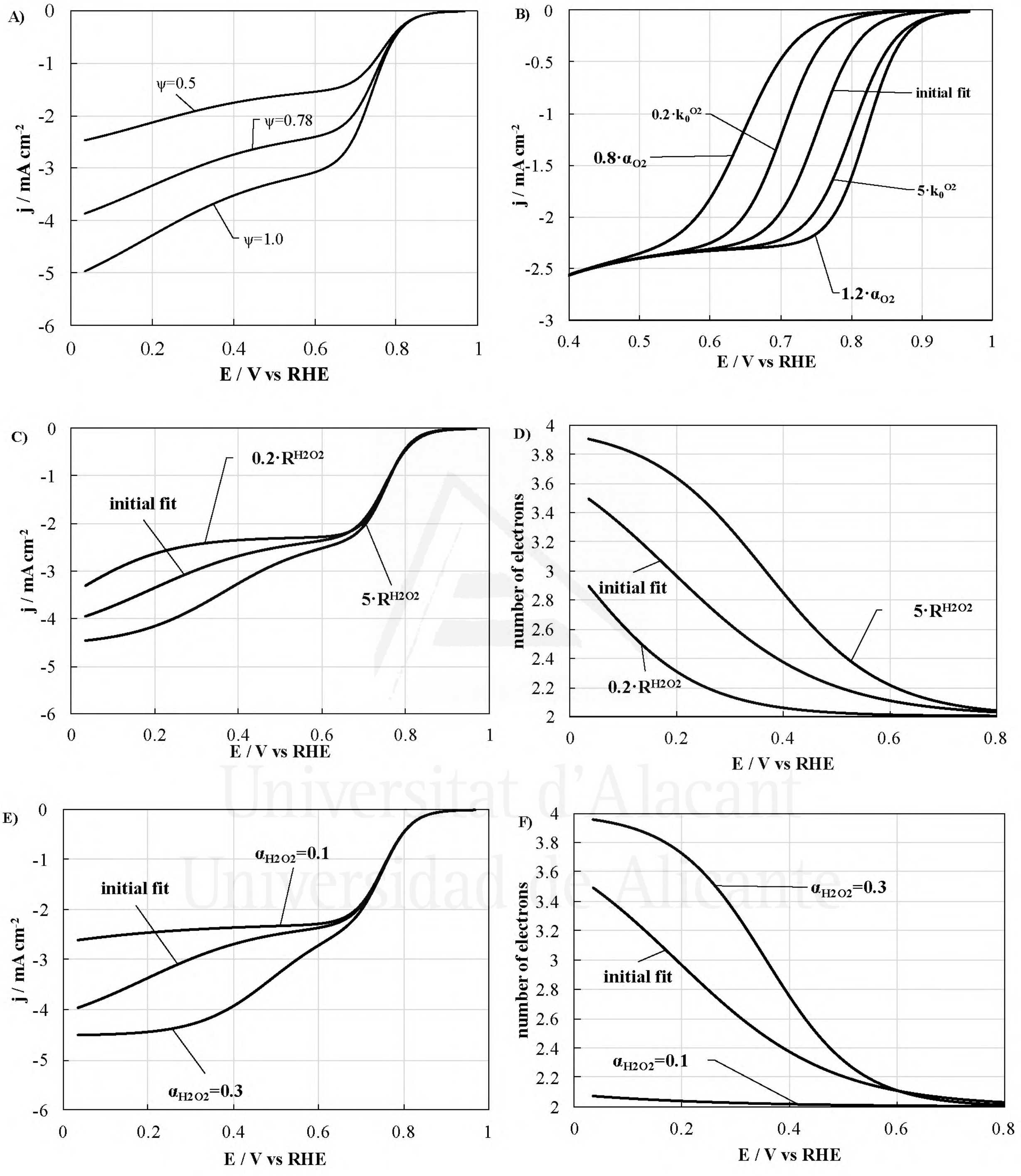

Figure 17. A) Effect of effective to geometric surface area factor and B) kinetic parameters related to oxygen reduction reaction on the simulated ORR behavior of KUA. C, D) Effects of kinetic to mass transfer constants ratio and E, F) electron transfer coefficient of the hydrogen peroxide reduction reaction on the ORR behavior of KUA.

4-5, Conclusions

The activity of porous carbon materials in the oxygen reduction reaction in alkaline media, and in absence of any additional catalyst, is undoubtedly related to their porosity. By fully characterizing carbon materials with different pore size distribution and pore structure, we have been able to demonstrate that the ORR is accurately described by a two-wave process, where oxygen is reduced to hydrogen peroxide in a first step at intermediate potentials, while hydrogen peroxide is subsequently reduced to hydroxide at low potentials. The combination of both reactions rises the number of transferred electrons rise to intermediate values between 2 and 4.

Interestingly, the onset potentials for both reactions seems to be related to the presence of a well-developed microporosity. ORR experiments in RDE have confirmed that microporosity is certainly correlated to a high activity in this reaction, and that the presence of H_2O_2 does not interfere in the rate of the oxygen reduction reaction. In addition, ORR experiments performed with different loadings demonstrated that the amount of sample has a critical impact on the ORR activity of highly microporous materials.

A mathematical model that describes the reaction rate and number of electrons transferred during ORR and that takes into account the O_2 and H_2O_2 mass transfer rate and two consecutive reduction reactions, has been derived from the proposed mechanism. The model has provided a successful description of the ORR activity of porous carbon electrodes, verifying the claims about the importance of microporosity on the reduction of dioxygen and hydrogen peroxide. This work can be a guideline for the proper analysis of ORR activity of new catalysts based on carbon materials, where the effect of porosity is frequently omitted.

4-6, References

[1] P. Trogadas, T.F. Fuller, P. Strasser, Carbon as catalyst and support for electrochemical energy conversion, Carbon. 75 (2014) 5–42. doi:10.1016/j.carbon.2014.04.005.

[2] L.R. Radovic, Surface Chemical and Electrochemical Properties of Carbons, in: F. Beguin, E. Frackowiak (Eds.), Carbons Electrochem. Energy Storage Convers. Syst., Taylor & Francis (CRC Press), Boca Raton, FL, 2010: pp. 163–219.

[3] A.L. Dicks, The role of carbon in fuel cells, J. Power Sources. 156 (2006) 128–141. doi:10.1016/j.jpowsour.2006.02.054.

[4] F. Jaouen, E. Proietti, M. Lefèvre, R. Chenitz, J.-P. Dodelet, G. Wu, H.T. Chung, C.M. Johnston, P. Zelenay, Recent advances in non-precious metal catalysis for oxygen-reduction reaction in polymer electrolyte fuel cells, Energy Environ. Sci. 4 (2010) 114–130. doi:10.1039/C0EE00011F.

[5] L. Dai, Y. Xue, L. Qu, H.-J. Choi, J.-B. Baek, Metal-Free Catalysts for Oxygen Reduction Reaction, Chem. Rev. 115 (2015) 4823–4892. doi:10.1021/cr5003563.

[6] A. Morozan, B. Jousselme, S. Palacin, Low-platinum and platinum-free catalysts for the oxygen reduction reaction at fuel cell cathodes, Energy Environ. Sci. 4 (2011) 1238–1254. doi:10.1039/C0EE00601G.

[7] Y. Nie, L. Li, Z. Wei, Recent advancements in Pt and Pt-free catalysts for oxygen reduction reaction, Chem. Soc. Rev. 44 (2015) 2168–2201. doi:10.1039/C4CS00484A.

[8] C. Tamain, S.D. Poynton, R.C.T. Slade, B. Carroll, J.R. Varcoe, Development of Cathode Architectures Customized for H_2/O_2 Metal-Cation-Free Alkaline Membrane Fuel Cells, J. Phys. Chem. C. 111 (2007) 18423–18430. doi:10.1021/jp076740c.

[9] M. Gara, R.G. Compton, Activity of carbon electrodes towards oxygen reduction in acid: A comparative study, New J. Chem. 35 (2011) 2647. doi:10.1039/c1nj20612e.

[10] H.-H. Yang, R.L. McCreery, Elucidation of the Mechanism of Dioxygen Reduction on Metal-Free Carbon Electrodes, J. Electrochem. Soc. 147 (2000) 3420–3428. doi:10.1149/1.1393915.

[11] T. Ikeda, M. Boero, S.F. Huang, K. Terakura, M. Oshima, J. Ozaki, Carbon alloy catalysts: Active sites for oxygen reduction reaction, J. Phys. Chem. C. 112 (2008) 14706–14709. doi:10.1021/jp806084d.

[12] M. Shao, Q. Chang, J.-P. Dodelet, R. Chenitz, Recent Advances in Electrocatalysts for Oxygen Reduction Reaction, Chem. Rev. 116 (2016) 3594–3657. doi:10.1021/acs.chemrev.5b00462.

[13] J. Quílez-Bermejo, C. González-Gaitán, E. Morallón, D. Cazorla-Amorós, Effect of carbonization conditions of polyaniline on its catalytic activity towards ORR. Some insights about the nature of the active sites, Carbon. 119 (2017) 62–71.

doi:10.1016/j.carbon.2017.04.015.

[14] A. Gabe, J. García-Aguilar, Á. Berenguer-Murcia, E. Morallón, D. Cazorla-Amorós, Key factors improving oxygen reduction reaction activity in cobalt nanoparticles modified carbon nanotubes, Appl. Catal. B Environ. 217 (2017) 303–312. doi:10.1016/j.apcatb.2017.05.096.

[15] T. Sharifi, G. Hu, X. Jia, T. Wågberg, Formation of active sites for oxygen reduction reactions by transformation of nitrogen functionalities in nitrogen-doped carbon nanotubes, ACS Nano. 6 (2012) 8904–8912. doi:10.1021/nn302906r.

[16] G.-L. Chai, Z. Hou, D.-J. Shu, T. Ikeda, K. Terakura, Active Sites and Mechanisms for Oxygen Reduction Reaction on Nitrogen-Doped Carbon Alloy Catalysts: Stone–Wales Defect and Curvature Effect, J. Am. Chem. Soc. 136 (2014) 13629–13640. doi:10.1021/ja502646c.

[17] C.V. Rao, C.R. Cabrera, Y. Ishikawa, In Search of the Active Site in Nitrogen-Doped Carbon Nanotube Electrodes for the Oxygen Reduction Reaction, J. Phys. Chem. Lett. 1 (2010) 2622–2627. doi:10.1021/jz100971v.

[18] L. Zhang, Z. Xia, Mechanisms of Oxygen Reduction Reaction on Nitrogen-Doped Graphene for Fuel Cells, J. Phys. Chem. C. 115 (2011) 11170–11176. doi:10.1021/jp201991j.

[19] R. Chen, H. Li, D. Chu, G. Wang, Unraveling Oxygen Reduction Reaction Mechanisms on Carbon-Supported Fe-Phthalocyanine and Co-Phthalocyanine Catalysts in Alkaline Solutions, J. Phys. Chem. C. 113 (2009) 20689–20697. doi:10.1021/jp906408y.

[20] U. Tylus, Q. Jia, K. Strickland, N. Ramaswamy, A. Serov, P. Atanassov, S. Mukerjee, Elucidating Oxygen Reduction Active Sites in Pyrolyzed Metal–Nitrogen Coordinated Non-Precious-Metal Electrocatalyst Systems, J. Phys. Chem. C. 118 (2014) 8999–9008. doi:10.1021/jp500781v.

[21] K. Waki, R.A. Wong, H.S. Oktaviano, T. Fujio, T. Nagai, K. Kimoto, K. Yamada, Non-nitrogen doped and non-metal oxygen reduction electrocatalysts based on carbon nanotubes: mechanism and origin of ORR activity, Energy Environ. Sci. 7 (2014) 1950–1958. doi:10.1039/C3EE43743D.

[22] C. Domínguez, F.J. Pérez-Alonso, M. Abdel Salam, S.A. Al-Thabaiti, A.Y. Obaid, A.A. Alshehri, J.L. Gómez de la Fuente, J.L.G. Fierro, S. Rojas, On the relationship between N content, textural properties and catalytic performance for

the oxygen reduction reaction of N/CNT, Appl. Catal. B Environ. 162 (2015) 420–429. doi:10.1016/j.apcatb.2014.07.002.

[23] G.A. Ferrero, K. Preuss, A.B. Fuertes, M. Sevilla, M.-M. Titirici, The influence of pore size distribution on the oxygen reduction reaction performance in nitrogen doped carbon microspheres, J. Mater. Chem. A. 4 (2016) 2581–2589. doi:10.1039/C5TA10063A.

[24] J. Park, Y. Nabae, T. Hayakawa, M. Kakimoto, Highly Selective Two-Electron Oxygen Reduction Catalyzed by Mesoporous Nitrogen-Doped Carbon, ACS Catal. 4 (2014) 3749–3754. doi:10.1021/cs5008206.

[25] J. Maruyama, K.I. Sumino, M. Kawaguchi, I. Abe, Influence of activated carbon pore structure on oxygen reduction at catalyst layers supported on rotating disk electrodes, Carbon. 42 (2004) 3115–3121. doi:10.1016/j.carbon.2004.07.023.

[26] F. Jaouen, M. Lefèvre, J.-P. Dodelet, M. Cai, Heat-Treated Fe/N/C Catalysts for O_2 Electroreduction: Are Active Sites Hosted in Micropores?, J. Phys. Chem. B. 110 (2006) 5553–5558. doi:10.1021/jp057135h.

[27] M. Lefèvre, E. Proietti, F. Jaouen, J.-P. Dodelet, Iron-Based Catalysts with Improved Oxygen Reduction Activity in Polymer Electrolyte Fuel Cells, Science (80-.). 324 (2009) 71–74. doi:10.1126/science.1170051.

[28] A.J. Appleby, J. Marie, Kinetics of oxygen reduction on carbon materials in alkaline solution, Electrochim. Acta. 24 (1979) 195–202. doi:10.1016/0013-4686(79)80024-9.

[29] Y. Liu, K. Li, B. Ge, L. Pu, Z. Liu, Influence of Micropore and Mesoporous in Activated Carbon Air-cathode Catalysts on Oxygen Reduction Reaction in Microbial Fuel Cells, Electrochim. Acta. 214 (2016) 110–118. doi:10.1016/j.electacta.2016.08.034.

[30] M. Seredych, A. Szczurek, V. Fierro, A. Celzard, T.J. Bandosz, Electrochemical Reduction of Oxygen on Hydrophobic Ultramicroporous PolyHIPE Carbon, ACS Catal. 6 (2016) 5618–5628. doi:10.1021/acscatal.6b01497.

[31] D. Qu, Investigation of oxygen reduction on activated carbon electrodes in alkaline solution, Carbon. 45 (2007) 1296–1301. doi:10.1016/j.carbon.2007.01.013.

[32] M.A. Lillo-Ródenas, D. Lozano-Castelló, D. Cazorla-Amorós, A. Linares-Solano, Preparation of activated carbons from Spanish anthracite - II. Activation by NaOH, Carbon. 39 (2001) 751–759. doi:10.1016/S0008-6223(00)00186-X.

[33] J. Jagiello, J.P. Olivier, 2D-NLDFT adsorption models for carbon slit-shaped pores with surface energetical heterogeneity and geometrical corrugation, Carbon. 55 (2013) 70–80.

[34] A.J. Bard, L.R. Faulkner, Electrochemical Methods: Fundamentals and Applications, 2a., Wiley, 2001.

[35] M. Thommes, K. Kaneko, A. V. Neimark, J.P. Olivier, F. Rodriguez-Reinoso, J. Rouquerol, K.S.W. Sing, Physisorption of gases, with special reference to the evaluation of surface area and pore size distribution (IUPAC Technical Report), Pure Appl. Chem. 87 (2015) 1051–1069. doi:10.1515/pac-2014-1117.

[36] M.A. Lillo-Ródenas, D. Cazorla-Amorós, A. Linares-Solano, Understanding chemical reactions between carbons and NaOH and KOH: An insight into the chemical activation mechanism, Carbon. 41 (2003) 267–275. doi:10.1016/S0008-6223(02)00279-8.

[37] F. Zaragoza-Martín, D. Sopeña-Escario, E. Morallón, C.S.-M. de Lecea, Pt/carbon nanofibers electrocatalysts for fuel cells, J. Power Sources. 171 (2007) 302–309. doi:10.1016/j.jpowsour.2007.06.078.

[38] D. Lozano-Castelló, D. Cazorla-Amorós, A. Linares-Solano, Usefulness of CO_2 adsorption at 273 K for the characterization of porous carbons, Carbon. 42 (2004) 1233–1242. doi:10.1016/j.carbon.2004.01.037.

[39] D. Cazorla-Amorós, J. Alcañiz-Monge, M.A. de la Casa-Lillo, A. Linares-Solano, CO_2 As an Adsorptive To Characterize Carbon Molecular Sieves and Activated Carbons, Langmuir. 14 (1998) 4589–4596. doi:10.1021/la980198p.

[40] M.A. Short, P.L. Walker, Measurement of interlayer spacings and crystal sizes in turbostratic carbons, Carbon. 1 (1963) 3–9. doi:http://dx.doi.org/10.1016/0008-6223(63)90003-4.

[41] M.C. Román-Martínez, D. Cazorla-Amorós, A. Linares-Solano, C.S.-M. de Lecea, Tpd and TPR characterization of carbonaceous supports and Pt/C catalysts, Carbon. 31 (1993) 895–902. doi:10.1016/0008-6223(93)90190-L.

[42] J.L. Figueiredo, M.F.R. Pereira, M.M.A. Freitas, J.J.M. Órfão, Modification of the surface chemistry of activated carbons, Carbon. 37 (1999) 1379–1389. doi:10.1016/S0008-6223(98)00333-9.

[43] K.J.J. Mayrhofer, D. Strmcnik, B.B. Blizanac, V. Stamenkovic, M. Arenz, N.M. Markovic, Measurement of oxygen reduction activities via the rotating disc

electrode method: From Pt model surfaces to carbon-supported high surface area catalysts, Electrochim. Acta. 53 (2008) 3181–3188. doi:10.1016/j.electacta.2007.11.057.

[44] U.A. Paulus, T.J. Schmidt, H.A. Gasteiger, R.J. Behm, Oxygen reduction on a high-surface area Pt/Vulcan carbon catalyst: A thin-film rotating ring-disk electrode study, J. Electroanal. Chem. 495 (2001) 134–145. doi:10.1016/S0022-0728(00)00407-1.

[45] J. Masa, C. Batchelor-McAuley, W. Schuhmann, R.G. Compton, Koutecky-Levich analysis applied to nanoparticle modified rotating disk electrodes: Electrocatalysis or misinterpretation, Nano Res. 7 (2014) 71–78. doi:10.1007/s12274-013-0372-0.

[46] A. Bonakdarpour, M. Lefevre, R. Yang, F. Jaouen, T. Dahn, J.-P. Dodelet, J.R. Dahn, Impact of Loading in RRDE Experiments on Fe–N–C Catalysts: Two- or Four-Electron Oxygen Reduction?, Electrochem. Solid-State Lett. 11 (2008) B105. doi:10.1149/1.2904768.

[47] M. Gara, K.R. Ward, R.G. Compton, Nanomaterial modified electrodes: evaluating oxygen reduction catalysts., Nanoscale. 5 (2013) 7304–11. doi:10.1039/c3nr01940c.

[48] K.R. Ward, M. Gara, N.S. Lawrence, R.S. Hartshorne, R.G. Compton, Nanoparticle modified electrodes can show an apparent increase in electrode kinetics due solely to altered surface geometry: The effective electrochemical rate constant for non-flat and non-uniform electrode surfaces, J. Electroanal. Chem. 695 (2013) 1–9. doi:10.1016/j.jelechem.2013.02.012.

[49] N.P. Subramanian, X. Li, V. Nallathambi, S.P. Kumaraguru, H. Colon-Mercado, G. Wu, J.W. Lee, B.N. Popov, Nitrogen-modified carbon-based catalysts for oxygen reduction reaction in polymer electrolyte membrane fuel cells, J. Power Sources. 188 (2009) 38–44. doi:10.1016/j.jpowsour.2008.11.087.

[50] G. Coria, T. Pérez, I. Sirés, J.L. Nava, Mass transport studies during dissolved oxygen reduction to hydrogen peroxide in a filter-press electrolyzer using graphite felt, reticulated vitreous carbon and boron-doped diamond as cathodes, J. Electroanal. Chem. 757 (2015) 225–229. doi:10.1016/j.jelechem.2015.09.031.

[51] R. Zhou, Y. Zheng, M. Jaroniec, S.-Z. Qiao, Determination of the Electron Transfer Number for the Oxygen Reduction Reaction: From Theory to Experiment, ACS Catal. 6 (2016) 4720–4728. doi:10.1021/acscatal.6b01581.

[52] P.H. Matter, U.S. Ozkan, Non-metal catalysts for dioxygen reduction in an acidic electrolyte, Catal. Letters. 109 (2006) 115–123. doi:10.1007/s10562-006-0067-1.

[53] P.H. Matter, L. Zhang, U.S. Ozkan, The role of nanostructure in nitrogen-containing carbon catalysts for the oxygen reduction reaction, J. Catal. 239 (2006) 83–96. doi:10.1016/j.jcat.2006.01.022.

[54] X. Chu, K. Kinoshita, Surface modification of carbons for enhanced electrochemical activity, Mater. Sci. Eng. B. 49 (1997) 53–60. doi:10.1016/S0921-5107(97)00100-1.

[55] Y. Garsany, I.L. Singer, K.E. Swider-Lyons, Impact of film drying procedures on RDE characterization of Pt/VC electrocatalysts, J. Electroanal. Chem. 662 (2011) 396–406. doi:10.1016/j.jelechem.2011.09.016.

[56] J.S. Jirkovský, M. Halasa, D.J. Schiffrin, Kinetics of electrocatalytic reduction of oxygen and hydrogen peroxide on dispersed gold nanoparticles, Phys. Chem. Chem. Phys. 12 (2010) 8042–8053. doi:10.1039/C002416C.

Chapter 5.

Key factors improving oxygen reduction reaction activity in cobalt nanoparticles modified carbon nanotubes.

5-1, Introduction

Fuel cells (FCs) are electrochemical devices which transform directly the heat of combustion of a fuel (hydrogen, natural gas, methanol, ethanol, hydrocarbons, etc.) into electricity. The fuel is oxidized electrochemically at the anode, without producing any pollutants (only water and/or carbon dioxide are rejected in the atmosphere), whereas the oxidant (oxygen from the air) is reduced at the cathode. For instance, Alkaline Fuel Cells (AFCs) work with pure hydrogen and oxygen from room temperature to 80°C. Alkaline electrolytes such as KOH used in AFCs (usually in concentrations of 30–45 wt. %) have an advantage over acidic fuel cells, i.e., the oxygen reduction kinetics is much faster than in acidic media [1]. The power output and lifetime of FCs are directly linked to the behavior of the cathode, where most of the polarization losses occur, because the oxygen reduction reaction (ORR) is a slow reaction compared to the hydrogen oxidation at the anode. As a consequence, cathode development requires special attention to find the best catalyst and electrode structure to combine performance and stability [2,3]. Platinum (Pt) is the most commonly used and active electrocatalyst for the ORR and all of the Pt-group metals reduce oxygen in alkaline media according to the direct 4-electron process [3]. However, their large-scale commercial application has been precluded due to high cost of Pt. In addition, the Pt-based electrodes suffer from low selectivity to ORR in the presence of other reactions (e.g., methanol oxidation derived from fuel crossover in FCs) and CO deactivation [2,4–6].

In contrast, the inherently faster kinetics of the ORR in alkaline media permits the use of non-noble metal catalysts as cathode electrodes [7,8]. In this sense, a wide range of catalysts including non-noble metals has been explored to replace the Pt-based cathode catalyst [3]. Indeed, metal-free heteroatom-doped carbon materials (N, S, P, B and F), transition metal oxides (e.g., CoO, Co_3O_4, Cu_2O, MnO_2) and metal nitrogen complexes (Co-N_x, Fe-N_x) on carbon nanomaterials can be promising candidates as non-precious metal catalysts [9–12].

Although transition metal oxides can be good materials for this application, unsupported metal oxide particles do not show a good performance at more negative potentials due to the poor transfer of substrate (O_2) and products (H_2O) [13], making necessary the synthesis of nanoparticles (NPs) supported on an adequate support like carbon materials. Carbon materials or nanomaterials are useful supports for non-noble metal-based systems, especially for those with low electrical conductivity. Furthermore, the carbon support can provide paths for the flow of electrons in the electrocatalytic system [14]. In this sense, new nanostructured carbon materials such as graphene and carbon nanotubes [15] have widely contributed to deriving advanced electrocatalysts due to their desirable electrical and mechanical properties as well as large surface area.

As non-noble metal catalyst, CoO_x (cobalt oxide)-based carbon catalysts are expected to be one of the promising alternatives to Pt-based electrocatalysts [16,17]. CoO_x supported on graphene and other carbon materials has been reported as highly active electrocatalysts for the ORR [13,18,19]. In order to improve the ORR catalytic activity and stability, some works have focused their research on CoO_x doped with N; for this reason various nitrogen containing ligands were used as precursors to form Co-complexes [20–22]. Liang et al. reported that NPs size of Co_3O_4 (~70 wt. %) grown on nitrogen doped reduced graphene oxide (4–8 nm in size) were smaller than those grown on reduced graphene oxide without nitrogen doping (12–25 nm in size). While the pure Co_3O_4 or reduced graphene oxide alone have a very low catalytic activity, the hybrid material with smaller NPs exhibited an unexpectedly high ORR activity that was further enhanced by nitrogen doping of grapheme [21]. Another example was proposed by Yuan et al. where a novel nanowire-structured polypyrrole-cobalt composite was successfully synthesized using cetyltrimetylammounnium bromide as surfactant [23]. This electrocatalyst showed a superior ORR performance than that of granular polypyrrole-cobalt catalyst prepared without the surfactant and also a better durability than the commercial 20 wt. % Pt/C catalyst. The high quantity of Co-pyridinic-N groups, which worked as ORR active sites, and its large specific surface area facilitated its ORR activity enhancement. Liu et al. investigated about the dependence of ORR activity on particle size of cobalt monoxides (CoO) and carbon composites [24]. Liu et al. prepared catalysts based on CoO (7 wt. %) supported on Vulcan, with an average size of 3.5, 4.9 and 6.5 nm, using a facile colloidal method avoiding any surfactants of long chain. It was concluded that the ORR activity is enhanced by the smaller CoO NPs due to enlarged interfaces between CoO and carbon materials [24].

Different oxidized phases of Co catalysts were prepared and their ORR activity were characterized by Liang et al. [25] Composites of CoO 40 wt. % on nitrogen doped carbon nanotube (NCNT) were obtained by thermal annealing of a mixture of $Co(OAc)_2$ and carbon nanotube at 400°C in NH_3/Ar atmosphere. Additionally, composites of Co_3O_4/NCNT and CoO_x/NCNT were also prepared by heat treatment in hydrothermal and

Ar atmosphere, respectively. Among them, the CoO/NCNT hybrid showed higher ORR current density than Co_3O_4/NCNT and CoO_x/NCNT hybrids due to the strong interaction between the cobalt oxide and carbon material [25]. Uhlig et al. prepared three plasma-treated (300, 450 or 600 W for 120 min) CoO_x catalysts supported on Vulcan containing ~20 wt. % of cobalt with a relatively homogeneous dispersion. Higher ORR activity was confirmed when using higher plasma treatment in KOH and K_2CO_3 electrolytes [26].

In summary, a variety of synthetic methods, conditions and carbon supports for Co modified carbon electrocatalysts have been explored for ORR. In this work, Multiwall carbon nanotubes (CNTs) loaded with different contents of Co NPs were prepared by a facile synthesis method consisting in a mixture of CNTs, a surfactant, a metal precursor (cobalt nitrate) and a reducing agent followed by their pyrolysis. Since the preparation method is able to determine the practicability and performance of electrocatalysts [10], several conditions were investigated to elucidate the relationships between properties of CoO_x, such as amount of CoO_x, NPs sizes, chemical composition and oxidation states of Co and ORR activities. Finally, a simple synthesis procedure of CoO_x NPs supported on CNTs that achieved high ORR catalytic activity with only 1 wt. % of Co NP is presented and insights into the factors governing the high catalytic activity are discussed.

5-2, Experimental section

5-2-1, Preparation of CNTs

CNTs were purchased from Cheap Tubes Inc. (Brattleboro, Vt, USA) with a 95% of purity, outer diameter < 8 nm, length: 10-30 µm and a BET surface area of 484 $m^2 g^{-1}$. Since some metal impurities can be present in the carbon material due to their synthetic procedure and they can affect the electrocatalyst activity [27,28], a purification treatment was performed to remove these impurities. The CNTs were purified by 1M hydrochloric acid solution for more than 12 hours (overnight) at room temperature followed by filtration and washing with distilled water. After the acidic treatment, the CNTs were treated with 6M sodium hydroxide for 6 hours at 50°C to remove the residual ash content. The resulting CNTs were filtered and washed several times by distilled water until the pH of the filtrate was the same as that of the distilled water. Finally the material was dried at 120°C.

5-2-2, Decorating CoO_x nanoparticles on CNTs

For the preparation of the CoOx-based CNTs materials, the following procedure was used. The necessary amount of Co precursor (cobalt(II) nitrate hexahydrate ($Co(NO_3)_2$•6 H_2O), Sigma-Aldrich) was dissolved in ethanol for a final nominal metal loading of 1, 9, and 17 wt. % of Co. Together with the Co precursor, the required amount of polyvinylpyrrolidone (PVP 40T, Sigma-Aldrich) were added to obtain a PVP/Co molar ratio of 10. After 2 hours under vigorous stirring, the purified CNTs were added to the solution. To favor the CNTs dispersion, the suspension was sonicated for 30s using an ultrasound probe (Bandelin Sonoplus GM2200, 200 W) at 25% output power. Afterwards, the suspension was stirred for 2 hours. The same sonication treatment was repeated before the addition of the reducing agent, sodium borohydride ($NaBH_4$, Sigma-Aldrich) at 0°C in an ice-bath. To ensure the total reduction of the Co(II), the suspension was stirred during 2 hours at 0°C followed by filtering and washing with ethanol. The prepared Co-based CNTs were dried at 80°C overnight. Finally, the obtained Co decorated CNTs were heat treated at 500°C under N_2 atmosphere for 1 hour to remove PVP [29]. In this study, the Co-based catalysts were named as CNT_Co_1%_500, in reference to the samples prepared with a nominal metal loading of 1 wt. % and treated under N_2 at 500°C during 1 hour. Some catalysts were tested without the N_2 heat treatment at 500°C.

For comparison purposes, additional Co-based CNTs were prepared modifying the described synthesis. One sample was prepared with a nominal metal loading of 1 wt. % without the presence of PVP during the reduction step of the Co precursor. Furthermore, one sample was prepared without using the Co precursor but in the presence of PVP (CNT_PVP_500 sample). The nomenclature used for these samples are CNT_Co_1%_noPVP_500 and CNT_PVP_500, respectively. Moreover, another sample was prepared changing from the reduction agent ($NaBH_4$) to an ammonia solution (NH_4OH, 0.8 ml of 25 wt. %) to increase the pH and produce the precipitation of the Co oxide/hydroxides, as in a related work [24]. This sample is labeled as CNT_Co_1%_NH_3_500.

5-2-3, Characterization and electrochemical measurements

Transmission electron microscopy (TEM) images of the materials were taken with a JEOL JEM-2010 microscope operated at 200 kV. The samples were suspended in ethanol to obtain a homogeneous dispersion before drop-casting them on a copper grid and then placed in the measurement chamber. The amount of introduced CoOx into the CNTs was examined by inductively coupled plasma-optical emission spectroscopy (ICP-OES). The ICP-OES results were obtained using a PerkinElmer Optima 4300 system. The samples were dissolved in 2 mL of concentrated aqua regia and filtered. The solutions were adjusted to a final Co concentration between 0-20 ppm for its determination in the linear signal range. The surface composition of the catalysts was investigated by using X-ray photoelectron spectroscopy (XPS) in a K-Alpha of Thermo-Scientific spectrometer, equipped with an Al anode. Elemental analysis of the surfaces was calculated from the areas under the main peak of each atom. Deconvolution of the XPS were done by least squares fitting using Gaussian-Lorentzian curves, and as the background determination, a Shirley line was used. X-ray diffraction (XRD) measurements were performed using Cu K radiation on a Bruker D8 Advance diffractometer.

Electrochemical activity tests towards ORR were carried out in a three-electrode cell using 0.1M KOH electrolyte, a Pt wire as counter electrode and Reversible Hydrogen Electrode (RHE) electrode as reference electrode. A rotating ring-disk electrode (RRDE, Pine Research Instruments, USA) equipped with a glassy carbon (GC) disk (5.61mm diameter) and a attached Pt ring was used as working electrode. The catalysts were dispersed in a solution of 75 vol. % of isopropanol, 25 vol. % of water and 0.02 vol. % of Nafion@ to prepare a final dispersion of 1 mg/ml of the CoOx-CNTs material. Typically, 100 µl (mass of electrode is 400 µg/cm^2) of the dispersion was pipetted on a GC electrode to obtain uniform catalysts layer for ORR study although the effect of the mass of electrode (80, 800 and 1600 µg/cm^2) was also studied. The sample on the GC was dried by heating lamp for evaporation of the solvent. Cyclic Voltammetry (CV) and linear sweep voltammetry (LSV) were carried out from 0 to 1 V (vs. RHE). The CV was performed in both N_2 and O_2 saturated atmosphere at 50 mVs-1. The LSV was done in an O_2-saturated atmosphere for different rotation rates of 400, 625, 900, 1025, 1600 and 2025 rpm at 5 mVs^{-1}. The potential of the ring was kept at 1.5 V (vs. RHE) and the ring current by H_2O_2 oxidation was also measured during the LSV measurement. The electron transffer number (n) of ORR on the catalysts modified electrode was determined by the following equation [30].

$$n = \frac{4 \times Id}{Id + Ir/N} \quad (1)$$

where Id is disk current, Ir is ring current, and N is the collection efficiency of the ring which was experimentally determined to be 0.37.

5-3, Results and Discussion

5-3-1, Chemical characterization

Table 1 shows the Co content in the prepared catalysts determined by ICP-OES analysis. These results reveal that CoOx loading on CNTs was successful and samples with sufficiently different Co contents were prepared. However, the amount of Co obtained for the highest Co contents were lower than the intended values probably due to the lack of adequate interaction between the CNTs surfaces and the Co NPs reactants or the limited surface area of CNTs. In this study, we will maintain in the nomenclature the nominal content of Co although the results, if necessary, will be referred to the real Co content of the catalysts.

Table 1. Composition of Co content calculated of CNT (purified CNTs), CNT_Co_1%_500, CNT_Co_9%_500 and CNT_Co_17%_500.

Sample	Co content / wt. %
CNT	0
CNT_Co_1%_500	1.0
CNT_Co_9%_500	4.7
CNT_Co_17%_500	8.2

Table 2 shows nitrogen atomic composition obtained from XPS (XPS survey spectra and C, N and O atomic compositions for prepared catalysts are shown in Figure 1 and Table 3, respectively). The catalysts prepared with PVP presents a detectable nitrogen content while for CNT and CNT_Co_1%_noPVP_500 nitrogen was not detected. This is because PVP decomposition during catalyst pretreatment may produce some carbon material which introduces some N doping near Co atoms since PVP molecules are initially coordinating Co atoms on the NPs surface. Specifically, the catalysts prepared with $NaBH_4$ reveal a relatively higher amount of nitrogen than that prepared with NH_3 (Table 2).

Table 2. N atomic composition obtained from XPS and content of different N species for CNT, CNT_Co_1%_500, CNT_Co_9%_500, CNT_Co_17%_500, CNT_Co_1%_NH$_3$_500 and CNT_Co_1%_noPVP_500.

Sample	N /	Quaternary	Pyrrolic/pyridonic	Pyridinic
	at. %	N / %	N / %	N / %
CNT	0	--	--	--
CNT_Co_1%_500	0.77	24.8	30.0	45.2
CNT_Co_9%_500	0.77	26.8	30.3	42.9
CNT_Co_17%_500	0.99	24.4	31.9	43.7
CNT_Co_1%_NH$_3$_500	0.28	17.1	53.5	29.4
CNT_Co_1%_noPVP_500	0	--	--	--

Table 3. C, N and O atomic composition obtained from XPS.

Sample	C (at. %)	N (at. %)	O (at. %)
CNT	96.45	0	3.55
CNT_500	97.11	0	2.89
CNT_Co_1%	89.28	2.03	8.51
CNT_Co_1%_500	95.93	0.77	3.08
CNT_Co_9%	48.01	2.07	47.73
CNT_Co_9%_500	86.87	0.77	12.25
CNT_Co_17%	56.85	2.60	38.36
CNT_Co_17%_500	77.34	0.99	21.25
CNT_Co_1%_noPVP	97.11	0	2.76
CNT_Co_1%_noPVP_500	96.24	0	3.65
CNT_Co_1%_NH$_3$	91.82	2.71	5.35
CNT_Co_1%_NH$_3$_500	95.05	0.28	4.45
CNT_Co_1%_noPVP_NH$_3$	94.85	0.13	4.85
CNT_Co_1%_noPVP_NH$_3$_500	95.97	0.19	3.73

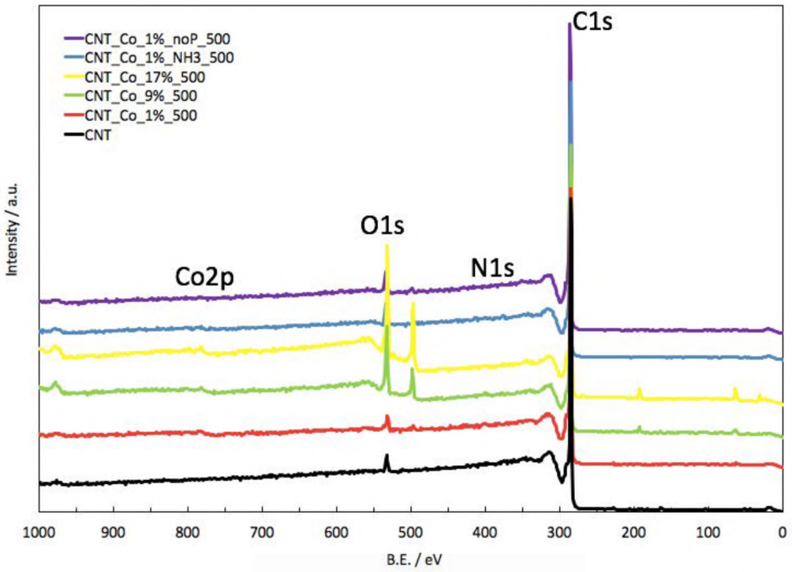

Figure 1. XPS survey spectrum of CNT, CNT_Co_1%_500, CNT_Co_9%_500, CNT_Co_17%_500, CNT_Co_1%_NH_3_500 and CNT_Co_1%_noP_500.

Figure 2 represents the high-resolution Co 2p and N 1s XPS spectra for a selection of CoOx decorated catalysts. The two peaks at binding energies (BE) around 780 eV and 795 eV are related to Co 2p(3/2) and Co 2p(1/2), respectively [31]. Although the Co(II) and Co(III) sites have similar 2p BE, they can be differentiated when Co_3O_4 species are formed. The BE of Co(II) is found to be at 781.3 eV for Co 2p(3/2) and 797.3 eV for Co 2p(1/2), whereas the BE of Co(III) is at around 780.0 eV for Co 2p(3/2) and 795.1 eV for Co 2p(1/2) [13,31]. The deconvolution profiles in Figure 2 show that the oxidation state of Co on the catalysts prepared herein was mainly Co(II). Figure 2a contains well defined Co(II) peaks for Co 2p(3/2) as well as Co 2p(1/2) for catalysts CNT_Co_1%_500, CNT_Co_9%_500 and CNT_Co_17%_500. In addition, strong satellite peaks at around 785.5 and 804.2 eV presenting 6 eV above the primary spin-orbit BE were observed. These peaks reveal another proof for high-spin Co(II) species [10,32]. Moreover, Co metallic peak at around BE of 778 eV and 793.3 eV were detected for CNT_Co_1%_500, CNT_Co_9%_500 and CNT_Co_17%_500 catalysts [33,34]. In contrast, as shown in Figure 2b, no clear Co 2p peaks, especially for Co 2p(1/2), are observed for 1 wt. % of Co-containing catalyst synthesized without PVP followed by heat-treatment (CNT_Co_1%_noPVP_500). Interestingly, metallic Co was not detected for CNT_Co_1%_NH_3_500 but the XPS suggests the presence of Co(III) species. In summary, XPS shows that in the synthesis method in which PVP and the reducing agent are used, most of the Co remains as Co(II) together with small amounts of metallic Co. If the reducing agent is not used, Co(III) species are detected. Figure 3 shows the XRD patterns of CNT, CNT_Co_1%_500, CNT_Co_9%_500, CNT_Co_17%_500 and CNT_Co_1%_NH_3_500. Peaks associated to CoO and Co are only barely observable for the samples with the highest Co content, indicating the existence of both CoO and Co species in these catalysts. However, for the samples with the lowest Co content (CNT_Co_1%_500 and CNT_Co_1%_NH_3_500) no clear features are distinguished due to the low amount of Co and the small particle size.

Figure 2c includes the high resolution XPS spectra for N 1s of CNT, CNT_Co_1%_noPVP_500, CNT_Co_1%_500, CNT_Co_9%_500, CNT_Co_17%_500 and CNT_Co_1%_NH_3_500. The spectra of CNT_Co_1%_500, CNT_Co_9%_500, CNT_Co_17%_500 and CNT_Co_1%_NH_3_500 could be deconvoluted into three peaks with maxima at 398.5, 399.8 and 401.5 eV which indicate pyridinic N, pyrrolic/pyridonic N and quaternary N, respectively [12,23,35,36]. The content of different N species for the catalysts are also indicated in Table 2. Larger N content and more pyridinic N and quaternary N species were detected in samples CNT_Co_1%_500, CNT_Co_9%_500 and CNT_Co_17%_500 than CNT_Co_1%_NH_3_500. To sum up, the preparation protocol using $NaBH_4$ favors the formation of pyridinic N and quaternary N groups as well as a higher amount of nitrogen content.

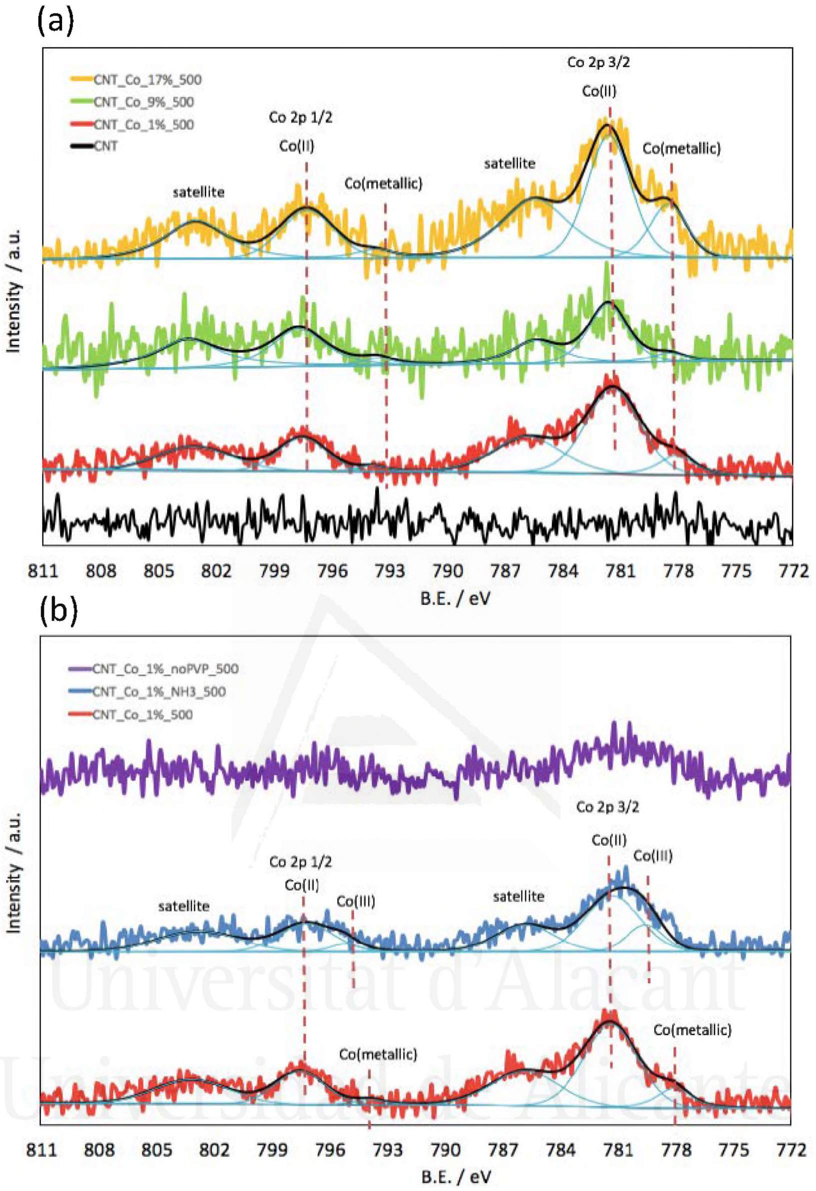
(a)
CNT_Co_17%_500
CNT_Co_9%_500
CNT_Co_1%_500
CNT
Co 2p 3/2
Co(II)
Co 2p 1/2
Co(II)
Co(metallic)
satellite
satellite
Co(metallic)
Intensity / a.u.
811 808 805 802 799 796 793 790 787 784 781 778 775 772
B.E. / eV
(b)
CNT_Co_1%_noPVP_500
CNT_Co_1%_NH3_500
CNT_Co_1%_500
Co 2p 3/2
Co(II)
Co(III)
Co 2p 1/2
Co(II)
Co(III)
satellite
satellite
Co(metallic)
Co(metallic)
Intensity / a.u.
811 808 805 802 799 796 793 790 787 784 781 778 775 772
B.E. / eV

(c)

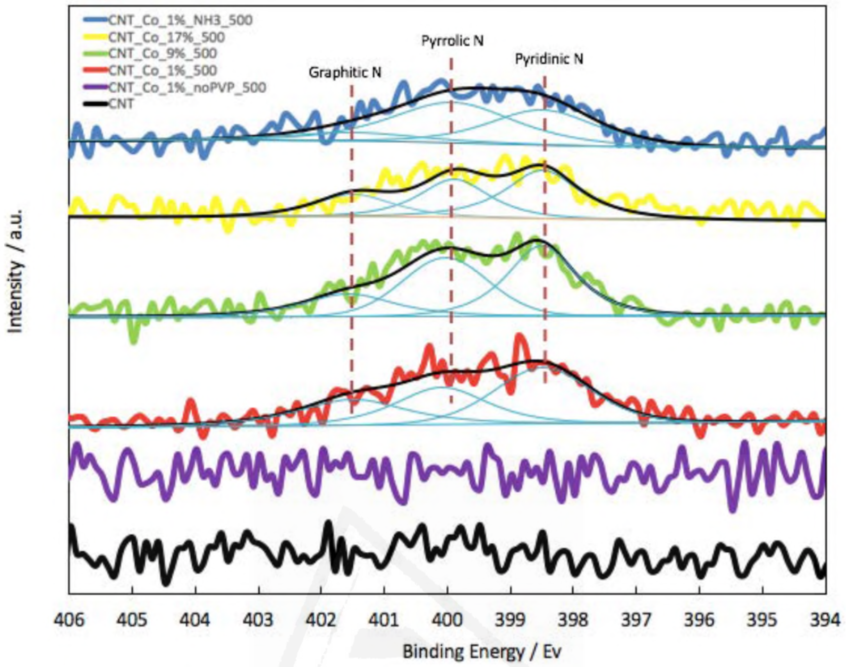

Figure 2. Co 2p spectra of (a) CNT, CNT_Co_1%_500, CNT_Co_9%_500 and CNT_Co_17%_500 (b) CNT_Co_1%_500, CNT_Co_1%_NH$_3$_500 and CNT_Co_1%_noPVP_500. N 1s spectra of (c) CNT, CNT_Co_1%_noPVP_500, CNT_Co_1%_500, CNT_Co_9%_500, CNT_Co_17%_500 and CNT_Co_1%_NH$_3$_500.

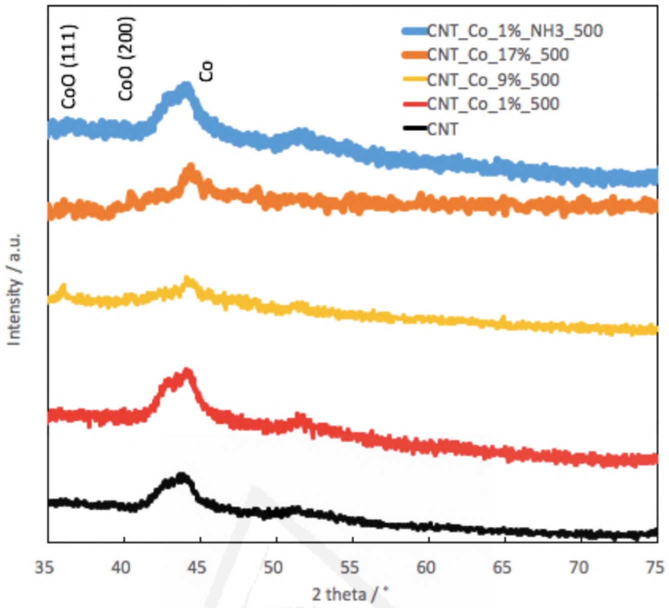

Figure 3. XRD patterns of CNT, CNT_Co_1%_500, CNT_Co_9%_500, CNT_Co_17%_500 and CNT_Co_1%_NH_3_500.

Figure 4 shows the TEM images for catalysts with different amounts of Co but prepared with the same method (CNT_Co_1%_500, CNT_Co_9%_500 and CNT_Co_17%_500) and 1 wt. % of Co-containing catalysts prepared by different synthesis methods (CNT_Co_1%_noPVP_500 and CNT_Co_1%_NH_3_500). About 100 particles are randomly selected for the analysis of CoOx NPs size distributions. Average NPs size increases with increasing Co content following the same preparation method. However, it remains nearly constant when 1 wt. % of Co is loaded using different preparation methods. These TEM results indicate that the concentration of Co in the catalysts has a greater contribution in the particle size of Co NPs than the chemical agents used in the synthesis. In addition, Figure 4f represents high resolution TEM image of CNT_Co_17%_500 as an example of the prepared catalysts using PVP and $NaBH_4$. As shown in Figure 4f, a thin deposit is observed around the CoOx NPs which could be due to the PVP carbonization which may contain most of the N species detected.

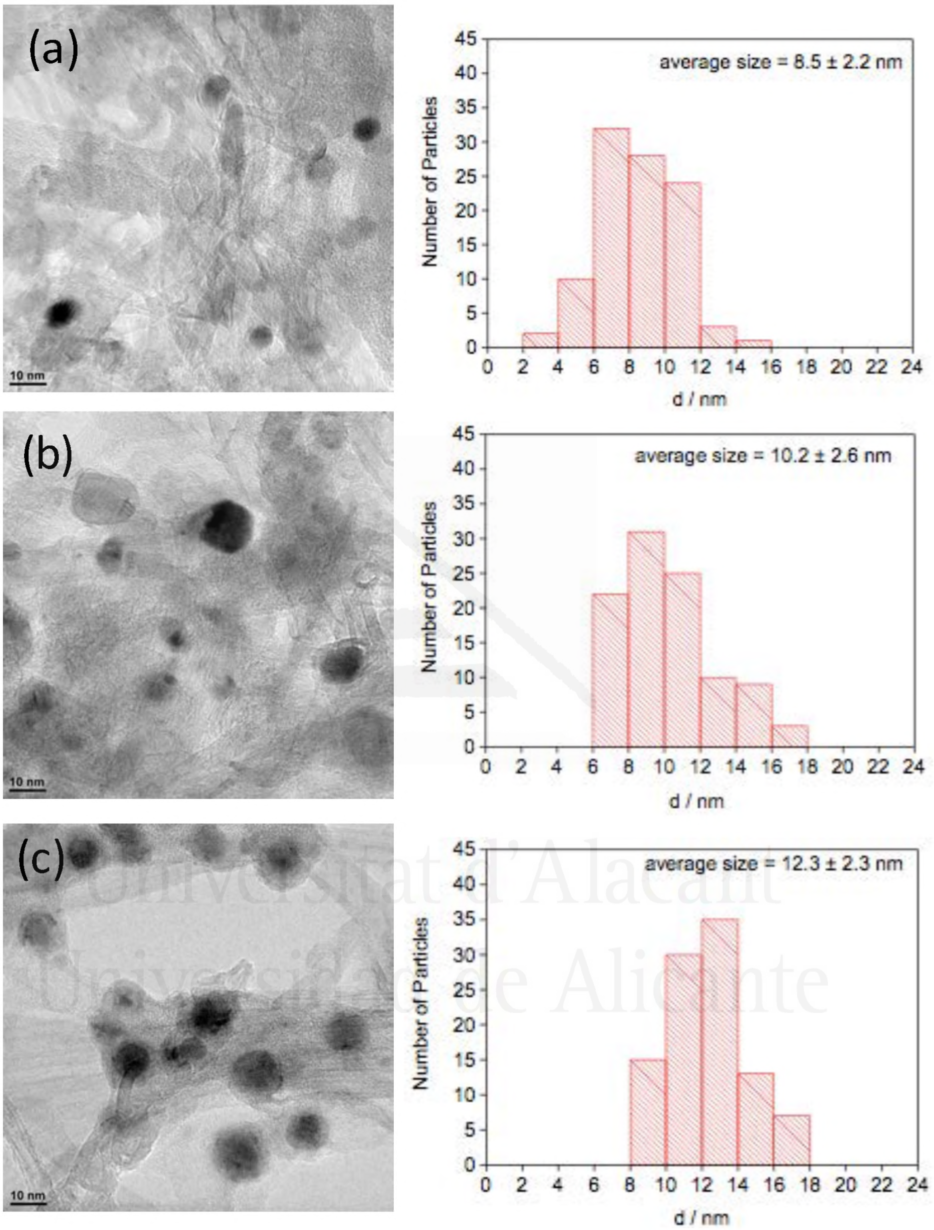
(a)
10 nm
average size = 8.5 ± 2.2 nm
Number of Particles
0 5 10 15 20 25 30 35 40 45
0 2 4 6 8 10 12 14 16 18 20 22 24
d / nm
(b)
10 nm
average size = 10.2 ± 2.6 nm
Number of Particles
0 5 10 15 20 25 30 35 40 45
0 2 4 6 8 10 12 14 16 18 20 22 24
d / nm
(c)
10 nm
average size = 12.3 ± 2.3 nm
Number of Particles
0 5 10 15 20 25 30 35 40 45
0 2 4 6 8 10 12 14 16 18 20 22 24
d / nm

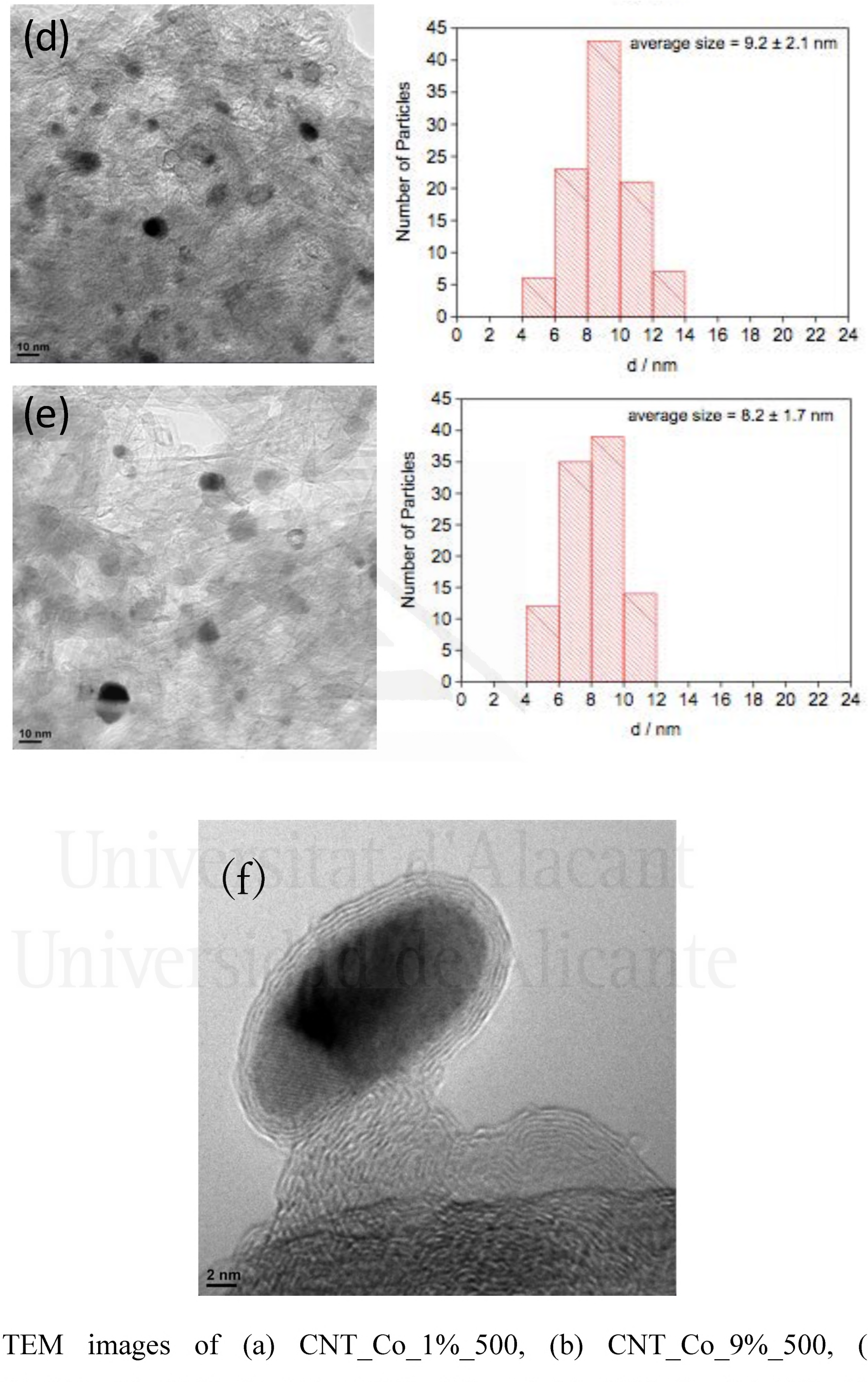

Figure 4. TEM images of (a) CNT_Co_1%_500, (b) CNT_Co_9%_500, (c) CNT_Co_17%_500, (d) CNT_Co_1%_noPVP_500 and (e) CNT_Co_1%_NH_3_500. TEM image of (f) CNT_Co_17%_500 with high resolution.

5-3-2, Electrochemical characterization

The ORR catalytic activity of the Co-containing samples was preliminary characterized by CV under N_2 and O_2 saturated atmosphere in 0.1M KOH. The CV curves for CNT, CNT_Co_1%_500 and CNT_Co_17%_500 in N_2 and O_2 saturated atmosphere are shown in Figure 5a, 5b and 5c respectively. The oxidation current observed for CNT_Co_17%_500 at potentials higher than 0.8 V vs RHE (Figure 5c), can be associated to the oxidation of Co(II) to Co(III) according to the following reaction: $3Co^{2+} + 8OH^- \rightarrow Co_3O_4 + 4H_2O + 2e^-$ [25,37]. This oxidation current is not clearly observed for sample CNT_Co_1%_500 due to the low Co content. The CV curves in Figure 5 in presence of O_2 show the reduction peak for O_2, which has a more positive onset potential for CNT_Co_1%_500 and CNT_Co_17%_500 than CNT. Moreover, the CNT_Co_1%_500 sample exhibits much higher reduction current than CNT_Co_17%_500.

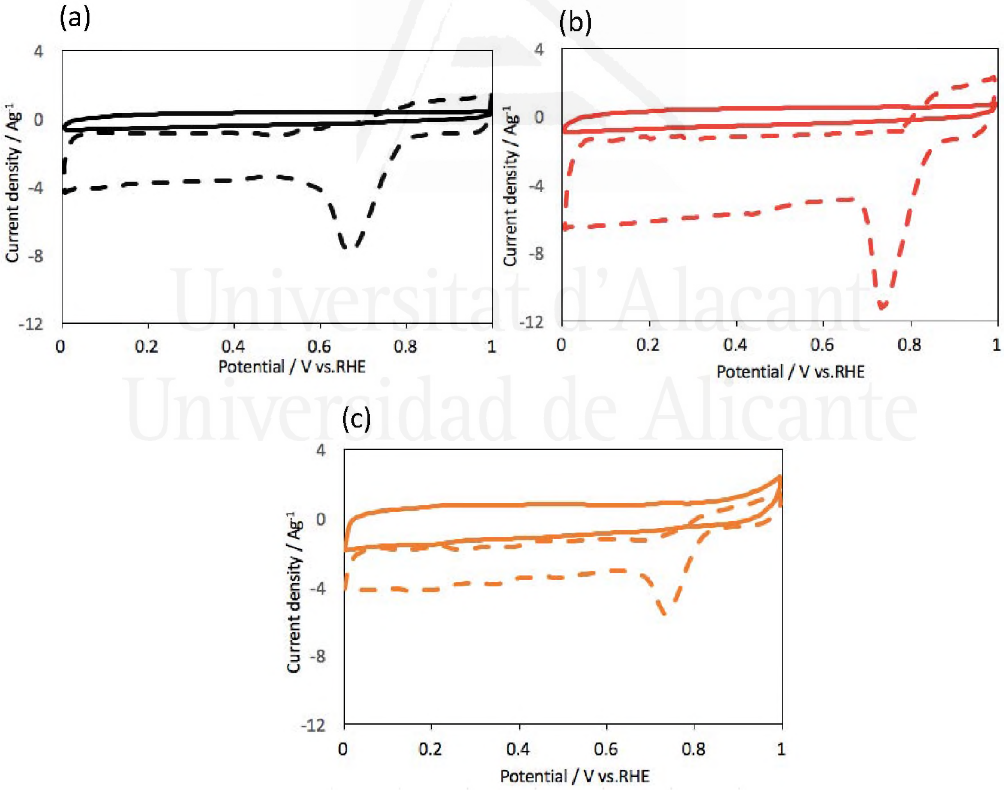

Figure 5. Steady state voltammograms for (a) CNT, (b) CNT_Co_1%_500 and (c) CNT_Co_17%_500 catalysts in N_2 (solid line) and O_2-saturated (dash line) 0.1M KOH solution at 50mVs^{-1} respectively. Catalyst loading is 400 μg/cm^2.

To quantitatively investigate the ORR performance, experiments with a RRDE were performed. Figure 6 represents LSVs and current during ORR for disk and ring electrodes at different rotating rates on CNT and CNT_Co_1%_500 catalysts. The Limiting Current (LC) increased with increasing the rotating rate due to shortened diffusion distance at high rotating rate [20]. CNT_Co_1%_500 showed wide current plateau and much higher LC as well as onset potential compared to CNT. These results imply that the addition of CoOx can significantly enhance the ORR activity. Similarly, the measured ring current which corresponds to the oxidation of hydrogen peroxide produced during the LSV curves in the disk electrode (divided by collection efficiency, 0.37) also increased with rotation rate as shown in Figure 6. CNT_Co_1%_500 demonstrated lower ring current than CNT which indicates the formation of lower amount of hydrogen peroxide.

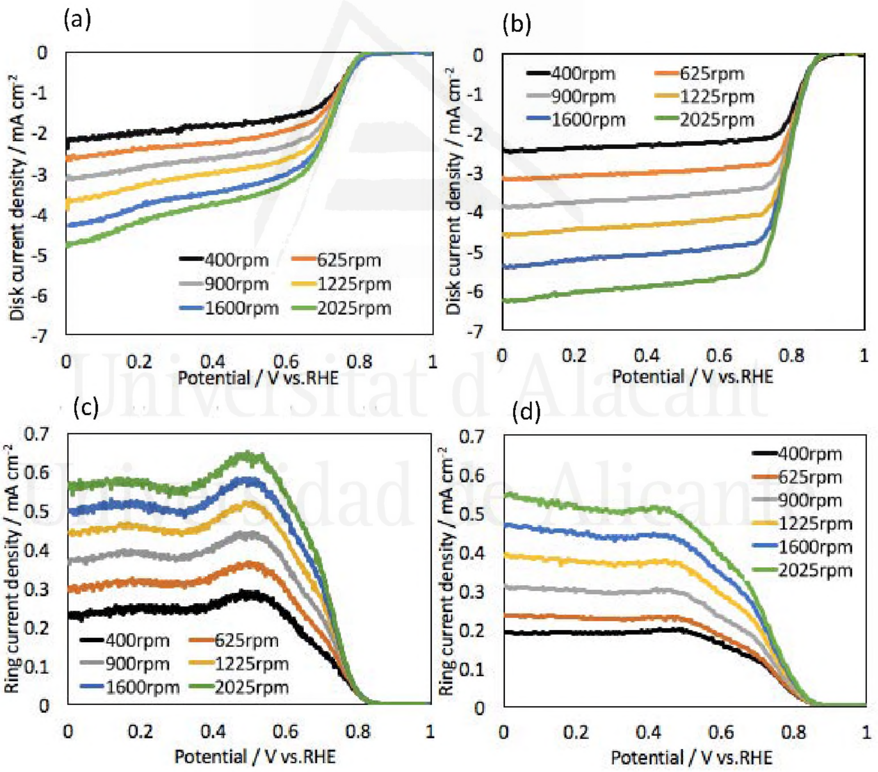

Figure 6. ORR current densities on the disk for (a) CNT and (b) CNT_Co_1%_500 and ring currents divided by collection efficiency for the (c) CNT and (d) CNT_Co_1%_500 in O_2 - saturated 0.1M KOH solution with a sweep rate of 5 mVs^{-1} respectively. Catalyst loading is 400 μg/cm^2.

Figure 7 presents the LSVs during ORR and electron transfer number (n) of the CNT, CNT_Co_1% (without heat treatment under N_2 at 500°C), CNT_Co_1%_500 and Pt/Vulcan (20 wt. % Pt on Vulcan) catalysts measured at an electrode rotating rate of 1600 rpm with a potential scanning rate of 5 mV/s. The heat-treatment at 500°C under N_2 was performed to remove the PVP from the catalysts [29]. As shown in Figure 7, the catalyst without heat-treatment (CNT_Co_1%) has much lower LC and n than CNT. This is because the remaining PVP in the catalyst hinders the accessibility of oxygen to the active sites for ORR. However, the onset potential as well as LC of the CNT_Co_1%_500 were dramatically improved, while the selectivity of the reaction towards water formation was also enhanced. The CNT_Co_1%_500 reached LC of -5.7 mA/cm^2 which is similar to that observed for Pt/Vulcan catalyst.

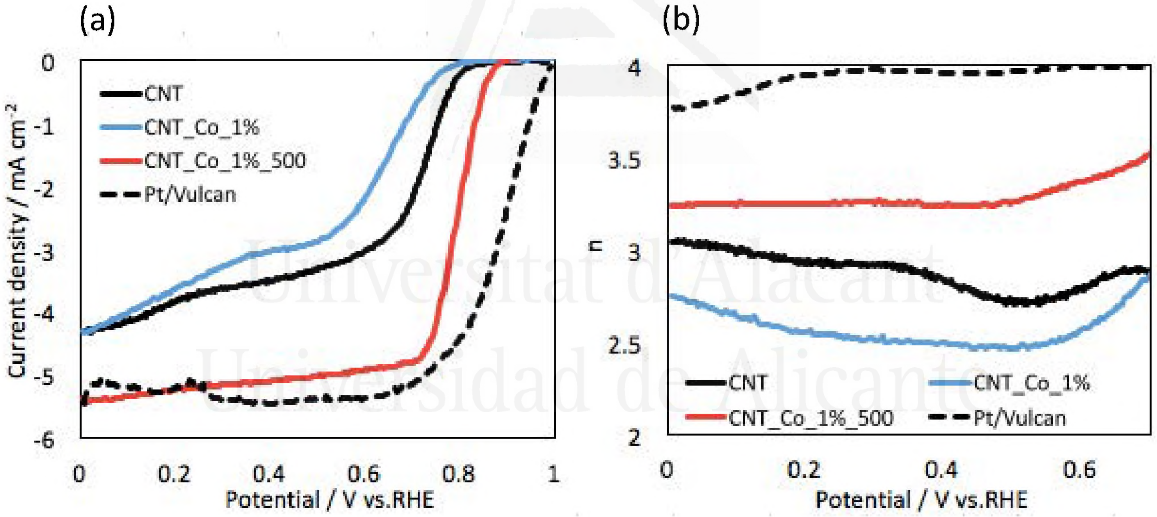

Figure 7. (a) ORR current densities on the disk and (b) electron transfer number (n) of the CNT, CNT_Co_1%, CNT_Co_1%_500 and Pt/Vulcan in O_2 - saturated 0.1M KOH solution at 1600 rpm with a sweep rate of 5 mV/s respectively. Catalyst loading is 400 μg/cm^2.

In order to clarify the influence of the PVP toward ORR activity, catalysts were also prepared without PVP (with Co precursor) or without Co precursor (with PVP). Figure 8 presents the ORR currents for the CNT, CNT_PVP_500, CNT_Co_1%_500 and CNT_Co_1%_noPVP_500 measured at an electrode rotating rate of 1600 rpm with a potential scanning rate of 5 mV/s. The LC and n of the catalyst without PVP were higher than that of CNT. However, LC and n of CNT_Co_1%_noPVP_500 were not as much enhanced as CNT_Co_1%_500. Especially, LC of catalyst prepared without PVP showed a significantly lower value than that of CNT_Co_1%_500. Likewise, LC and n of the catalyst prepared without Co precursor (CNT_PVP_500) were not highly improved as CNT_Co_1%_500 showed, which implies that the effect of PVP toward ORR is negligible when the Co is not present on CNT.

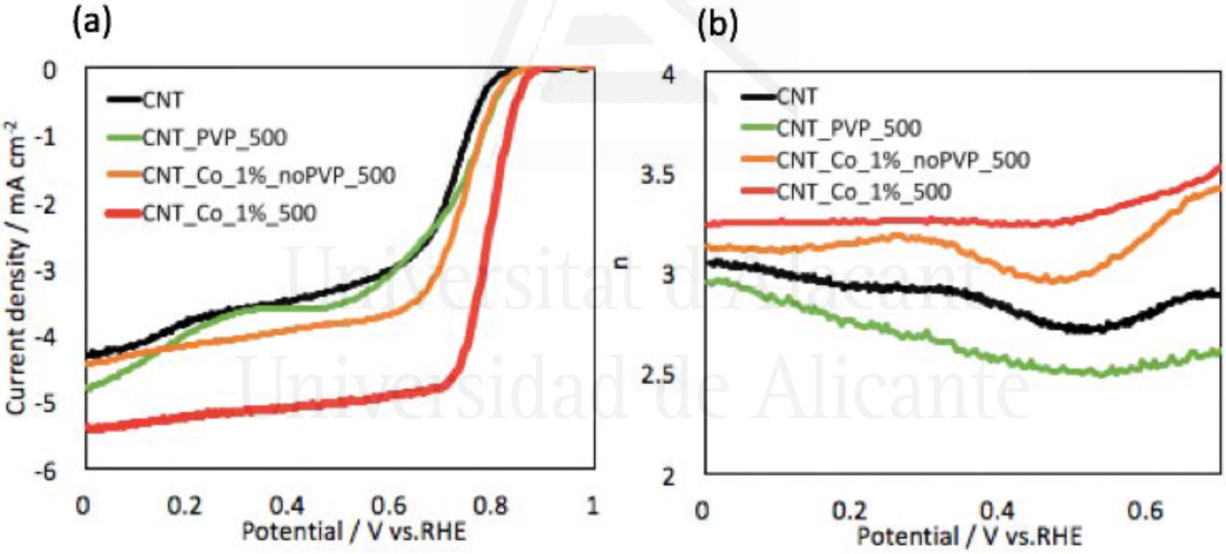

Figure 8. (a) LSVs during ORR on the disk electrode and (b) n of the CNT, CNT_PVP_500, CNT_Co_1%_noPVP_500 and CNT_Co_1%_500 in O_2 - saturated 0.1M KOH solution at 1600rpm with a sweep rate of 5 mV/s respectively. Catalyst loading is 400 µg/cm^2.

These results reveal that PVP plays an important role during the synthesis of Co-containing catalyst, either favoring the formation of well dispersed NPs or introducing some electronic or chemical changes on the catalytic species. It is well known that PVP acts as a protecting agent of the colloidal particles preventing agglomeration. This has been manifested in different NPs composition like Pd nanoparticles and Sn-3.5Ag alloy NPs [29,38]. However, TEM images in Figure 4 do not show relevant differences between both catalysts in terms of average particle size, suggesting that this is not the main factor explaining the effect of PVP.

On the other hand, as demonstrated in XPS N1s in Figure 2c and TEM image in Figure 4f, PVP decomposition during catalyst pretreatment produces a N-doped carbon shell on Co NP. Moreover, Figure 2c shows that pyridinic-N and quaternary N groups are present on CNT_Co_1%_500. The presence of these Co-N-C species constitute active sites which facilitate the adsorption of oxygen, leading to improved ORR performance as it has been proposed by other authors [12,23]. It must be emphasized that when PVP is not used this carbon shell is not formed and N is not detected, which results in a lower activity of the Co-containing catalyst.

Different amounts of CoOx NPs loaded on CNTs have been prepared to identify their effect on ORR activity. The ORR current densities and n of the catalysts with different Co contents (1, 9 and 17 wt. %) have been studied, Figure 9.

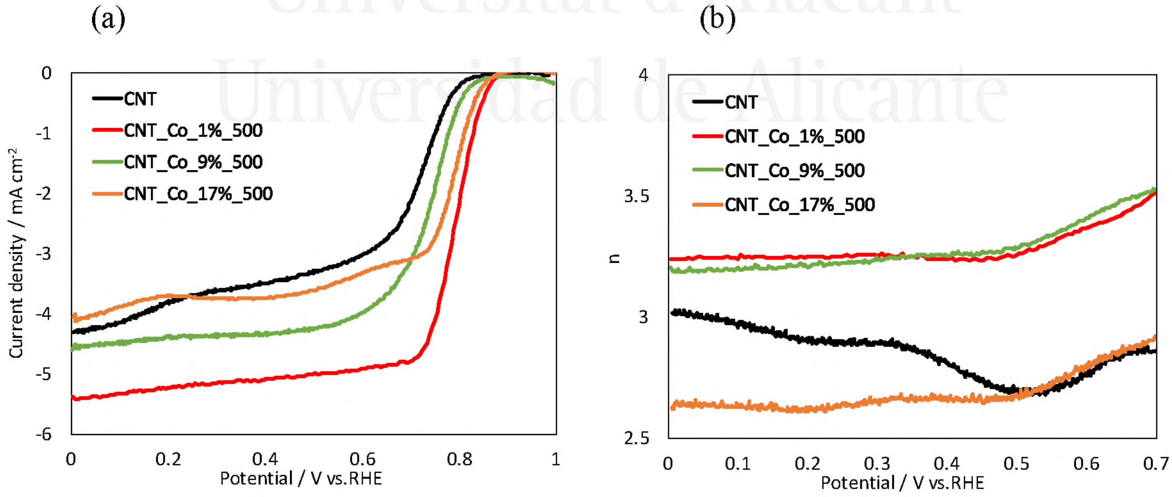

Figure 9. (a) ORR currents on the disk and (b) n of different amounts of CoOx contacted in O_2 - saturated 0.1M KOH solution at 1600 rpm with a sweep rate of 5mV/s respectively. Catalyst loading is 400 µg/cm^2.

The relationship between the Co content in the catalyst and LC as well as n at 0.3 V and 0.7 V (vs RHE) are summarized in Figure 10. Remarkably, LC and n of the catalyst with 1 wt. % of CoOx showed the highest values. As shown in Figure 10, the LC increased significantly up to a Co content of 1 wt. %, above which it decreased. The correlations of n and Co content in Figure 10b presented similar behavior as LC. As displayed in Figure 4, the average CoOx NPs size follows the order of CNT_Co_17%_500 (13.1 nm) > CNT_Co_9%_500 (10.8 nm) > CNT_Co_1%_500 (8.9 nm). In contrast, LC and n follow the order CNT_Co_1%_500 > CNT_Co_9%_500 > CNT_Co_17%_500. In this sense, the results suggest that as the size of CoOx NPs decreased, their ORR activities increased, which can be explained considering that ORR activity is enhanced by the smaller CoOx NPs due to the enlarged interface between CoOx and CNTs [24].

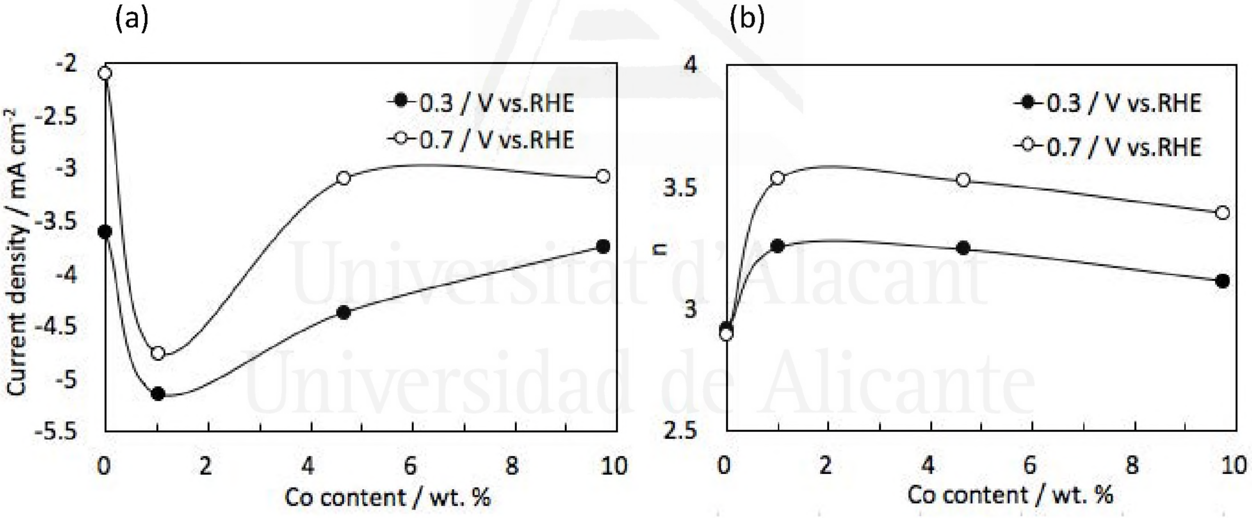

Figure 10. Relationship between Co content and (a) LC as well as (b) n measured at 0.3 V and 0.7 V vs.RHE in O_2 - saturated 0.1M KOH solution at 1600 rpm. Catalyst loading is 400 µg/cm^2. These catalysts were prepared with PVP and $NaBH_4$.

Though the LC of CNT_Co_1%_500 at 0.3 V (vs RHE) were similar to Pt/Vulcan (similar activity), the n value (~3.5) was lower than that of Pt/Vulcan (~4.0). It means that selectivity of CNT_Co_1%_500 is lower than Pt/Vulcan and follows a mix of a two and four electron pathway [26]. An associative pathway has been recently elucidated over CoOx/C catalyst, which involves the following reactions: (i) $O_2 + H_2O + 2e^- \rightarrow HO_2^- + OH^-$; (ii) $HO_2^- + H_2O + 2e^- \rightarrow 3OH^-$ and (iii) $2\,HO_2^- \rightarrow O_2 + 2OH^-$. The interface between carbon and Co NPs can be identified as the most active sites for the first $2e^-$ reduction of oxygen to form HO_2^- [39]. Amount of active sites, which are responsible for reaction (i) in Co-containing catalysts, are larger than the amount of active sites for $4e^-$ electron pathway on Pt/Vulcan and thus, high LC for CNT_Co_1%_500 are obtained. In fact, the LC values are similar to Pt/Vulcan catalyst with a 20 wt. % of Pt in spite of the fact that the Co catalyst has only 1 wt. %. Thus, it might be explained that the first two electrons pathway reaction (i) $O_2 + H_2O + 2e^- \rightarrow HO_2^- + OH^-$ proceeds efficiently for CNT_Co_1%_500 due to their smaller Co NPs size which results in a larger interface between Co species and carbon producing a much higher amount of HO_2^- [24].

In addition, Bonakdarpour et al. [40] reported that when the catalyst loading is low enough, the H_2O_2 molecules have a higher probability of diffusing away into the electrolyte than being reduced to water at a nearby site through reaction (ii). Therefore, the percentage of H_2O_2 released into the electrolyte strongly depends on the amount of electrocatalyst used on the RRDE [40]. Figure 11 shows the ORR current densities and ring current densities as well as n for the CNT_Co_1%_500 measured for different loadings at rotation speed of 1600 rpm. At all potentials, the LC and n increased when larger loadings are used. At 1600 $\mu g/cm^2$, well defined mass transfer LC plateau of -6 mA/cm^2 as well as higher n (selectivity) was observed, probably indicating that close to four electrons are being generated for each oxygen molecule reaching the electrode through reaction (i) on the interface and (ii) $HO_2^- + H_2O + 2e^- \rightarrow 3OH^-$ on the Co NPs surface [24]. As revealed in Figure 11, the HO_2^- yield decreased with increasing the loading (thickness) of the catalyst over the GC electrode.

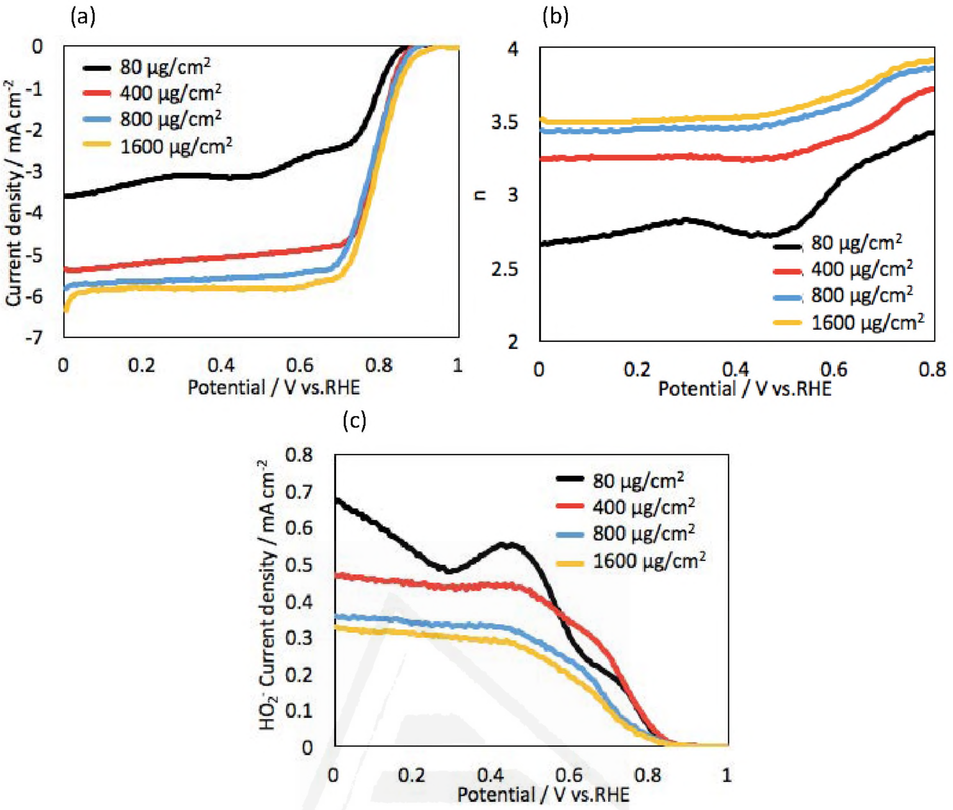

Figure 11. (a) LSVs for ORR on the disk electrode, (b) n and (c) ring current of CNT_Co_1%_500 with different loadings in O_2 - saturated 0.1M KOH solution at 1600 rpm with a sweep rate of 5 mV/s respectively.

Additional experiments were designed to investigate about the effect of $NaBH_4$ towards ORR activity. Instead of $NaBH_4$, 1 wt. % of Co decorated catalysts synthesized with NH_3 were prepared. Two advantages for using NH_3 can be mentioned: first, the ammonia molecules tend to be strongly bonded to cobalt cations, working as a capping agent to hinder particle growth; second, the hydrolysis rate of cobalt salt can be well controlled by ammonia which releases hydroxyl ions [21,24]. Figure 12 shows LSV curves for ORR and n for the catalysts prepared with and without NH_3. The LC of CNT_Co_1%_NH_3_500 is much lower than that of CNT_Co_1%_500.

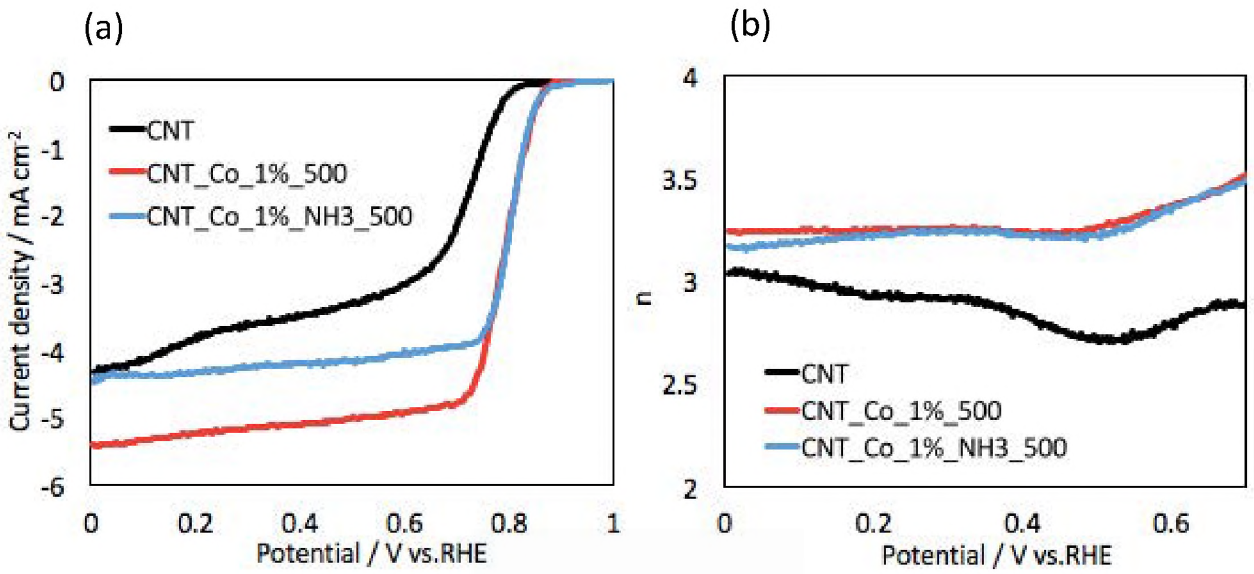

Figure 12. (a) Oxygen reduction currents on the disk and (b) n of the CNT, CNT_Co_1% and CNT_Co_1%_NH_3_500 in O_2 - saturated 0.1M KOH solution at 1600rpm with a sweep rate of 5 mV/s respectively. Catalyst loading is 400 µg/cm^2.

Figure 4a and 4e show that the average CoOx NPs sizes of CNT_Co_1%_500 and CNT_Co_1%_NH_3_500 are about 9 nm. This means that Co NPs size of the catalysts prepared with NH_3 or $NaBH_4$ are very similar. It can be mentioned that not only Co NPs sizes but also the catalyst preparation procedure affects the ORR activity. According to the results of catalysts prepared herein, contribution towards ORR activity of catalysts prepared using $NaBH_4$ was higher than that of NH_3.

The XPS results show three important differences among the two samples: (i) Figure 2b suggests the presence of Co(II) and Co(III) for CNT_Co_1%_NH_3 _500, probably forming Co_3O_4 species, when $NaBH_4$ is not used; (ii) metallic Co is observed when NaBH4 is used and (iii) pyridinic-N and quaternary N groups improving ORR performance are present in all the catalysts prepared with $NaBH_4$ (see Figure 2c and Table 2). Thus, it seems that the interaction of reduced Co with PVP is more efficient making that some Co-N species which work as active sites for ORR are formed after the heat treatment.

Dong et al. reported that Co^{2+} ions coordinated with NH_3 form $[Co(NH_3)6]^{2+}$ ions and most them were immediately oxidized to $[Co(NH_3)_6]^{3+}$ by O_2 according to the reaction $4[Co(NH_3)_6]^{2+} + O_2 + 2H_2O = 4[Co(NH_3)_6]^{3+} + 4OH^-$; then, after heat treatment Co_3O_4 nanomaterials are obtained [41]. Therefore Co(III) could be detected on CNT_Co_1%_NH_3_500. Liang et al. suggested that the carbon hybrid materials prepared with CoO contain larger amount of effective active or accessible ORR active sites than the carbon hybrid materials containing Co_3O_4 [25]. Furthermore, Xiao et al. investigated the relationship between surface structure of various types of cobalt oxide nanoparticles and their ORR activities [42]. It was concluded that the catalytically active sites for ORR should be the surface tetrahedral Co(II) sites.

Regarding metallic Co, it must be mentioned that Co(II) or Co(III) cannot be reduced in absence of $NaBH_4$. Actually, Co metallic was not found in other catalysts prepared with NH_3 [21,22] which is in agreement with our results. Wang et al. showed that in the catalysts with N-doped reduced graphene oxide aerogel (NGA), CoO and Co (CoO/Co-NGA) subunits had higher ORR activity than the catalysts without Co metallic (CoO-NGA) composites [43]. Highly integrated NGA, CoO and Co, suggests strong bonding between them, which would enhance the interaction between the metal oxide NPs and the graphene support, promoting electron and charge transfer among the active sites. Finally, the presence of Co-pyridinic-N and quaternary N groups, formed through the interaction of PVP and Co during the NPs synthesis when $NaBH_4$ is used, results in higher catalytic activity species as indicated by other authors [12,23].

In summary, different factors contribute to the optimum catalytic activity of Co NPs supported on nanostructured carbons. On the one hand, particle size has an important role since lower particle size results in larger amount of Co-Carbon interface sites. On the other hand, the Co-species composition has an important contribution since the presence of lower oxidation state Co sites and Co-N species results in enhanced catalytic activity when comparing catalysts with similar particle size.

5-3-3, Durability tests

The durability of an ORR catalyst is a factor which determines the life of a fuel cell [9]. The stability of the Co-containing catalyst was measured by RDE chronoamperometry under steady state mass transport conditions (0.65 V vs RHE). Figure 13 shows the stability of the CNT_Co_1%_500 and Pt/Vulcan catalysts on normalized current base. The current density calculated on Co and Pt content in molar basis is also included in Figure 13. Additionally, methanol poisoning test was performed by adding 1M methanol into the electrolyte after 2 hours reaction [31]. As shown in Figure 13, even after adding methanol, CNT_Co_1%_500 catalyst activity is more than 80% of the initial value over 3 hours. However, the current of the Pt/vulcan dropped to zero immediately after addition of methanol. The experiment supports that the Co-containing catalysts are suitable in terms of stability and resistance towards methanol. Furthermore, the current of CNT_Co_1%_500 per mole of metal content is higher than for Pt/Vulcan, showing that it is possible to achieve higher current densities than for Pt based catalysts with very low amounts of CoOx (i.e., 1 wt. % in this study). In addition, potential cycling durability tests were carried out by cyclic voltammetry. The cycling was repeated under O_2-saturated 0.1M KOH solution at 50 mVs-1 from 0 to 1 V (vs.RHE) for 500 cycles. Figure 14 presents the LSV curves before and after the 500 cycling (LSV curve after 100 cycles is indicated only for CNT_Co_1%_500). As demonstrated in Figure 14, the half-wave potential for CNT_Co_1%_500 and Pt/Vulcan catalysts shifted to lower potentials by only 5 mV and 15 mV after 500 cycles, respectively. These results imply that our catalysts show good stability in alkaline solution which means that they are interesting as catalysts for alkaline fuel cells.

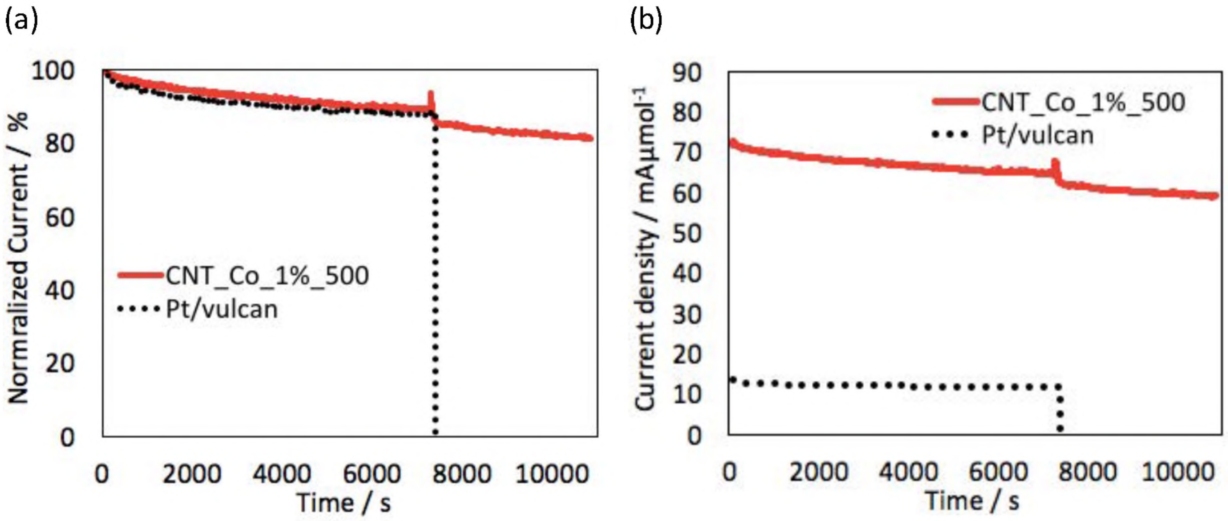

Figure 13. Current versus time for CNT_Co_1% and Pt/Vulcan at 0.65V vs. RHE in O_2 - saturated 0.1M KOH solution at 1600 rpm referred to (a) disk electrode area on normalized current base and (b) mol of Co or Pt in the catalyst. Catalyst loading is 400 μg/cm^2.

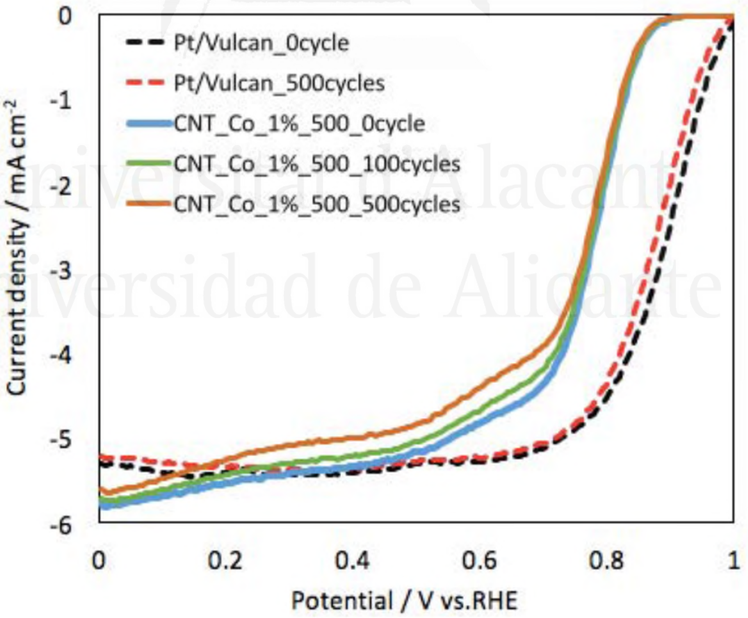

Figure 14. LSV curves for CNT_Co_1% and Pt/Vulcan before and after the cycling in O_2 - saturated 0.1M KOH solution at 1600rpm with a sweep rate of 5 mV s-1. Catalyst loading is 400 μg/cm^2.

5-4. Conclusions

A facile method to synthesize Co NPs decorated CNTs catalysts which show efficient and stable activity for ORR was developed. Our catalyst containing 1 wt. % of Co NPs (average NPs: 8.9 nm) prepared with PVP as protecting agent and $NaBH_4$ has surprisingly high LC in alkaline solution which is similar to commercial Pt/Vulcan. The catalyst showed higher selectivity towards 4e- electron pathway than CNT. Higher ORR activity is possible for smaller size of Co NPs catalysts due to the enlarged interfaces between Co species and CNTs. The addition of PVP and $NaBH_4$ during the preparation procedure is necessary for obtaining the highest activity since it favors the formation of lower oxidation states for Co species and the formation of a N-doped carbon shell. The Co-containing catalysts with small particle sizes, low Co oxidation states and pyridinic N and quaternary N groups in the carbon framework seem to have the optimum combination to create the most active sites for this reaction. These results suggest that the synthesis of smaller particle sizes than those used in this study (below 8 nm) employing this preparation method can produce improved Co-based ORR catalysts and that this methodology could also be applied to other metal oxides to achieve improved ORR catalysts.

5-5. References

[1] C. Lamy, Fuel Cell Systems : Which Technological Breakthrough for Industrial Development ?, in: E.F. François Béguin (Ed.), Carbons Electrochem. Energy Storage Convers. Syst., CRC Press, 2010: pp. 377–410.

[2] M. Winter, R.J. Brodd, What Are Batteries, Fuel Cells, and Supercapacitors?, Chem. Rev. 104 (2004) 4245–4270. doi:10.1021/cr020730k.

[3] F. Bidault, D.J.L. Brett, P.H. Middleton, N.P. Brandon, Review of gas diffusion cathodes for alkaline fuel cells, J. Power Sources. 187 (2009) 39–48. doi:10.1016/j.jpowsour.2008.10.106.

[4] N. Daems, X. Sheng, I.F.J. Vankelecom, P.P. Pescarmona, Metal-free doped carbon materials as electrocatalysts for the oxygen reduction reaction, J. Mater. Chem. A. 2 (2014) 4085–4110. doi:10.1039/C3TA14043A.

[5] Z. Yang, H. Nie, X. Chen, X. Chen, S. Huang, Recent progress in doped carbon

nanomaterials as effective cathode catalysts for fuel cell oxygen reduction reaction, J. Power Sources. 236 (2013) 238–249. doi:10.1016/j.jpowsour.2013.02.057.

[6] K. Gong, F. Du, Z. Xia, M. Durstock, L. Dai, Nitrogen-doped carbon nanotube arrays with high electrocatalytic activity for oxygen reduction, Science (760-764). 323 (2009) 760–764. doi:10.1126/science.1168049.

[7] G.F. McLean, T. Niet, S. Prince-Richard, N. Djilali, An assessment of alkaline fuel cell technology, Int. J. Hydrogen Energy. 27 (2002) 507–526. doi:10.1016/S0360-3199(01)00181-1.

[8] P. Trogadas, T.F. Fuller, P. Strasser, Carbon as catalyst and support for electrochemical energy conversion, Carbon. 75 (2014) 5–42. doi:10.1016/j.carbon.2014.04.005.

[9] B. You, P. Yin, J. Zhang, D. He, G. Chen, F. Kang, H. Wang, Z. Deng, Y. Li, Hydrogel-derived non-precious electrocatalysts for efficient oxygen reduction., Sci. Rep. 5 (2015) 11739. doi:10.1038/srep11739.

[10] G. Zhang, W. Lu, F. Cao, Z. Xiao, X. Zheng, N-doped graphene coupled with Co nanoparticles as an efficient electrocatalyst for oxygen reduction in alkaline media, J. Power Sources. 302 (2016) 114–125. doi:10.1016/j.jpowsour.2015.10.055.

[11] A. Pendashteh, J. Palma, M. Anderson, R. Marcilla, NiCoMnO4nanoparticles on N-doped graphene: Highly efficient bifunctional electrocatalyst for oxygen reduction/evolution reactions, Appl. Catal. B Environ. 201 (2017) 241–252. doi:10.1016/j.apcatb.2016.08.044.

[12] T. Sun, L. Xu, S. Li, W. Chai, Y. Huang, Y. Yan, J. Chen, Cobalt-nitrogen-doped ordered macro-/mesoporous carbon for highly efficient oxygen reduction reaction, Appl. Catal. B Environ. 193 (2016) 1–8. doi:10.1016/j.apcatb.2016.04.006.

[13] P.W. Menezes, A. Indra, D. González-Flores, N.R. Sahraie, I. Zaharieva, M. Schwarze, P. Strasser, H. Dau, M. Driess, High-Performance Oxygen Redox Catalysis with Multifunctional Cobalt Oxide Nanochains: Morphology-Dependent Activity, ACS Catal. 5 (2015) 2017–2027. doi:10.1021/cs501724v.

[14] Y. Liang, Y. Li, H. Wang, H. Dai, Strongly Coupled Inorganic / Nanocarbon Hybrid Materials for Advanced Electrocatalysis, J. Am. Chem. Soc. 135 (2013) 2013–2036. doi:Doi 10.1021/Ja3089923.

[15] C.H. Choi, M.W. Chung, H.C. Kwon, J.H. Chung, S.I. Woo, Nitrogen-doped graphene/carbon nanotube self-assembly for efficient oxygen reduction reaction in acid

media, Appl. Catal. B Environ. 144 (2014) 760–766. doi:10.1016/j.apcatb.2013.08.021.

[16] S. Zhao, B. Rasimick, W. Mustain, H. Xu, Highly durable and active Co3O4 nanocrystals supported on carbon nanotubes as bifunctional electrocatalysts in alkaline media, Appl. Catal. B Environ. 203 (2017) 138–145. doi:10.1016/j.apcatb.2016.09.048.

[17] G. Wu, K.L. More, C.M. Johnston, P. Zelenay, High-Performance Electrocatalysts for Oxygen Reduction Derived from Polyaniline, Iron, and Cobalt, Science (443-447). 332 (2011) 443–447. doi:10.1126/science.1200832.

[18] M. Wang, J. Huang, M. Wang, D. Zhang, W. Zhang, W. Li, J. Chen, Co3O4 nanorods decorated reduced graphene oxide composite for oxygen reduction reaction in alkaline electrolyte, Electrochem. Commun. 34 (2013) 299–303. doi:10.1016/j.elecom.2013.07.017.

[19] J. Xu, P. Gao, T.S. Zhao, Non-precious Co3O4 nano-rod electrocatalyst for oxygenreduction reaction in anion-exchange membranefuelcells, Energy Environ. Sci. 5 (2012) 5333–5339. doi:10.1039/C1EE01431E.

[20] S. CHAO, W. GUO, Using 2-Mercaptobenzothiazole as a Nitrogen and Sulfur Precursor to Synthesize Highly Active Co-N-S/C Electrocatalysts for Oxygen Reduction, Anal. Sci. 29 (2013) 619–623. doi:10.2116/analsci.29.619.

[21] Y. Liang, Y. Li, H. Wang, J. Zhou, J. Wang, T. Regier, H. Dai, Co3O4 nanocrystals on graphene as a synergistic catalyst for oxygen reduction reaction, Nat. Mater. 10 (2011) 780–786. doi:10.1038/nmat3087.

[22] Q. He, Q. Li, S. Khene, X. Ren, F.E. López-Suárez, D. Lozano-Castelló, A. Bueno-López, G. Wu, High-loading cobalt oxide coupled with nitrogen-doped graphene for oxygen reduction in anion-exchange-membrane alkaline fuel cells, J. Phys. Chem. C. 117 (2013) 8697–8707. doi:10.1021/jp401814f.

[23] X. Yuan, L. Li, Z. Ma, X. Yu, X. Wen, Z.-F. Ma, L. Zhang, D.P. Wilkinson, J. Zhang, Novel nanowire-structured polypyrrole-cobalt composite as efficient catalyst for oxygen reduction reaction, Sci. Rep. 6 (2016) 20005. doi:10.1038/srep20005.

[24] J. Liu, L. Jiang, B. Zhang, J. Jin, D.S. Su, S. Wang, G. Sun, Controllable synthesis of cobalt monoxide nanoparticles and the size-dependent activity for oxygen reduction reaction, ACS Catal. 4 (2014) 2998–3001. doi:10.1021/cs500741s.

[25] Y. Liang, H. Wang, P. Diao, W. Chang, G. Hong, Y. Li, M. Gong, L. Xie, J. Zhou, J. Wang, T.Z. Regier, F. Wei, H. Dai, Oxygen reduction electrocatalyst based on strongly coupled cobalt oxide nanocrystals and carbon nanotubes, J. Am. Chem. Soc. 134 (2012)

15849–15857. doi:10.1021/ja305623m.

[26] L.M. Uhlig, G. Sievers, V. Brüser, A. Dyck, G. Wittstock, Characterization of different plasma-treated cobalt oxide catalysts for oxygen reduction reaction in alkaline media, Sci. Bull. 61 (2016) 612–618. doi:10.1007/s11434-016-1025-y.

[27] Y. Li, W. Zhou, H. Wang, L. Xie, Y. Liang, F. Wei, J.C. Idrobo, S.J. Pennycook, H. Dai, An oxygen reduction electrocatalyst based on carbon nanotubeĝ€ "graphene complexes, Nat. Nanotechnol. 7 (2012) 394–400. doi:10.1038/nnano.2012.72.

[28] C.W.B. Bezerra, L. Zhang, K. Lee, H. Liu, A.L.B. Marques, E.P. Marques, H. Wang, J. Zhang, A review of Fe-N/C and Co-N/C catalysts for the oxygen reduction reaction, Electrochim. Acta. 53 (2008) 4937–4951. doi:10.1016/j.electacta.2008.02.012.

[29] I. Miguel-García, Á. Berenguer-Murcia, T. García, D. Cazorla-Amorós, Effect of the aging time of PVP coated palladium nanoparticles colloidal suspensions on their catalytic activity in the preferential oxidation of CO, Catal. Today. 187 (2012) 2–9. doi:10.1016/j.cattod.2012.02.015.

[30] U.A. Paulus, T.J. Schmidt, H.A. Gasteiger, R.J. Behm, Oxygen reduction on a high-surface area Pt/Vulcan carbon catalyst: A thin-film rotating ring-disk electrode study, J. Electroanal. Chem. 495 (2001) 134–145. doi:10.1016/S0022-0728(00)00407-1.

[31] Y. Huang, M. Zhang, P. Liu, L. Wang, F. Cheng, Improved performance of cobalt-based spinel by the simple solvothermal method as electrocatalyst for oxygen reduction reaction in alkaline solution, Ionics. 22 (2016) 1425–1432. doi:10.1007/s11581-016-1667-4.

[32] D. Barreca, C. Massignan, S. Daolio, M. Fabrizio, C. Piccirillo, L. Armelao, E. Tondello, Composition and microstructure of cobalt oxide thin films obtained from a novel cobalt(II) precursor by chemical vapor deposition, Chem. Mater. 13 (2001) 588–593. doi:10.1021/cm001041x.

[33] K. Niu, B. Yang, J. Cui, J. Jin, X. Fu, Q. Zhao, J. Zhang, Graphene-based non-noble-metal Co/N/C catalyst for oxygen reduction reaction in alkaline solution, J. Power Sources. 243 (2013) 65–71. doi:10.1016/j.jpowsour.2013.06.007.

[34] P. Bazylewski, D.W. Boukhvalov, A.I. Kukharenko, E.Z. Kurmaev, A. Hunt, A. Moewes, Y.H. Lee, S.O. Cholakh, G.S. Chang, The characterization of Co-nanoparticles supported on graphene, RSC Adv. 5 (2015) 75600–75606. doi:10.1039/C5RA12893E.

[35] E. Raymundo-Piñero, D. Cazorla-Amorós, A. Linares-Solano, J. Find, U. Wild, R. Schlögl, Structural characterization of N-containing activated carbon fibers prepared

from a low softening point petroleum pitch and a melamine resin, Carbon. 40 (2002) 597–608. doi:10.1016/S0008-6223(01)00155-5.

[36] E. Raymundo-Piñero, D. Cazorla-Amorós, A. Linares-Solano, The role of different nitrogen functional groups on the removal of SO_2 from flue gases by N-doped activated carbon powders and fibres, Carbon. 41 (2003) 1925–1932. doi:10.1016/S0008-6223(03)00180-5.

[37] I.G. Casella, M. Contursi, Cobalt oxide electrodeposition on various electrode substrates from alkaline medium containing Co-gluconate complexes: A comparative voltammetric study, J. Solid State Electrochem. 16 (2012) 3739–3746. doi:10.1007/s10008-012-1794-4.

[38] H.J. Pan, C.Y. Lin, U.S. Mohanty, J.H. Chou, Synthesis of Sn-3.5Ag Alloy Nanosolder by Chemical Reduction Method, Mater. Sci. Appl. 2 (2011) 1480–1484. doi:10.4236/msa.2011.210199.

[39] J. Liu, L. Jiang, Q. Tang, B. Zhang, D.S. Su, S. Wang, G. Sun, Coupling effect between cobalt oxides and carbon for oxygen reduction reaction, ChemSusChem. 5 (2012) 2315–2318. doi:10.1002/cssc.201200563.

[40] A. Bonakdarpour, M. Lefevre, R. Yang, F. Jaouen, T. Dahn, J.-P. Dodelet, J.R. Dahn, Impact of Loading in RRDE Experiments on Fe–N–C Catalysts: Two- or Four-Electron Oxygen Reduction?, Electrochem. Solid-State Lett. 11 (2008) B105. doi:10.1149/1.2904768.

[41] Y. Dong, K. He, L. Yin, A. Zhang, A facile route to controlled synthesis of Co 3 O 4 nanoparticles and their environmental catalytic properties, Nanotechnology. 18 (2007) 435602. doi:10.1088/0957-4484/18/43/435602.

[42] J. Xiao, Q. Kuang, S. Yang, F. Xiao, S. Wang, L. Guo, Surface structure dependent electrocatalytic activity of Co_3O_4 anchored on graphene sheets toward oxygen reduction reaction., Sci. Rep. 3 (2013) 2300–2307. doi:10.1038/srep02300.

[43] M. Wang, Y. Hou, R.C.T. Slade, J. Wang, D. Shi, D. Wexler, H. Liu, J. Chen, Core-Shell Co/CoO Integrated on 3D Nitrogen Doped Reduced Graphene Oxide Aerogel as an Enhanced Electrocatalyst for the Oxygen Reduction Reaction, Front. Chem. 4 (2016) 1–10. doi:10.3389/fchem.2016.00036.

Chapter 6.

General conclusions

General Conclusions

This PhD thesis focuses on understanding the performance of electrocatalysts based on carbon materials for ORR. In order to get knowledge about the nature of active sites of these catalysts for ORR, carbon based samples with different compositions, porosities and structures were prepared and/or selected. Regarding the ORR catalysts doped with non-noble metal and heteroatoms, catalysts based on cobalt nanoparticles supported on MWCNTs have been synthesized using different synthesis strategies. Furthermore, as the metal and heteroatoms free ORR catalysts, carbon materials containing different carbon structures and porous textures were selected. These samples include graphite, carbon blacks, microporous char, commercial and KOH activated carbons, carbon nanofiber, MWCNTs, SWCNTs and herringbone CNTs. The prepared and selected samples were extensively characterized regarding physicochemical and electrochemical properties and their electrocatalytic activity to ORR has been measured. From these results, important insights regarding the nature of the catalytic active sites of ORR were obtained which could be applied in the development of cathodic materials in FCs.

The relationship between ORR activities and carbon-oxygen gasification properties were quantitatively identified for the materials with different carbon structures and porosities. As the gasification parameters, active surface area (ASA) and reactivity for carbon-oxygen reaction were determined. In general, the ORR activities of carbon materials increase with increasing the ASA. However, the sample containing the highest ASA does not show the highest ORR current and electron transfer numbers. Interestingly, for a similar ASA value, CNTs based samples showed higher ORR activities and carbon gasification reactivities than non-CNTs based samples. These results suggest that the active sites on CNTs have higher activity toward ORR and carbon gasification. By checking the absence of impurities and the presence of a low amount of surface oxygen groups by TPD and XPS analyses, it was clarified that not only active edge sites measured by ASA but also the structure of carbon materials are the critical factors determining ORR activity and the possibility of enabling a 4e$^-$ reaction pathway. The unique features of CNTs structure (curvature, helicity, bond strains, presence of Stone-Wales defects) can be responsible for such increase in ORR activity. In addition, ORR activity and carbon gasification reactivity were linearly correlated which suggests that both reactions share the same active sites as well as some steps of the reaction mechanisms. In addition, it has been found that CNTs containing the highest amount of ASA and a low number of graphene layers (as in the case of SWCNT) could be promising materials for designing effective ORR catalysts, what could be a potential alternative for the development of cathodic materials in FCs.

The role of porosity, and more specifically, microporosity, in the performance of carbon materials as ORR catalysts in alkaline medium was studied. Porous carbons with different porosities such as two carbon blacks, a microporous char and a KOH-activated activated carbon in absence of any additional catalysts, have been selected and their ORR performance in alkaline-media was determined. All the selected carbon materials showed a two-wave electrocatalytic process, where the limiting current and the number of electron transferred increase as the potential decreases. This two-wave process indicates that oxygen is reduced to hydrogen peroxide in a first step at intermediate overpotentials, while hydrogen peroxide is subsequently reduced to water at higher overpotentials. The limiting current and onset potential of the second wave is undoubtedly related to the amount of microporosity, and H_2O_2 electrochemical reduction tests have confirmed that the second wave could be related to the reduction of this molecule. In accordance to these findings, a model that takes into account both charge transfer reactions and the mass transfer rate of O_2 and H_2O_2 has been proposed. This mathematical model successfully reproduces the experimental electrochemical response during ORR of the analyzed porous carbon materials.

CNTs (MWCNTs) loaded with different contents of Co nanoparticles were prepared by a facile synthesis method consisting in a mixture of CNTs, a surfactant, cobalt nitrate and a reducing agent followed by their pyrolysis. The CNTs loaded with only 1 wt.% of Co NPs prepared by a facile method using PVP, $NaBH_4$ and a subsequent heat treatment at 500 °C under N_2 atmosphere, demonstrates both similar catalytic activity and stability than Pt/Vulcan (20 wt.% Pt on Vulcan) in alkaline electrolyte. Higher ORR activity is observed for smaller size of Co NPs catalysts due to the enlarged interface between Co species and CNTs. Moreover, the addition of PVP and $NaBH_4$ during the preparation procedure is necessary for obtaining the highest activity since it favors the formation of lower oxidation states for Co species and the formation of a N-doped carbon shell. Finally, it was elucidated that the Co-containing catalysts with small particle size, low Co oxidation states and pyridinic N and quaternary N groups in the carbon framework, have the optimum combination to create the most active sites for ORR.

Chapter 7.

Resumen y conclusiones generales

7-1, Resumen

En los últimos años una gran variedad de catalizadores basados en materiales carbonosos y libres de metales, se han estudiado para mejorar su actividad catalítica en la reacción de reducción de oxígeno (ORR de sus siglas en inglés). Sin embargo, el conocimiento sobre los sitios activos y el mecanismo de reacción aún es confuso y controvertido. Por otro lado, sí se ha realizado una investigación extensa sobre la reacción de gasificación carbón-oxígeno de la que se obtuvieron evidencias claras sobre los sitios activos y el mecanismo de reacción. Se concluye que las reacciones de transferencia de oxígeno en los materiales carbonosos son el núcleo de los procesos de gasificación y combustión y, se ha avanzado significativamente en la compresión de los aspectos fundamentales. Si fuera posible comprender si los sitios que participan en la gasificación y en la ORR son diferentes o no, se podría llegar a entender el mecanismo de la ORR y diseñar adecuadamente la superficie de los materiales carbonosos. Por tanto, el objetivo de la primera parte de la Tesis (Capítulo 3) es intentar elucidar la relación entre las propiedades de la reacción de la gasificación carbón-oxígeno y la actividad electrocatalítica en la ORR.

Por este motivo, se han seleccionado materiales carbonosos de diferentes estructuras y porosidades tales como, grafito (KS4), carbonizado microporoso (AC), carbón activado (YPF), negro de carbón (Vulcan y CB), nanofibras de carbón (CNF) y nanotubos de carbono (CNTs, de sus siglas en inglés) (MWCNT, SWCNT y herring). Todos estos materiales fueron desmineralizados para eliminar la materia inorgánica. En la reacción de gasificación carbón-oxígeno se han determinado los parámetros de reactividad y área superficial activa (ASA). El concepto de ASA, que se deriva de los estudios de gasificación, ha sido extremadamente útil para comprender la reactividad de los materiales carbonosos. La reactividad es otra medida muy utilizada para caracterizar el comportamiento en la reacción de gasificación de estos materiales. Una vez que se han determinado las propiedades estructurales y electroquímicas de estos materiales seleccionados, se han llegado a conclusiones sobre el mecanismo de la ORR en relación con las propiedades de la reacción de gasificación carbón-oxígeno.

Las imágenes de microscopía electrónica de transmisión (TEM, de sus siglas en inglés), indican que las muestras seleccionadas en este estudio tienen una estructura muy diferente. Estructuras tubulares, esféricas y ordenadas se observan para las muestras KS4, Vulcan, MWCNT, SWCNT y herring. Por el contrario, las muestras AC, CB, YPF y CNF presentan una estructura altamente desordenada. Además, el diámetro de los nanotubos sigue el orden Herring>MWCNT>SWCNT, lo que está de acuerdo con sus valores de área superficial específica. Los perfiles de desorción a temperatura programada (TPD, de sus siglas en inglés) confirman la eliminación de la mayoría de los complejos oxigenados de la superficie del material de carbón mediante un tratamiento térmico a 920ºC. Por tanto, el efecto de los grupos funcionales oxigenados en la actividad electrocatalítica a ORR debería ser despreciable para estas muestras seleccionadas. El ASA de las muestras preparadas se midió en aire sintético a 250ºC empleando un equipo de termogravimetría. La reactividad para la reacción carbón-oxígeno se determinó en aire sintético a temperaturas entre 480ºC y 550ºC. Para las muestras estudiadas KS4, Vulcan, CB y CNTs se ha medido un ASA relativamente baja (menor de 14 $m^2 g^{-1}$). Por el contrario, las muestras AC, CNF e YPF, que presentan una estructura desordenada, tienen mayores valores de ASA (>20 $m^2 g^{-1}$).

De acuerdo con resultados previos, en esta Tesis Doctoral se ha observado una buena correlación entre el ASA y la reactividad para los materiales carbonosos estudiados. Es interesante destacar que la pendiente de la representación de la reactividad frente al ASA para los CNTs es mayor que para el resto de muestras, independientemente de la temperatura empleada para determinar la reactividad.

A pesar de que la etapa de disociación del O_2 en CNTs puede ser más exotérmica y espontánea que en el grafeno, las mayores reactividades de las muestras CNTs probablemente estén relacionadas con su estructura tubular única. Ebbesen y col [1]. han investigado la gasificación de CNTs con oxígeno y han reportado que la acusada curvatura local, la geometría imperfecta y la presencia de anillos de carbono de 5 miembros son los responsables de las mayores reactividades de estos materiales. Yao y col [2]. han concluido que la oxidación de CNTs está influenciada por la curvatura, anillos de 5 y 7 miembros y probablemente, por la helicidad. La helicidad es un factor característico de los CNTs que implica la existencia de sitios con mayor potencial químico donde la oxidación puede ocurrir preferencialmente. Más específicamente, se mencionó que al disminuir el diámetro del tubo aumenta la curvatura y la deformación de los pentágonos localizados en el extremo del tubo. Por tanto, los CNTs con menor diámetro se oxidan antes que los de mayor diámetro. Las elevadas reactividades de la muestra SWCNTs y de ésta tratada con HNO_3 (SWCNT_ HNO_3), se podría explicar por su menor diámetro (1-2 nm). Morishita y col [3]. estudiaron la gasificación de MWCNTs. Los cambios en el aspecto de un MWCNT en la etapa inicial de gasificación se evaluaron mediante observación TEM en un punto fijo. Estas imágenes TEM indicaron que la gasificación ocurría preferencialmente en los defectos estructurales de los MWCNTs. Puesto que la muestra SWCNT_ HNO_3 contiene una mayor concentración de defectos que SWCNTs su reactividad es mayor.

En resumen, muestras de materiales carbonosos basadas en CNTs muestran mayores reactividades que los materiales que no poseen esta estructura, a pesar de su menor ASA (< 9.4 $m^2 g^{-1}$). Como se ha mencionado anteriormente, el ASA se puede considerar como una medida del número de sitios activos para la gasificación del carbón. Por tanto, se puede concluir que la actividad intrínseca de los sitios activos en CNTs es mayor que en los otros materiales carbonosos de estructura no tubular. En lo que respecta a la actividad en ORR, SWCNT_ HNO_3 presenta la mayor densidad de corriente y el mayor número de electrones (n) en la reacción, mientras que la muestra KS4 presenta los valores más bajos de ambos parámetros. En general, las muestras basadas en CNTs tienen mayor actividad electrocatalítica que las que no tienen esta estructura tubular. Además, la densidad de corriente que se alcanza en la región controlada por difusión para las muestras CNTs es mayor de 2.9 mA cm^{-2}, lo que corresponde a un mecanismo de ORR mediante 2 electrones. Puesto que el número de electrones intercambiados en la reacción, no alcanza el valor de 4, las densidades de corriente medidas para las muestras CNTs podrían ser el resultado de la combinación de diferentes sitios activos que catalizan mediante mecanismos de transferencia electrónica de 2 y 4 electrones. Esto indica que existen sitios en la superficie del material carbonoso que pueden catalizar la reacción mediante una etapa de 4 electrones y que su concentración es mayor en la muestra SWCNT_ HNO_3.

Para profundizar en la relación entre las propiedades de gasificación de carbón con oxígeno y en las actividades en ORR, se ha estudiado la relación entre densidad de corriente y n con el ASA y con la reactividad. Los resultados muestran que la densidad de corriente y n aumentan con el ASA, lo que indica que los sitios medidos son sitios con mayor actividad hacia la ORR. Merece destacar que, como se observó anteriormente en los experimentos de reactividad, la pendiente de la densidad de corriente frente al ASA es mayor para las muestras CNTs que para las muestras que no presentan esta estructura. Sin embargo, tanto la densidad de corriente como n se pueden describir correctamente para ambos tipos de muestras mediante la medida de la reactividad de la reacción de gasificación. Esta relación proporcional entre reactividad y densidad de corriente y n, muestra por primera vez que la reacción de gasificación de carbón y la ORR comparten sitios activos y, probablemente también, algunas de las etapas iniciales del mecanismo de reacción, independientemente de la porosidad y estructura de los materiales carbonosos. Las observaciones mediante TEM han mostrado que los materiales estudiados tienen diferentes estructuras, mientras que los análisis mediante TPD y XPS indican que todas las muestras tienen una cantidad muy pequeña de grupos oxigenados, así como de otros heteroátomos. Puesto que el efecto de los heteroátomos en la actividad en ORR se puede descartar, las diferencias observadas deben estar determinadas por las diferencias estructurales. En este trabajo de Tesis, la mayor actividad hacia la ORR y la mayor reactividad de gasificación se han medido para los SWCNT que tienen una mayor concentración de defectos (SWCNT_ HNO_3). Esto confirma que la combinación entre un gran número de sitios activos de tipo borde, una elevada curvatura, la helicidad y una elevada conductividad eléctrica, es la más adecuada para el desarrollo de los materiales carbonosos más activos hacia la ORR.

El efecto de la porosidad en la cinética y mecanismo de la ORR por materiales carbonosos es a menudo ignorado y cuando éste se tiene en cuenta la presencia de especies catalíticas dificulta la obtención de conclusiones definitivas. Así, solo existen unos pocos trabajos donde se estudia de forma sistemática el papel de la microporosidad en la ORR en materiales carbonosos. En este sentido Appleby y Marie [4] han publicado estudios cinéticos de ORR realizados en un gran número de materiales carbonosos en disolución alcalina, incluyendo varios negros de carbón y carbones activados. Estos autores han encontrado que la actividad hacia la ORR aumenta linealmente con el área BET para negros de carbón, mientras que no se encontró una tendencia clara en el caso de carbones activados. Estos autores indican que aunque la elevada área superficial de los carbones activados debería proporcionar una mayor cantidad de sitios activos para la ORR, éstos, que en estos materiales se encuentran mayoritariamente en los microporos, no son accesibles al electrolito, al oxígeno disuelto o a las especies HO_2^- solvatadas, lo que explica por qué su actividad catalítica es menor que la esperada atendiendo a su área BET. Recientemente, Liu y col [5]. analizaron la influencia de la micro y meso porosidad en la ORR y pudieron concluir que la actividad aumenta por la presencia de microporosidad y que la mesoporosidad es necesaria para facilitar la accesibilidad a los sitios activos. Por otro lado, Seredych y col [6]. prepararon catalizadores a partir de un material carbonoso ultramicroporoso hidrofóbico. Los experimentos de ORR mostraron una relación inversa entre el tamaño del microporo y el volumen de éstos (especialmente para los de tamaño menor de 0.7 nm) y la actividad catalítica a bajos potenciales. Los autores proponen que el dioxígeno puede adsorberse fuertemente en los ultramicroporos hidrofóbicos, lo que produce un debilitamiento en el enlace O-O que favorece la disociación del dioxígeno. Así mismo, también observan que la presencia de porosidad ancha de carácter hidrofílico es crítica para conseguir una buena transferencia de oxígeno a los ultramicroporos.

Así, en la segunda parte de esta Tesis (Capítulo 4) se presenta un estudio detallado del efecto de la porosidad, y en particular de la microporosidad, en electrodos preparados con materiales carbonosos en la ORR en condiciones alcalinas. Así, se han seleccionado varios materiales carbonosos con propiedades texturales diferentes pero química superficial parecida. Tras determinar la actividad hacia la ORR se ha propuesto un modelo cinético para esta reacción en materiales carbonosos porosos que tiene en cuenta el papel crítico de la microporosidad en la ORR. De acuerdo con este modelo, es posible calcular la densidad de corriente para esta reacción con buena correlación con los datos experimentales.

En este estudio se utilizaron: un carbón activado microporoso obtenido mediante activación química con KOH de una antracita española (KUA), un carbonizado microporoso (AC) y dos negros de carbón (Vulcan y CB). Los resultados de adsorción de gases muestran que en el caso del Vulcan y CB la mayor parte del área superficial procede de la superficie externa de las partículas del negro de carbón, puesto que la contribución de la microporosidad es pequeña comparada con el volumen total de poros (< 25%). La muestra KUA tiene una microporosidad bien desarrollada y también presenta una cierta cantidad de mesoporos. Las muestras AC y CB tienen un volumen de microporos y área BET similares pero un desarrollo de mesoporosidad muy diferente, siendo el volumen de mesoporos cuatro veces mayor en la muestra CB. Finalmente, la muestra Vulcan no contiene microporosidad. Es importante destacar que la porosidad de las muestras de negro de carbón está principalmente relacionada con el tamaño de partícula y que los micro y mesoporos resultan de los espacios vacíos entre las nanopartículas de negro de carbón. Las distribuciones de tamaños de poro confirman que la distribución de tamaños de microporos para la muestra KUA es ancha y estrecha para los otros materiales carbonosos. La mayor parte de la porosidad de la muestra KUA corresponde a la región de los microporos; sin embargo, su amplia distribución de tamaños de poro se extiende a la región de los mesoporos más estrechos. En la región de los mesoporos es posible observar que las muestras AC y negros de carbón presentan una amplia distribución de tamaños, siendo los mesoporos de unos 10 nm los mayoritarios para AC y CB y los de 25 nm para el Vulcan.

Los experimentos de voltametría de barrido lineal (LSV de sus siglas en inglés) realizados en un electrodo rotatorio disco-anillo (RRDE, de sus siglas en inglés) de las muestras AC y CB a una velocidad de rotación de 1600 rpm, muestran un potencial de inicio de reacción similar (0.80 y 0.79 V/RHE, respectivamente). Se debe destacar que la muestra KUA tiene un mayor potencial de inicio de reacción (0.85 V/RHE). El perfil voltamétrico de todas las muestras presenta dos ondas de reducción, que están menos pronunciadas en la muestra KUA. La forma de los perfiles voltamétricos para todas las muestras es independiente de la velocidad de rotación, lo que demuestra que este comportamiento no está relacionado con problemas de transferencia de materia externa.

El número de electrones transferidos durante la ORR se ha calculado a partir de la relación entre las corrientes de los electrodos del disco y del anillo de Pt a una velocidad de 1600 rpm y a partir de la ecuación Koutecky-Levich (K-L). La actividad de estas muestras implica un mecanismo de 2 electrones. Un aumento de la polarización catódica del electrodo del disco aumenta la velocidad de la ORR con la participación de un mayor número de electrones (así a 0.05 V/RHE, el número de electrones que se obtiene mediante RRDE es 2.4, 2.7, 2.6 y 3.0 para las muestras Vulcan, CB, AC y KUA, y 2.5, 3.1, 2.8 y 3.4 de acuerdo con la ecuación K-L). El aumento en el número de electrones transferidos en dicha región de potencial parece estar relacionado con la presencia de microporosidad más que con cualquier otro parámetro textural, estructural o de química superficial.

Por otro lado, se ha analizado la reducción electroquímica de H_2O_2 en condiciones similares a las empleadas en las medidas de ORR. El potencial de inicio de la reducción electroquímica de este compuesto sigue el orden KUA >> CB ~ AC > Vulcan, que es similar al del volumen de microporos. De estos resultados podemos proponer que la reducción de dioxígeno a agua en los materiales carbonosos ocurre mediante dos etapas consecutivas de dos electrones; la reducción de O_2 a H_2O_2 seguida de la reducción de H_2O_2 a H_2O y que la presencia de microporos influye en el tiempo de residencia de los reactivos y productos de la reacción en el material carbonoso.

El modelo cinético de ORR propuesto en este trabajo de Tesis se ha utilizado para ajustar los perfiles LSV a 1600 rpm de los materiales de carbón estudiados y se han obtenido los parámetros cinéticos optimizados para cada muestra. Este modelo cinético puede reproducir los experimentos de LSV de ORR de los materiales carbonosos porosos obtenidos en el sistema RRDE.

Se ha realizado un análisis de la representaciones de Tafel de las curvas LSV en la región de control cinético de transferencia electrónica, con el fin de calcular los parámetros cinéticos de dicha etapa de transferencia electrónica correspondiente a la reducción de O_2 a H_2O_2. El parámetro $\boldsymbol{\alpha_{O2}}$ (coeficiente de transferencia de electrones del O_2) se calculó de la pendiente de Tafel, y k^r_{0,O_2} (constante de velocidad de transferencia electrónica del O_2) de la intersección con el eje de ordenadas (densidad de corriente de intercambio). Los parámetros cinéticos obtenidos de las representaciones de Tafel y del ajuste de los datos experimentales con el modelo propuesto son comparables. Además, hay que destacar que las constantes de velocidad transferencia electrónica están linealmente relacionadas con el volumen de microporos de las muestras. También se observa una correlación similar entre este parámetro y el área BET. Sin embargo, no hay relación con el volumen de mesoporos. Todos estos resultados muestran que la mayor cantidad de sitios activos para la ORR se encuentran en los microporos. En el caso de la relación $\boldsymbol{k^r_{0,H_2O_2}/k^f_{H_2O_2}}$ (constante de velocidad de transferencia electrónica del H_2O_2/coeficiente efectivo de transferencia de materia del H_2O_2 dentro de los poros), la mejor correlación observada con los diferentes parámetros texturales es con el volumen de microporos. El bajo valor del coeficiente de transferencia electrónica del H_2O_2 ($\alpha_{H_2O_2}$) y la correlación positiva entre $\boldsymbol{k^r_{0,H_2O_2}/k^f_{H_2O_2}}$ y el volumen de microporos podrían indicar que la reacción tiene lugar dentro de la microporosidad, donde existe una mayor resistencia a la transferencia electrónica. En este sentido, se observa una tendencia negativa entre $\alpha_{H_2O_2}$ y el volumen de microporos.

En resumen, la actividad de los materiales carbonosos porosos en la ORR en medio alcalino y en ausencia de otra especie catalítica, está indudablemente relacionada con su porosidad. Mediante la caracterización de materiales carbonosos con diferentes distribuciones de tamaños de poro y estructura porosa, se ha podido demostrar en esta Tesis Doctoral que la ORR se puede describir adecuadamente mediante un proceso en dos etapas en el cual el dioxígeno se reduce a peróxido de hidrógeno en una primera etapa a potenciales intermedios, mientras que el peróxido de hidrógeno es posteriormente reducido a hidróxido a potenciales más negativos. La combinación de estas dos reacciones aumenta el número de electrones transferidos de la reacción global a valores intermedios entre 2 y 4. Cabe destacar que los potenciales de inicio para ambas reacciones de reducción están relacionados con la presencia de microporosidad.

En este trabajo de Tesis se ha desarrollado un modelo matemático de dos etapas de reducción consecutivas que describe adecuadamente la velocidad de reacción y el número de electrones transferidos durante la ORR y medidos experimentalmente y que tiene en cuenta la velocidad de transferencia de materia de O_2 y H_2O_2 en la porosidad de los materiales carbonosos. Este trabajo puede ser una referencia para un análisis más detallado de la ORR de nuevos electrocatalizadores basados en materiales carbonosos en los que el efecto de la porosidad es frecuentemente ignorado.

La mayor velocidad de la ORR en medio alcalino permite el uso de electrocatalizadores basados en metales no preciosos. En este sentido se ha estudiado una gran variedad de electrocatalizadores para reemplazar a los basados en platino. En este sentido los materiales carbonosos libres de metales y dopados con heteroátomos (N, S, P, B y F), óxidos de metales de transición (p.e., CoO, Co_3O_4, Cu_2O, MnO_2) y complejos metal-nitrógeno (Co-Nx, Fe-Nx) soportados en nanomateriales carbonosos son candidatos prometedores como catalizadores basados en metales no preciosos. En concreto, los catalizadores basados en CoOx soportados en materiales carbonosos constituyen una de las alternativas más prometedoras como electrodos para esta reacción. Se ha publicado que CoOx soportados en grafeno y otros materiales carbonosos son electrocatalizadores con una elevada actividad. Con el fin de mejorar la actividad catalítica y la estabilidad algunos estudios se han centrado en la preparación de CoOx dopado con nitrógeno; por este motivo, diferentes ligandos que contienen nitrógeno se han utilizado como precursores de estos compuestos de cobalto.

En la tercera parte de esta Tesis Doctoral (Capítulo 5) se han analizado diferentes métodos de síntesis y soportes carbonosos para la obtención de electrocatalizadores basados en nanopartículas de CoOx (CoNPs). En este trabajo se han preparado catalizadores basados en CoNPs soportados en MWCNTs mediante un método de síntesis sencillo consistente en la pirólisis de una mezcla de los MWCNTs, un surfactante, un precursor metálico ($Co(NO_3)_2{\bullet}6H_2O$) y un agente reductor. Se han aplicado diferentes condiciones de síntesis para poder investigar la relación entre diferentes propiedades, tales como la cantidad de CoOx, tamaño de las CoNPs, composición química y estados de oxidación del Co, en la actividad frente a la ORR. Para la preparación de las muestras los MWCNTs se purificaron usando acido clorhídrico 1 M e hidróxido de sodio 6 M. La cantidad necesaria del precursor de cobalto ($Co(NO_3)_2{\bullet}6H_2O$) se disuelve en etanol para tener una cantidad final nominal de metal de 1, 9 y 17 % en peso de Co. Junto con el precursor de cobalto se añade la cantidad necesaria de polivinilpirrolidona (PVP) para conseguir una relación molar PVP/Co=10. Tras una agitación vigorosa, se añaden los MWCNTs. Posteriormente se añade borohidruro sódico, agente redactor, a la mezcla de reacción que se encuentra a 0ºC y en un baño de hielo. Los materiales basados en Co y MWCNT se filtran y se secan a 80ºC. Finalmente, las muestras se tratan térmicamente a 500 ºC en nitrógeno durante 1 h para eliminar el PVP. Estas muestras se han nombrado como CNT_Co_1%_500, CNT_Co_9%_500 y CNT_Co_17%_500. A efectos comparativos se prepararon muestras adicionales modificando el procedimiento de síntesis, así una muestra se preparó con un contenido nominal de metal del 1 % sin utilizar PVP durante la etapa de reducción del precursor de Co (CNT_Co_1%_noPVP_500). Se preparó otra muestra usando una disolución de amoniaco, pero sin la adición del agente reductor, con el fin de aumentar el pH y provocar la precipitación de los óxidos/hidróxidos de cobalto (CNT_Co_1%_NH_3_500).

El análisis químico mediante ICP-OES muestra que el contenido en cobalto de las muestras CNT, CNT_Co_1%_500, CNT_Co_9%_500 y CNT_Co_17%_500 es 0, 1.0, 4.7 y 8.2 % en peso, respectivamente, mostrando que fue posible la incorporación del CoOx en los MWCNTs con contenidos en cobalto suficientemente diferentes. Los resultados de XPS indican que en las síntesis realizada empleando PVP y el agente reductor, la mayoría del cobalto se encuentra como Co(II), junto con pequeñas cantidades de Co metálico. Si no se emplea agente reductor se detectan especies de Co(III). Además, la utilización de borohidruro sódico favorece la formación de grupos nitrogenados piridínicos y nitrógeno cuaternario así como un mayor contenido en nitrógeno tras la etapa de pirólisis. Las imágenes TEM de las muestras preparadas muestran que el tamaño medio de las nanopartículas aumenta con el contenido en Co cuando se comparan muestras preparadas con el mismo procedimiento experimental. Sin embargo, el tamaño medio de nanopartícula es prácticamente el mismo en todas las muestras que contienen un 1 % en peso de Co y que se han preparado con diferentes métodos. Estos resultados TEM indican que la cantidad de Co en los catalizadores tiene una mayor contribución al tamaño de partícula de las CoNPs que los agentes químicos utilizados en la síntesis. Además, la imagen TEM del catalizador CNT_Co_17%_500, que es uno de los materiales preparados usando PVP y borohidruro sódico, muestra la existencia de una película delgada de carbono alrededor de las CoNPs que podría proceder de la carbonización del PVP y que es quien contiene la mayoría de las especies nitrogenadas detectadas.

Las medidas de ORR en estos catalizadores muestran que existe una relación entre el contenido en cobalto y el valor de la corriente límite (LC, de sus siglas en inglés) entre 0.3 y 0.7 V/RHE, observándose una disminución con el contenido en Co. El tamaño medio de CoNPs sigue el orden CNT_Co_17%_500 (13.1 nm) > CNT_Co_9%_500 (10.8 nm) > CNT_Co_1%_500 (8.9 nm). Por el contrario, la LC sigue el orden CNT_Co_1%_500 > CNT_Co_9%_500 > CNT_Co_17%_500. Los resultados sugieren que al disminuir el tamaño de las CoNPs, la actividad electrocatalítica aumenta lo que puede explicarse considerando que la actividad aumenta debido al incremento en la interfase entre las CoNPs y los MWCNTs.

Las corrientes de ORR de los catalizadores que tienen tamaño de partícula similar pero obtenidos mediante diferentes procedimientos, proporcionan resultados sumamente interesantes. La muestra CNT_Co_1%_500 presenta la mayor actividad hacia la ORR. El contenido en nitrógeno de esta muestra es 0.77 % atómico mientras que en el catalizador CNT_Co_1%_noPVP_500 no se detecta nitrógeno. Esto es debido a que la descomposición del PVP durante el pretratamiento del catalizador, genera la presencia de una cierta cantidad de nitrógeno en las proximidades de los iones Co puesto que las moléculas de PVP están inicialmente coordinando a los iones Co en la superficie de las CoNPs. La presencia de las especies Co-N en contacto con los MWCNTs pueden constituir sitios activos con una mayor actividad hacia la ORR como así ha sido propuesto por otros autores. Como se explicó anteriormente, los resultados de XPS muestran tres diferencias importantes entre las muestras CNT_Co_1%_500 y CNT_Co_1%_NH_3_500: (i) se detecta un mayor estado de oxidación en el Co cuando no se usa borohidruro sódico; (ii) se observa Co metálico cuando se emplea borohidruro sódico y (iii) el contenido en nitrógeno de los catalizadores preparados con borohidruro sódico es mayor. Por tanto, parece que la interacción del Co reducido con PVP es más eficiente favoreciendo la formación de especies Co-N tras el tratamiento térmico que son las que presentan una mayor actividad electrocatalítica.

La durabilidad de los electrocatalizadores es un factor que determina la vida de la pila de combustible. La estabilidad de los catalizadores basados en cobalto se ha medido mediante cronoamperometría en un electrodo rotatorio (RDE) bajo condiciones de estado estacionario de transferencia de materia (0.65 V/RHE). Estos tests de estabilidad se han comparado con los de un electrocatalizador comercial Pt/Vulcan con un contenido en platino del 20 % en peso. También se ha analizado el envenenamiento por metanol mediante la adición de metanol 1 M en el electrolito tras 2 h de reacción. Incluso tras la adición de metanol, el catalizador CNT_Co_1%_500 mantiene más de un 80 % del valor inicial de corriente durante 3 h. Sin embargo, la corriente del catalizador Pt/Vulcan disminuyó inmediatamente tras la adición a corriente prácticamente cero. Estos resultados indican que los catalizadores basados en cobalto son adecuados en lo que respecta a estabilidad y resistencia al envenenamiento por metanol. Además, también se realizaron ensayos de durabilidad mediante ciclado de potencial empleando voltametría cíclica. El ciclado se realizó en una disolución saturada en oxígeno durante 500 ciclos. Las curvas LSV antes y después de los 500 ciclos demuestran que el potencial a mitad de onda para las muestras CNT_Co_1%_500 y Pt/Vulcan se desplazó en 5 mV y 15 mV respectivamente a valores menos positivos. Estos resultados implican que nuestros catalizadores presentan una buena estabilidad en medio alcalino y son muy interesantes como catalizadores en el cátodo de pilas de combustible alcalinas.

7-2, Conclusiones generales

Este trabajo de Tesis Doctoral se ha centrado en comprender el comportamiento de electrocatalizadores basados en materiales carbonosos para la reacción de reducción de oxígeno. Con el fin de profundizar en el conocimiento de la naturaleza de los sitios activos de catalizadores basados en materiales carbonosos para esta reacción, se han seleccionado o preparado muestras con diferentes composiciones, texturas porosas y estructuras. En lo que respecta a electrocatalizadores dopados con metales no preciosos y heteroátomos, se han preparado catalizadores de nanopartículas de cobalto soportadas en nanotubos de carbono de pared múltiple y se han empleado diferentes estrategias de síntesis. En lo que respecta a catalizadores libres de metales y heteroátomos, se han seleccionado materiales carbonosos con diferentes estructuras y texturas porosas. Estas muestras incluyen grafito, negros de carbón, un carbonizado microporoso, un carbón activado comercial, un carbón activado preparado mediante activación con KOH, nanofibras de carbón, nanotubos de carbono de pared múltiple, nanotubos de carbono de pared sencilla y nanotubos de carbono de tipo “herringbone”. Las muestras preparadas y seleccionadas se han caracterizado de forma muy detallada en lo que respecta a sus propiedades físicoquímicas y electroquímicas, y se ha medido su actividad electrocatalítica hacia la ORR. De estos resultados se han conseguido importantes avances en el conocimiento del papel que los sitios activos de catalizadores basados en materiales carbonosos desempeñan en dicha reacción. Estos conocimientos y los materiales derivados pueden utilizarse en el desarrollo de cátodos para pilas de combustible en medio alcalino.

En esta Tesis Doctoral, además, se ha podido identificar de forma cuantitativa la relación entre la actividad hacia la ORR y parámetros de la reacción de gasificación carbón-oxígeno con materiales con diferentes estructuras y porosidades y con una baja cantidad de grupos oxigenados superficiales. En lo que respecta a los parámetros de gasificación, se han determinado el área superficial activa y la reactividad para la reacción carbón-oxígeno en los diferentes materiales. En general la actividad electrocatalítica de los materiales carbonosos aumenta con el ASA; sin embargo, la muestra con la mayor ASA no presenta la mayor actividad electrocatalítica y el mayor número de electrones transferidos en la reacción. Además, para un valor de ASA comparable, las muestras basadas en nanotubos de carbono presentan mayores actividades electrocatalíticas y reactividades de gasificación de carbón que las muestras que no tienen esta estructura. Estos resultados sugieren que los sitios activos presentes en los CNTs tienen una mayor actividad hacia la ORR y la gasificación de carbón. Por tanto, no solo los sitios activos medidos mediante el ASA sino también la estructura de los materiales carbonosos, son factores críticos que determinan la actividad electrocatalítica y la posibilidad de que la reacción transcurra mediante la transferencia de 4 electrones hacia la formación de agua. Las propiedades únicas estructurales de los CNTs (curvatura, helicidad, deformación de enlaces y presencia de defectos) pueden ser las responsables del aumento observado de la actividad electrocatalítica, con respecto al resto de materiales carbonosos. Además, la actividad electrocatalítica y la reactividad de gasificación de carbón están linealmente relacionadas, lo que sugiere que ambas reacciones comparten los mismos sitios activos así como algunas etapas de los mecanismos de reacción. Finalmente, se ha encontrado que los CNTs de mayor área superficial activa y menor número de capas de grafeno (como es el caso de SWCNTs) podrían ser materiales prometedores para diseñar catalizadores excelentes para la reacción estudiada, lo que puede ser una alternativa potencial para el desarrollo de electrocatalizadores para las pilas de combustible alcalinas.

El papel de la porosidad, y más específicamente, la microporosidad en el comportamiento de materiales carbonosos como catalizadores de la ORR en medio alcalino, se ha analizado con detalle en esta Tesis Doctoral. Para dicho estudio, se han seleccionado o preparado materiales carbonosos porosos con diferentes porosidades tales como negros de carbón, un carbonizado microporoso y un carbón activado mediante KOH, que no contienen ningún otro catalizador. Todos los materiales estudiados mostraron un perfil voltamétrico con la presencia de dos ondas de reducción, en las cuales la corriente límite y el número de electrones transferidos aumentan al desplazarse a potenciales menos positivos. El primero de estos procesos corresponde a la reducción del dioxígeno a peróxido de hidrógeno, que sucede a potenciales intermedios; y el segundo a la reducción de este intermedio a agua a potenciales menos positivos. La corriente límite y el potencial de inicio del segundo proceso están indudablemente relacionados con la cantidad de microporosidad, y los ensayos de reducción de peróxido de hidrógeno confirman que el segundo proceso está relacionado con la reducción de este compuesto. Con estos resultados se ha propuesto un modelo que tiene en cuenta las reacciones de transferencia electrónica y la velocidad de transferencia de materia del O_2 y H_2O_2. Este modelo matemático describe satisfactoriamente los resultados experimentales durante los experimentos de ORR de todos los materiales carbonosos porosos analizados.

Se han preparado catalizadores basados en nanopartículas de cobalto soportadas en MWCNTs con diferentes contenidos en Co y utilizando un método muy sencillo que emplea CNTs, un precursor de cobalto, un surfactante y un agente reductor que son sometidos a un tratamiento térmico. Los CNTs con un contenido en cobalto de un 1 % en peso y preparados empleando PVP, borohidruro sódico y un tratamiento térmico en nitrógeno a 500 ºC presentan una actividad catalítica y estabilidad similares a las del catalizador comercial Pt/Vulcan con un 20 % en peso de Pt. Los resultados demuestran que la actividad electrocatalítica aumenta al disminuir el tamaño de las nanopartículas debido al aumento de la interfase entre las especies de cobalto y los CNTs. Además, la adición de PVP y borohidruro sódico durante la preparación del catalizador es necesaria para conseguir la máxima actividad catalítica, puesto que favorece la formación de especies de cobalto de menor estado de oxidación y de una película de material carbonoso dopado con nitrógeno. Finalmente, se ha demostrado que los catalizadores que contienen cobalto con tamaños de partícula pequeños, bajos estados de oxidación del cobalto y grupos nitrogenados piridínicos y cuaternarios en la estructura carbonosas tienen la combinación optima de propiedades para conseguir los sitios más activos para la ORR.

7-3, Bibliografía

[1] T.W. Ebbesen, P.M. Ajayan, H. Hiura, K. Tanigaki, Purification of nanotubes, Nature. 367 (1994) 519–519. doi:10.1038/367519a0.

[2] N. Yao, V. Lordi, S.X.C. Ma, E. Dujardin, A. Krishnan, M.M.J. Treacy, T.W. Ebbesen, Structure and oxidation patterns of carbon nanotubes, J. Mater. Res. 13 (1998) 2432–2437. doi:10.1557/JMR.1998.0338.

[3] K. Morishita, T. Takarada, Scanning electron microscope observation of the purification behaviour of carbon nanotubes, J. Mater. Sci. 34 (1999) 1169–1174. doi:10.1023/A:1004544503055.

[4] A.J. Appleby, J. Marie, Kinetics of oxygen reduction on carbon materials in alkaline solution, Electrochim. Acta. 24 (1979) 195–202. doi:10.1016/0013-4686(79)80024-9.

[5] Y. Liu, K. Li, B. Ge, L. Pu, Z. Liu, Influence of Micropore and Mesoporous in Activated Carbon Air-cathode Catalysts on Oxygen Reduction Reaction in Microbial Fuel Cells, Electrochim. Acta. 214 (2016) 110–118. doi:10.1016/j.electacta.2016.08.034.

[6] M. Seredych, A. Szczurek, V. Fierro, A. Celzard, T.J. Bandosz, Electrochemical Reduction of Oxygen on Hydrophobic Ultramicroporous PolyHIPE Carbon, ACS Catal. 6 (2016) 5618–5628. doi:10.1021/acscatal.6b01497.